EFFECT OF TEMPERATURE VARIATION ON THE INTERFACIAL DEBONDING MECHANISMS OF FRP-STRENGTHENED STEEL BEAMS

GUO DONG

PhD

The Hong Kong Polytechnic University
2022

The Hong Kong Polytechnic University

Department of Civil and Environmental Engineering

Effect of Temperature Variation on the Interfacial Debonding Mechanisms of FRP-strengthened Steel Beams

GUO Dong

A thesis submitted in partial fulfilment of the requirements for the degree
of Doctor of Philosophy

July 2022

CERTIFICATE OF ORIGINALITY

I hereby declare that this thesis is my own work and that, to the best of my knowledge and belief, it reproduces no material previously published or written, nor material that has been accepted for the award of any other degree or diploma, except where due acknowledgement has been made in the text.

____ (Signed)

______________Guo Dong_______________(Name of student)

ABSTRACT

Fiber-reinforced polymer (FRP)-strengthened steel structures in service are likely to experience significant temperature variations due to seasonal and diurnal service temperature changes. The temperature variations may influence the interfacial debonding mechanisms in FRP-strengthened steel structures and reduce their load-carrying capacities. The temperature variation effects can be attributed to two aspects: (1) the interfacial thermal stress induced by the different thermal expansion coefficients of FRP and the substrate material; (2) the temperature-dependent properties of the bond line. For FRP-strengthened steel beams, the interfacial debonding may occur at the plate end (i.e., plate-end debonding) and the cracked locations at the intermediate part of beams (i.e., IC debonding). The occurrence of interfacial debonding is relevant to the interfacial bond behavior in these areas. In this thesis, the effects of temperature variation on both plate-end and IC debonding failure mechanisms of FRP-strengthened steel beams are investigated through a comprehensive research program comprising of theoretical derivations, experimental studies and finite element analyses. The work in the thesis is distributed to four major parts: the first part presents the theoretical solutions for analyzing the effect of thermal stress on the plate-end and IC debonding failure of FRP-strengthened un-notched and notched steel beams, respectively; the second part is concerned with the experimental study on the local bond behavior of FRP-to-steel bonded joints at different temperatures; the third and fourth parts are concerned with flexural tests of FRP-strengthened un-notched and notched steel beams, at various temperatures, which corresponded to the plate-end debonding and IC debonding, respectively.

In the first part of this thesis, three closed-form analytical solutions were proposed for analyzing the effect of thermal stress on the debonding failure mechanisms of FRP-strengthened steel beams. The occurrence of plate-end debonding of FRP-strengthened steel beams is associated with the high interfacial stress concentration in both tangential (mode II) and normal (mode I) directions. Two different closed-form solutions were derived based on a simplified mode II analysis and a coupled mixed-mode analysis for predicting the effect of temperature variation on the plate-end debonding failure mechanisms. Regarding the IC debonding, in view of the compressive interfacial stress in the mode I direction near the central notch of FRP-strengthened steel beams, which does not generate damage to the interface, only mode II analysis is considered in the derivation of theoretical solutions to predict IC debonding failure of FRP-strengthened notched steel beams. In all these above-mentioned theoretical analyses, bilinear bond-slip/separation relationships are used for describing the non-linear fracture process of the bond interface in both mode II and mode I directions. All the analytical solutions were validated through comparisons with finite element (FE) analysis results. Then parametric investigations were conducted to indicate how the temperature influences the debonding mechanisms, i.e., a temperature increase leads to a reduced plate-end debonding load while an enhanced IC debonding load and vice versa. The thermal stress effect is more significant when a thicker and stiffener FRP plate is applied.

In the second part of this thesis, double-lap shear tests were conducted on five FRP-to-steel bonded joints at temperatures from -20 ℃ to 60 ℃, to reveal the mode II bond behavior between the FRP plate and the steel substrate. The temperature-dependent bond-slip relationships were derived based on the measured FRP strains. The interfacial shear stiffness was found to decrease as the temperature increases, while the interfacial fracture energy increases from -20 ℃ to 45 ℃ but drops at 60 ℃. While the stiffness of the bonded joints under different temperatures is influenced by the bond-slip relationships and the debonding load is solely dependent on the interfacial fracture energy.

In the third part of this thesis, three-point bending tests were conducted on eleven FRP-strengthened intact steel beams at temperatures from -20 ℃ to 60 ℃, to examine the thermal effect on the structural behavior and plate-end debonding failure of FRP-strengthened steel beams. It was found that the steel beams strengthened with shorter and longer FRP plates failed due to plate-end debonding and FRP rupture, respectively. The debonding load was found to increase slightly when the temperature decreases but drops at an elevated temperature (60 ℃). The plate-end debonding could be eliminated by extending the length of FRP plate to the support location at normal and decreased temperatures, but it still occurred at 60 ℃ because of the significant deterioration of the bonding interface under thermal loading. The two-dimensional (2D) FE analysis incorporating the interfacial bond-slip relationship (i.e., obtained from the double-lap shear tests) was conducted to reproduce the test results and good agreement has been achieved between the FE and experimental results, in terms of the load-deflection curves and local interfacial bond behavior.

In the fourth part of this thesis, four-point bending tests were conducted on twelve FRP-retrofitted steel beams with precast notch at temperatures from -20 ℃ to 80 ℃. All the FRP-retrofitted beams failed by IC debonding. The debonding load was found to increase continuously from -20 ℃ to 60 ℃ but drop significantly at 80 ℃. Considering the FRP-strengthened notched steel beams had different adhesive curing schemes, which may affect the bond-slip relationship between the FRP plate and the steel substrates, a new approach was deployed to define the local bond-slip relationships for FRP retrofitted notched steel beams at various temperatures. Such bond-slip relationships were then adopted in FE modeling to predict the structural responses of FRP retrofitted notched steel beams. The validation of the proposed bond-slip relationship and FE model was verified through comparisons with the experimental results.

Overall, this dissertation provides an in-depth understanding of the effects of temperature variation on the structural behavior and debonding mechanisms of FRP-to-steel bonded joints and FRP-strengthened steel beams. The scientific findings arisen from this dissertation work have provided a solid theoretical background for developing technical guidelines for predicting the debonding failure in FRP-strengthened steel beams with appropriate consideration of the service temperature effect, thus ensuring the safety of the strengthened members.

PUBLICATIONS ARISING FROM THE THESIS

Guo D., Gao W. Y., Fernando D., and Dai Jian-Guo, (2021), "Effect of temperature variation on the plate-end debonding of FRP-strengthened beams: A theoretical study", *Advances in Structural Engineering*, 25:290–305. (Contents of **Chapter 3**)

Guo, D., Zhou, H., Wang, H.P., and Dai Jian-Guo, (2022). "Effect of temperature variation on the plate-end debonding of FRP-strengthened steel beams: coupled mixed-mode cohesive zone modeling." *Engineering Fracture Mechanics*, 108583. (Contents of **Chapter 4**)

Guo D., Gao W. Y., and Dai Jian-Guo, (2021), "Effects of temperature variation on intermediate crack-induced debonding and stress intensity factor in FRP-retrofitted cracked steel beams: An analytical study", *Composite Structures*, 114776. (Contents of **Chapter 5**)

Guo D., Liu Y.L., Gao W. Y., and Dai Jian-Guo, "Bond behavior of CFRP-to-steel bonded joints at different service temperatures: Experimental study and FE modeling." *Construction and Building materials*. (Revised submission, Contents of **Chapter 6**)

Guo D., Gao W.Y., Liu Y.L., and Dai Jian-Guo, "Structural behavior of CFRP-strengthened steel beams at different service temperatures: experimental study and FE modeling." (Under preparation, Contents of **Chapter 7**)

Guo D., Gao W.Y., Liu Y.L., and Dai Jian-Guo, (2023), "Intermediate crack-induced debonding in CFRP-retrofitted notched steel beams at different service temperatures: experimental test and finite element analysis." *Composite structures*, 116388. (Contents of **Chapter 8**)

ACKNOWLEDGEMENTS

First and foremost, I would like to express my sincere gratitude to my PhD supervisor, Prof. Jian-Guo Dai, for his enlightening guidance, enthusiastic supports, continuous encouragements throughout the course of my research. During the past five years, I was very impressed by his deep insight into scientific problems, rigorous attitude to academic research, and responsibility to students. All of these qualities have greatly benefited me, not only in my PhD study but also in my future life.

I am grateful to The Hong Kong Polytechnic University for providing me a PhD studentship and excellent research facilities.

I am grateful to Prof. Wan-Yang Gao at Shanghai Jiaotong University, for helping me to polish my papers and giving me the detailed guidance in research.

I want to express my sincere thanks to Prof. Yun-Lin Liu at Anhui Jianzhu University, not only for providing me the experimental space and facilities but also for giving me the encouragement.

Special thanks are extended to my friends and colleagues at the Department of Civil and Environmental Engineering of the Hong Kong Polytechnic University, especially, Dr. Jun-Qi Huang, Dr. Kai-Di Peng, Dr. Yan-Shuai Wang, Mr. Fei-Long Li, Ms. Lan-Ping Qian, Mr. Ling-Yu Xu, Mr. Zhi-Hao Hao, Mr. Ke-Fan Weng, Mr. Ji-Xiang Zhu, Mr. Sushil Kumar, Dr. Yazan Alrefaei, and Dr. Asad Riaz, not only for their discussions and constructive comments, but also for their encouragement at the difficult times of my studies.

I want to express my sincere thanks to my friends at the Anhui Jianzhu University, especially, Mr. Shi-Tao Zhu, Ms. Ji-Yun Wang, Mr. Kai Liao, Mr. Xiao-Qian Cheng, Mr. Zi-Heng Wang, Mr. Ruo-Yu Wang, Mr. Jia-Qiang Hong, Ms. Meng-Ting Li, Mr. Qiao-Hu, Mr. Fu-Qiang Zhang, Mr. Wen-Hao Zhang, Mr. Yang Yang, Mr. Bei-Jing Hao, Mr. Chang Liu, Mr. Chao-Fan Li, Mr. Hao Cao, Mr. Yi-Fan Han, Mr. Xing-Yu Zhou, Mr. Shao-Cai Wu, Ms. Chun-Ming Wang, Ms. Shang-Wei Huo, Mr. Xu-Dong Chen, not only for their help in the experiment, but also for their useful advises.

Last but, not the least, special thanks are given to my parents, fiancée, grandparents, uncles for their patience, love, support, and encouragement. I want to thank my parents for providing me good study conditions and entitling me with the opportunity to pursue my dream. They shared with me every moment of this work; to them all, this thesis shall be dedicated.

TABLE OF CONTENTS

LIST OF FIGURES

LIST OF TABLES

CHAPTER 1

INTRODUCTION

1.1. GENERAL

Fiber-reinforced polymer (FRP) composites have been widely used in strengthening and retrofitting of reinforced concrete (RC) and steel structures as an externally bonded material in the past two decades, due to their excellent mechanical properties, corrosion-resistance, easy construction, and cost-efficiency. The FRP composite materials used in structural engineering typically consist of glass fibers (i.e., GFRP), aramid fibers (i.e., AFRP), carbon (i.e., CFRP) or basalt fibers (i.e., BFRP) embedded in a matrix of epoxy, polyester, or vinyl ester resin. The type and orientation of fibers can be specifically chosen for a particular application.

The applications of externally bonded (EB) FRP composites in strengthening structural members are based on the exploitation of the high tensile strength and generally can be classified into two categories, bond-critical applications and contact-critical applications. The bond-critical applications mean externally bonding FRP composites on the tensile soffit/flange of the structural members (e.g., beams), to enhance their flexural/shear load-carrying capacity. The contact-critical applications are meant for enhancement of the axial load-carrying capacity and seismic performance of columns by supplying lateral FRP confinement. The present dissertation is focused on the bond-critical applications of EB-FRP in steel structures, and more specifically, on EB-FRP flexurally strengthened steel beams considering combined mechanical and thermal loading effects.

1.2. FRP COMPOSITES IN STRENGTHENING STEEL STRUCTURES

The mechanical performance of steel structures can be deteriorated after a long service period, because of environmental attacks, corrosion, and fatigue loading. To ensure their serviceability and safety, proper remedial actions are needed to recover or even strengthen their load-carrying capacity (e.g., in case of increased service load).

Traditional methods of retrofitting or strengthening steel structures are usually based on bolting or welding extra steel patches to the original structure, to which both methods will impose a considerable amount of dead load besides the corrosion problem and the construction difficulty. In addition, the welding approach may cause fatigue problems and bolting connections may cause damages to the original structure. Therefore, use of FRP composites in strengthening and retrofitting steel structures has drawn significant attention in recent years. Compared to steel, FRP composites have the advantages of corrosion immunity and high strength-to-weight ratio, which leads to easy transportation and speedy installation. In addition, dry fiber sheets can be bonded to the steel structures by wet layup methods, which can adapt any structural geometry.

A significant number of studies have proved the effectiveness of EB-FRP composites in improving the flexural strength of steel beams (Colombi and Poggi 2006; Deng and Lee 2007; Lenwari *et al.* 2006; Yu *et al.* 2011; Zeng *et al.* 2018). In addition, for steel beams with cracks (i.e., represented by notches), EB-FRP composites bridge the cracks and reduce the stress intensity at the notch tip and thus extend the fatigue life (Chen and Huang 2019; Colombi and Fava 2015; Deng *et al.* 2018; Hmidan *et al.* 2011; Yu and Wu 2017). For fatigue strengthening purpose, CFRP in plate form are usually preferred over other types of FRP composites due to its higher elastic modulus.

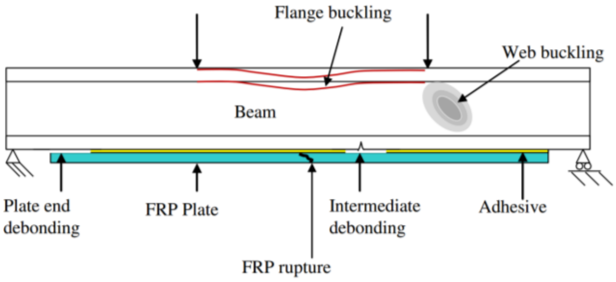

Fig. 1-1 Failure modes of FRP-strengthened steel beams (Teng *et al.* 2012).

Fig. 1-1 shows the possible failure modes that may occur in EB FRP-strengthened steel beams (Teng *et al.* 2012). Besides the commonly observed failure modes in steel beams under flexural loading, such as local buckling in the flange and web, the rupture failure of FRP and the interface debonding between FRP and steel substrate are also possible failure modes.

The high-strength epoxy adhesives are often used to bond FRP composites to the steel surface to ensure a full composite action of the entire strengthening system. Therefore, the structural performance of the strengthened steel beams highly relies on the stress transfer between the FRP composites and the steel beam. The high magnitude of interfacial stresses existing at the FRP-to-steel interface is the main reasons leading to the failure of the bonding interface (i.e., interfacial debonding) (Colombi and Poggi 2006; Deng and Lee 2007; Lenwari *et al.* 2006; Yu *et al.* 2011; Zeng *et al.* 2018). For FRP-strengthened steel beams without a notch, the interfacial debonding occurs at the FRP plate ends, which is termed as plate-end debonding. In addition, for FRP-retrofitted steel beam with an intermediate notch, the interfacial debonding usually initiate at the notched section, which is termed as intermediate crack-induced (IC) debonding. Both types of interfacial debonding limit the full utilization of the tensile strength in the FRP plate and the ductility of the strengthened steel beam. According to the theoretical analyses, the occurrence of interfacial debonding is due to the high stress concentrations at the interface in both mode I (i.e., normal to the interface) and mode II (i.e., parallel to the interface) (Smith and Teng, 2001; Stratford and Cadei, 2006; Deng *et al.*, 2016). Moreover, the interfacial debonding may occur under a lower level of mechanical loading when the bonding adhesives is deteriorated because of the severe environmental exposure (e.g., Gholami *et al.* 2013). It is particularly worth noting that the bonding adhesives are polymeric materials and thus the mechanical properties are sensitive to temperature change due to the existence of glass transition temperature (T_g) of polymer materials.

1.3 THERMAL EFFECTS ON THE PERFORMANCE OF FRP-STRENGTHENED STEEL BEAMS

FRP-strengthened steel beams are subjected to thermal loading due to the seasonable temperature changes, i.e., the temperature during the service life will be different from that at the installation of EB-FRP. Although the fibers itself usually hold a stable mechanical performance under service temperature, the polymer matrix of the FRP composites and the interfacial bonding adhesive, both typically being epoxies, may deteriorate at elevated temperatures, especially when their glass transition temperatures (T_g) are exceeded. Normally, the glass transition temperature (T_g) of epoxy matrix in a pultruded FRP plate is much higher than that of the bonding material, which is due to the difference in curing temperatures. The former adopts the heat curing process, while the latter cures under ambient-temperature conditions. Thus, the mechanical properties of the ambient-cured structural adhesive deteriorate more significantly under the service environment variation. The reported T_g of most commercially available epoxy resin for structure bonding is around 65 ℃ (Ko *et al.* 2014), which is often achieved when the steel surface is directly exposed to sunlight (Krzywoń 2017). In addition, the decrease in the deformability of the structural adhesive was reported at low temperatures, which may result in brittle failure and reduced ductility of the bonded interface (Al-Shawaf *et al.* 2006; Al-Shawaf and Zhao 2013; Di Tommaso *et al.* 2001). Another important issue caused by the thermal loading is the different coefficients of thermal expansion (CTE) of FRP plate and steel. For instance, the CTE of CFRP is usually lower than 1.0×10^{-6} for CFRP while the value is 1.2×10^{-5} for structural steel. That means, the expansion/contract of the steel beam is much larger than the FRP plate at an increased/decreased temperature. Such thermal mismatch will cause significant thermal stresses at the bonding interface (Deng *et al.*, 2004; Stratford and Cadei, 2006), which may intensify the interfacial stress concentration and decrease the debonding load of FRP-bonded steel interfaces or beams.

Up to now, there is no systematic research conducted on the effect of temperature variation on the structural behavior of FRP-strengthened steel beams considering the combined thermal and mechanical loading actions, which has imposed a potential risk on the use of FRP composites in the strengthening applications of steel structures.

1.4 OBJECTIVE, SCOPE, AND CONTENTS OF THIS DISSERTATION

The primary aim of this dissertation is to achieve a comprehensive understanding of the thermal effect on the structural behavior and debonding mechanisms of FRP-strengthened steel beams. The specific objectives are as follows:

a) To develop rigorous theoretical solutions for predicting the plate-end debonding loads of FRP-strengthened steel beams subjected to combined mechanical and thermal loading based on assumptions of different interface failure mechanisms (e.g., Mode II dominant failure or Mixed-mode failure).
b) To derive a rigorous theoretical solution for predicting the IC debonding failure loads of FRP-strengthened notched steel beams subjected to combined

mechanical and thermal loading.

c) To reveal the temperature-dependent bond-slip behaviors of CFRP-to-steel interface subjected to mode II loading through double-lap shear tests of CFRP bonded steel joints under various temperatures.
d) To experimentally study the structural performance and the debonding mechanisms of CFRP-strengthened cracked and uncracked steel beams under flexure and varied temperatures.
e) To conduct finite element (FE) modeling to predict the full-range structural performance of CFRP-strengthened steel beam under mechanical loading and varied temperatures so as to achieve an in-depth understanding of the debonding mechanisms.

A total of nine chapters are included in this dissertation. **Fig. 1-2** illustrates the structure of the whole dissertation in which six main chapters are presented to address the above-mentioned five specific research objectives: Three chapters (**Chapters 3, 4 and 5**) are relevant to theoretical analyses of the interfacial behavior and debonding loads of FRP-strengthened steel beams under combined mechanical and thermal loading. One chapter (**Chapter 6**) is presented on the double-lap shear tests of CFRP-to-steel joints. Two chapters (**Chapter 7** and **8**) are presented on the flexural tests of CFRP-strengthened steel uncracked and cracked beams, respectively, under various temperatures and the corresponding FE analyses.

Below are brief descriptions of each chapter of the dissertation:

Chapter 1 presents the overall background and the objective of the research.

Chapter 2 presents a state-of-the-art literature review on the research topic, including existing double-lap shear tests for obtaining the temperature-dependent bond-slip models, flexural tests for examining the structural performance of FRP-strengthened steel beams at mild temperatures, existing analytical models for predicting the interfacial bond behavior in FRP-bonded steel joints and FRP-strengthened steel beam, and identifies the research needs in the present study.

Chapter 3 is concerned the development of closed-form analytical solutions in predicting the interfacial behavior and plate-end debonding load of FRP-strengthened steel beams under combined mechanical and thermal loading based on the Mode II dominant failure assumption. The cohesive zone (CZ) model with simplified bi-linear bond-slip law is adopted for describing the nonlinear interfacial behavior of FRP-to-steel interface. The validity of the solution is demonstrated through comparisons with the finite element (FE) analysis results. The effects of temperature variation on the plate-end debonding loads are further parametrically investigated.

Chapter 4 further presents a coupled mixed-mode analysis approach for predicting the plate-end debonding of FRP-strengthened steel beam under combined mechanical and thermal loading considering the effects of interfacial stresses in both mode I and mode II directions. The ‘effective tangential cohesive zone law’ concept is adopted to alleviate the complexity of the proposed analytical solutions. The predicted distributions of interfacial stresses are compared with precise FE results to validate the proposed analytical model. The obtained plate-end debonding loads based on the coupled mixed-mode analysis in this chapter are also compared with the mode II based analytical results in **Chapter 3**. Finally, parametric studies are carried out based on the proposed analytical solution to show how the thermal loading affects the failure given different FRP properties.

Chapter 5 is concerned with the theoretical analysis of the thermal effect on the IC debonding mechanisms of CFRP-retrofitted steel beam with an intermediate crack on its tensile soffit. The interfacial bond behavior, axial force sustained by the CFRP plate, and stress intensity factor (SIF) at the notch tip are theoretically predicted under various temperatures. Then the predicted interfacial behavior, debonding load and SIF are also compared with the FE results for validation.

Chapter 6 presents the results of CFRP-to-steel double-lap shear tests at temperatures varied from -20 ℃ to 60 ℃. The debonding load, full-range load-displacement behavior, and strain distributions in the CFRP plate are carefully investigated and compared at different temperatures and magnitudes of mechanical loading. The temperature-dependent local bond-slip relationships are determined based on the measured data, which reliability are further demonstrated through comparing the experimental, analytical and FE modeling results.

Chapter 7 presents the flexural test results of eleven CFRP-strengthened steel beams at temperatures varied from -20 ℃ to 60 ℃. The structural performance, including peak load, full-range load-deflection behavior, and the strain distributions of CFRP, are reported and compared at different temperatures. Then the FE modeling is conducted to reproduce the test results of CFRP-strengthened steel beams, into which the temperature bond-slip relationships obtained in **Chapter 6** are implemented.

Chapter 8 presents the flexural tests of twelve CFRP-retrofitted steel beams with a preset notch at temperatures varied from -20℃ to 80℃, which all failed by IC debonding. The structural performances, including the full-range load-deflection behavior, crack opening displacement (COD)-load relationships, strain distributions of the CFRP plate are reported and compared at different temperatures. FE modeling is also conducted to reproduce the test results and the applicability of using the temperature-dependent local bond-slip relationships in the prediction are discussed.

Chapter 9 summarizes the main conclusions drawn from **Chapter 3** to **Chapter 8**, and recommends future research directions.

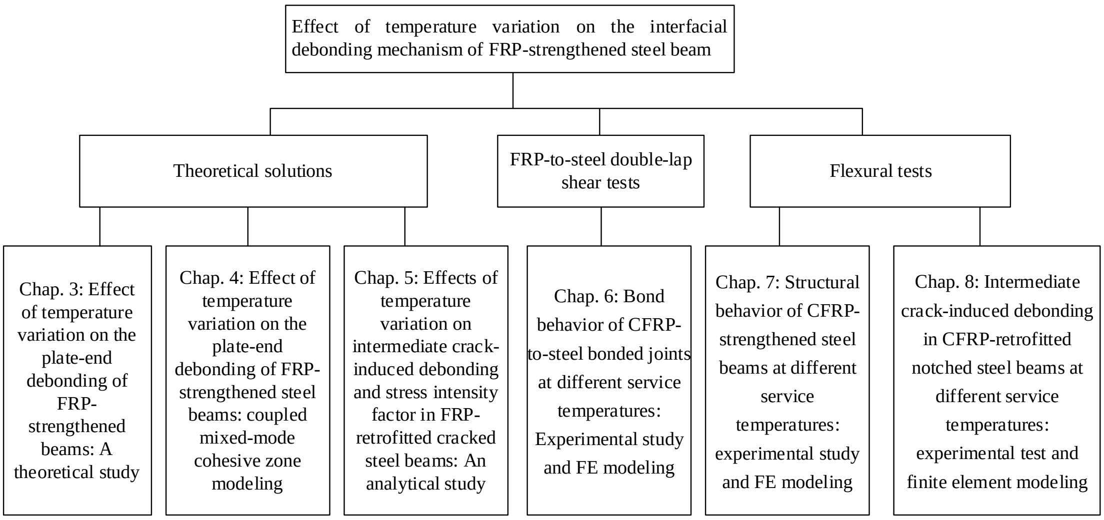

Fig. 1-2 Structure of the dissertation

1.5 REFERENCES

Al-Shawaf, A., Al-Mahaidi, R., and Zhao, X. L. (2006). "Study on bond characteristics of CFRP steel double lap shear joints at subzero temeprature exposure." In Proceeding of Third International Conference on FRP Composites in Civil Engineering (CICE 2006), December 13-15 2006, Miami, Florida, USA.

Al-Shawaf, A., and Zhao, X. L. (2013). "Adhesive rheology impact on wet lay-up CFRP/steel joints' behaviour under infrastructural subzero exposures." *Composites Part B: Engineering*, 47, 207-219.

Chen, T., and Huang, C. (2019). "Fatigue tests on edge cracked four-point bend steel specimens repaired by CFRP." *Composite Structures*, 219, 31-41.

Colombi, P., and Fava, G. (2015). "Experimental study on the fatigue behaviour of cracked steel beams repaired with CFRP plates." *Engineering Fracture Mechanics*, 145, 128-142.

Colombi, P., and Poggi, C. (2006). "An experimental, analytical and numerical study of the static behavior of steel beams reinforced by pultruded CFRP strips." *Composite Part B-Engineering*, 37(1), 64-73.

Deng, J., and Lee, M. M. K. (2007). "Behaviour under static loading of metallic beams reinforced with a bonded CFRP plate." *Composite Structures*, 78(2), 232-242.

Deng, J., Li, J. H., Wang, Y., and Xie, W. Z. (2018). "Numerical study on notched steel beams strengthened by CFRP plates." *Construction Building Materials*, 163, 622-633.

Deng, J., M.M.K. Lee and S.S.J. Moy (2004). "Stress analysis of steel beams reinforced with a bonded CFRP plate." *Composite Structures*, 65(2): 205-215.

Deng, J., Jia Y. H., and Zheng H. Z. (2016). "Theoretical and experimental study on notched steel beams strengthened with CFRP plate." *Composite Structures*, 136: 450-459.

Di Tommaso, A., Neubauer, U., Pantuso, A., and Rostasy, F. S. (2001). "Behavior of Adhesively Bonded Concrete-CFRP Joints at Low and High Temperatures." *Mechanics of Composite Materials*, 37(4), 327-338.

Gholami, M., Sam, A. R. M., Yatim, J. M., and Tahir, M. M. (2013). "A review on steel/CFRP strengthening systems focusing environmental performance." *Construction Building Materials*, 47, 301-310.

Hmidan, A., Kim, Y. J., and Yazdani, S. (2011). "CFRP Repair of Steel Beams with Various Initial Crack Configurations." *Journal of Composites for Construction*, 15(6), 952-962.

Ko, H., Matthys, S., Palmieri, A., and Sato, Y. (2014). "Development of a simplified bond stress–slip model for bonded FRP–concrete interfaces." *Construction Building Materials*, 68, 142-157.

Krzywoń, R. (2017). "Behavior of EBR FRP Strengthened Beams Exposed to Elevated Temperature." *Procedia Engineering*, 193, 297-304.

Lenwari, A., Thepchatri, T., and Albrecht, P. (2006). "Debonding strength of steel beams strengthened with CFRP plates." *Journal of Composites for Construction*, 10(1), 69-78.

Smith, S. T. and J. G. Teng (2001). "Interfacial stresses in plated beams." *Engineering Structures*, 23(7): 857-871.

Stratford, T. and J. Cadei (2006). "Elastic analysis of adhesion stresses for the design of a strengthening plate bonded to a beam." *Construction and Building Materials*, 20(1-2): 34-45.

Teng, J. G., Yu, T., and Fernando, D. (2012). "Strengthening of steel structures with fiber-reinforced polymer composites." *Journal of Constructional Steel Research*, 78, 131-143.

Yu, Q. Q., and Wu, Y. F. (2017). "Fatigue Strengthening of Cracked Steel Beams with Different Configurations and Materials." *Journal of Composites for Construction*, 21(2).

Yu, Y., Chiew, S. P., and Lee, C. K. (2011). "Bond failure of steel beams strengthened with FRP laminates - Part 2: Verification." *Composite Part B-Engineering*, 42(5), 1122-1134.

Zeng, J. J., Gao, W. Y., and Liu, F. (2018). "Interfacial behavior and debonding failures of full-scale CFRP-strengthened H-section steel beams." *Composite Structures*, 201, 540-552.

CHAPTER 2

LITERATURE REVIEW

2.1 GENERAL

Fiber-reinforced polymer (FRP) composites, especially pultruded CFRP plates, have been widely adopted in strengthening and retrofitting steel beam structures through externally bonded (EB) technology. The structural performance of a FRP-strengthened steel beam relies on the stress transfer between steel beam and FRP plate. Thus, stress concentration is generated at the interface at the plate end and crack locations, which results in plate-end debonding and IC debonding, respectively. The load-carrying capacity of the FRP-strengthened steel beam is highly dependent on the bond strength, which can be significantly affected by the thermal loading at even mild temperatures. This situation has motivated researchers to investigate the thermal effect on the interfacial debonding mechanism of FRP-strengthened steel beams, in terms of temperature-dependent bond behavior and interfacial thermal stress.

This chapter presents a review of existing knowledge on the effect of temperature variation on the structural performance and debonding mechanism of FRP-strengthened steel beams obtained from experimental and theoretical studies.

2.2 THERMAL EFFECT ON THE PROPERTIES OF THE BONDING ADHESIVE

The current understanding of the thermal behaviour of adhesives used in civil engineering applications is mainly from the research outputs in the aerospace and automotive industries. The existing knowledge on the mechanism of thermal effect on properties of the bonding adhesive used in others domains is also included in this section.

The strength of polymers is based on the bond between molecules and polymer chains, which can be further classified into primary and secondary bonds (Mahieux and Reifsnider 2001, Moussa *et al.* 2012). The primary bonds result from the strong covalent intramolecular bonds, while the secondary ones come from the hydrogen bonds, dipole interaction, Vander Walls intersections, and ionic bonds. The covalent intramolecular bonds exist between the polymer chains and form the well-ordered molecular structure, i.e., crystalline regions. The secondary bonds mainly exist in the amorphous regions, where the polymer chains are organized randomly. The primary bonds exhibit much higher resistance to the dislocation of polymer than the secondary bonds (Moussa *et al.* 2012). In addition, as the service temperature increases, the secondary bonds are broken much earlier than the primary ones, resulting in easier differential movement between polymer chains (Mahieux and Reifsnider 2001) and lower elastic modulus of the adhesive. As a result, the stiffness and strength of adhesive can be reduced by temperature elevation. In contrast, extremely low temepratures can increase the stiffness of typical adhesives and may also result in embrittlement (Harries and Dawood 2012). Moussa et al. (2012) tested the coupons made by Sikadur-30 adhesive at temperatures varying from -35 ℃ to 60 ℃ to obtain the stress-strain responses. The test results demonstrated that the specimens exhibited a stiff and almost linear-elastic behavior at temperatures lower than 40 ℃ and viscoelastic non-linear response at temperatures higher than 40 ℃. In addition, the modulus of elasticity and strength reduced with the increase in temperature.

The behavior of typical bonding adhesive under increasing thermal loading can be divided into four stages: glassy state, glass transition, rubbery state and decomposition. During the glassy state, the property of the polymer is nearly elastic and marginally affected by the temperature variation. It is because the temperature increase only results in very localized molecular movement. In comparison, the elastic modulus of the adhesive drops significantly during the glass transition stage. During this stage, the decrease rate first increases and then decreases. As the decrease rate reduces to almost zero, the adhesive enters the rubbery state, resulting in a very low value of elastic modulus, which remains almost invariant as the further temperature increases. During this stage, molecules start sliding with each other, and the secondary bonds start to break because of the molecular movement. With further temperature increase, the adhesive's elastic modulus gradually decreases to zero because of the chemical decomposition (Boyce, Parks et al. 1988; Mahieux and Reifsnider 2001; Moussa, Vassilopoulos et al. 2012).

Although the glass transition takes place in a wide range of temperatures, it is usually described by one critical value, which is termed as the glass transition temperature (T_g).

T_g can be taken as a measurement of molecular mobility (Carbas, Marques et al. 2014) and reflects the adhesive's thermal behaviour. There are several definitions of T_g based on the measured stiffness-temperature curves through dynamic mechanical analysis (DMA), including T_g onset, which is defined by the intersection of a tangent to the storage modulus curve below the transition with a second tangent during the transition; T_g 2% offset, at which the storage modulus drops by 2% compared to a tangent to the storage modulus below transition; the point of inflection in the storage modulus curve; the peak in the loss modulus curve or the peak in the tan δ curve (Othman et al. 2013).

Currently, there are hundreds of adhesive formulations on the market. Different structural adhesives exhibit distinct properties in normal and altered temperatures because of the different chemical compositions and microstructures. The polymer consists of only or predominantly crystalline structures, termed thermal setting adhesives, and exhibits much higher resistance at increased temperatures than that which contains a higher proportion of amorphous regions, termed thermal plastic adhesives. In addition, the properties of adhesive at increasing temperatures are also dependent on the curing period and environments. Previous studies proved that the longer curing period at elevated temperatures is capable of improving tensile strength because of the enhancement in the chain branching and molecular bond (Silva, Fernandes et al. 2016). In addition, the higher curing temperature was also proved to enhance the degree of curing and increase the resulting glass transition temperatures (Moussa, Vassilopoulos et al. 2012).

2.3 THERMAL EFFECT ON THE FRP-TO-STEEL BONDED JOINT

As discussed above, the bonding adhesive transforms from a rigid to a soft and rubbery state, as the service temperature increases close to or overpass the glass transition temperature. Accordingly, the bond behavior between the FRP and steel substrate also deteriorates at higher temperatures.

Numerous FRP-to-steel double- or single-lap shear tests have been conducted at mild temperatures (Al-Shawaf *et al.* 2009; Al-Shawaf 2010; Biscaia and Ribeiro 2019; Chandrathilaka *et al.* 2019; Hassein Abed 2012; He *et al.* 2020; Li *et al.* 2018; Li *et al.* 2016; Liu *et al.* 2014; Nguyen *et al.* 2011; Wang and Xian 2020; Zhou *et al.* 2017), in order to find out the thermal deterioration of the bond performance between the FRP and steel substrate in mode II direction as the temperature increases. Heshmati *et al.* (2015) reviewed several existing tests conducted (Al-Shawaf *et al.* 2009; Al-Shawaf 2010; Nguyen *et al.* 2011; Zhang *et al.* 2010) and found that the debonding load and stiffness of the specimens decreased gradually at average rates of 3.3% and 4.4% per degree Celsius when the exposure temperature is higher than T_g minus 5 ℃. In addition, the stiffness of the joints when the exposure temperature decreases from room temperature to 5 ℃ below T_g. However, the debonding load remains constant in this temperature range. By contrast, at decreased temperatures, the elastic modulus and peak shear stress of the bonding interface were found to be maintained or slightly increased (Al-Shawaf 2006; Al-Shawaf and Zhao 2013; Park *et al.* 2010; Yao *et al.* 2016). However, the temperature decrease lowered the deformability, which resulted in brittle failure (Al-Shawaf *et al.* 2006; Al-Shawaf and Zhao 2013; Di Tommaso *et al.* 2001) and decreased interfacial fracture energy (Zhang *et al.* 2010).

For describing the temperature-dependent bond behavior in mode II direction (i.e., bond-slip relationship) at the FRP-to-concrete interface, a non-linear bond-slip model was proposed by (Dai *et al.* 2013) as a generalization of a two-parameter model for ambient temperature. Based on the extension of Dai *et al.*'s model, Li *et al.* (2016) proposed a similar analytical model for describing the bond behavior of the FRP-to-steel interface at increased temperatures. Afterwards, Biscaia and Ribeiro (2019) proposed a temperature-dependent bond-slip model for FRP-to-steel interface with a bilinear shape based on the reviewed experimental results.

Apart from the thermal deterioration of the bonding material, the effect of thermal stress was also proved to be significant on the interfacial bond behavior of FRP-to-steel joints under mode II loading (Gao *et al.* 2012, 2015). Specifically, the interfacial thermal stress/slip at increased temperatures was in the opposite direction from that generated by the mechanical loading, which delays the occurrence of interfacial debonding and increases the debonding load.

2.4 THERMAL EFFECT ON THE PLATE-END DEBONDING OF FRP-STRENGTHENED STEEL BEAM

The structural performance of a FRP-strengthened steel beam relies on the interfacial stress transfer of the bonding adhesive (Karbhari 2014). Thus, the property variations of the bonding adhesive at changed temperatures may result in the deterioration of structural performance of the FRP-strengthened steel beams. The flexural tests on FRP-strengthened steel beams were conducted at moderately elevated temperatures (Sahin and Dawood 2016; Stratford and Bisby 2012; Teng *et al.* 2021) and decreased temperatures (Yoshitake *et al.* 2014). Stratford's experiments (2012) subjected the FRP-strengthened beams to sustained load with increasing temperature. It was reported that warm temperatures (i.e., higher than 40 ℃) could significantly decrease debonding load and bond strength between FRP plate and steel beam. A similar phenomenon was observed by Teng *et al.* (2021), in which the temperature elevation at 60 ℃ deteriorated the interfacial stress transfer and decreased the flexural stiffness of the FRP-strengthened steel beam. In comparison, Sahin and Dawood (2016) observed enhancement in the debonding load as the temperature increased from 25 ℃ to 50 ℃. The authors attributed this phenomenon to the increased toughness of the adhesive at mild temperatures.

By contrast, the thermal effect on the load-carrying capacity of FRP-strengthened steel beam in cold temperatures was found to be negligible in Yoshitake *et al.*'s experiments (2014). It should be noted that the thermal effect on the bond behavior was not revealed in this experiment because the strengthened steel beam failed by FRP rupture rather than interfacial debonding.

In summary, some variations exist in the experimental observations in the above-mentioned flexural tests at elevated temperatures, which brings uncertainties in predicting the structural performance at mild temperatures. In addition, these researchers focused on the thermal effect on the structural performance of the FRP-strengthened steel beam and paid less attention to the interfacial bond behavior, which is believed to be a determinant of the structural performance and sensitive to temperature variation.

Apart from the experimental studies, some theoretical analyses were proposed by (Deng *et al.*, 2004; Stratford and Cadei, 2006) for analyzing the effect of thermal stress on plate-end debonding load of FRP-strengthened steel beams. It revealed that the interfacial thermal stress at increased temperatures may lead to intensified interfacial stress concentration at the plate end and reduce the plate-end debonding load. However, these analytical solutions were derived based on elastic bond assumption, which neglects the nonlinear bond properties and results in an underestimation of the debonding load (Teng *et al.* 2012). Furthermore, the bond behavior has been found to be increasingly nonlinear at elevated service temperatures due to softening of the bonding adhesive (Dai *et al.*, 2013). Therefore, new theoretical analyses based on the nonlinear bond behavior need to be developed, which requires rigorous analyses of effect of the thermal stress on the interfacial behavior and plate-end debonding load.

2.5 THERMAL EFFECT ON THE IC DEBONDING OF FRP-RETROFITTED STEEL BEAM

Currently, the flexural test on FRP-retrofitted cracked steel beams at changed temperatures is not available in the literature. Despite that, some analytical solutions were proposed for predicting the interfacial bond behavior of the FRP-retrofitted steel beams (Bocciarelli *et al.* 2018; Bocciarelli *et al.* 2016; Deng *et al.* 2016; Wang 2006). The effect of interfacial thermal stress is not considered in these analytical solutions.

In summary, the understanding of the thermal effect on the IC debonding mechanism of FRP-retrofitted steel beam with a precast notch is very limited, which calls for both the flexural test at various temperatures and the theoretical analysis on the thermal stress effect.

2.6 CONCLUSIONS AND RESEARCH NEEDS

Currently, research on the effect of temperature variation on the plate-end and IC debonding mechanism of FRP-strengthened steel beam is limited. Based on these limited research outputs, it can be concluded that the thermal deterioration of the bonding material and the interfacial thermal stress influence the debonding mechanism and structural performance. Up to now, the effect of thermal stress has only been investigated theoretically based on the elastic bond assumption in previous research. Further, the effect of bond deterioration on structural performance has not been rigorously measured and discussed. The following issues need to be addressed to achieve a comprehensive understanding of the thermal effect on the debonding load of FRP-strengthened steel beam at various temperatures.

a) The effect of thermal stress on the debonding mechanism of FRP-strengthened steel beams needs to be further investigated based on the theoretical analysis for beams failed by both plate-end and IC debonding. In addition, the nonlinear bond behavior should be considered in the theoretical analyses.

b) To facilitate a comprehensive understanding of the bond deterioration effect on the debonding mechanism of FRP-strengthened steel beam, the local bond parameters at various temperatures need to be measured and utilized in modeling the structural performance of FRP-strengthened steel beam.

c) The structural performances of FRP-strengthened steel beams at both decreased and increased temperatures need to be examined by flexural tests. For comprehensive analyses of the debonding mechanism, the interfacial behavior at various temperatures needs to be carefully investigated.

2.7 REFERENCES

Al-Shawaf, A., Al-Mahaidi, R., and Zhao, X.L. (2006). "Study on bond characteristics of CFRP steel double lap shear joints at subzero temeprature exposure." *In Proceeding of Third International Conference on FRP Composites in Civil Engineering (CICE 2006),* December 13-15 2006, Miami, Florida, USA.

Al-Shawaf, A., Al-Mahaidi, R., and Zhao, X.L. (2009). "Effect of elevated temperature on bond behaviour of high modulus CFRP/steel double-strap joints." *Australian Journal of Structural Engineering*, 10(1), 63-74.

Al-Shawaf, A., and Zhao, X.L. (2013). "Adhesive rheology impact on wet lay-up CFRP/steel joints' behaviour under infrastructural subzero exposures." *Composites Part B: Engineering*, 47, 207-219.

Al-Shawaf, A. K. (2010). "Characterization of bonding behavior between wet lay-up carbon fibre reinforced polymer and steel plates in double-strap joints under extreme environmental temperatures." PhD Thesis, Monash University, Australia.

Al-Shawaf, A.K. (2010). "Characterization of Bonding Behavior Between Wet Lay-up Carbon Fibre Reinforced Polymer and Steel Plates in Double-strap Joints Under Extreme Environmental Temperatures." Monash University.

Biscaia, H.C., and Ribeiro, P. (2019). "A temperature-dependent bond-slip model for CFRP-to-steel joints." *Composite Structures*, 217, 186-205.

Bocciarelli, M., Colombi, P., D'Antino, T., and Fava, G. (2018). "Intermediate crack induced debonding in steel beams reinforced with CFRP plates under fatigue loading." *Engineering Structures*, 171: 883-893.

Bocciarelli, M., Colombi, P., Fava, G., and Sonzogni, L. (2016). "Energy-based analytical formulation for the prediction of end debonding in strengthened steel beams." *Composite Structures*, 153, 212-221.

Boyce, M.C., Parks D.M., and Argon A.S. (1988). "Large inelastic deformation of glassy polymers. Part I: rate dependent constitutive model." *Mechanics of materials*, 7(1): 15-33.

Carbas, R. J. C., E. A. S. Marques, L. F. M. da Silva and A. M. Lopes (2014). "Effect of Cure Temperature on the Glass Transition Temperature and Mechanical Properties of Epoxy Adhesives." *The Journal of Adhesion*, 90(1): 104-119.

Chandrathilaka, E., Gamage, J., and Fawzia, S. (2019). "Mechanical characterization of CFRP/steel bond cured and tested at elevated temperature." *Composite Structures*, 207, 471-477.

Dai, J.G., Gao, W.Y., and Teng, J.G. (2013). "Bond-Slip Model for FRP Laminates Externally Bonded to Concrete at Elevated Temperature." *Journal of Composites for Construction*, 17(2), 217-228.

Deng, J., M.M.K. Lee and S.S.J. Moy (2004). "Stress analysis of steel beams reinforced with a bonded CFRP plate." *Composite Structures* 65(2): 205-215.

Deng, J., Jia, Y.H., and Zheng, H.Z. (2016). "Theoretical and experimental study on notched steel beams strengthened with CFRP plate." *Composite Structures*, 136, 450-459.

Di Tommaso, A., Neubauer, U., Pantuso, A., and Rostasy, F. S. (2001). "Behavior of Adhesively Bonded Concrete-CFRP Joints at Low and High Temperatures." *Mechanics of Composite Materials*, 37(4), 327-338.

Gao, W.Y., Dai, J.G., and Teng, J.G. (2015). "Analysis of Mode II debonding behavior of fiber-reinforced polymer-to-substrate bonded joints subjected to combined thermal and mechanical loading." *Engineering Fracture Mechanics*, 136, 241-264.

Gao, W.Y., Teng, J.G., and Dai, J.G. (2012). "Effect of Temperature Variation on the Full-Range Behavior of FRP-to-Concrete Bonded Joints." *Journal of Composites for Construction*, 16(6), 671-683.

Harries, K.A. and M. Dawood (2012). "Behavior and performance of fiber-reinforced polymer-to-steel bond." *Transportation research record*. 2313(1): 181-188.

Hassein Abed, G. (2012). "Effects of temperature on the adhesive bonding in steel beams reinforced with CFRP composites." University of Southampton.

He, J., Xian, G., and Zhang, Y.X. (2020). "Effect of moderately elevated temperatures on bond behaviour of CFRP-to-steel bonded joints using different adhesives." *Construction and Building Materials*, 241, 118057.

Heshmati, M., Haghani, R., and Al-Emrani, M. (2015). "Environmental durability of adhesively bonded FRP/steel joints in civil engineering applications: State of the art." *Composites Part B: Engineering*, 81, 259-275.

Karbhari, V. M. (2014). *Rehabilitation of metallic civil infrastructure using fiber-reinforced polymer (FRP) composites*. Elsevier.

Li, N., Li, S., Liu, C., and Zhu, T. (2018). "Bond behavior of CFRP/steel double strap joint at elevated temperatures." *Preprints*, 201808.0070.

Li, S., Zhu, T., Lu, Y., and Li, X. (2016). "Effect of Temperature Variation on Bond Characteristics between CFRP and Steel Plate." *International Journal of Polymer Science*, 2016, 5674572.

Liu, H.B., Zhao, X.L., Bai, Y., Singh, R. K., Rizkalla, S., and Bandyopadhyay, S. (2014). "The Effect of Elevated Temperature on the Bond Between High Modulus Carbon Fibre-Reinforced Polymer Sheet and Steel." *Australian Journal of Structural Engineering*, 15(4), 355-366.

Mahieux, C. A. and K. L. Reifsnider (2001). "Property modeling across transition temperatures in polymers: a robust stiffness–temperature model." *Polymer*, 42(7): 3281-3291.

Moussa, O., A. P. Vassilopoulos, J. de Castro and T. Keller (2012). "Time–temperature dependence of thermomechanical recovery of cold-curing structural adhesives." *International Journal of Adhesion and Adhesives*, 35: 94-101.

Nguyen, T.C., Bai, Y., Zhao, X.L., and Al-Mahaidi, R. (2011). "Mechanical characterization of steel/CFRP double strap joints at elevated temperatures." *Composite Structures*, 93(6), 1604-1612.

Othman, D., T. Stratford and L. Bisby (2013). "A Comparison of on-site and elevated temperature cure of an FRP strengthening adhesive." *Proceedings of the FRPRCS11, UM, Guimarães*.

Park, Y.B., Song, M.G., Kim, J.J., Kweon, J.H., and Choi, J.H. (2010). "Strength of carbon/epoxy composite single-lap bonded joints in various environmental conditions." *Composite Structures*, 92(9), 2173-2180.

Sahin, M.U., and Dawood, M. (2016). "Experimental Investigation of Bond between High-Modulus CFRP and Steel at Moderately Elevated Temperatures." *Journal of Composites for Construction*, 20(6), 04016049.

Silva, P., P. Fernandes, J. Sena-Cruz, J. Xavier, F. Castro, D. Soares and V. Carneiro (2016). "Effects of different environmental conditions on the mechanical characteristics of a structural epoxy." *Composites Part B: Engineering* 88: 55-63.

Stratford, T.J., and Bisby, L.A. (2012). "Effect of Warm Temperatures on Externally Bonded FRP Strengthening." *Journal of Composites for Construction*, 16(3), 235-244.

Stratford, T. and Cadei J. (2006). "Elastic analysis of adhesion stresses for the design of a strengthening plate bonded to a beam." *Construction and Building Materials* 20(1-2): 34-45.

Teng, J.G., Yu, T., and Fernando, D. (2012). "Strengthening of steel structures with fiber-reinforced polymer composites." *Journal of Constructional Steel Research*, 78, 131-143.

Teng, R., Guo, Y., Wang, H., Zhao, Z., and Wang, X. (2021). "Experimental study of bending interface characteristics of CFRP-strengthened long-span steel main beams at different temperatures." *Engineering Structures*, 235.

Wang, J.L. (2006). "Cohesive zone model of intermediate crack-induced debonding of FRP-plated concrete beam." *International Journal of Solids and Structures*, 43(21), 6630-6648.

Wang, Z., and Xian, G. (2020). "Effects of thermal expansion coefficients discrepancy on the CFRP and steel bonding." *Construction and Building Materials*.

Yao, M.X., Zhu, D.J., Yao, Y.M., Zhang, H.A., and Mobasher, B. (2016). "Experimental study on basalt FRP/steel single-lap joints under different loading rates and temperatures." *Composite Structures*, 145, 68-79.

Yoshitake, I., Tsuda, H., Itose, J., and Hisabe, N. (2014). "Effect of discrepancy in thermal expansion coefficients of CFRP and steel under cold temperature." *Construction and Building Materials*, 59, 17-24.

Zhang, Y., Vassilopoulos, A.P., and Keller, T. (2010). "Effects of low and high temperatures on tensile behavior of adhesively-bonded GFRP joints." *Composite Structures*, 92(7), 1631-1639.

Zhou, H., Urgel, J.M., Emberley, R., Maluk, C., and Fernando, D. (2017). "Behaviour of the FRP-to-steel bonded joints under elevated temperature." *In Proceeding of 6th Asia-Pacific Conference on FRP in Structures*, At: Singapore.

CHAPTER 3

THERMAL EFFECT ON PLATE-END DEBONDING OF FRP-STRENGTHENED BEAMS: A THEORETICAL STUDY

3.1. INTRODUCTION

Externally bonded fiber-reinforced polymer (FRP) sheets and plates (hereafter "plates" for brevity) have been widely used for flexural strengthening of steel/concrete beams (hereafter "beams" for brevity) (Idris and Ozbakkaloglu, 2014; Teng *et al.*, 2012; Al-Tamimi *et al.*, 2015; Wang and Wu, 2018; Zhang *et al.*, 2017; Zhang and Teng, 2016; Choobbor *et al.* 2019; Al Nuaimi *et al.* 2021). Plate-end debonding is a very common failure mode for these strengthened beams under loading, and therefore, it has become one of the most fundamental research topics in the past few decades. Numerous experimental (Deng and Lee, 2007; Lenwari *et al.*, 2006; Rizkalla *et al.*, 2008; Yu *et al.*, 2011; Zeng *et al.*, 2018) and theoretical studies (De Lorenzis and Zavarise, 2009; De Lorenzis *et al.*, 2013; Haghani *et al.*, 2009; Schnerch *et al.*, 2007; Smith and Teng, 2001; Stratford and Cadei, 2006; Teng *et al.*, 2015; Teng *et al.*, 2002) have been conducted to investigate the plate-end debonding failure in the FRP-strengthened beams at ambient temperature. The existing studies have demonstrated that high interfacial shear and peeling stresses at the plate end contribute towards the plate-end debonding failure. In quantification of the interfacial shear and peeling stresses at the plate end, early analytical studies have considered the constitutive behavior of the bond interface as linear elastic (Smith and Teng, 2001; Teng *et al.*, 2002). Recent studies on FRP-to-steel/concrete bonded joints have revealed that the bond strengths of such bonded joints with long enough bond lengths are governed by interfacial fracture energy rather than interfacial shear stress (Dai *et al.*, 2005; Dong and Hu, 2016; Ouyang and Wan, 2009; Teng *et al.*, 2012; Yu *et al.*, 2012; Yuan *et al.*, 2004; Yuan *et al.*, 2012). More importantly, the use of stress-based failure criteria combined with the consideration of linear elastic behavior of the bond interface may significantly underestimate the plate-end debonding loads (Teng *et al.*, 2015). Therefore, some efforts have been made in considering the nonlinear behavior of the bond interface in predicting the plate-end debonding failure modes in the FRP-strengthened beams.

A cohesive-zone modeling approach is one of the most commonly used approaches in modeling the nonlinear behavior of the FRP-to-steel/concrete interface (De Lorenzis *et al.*, 2013; De Lorenzis and Zavarise, 2009), in which appropriate traction-separation constitutive laws are usually adopted to describe both mode I and mode II behavior of the bond interface. For a pure mode II behavior, a bond-slip model is usually needed to define the relationship between interfacial shear stress and slip. Therefore, some bond-slip models for the FRP-to-steel/concrete interface at ambient temperature are well established (e.g., Dai *et al.*, 2005; Liu and Dawood, 2018; Lu *et al.*, 2005; Yu *et al.*, 2012; Zheng *et al.*, 2020; Teng *et al.*, 2021). Traction-separation models for pure mode I behavior are much less known and often approximated using either the uniaxial stress-strain behavior of the constituents or the mode I fracture energy of the bond interface (Dai *et al.*, 2003; Fernando *et al.*, 2015; Teng *et al.*, 2015). Amongst the existing solutions for the cohesive zone modeling approach of the FRP-strengthened beams, early models have only considered mode II behavior (De Lorenzis and Zavarise, 2009), while later those have been further extended to consider both mode I and mode II behavior using a mixed-mode cohesive law (De Lorenzis *et al.*, 2013; Teng *et al.*, 2015; Bruno *et al.*, 2016). However, such modeling approaches so far have been limited to the behavior of FRP-strengthened beams at ambient temperature.

The FRP-strengthened beams in service are likely to experience significant temperature variations due to the seasonable and diurnal temperature changes (Al-Shawaf, 2010; Biscaia, 2019; Sahin and Dawood, 2016; Stratford and Bisby, 2012; Ghous Sohail *et al.* 2021; Teng *et al.*, 2021). The temperature variations (i.e., thermal loadings) have two different effects on the interfacial behavior and the associated debonding failure: (a) thermal stresses at the FRP-to-steel/concrete interface that are induced by different thermal expansion coefficients of the FRP plate and the steel or concrete substrate (e.g., Gao *et al.*, 2012, 2015; Silva and Biscaia, 2008); (b) bond degradation of the FRP-to-steel/concrete interface due to the temperature sensitivity of the mechanical properties (e.g., strength and stiffness) of the bonding adhesive (e.g., Dai *et al.*, 2013; Zhou *et al.*, 2019; Ahmed and Kodur, 2011). It is noteworthy that the effects of thermal loadings on the mechanical properties of the reinforcing fibers of the FRP plate as well as the steel/concrete substrates are negligible (Nguyen *et al.*, 2011; Sauder *et al.*, 2004;

Hawileh *et al.*, 2015) compared with those of the bonding adhesives. That is, the bond degradations at elevated service temperatures are of higher concern than the mechanical property degradations of the FRP plate and the steel/concrete substrate under the same temperature exposure. Therefore, a number of bonded joint tests have been conducted in the literature to investigate the bond performance between FRP and steel/concrete structures at various temperatures (e.g., Al-Shawaf *et al.*, 2009; Zhang *et al.* 2015; Biscaia and Ribeiro, 2019; Chandrathilaka *et al.*, 2019; Ferrier *et al.*, 2016; Ke *et al.*, 2020; Yu and Kodur 2014; Korayem *et al.*, 2016; Nguyen *et al.*, 2011; Nguyen *et al.*, 2019; Zhou *et al.*, 2020), and some temperature-dependent bond-slip models have already been established based on the test results (e.g., Dai *et al.*, 2013; Zhou *et al.*, 2019; Nguyen *et al.*, 2011; Biscaia and Ribeiro, 2019). Also, differential deformations between the FRP plate and the steel/concrete substrate may occur at elevated service temperatures due to different thermal expansions of the FRP plate and the steel/concrete substrate (Biscaia *et al.*, 2017; Biscaia, 2019; Deng *et al.*, 2004; Stratford and Cadei, 2006). Such deformations may lead to increased interfacial shear and peeling stresses within the bond interface, thus influencing the behavior of the FRP-strengthened beam under combined thermal and mechanical loading. The effect of such thermally induced deformations on the interfacial stress distributions at the plate-ends has been analytically studied only using linear elastic material behaviors (Deng *et al.*, 2004; Stratford and Cadei, 2006). As previously discussed, the consideration of the nonlinear behavior of the bond interface is essential even at ambient temperatures. At elevated service temperatures, the behavior of the bond interface becomes increasingly nonlinear (Dai *et al.*, 2013; Zhou *et al.*, 2019). Therefore, to account for a more realistic estimation of interfacial stresses at the plate ends, the consideration of nonlinear behavior of the bond interface is necessary.

The above literature review indicates that there is a lack of research on the effects of interfacial thermal stress on the plate-end debonding failure of the FRP-strengthened beam under combined thermal and mechanical loading. This chapter presents a new and closed-form analytical solution to investigate the effects of thermal loadings on the plate-end debonding propagation in the FRP-strengthened beam, for the first time considering the nonlinear bond-slip behavior between the FRP plate and the substrate beam. The proposed analytical solution aims to capture the interfacial shear stress distributions near the plate ends, resulting from the combined thermal and mechanical loading. During the theoretical analysis, the effect of interfacial peeling stresses is ignored, considering that the thermal incompatibility between the FRP plate and the substrate is parallel to the longitudinal axis of the beam. Moreover, when the bending stiffness of the original steel/concrete beam is much larger than the externally bonded FRP plate, which is a most common condition for the FRP-strengthened steel/concrete beams, the bending moments in the FRP plate and the relevant peeling stresses at the interface may be insignificant (De Lorenzis and Zavarise, 2009; Mohammadi *et al.*, 2017; Taljsten, 1997). It should be mentioned that a proper consideration of the peeling stresses complicates the analytical solution significantly, and thus a closed-form analytical solution may not be easily achieved. Considering that even for the FRP-strengthened beams at ambient temperature pure mode II stress-based models are often used to simplify the theoretical solutions (Bennati *et al.*, 2016; Bocciarelli *et al.*, 2016; Cornetti *et al.*, 2015; De Lorenzis and Zavarise, 2009; Mohammadi *et al.*, 2017), only mode II stresses are considered in this chapter to understand the thermo-mechanical coupling effect on the plate-end debonding failure.

3.2. NEW ANALYTICAL SOLUTION

3.2.1 Assumption and Notation

As stated in the introductory section, a cohesive zone modeling method was developed by De Lorenzis and Zavarise (2009) to predict the plate-end debonding failure in the FRP-strengthened beam under mechanical loading only. This chapter proposes a new analytical approach to consider the thermal loading effect on the plate-end debonding mechanism following De Lorenzis and Zavarise’s method (2009). Similar to the assumptions adopted in the previous study, in the present study also: (a) both the beam and the FRP plate are assumed to be linear elastic, without consideration of the stress-strain response of steel after yielding, (b) shear deformations of the beam and the FRP plate are neglected, and (c) interfacial shear stresses are assumed to be invariant across the thickness of the adhesive layer. In addition, the temperature variation and the associated thermal expansions of the FRP and the substrate are assumed to be uniformly distributed along the full length of the beam.

3.2.2 *Mode II Cohesive Law*

A bilinear bond-slip relationship (**Fig. 3-1**), which consists of a linear elastic branch and a subsequently linear softening branch, is adopted to describe the cohesive law of the interface between the FRP and the beam. Although such a bi-linear model is simple, it can capture the essential properties of the interface. Therefore, it is the most widely used bond-slip constitutive law in modeling the mode II behavior of the FRP-to-steel/concrete interface in the literature (De Lorenzis and Zavarise, 2009; De Lorenzis *et al.*, 2013; Gao *et al.*, 2012, 2015; Teng *et al.*, 2015; Yuan *et al.*, 2004). The key parameters of a bi-linear bond-slip model are the interfacial fracture energy (i.e., G_{IIc} area underneath the interfacial shear stress-slip curve), the interfacial shear strength (τ_p), and the interfacial elastic shear stiffness (K_T) (**Fig. 3-1**).

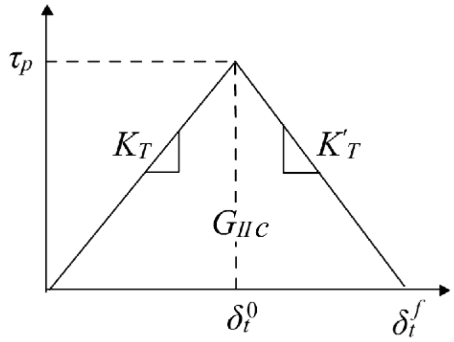

Fig. 3-1 Bilinear bond-slip relationship in cohesive zone analysis.

The bi-linear bond-slip model can be described by the following formulas

$$\begin{cases} \tau^e = K_T \delta_t & 0 < \delta_t \leq \delta_t^0 \\ \tau^s = \tau_0 - K'_T \delta_t & \delta_t^0 < \delta_t \leq \delta_t^f \\ \tau^d = 0 & \delta_t > \delta_t^f \end{cases} \tag{3-1}$$

where τ^e, τ^s, and τ^d are the interfacial shear stress at elastic, softening and debonding stages respectively, δ_t is the interfacial shear slip, τ_0 is a stress value given by $\tau_0 = \tau_p \delta_t^f / (\delta_t^f - \delta_t^0)$, δ_t^0 and δ_t^f are the interfacial shear slips at τ_p and at the initiation of debonding respectively, and K'_T is the absolute value of the gradient of the softening branch. The slopes of the elastic branch (K_T) and the softening branch (K'_T) can be written as:

$$K_T = \tau_p / \delta_t^0 \tag{3-2}$$

$$K'_T = \tau_p / (\delta_t^f - \delta_t^0) \tag{3-3}$$

δ_t^f can be related to G_{IIc} and τ_p as:

$$G_{IIc} = \tau_p \delta_t^f / 2 \tag{3-4}$$

Existing research has shown that the mechanical properties of the bonding adhesive changes with temperature with significant stiffness and strength reductions at elevated service temperatures (Zhou *et al.*, 2020). Therefore, the bond-slip behavior of the interface in fact varies with the temperature variation. However, the experimental study conducted by Zhou *et al.* (2019) has indicated that the strength of the bond joint depends only on the bond-slip behavior at the final temperature of the bonded joint, provided the interfacial fracture energy changes monotonically with the temperature variation. Therefore, the above bond-slip model is assumed to be the model at the final temperature concerned during the analysis of the temperature variation effect.

3.2.3 Governing Equation and General Solution

Fig. 3-2 schematically illustrates a typical FRP-strengthened beam under three-point bending loading. The beam is strengthened at its soffit by an FRP plate with a length of L_P and supported at two ends with a clear distance of L. b and d denote the width and thickness of the two adherends and the subscripts of 1 and 2 denote the beam and the FRP plate respectively. In addition, the thickness of the adhesive layer is denoted as t_a.

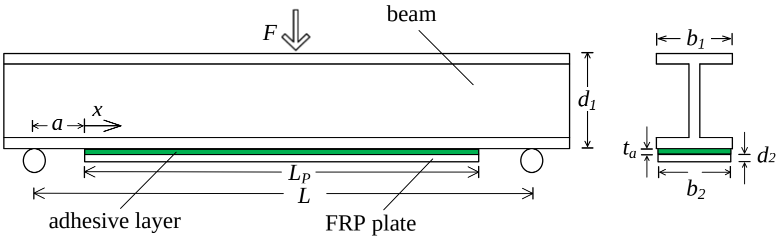

Fig. 3-2 Schematic of the FRP-strengthened beam.

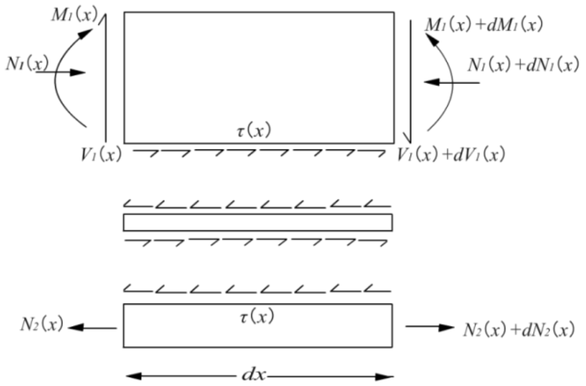

Fig. 3-3 Schematic of a differential element of FRP-plated steel beam.

Fig. 3-3 illustrates the free-body diagram of the differential element (of a length dx) of the FRP-strengthened beam. Each adhered is subjected to axial ($N(x)$) and shear ($V(x)$) forces as well as bending moments ($M(x)$). Shear stresses acting on the element interfaces are denoted as ($\tau(x)$) (**Fig. 3-3**). Considering the significantly lower axial stiffness of the adhesive layer compared to that of the beam and the FRP plate, axial forces in the adhesive are ignored.

From the horizontal force equilibrium of the beam and the FRP plate, following equations can be obtained:

$$\frac{dN_1(x)}{dx} = \tau(x)b_2 \qquad \frac{dN_2(x)}{dx} = \tau(x)b_2 \tag{3-5}$$

where b_2 denotes the width of FRP plate which is also the width of the adhesive layer. Considering the overall horizontal force equilibrium, relationship between the axial forces on beam and FRP plate can be obtained as:

$$N_1(x) = N_2(x) \tag{3-6}$$

The relationship between the overall moment and shear distribution of the beam can be written as:

$$\frac{dM_T(x)}{dx} = V_T(x) \tag{3-7}$$

Considering the flexural stiffness of the FRP plate is negligible compared to the flexural stiffness of the beam, it is ignored and the overall moment equilibrium is expressed as follows:

$$M_T = M_1 + N_1(y_1 + y_2 + t_a) \tag{3-8}$$

where y_1 and y_2 are the distances from the neutral axes of each adherend to the corresponding interface (**Fig. 3-3**), respectively. Considering that the transverse shear deformations in both the beam and the FRP plate are negligible, strains at bottom of the beam (ε_1) and at top of the FRP plate (ε_2) can be calculated as:

$$\varepsilon_1(x) = \frac{y_1}{E_1 I_1} M_1(x) - \frac{1}{E_1 A_1} N_1(x) + \alpha_1 \Delta T \tag{3-9}$$

$$\varepsilon_2(x) = \frac{1}{E_2 A_2} N_2(x) + \alpha_2 \Delta T \tag{3-10}$$

where E, A, I and α are the elastic modulus, sectional area, second moment of area, and thermal expansion coefficient respectively, the subscripts 1 and 2 denote the beam and the FRP plate, respectively, ΔT is the temperature variation.

Interfacial shear slip at distance x can be expressed as

$$\delta_t(x) = u_2(x) - u_1(x) \tag{3-11}$$

where u_1 and u_2 are the axial displacements at bottom of the beam and top of the FRP plate, respectively.

Differentiating Eq. (3-11) and with the substitution of Eq. (3-9) and Eq. (3-10), the following can be derived:

$$\begin{aligned}\frac{d\delta}{dx} &= \varepsilon_2(x) - \varepsilon_1(x) \\ &= -\frac{y_1}{E_1 I_1} M_1(x) + \frac{1}{E_2 A_2} N_2(x) + \frac{1}{E_1 A_1} N_1(x) + (\alpha_2 - \alpha_1)\Delta T\end{aligned} \tag{3-12}$$

By substituting Eq. (3-11) into Eq. (3-1), shear stress at the elastic stage of the interface can be calculated by:

$$\tau^e(x) = K_T[u_2(x) - u_1(x)] \tag{3-13}$$

Furthermore, differentiating Eq. (3-13) twice and with the substitution of Eqs. (3-12), (3-8), (3-7) and (3-5). The final governing differential equations of the interfacial shear stress can be obtained as:

$$\frac{d^2\tau^e(x)}{dx^2} - K_T b_2[\frac{y_1(y_1+y_2+t_a)}{E_1 I_1} + \frac{1}{E_1 A_1} + \frac{1}{E_2 A_2}]\tau^e(x) + \left(\frac{K_T y_1}{E_1 I_1}\right) V_T(x) = 0 \tag{3-14}$$

By setting $\lambda^2 = K_T b_2[\frac{y_1(y_1+y_2+t_a)}{E_1 I_1} + \frac{1}{E_1 A_1} + \frac{1}{E_2 A_2}]$ and $m_1 = \frac{1}{\lambda^2}\left(\frac{K_T y_1}{E_1 I_1}\right)$, Eq. (3-14) can be simplified as:

$$\frac{d^2\tau^e(x)}{dx^2} - \lambda^2\tau^e(x) + m_1\lambda^2 V_T(x) = 0 \tag{3-15}$$

General solution of Eq. (3-15) is:

$$\tau^e(x) = B_x \cosh(\lambda x) + B_y \sinh(\lambda x) + m_1 V_T(x) \tag{3-16}$$

where B_x, B_y are the integration constants. Correspondingly, the interfacial slip in the elastic region can be obtained as:

$$\delta_t^e(x) = \frac{1}{K_T}[B_x \cosh(\lambda x) + B_y \sinh(\lambda x) + m_1 V_T(x)] \tag{3-17}$$

In comparison, for interfacial stress calculation in the softening region, shear stress distribution can be expressed as

$$\tau^s(x) = \tau_0 - K_T'[u_2(x) - u_1(x)] \tag{3-18}$$

With the similar approach to the analysis in elastic region, governing equation of shear stress distribution in the softening region can be derived as:

$$\frac{d^2\tau^s(x)}{dx^2} + K_T' b_2[\frac{y_1(y_1 + y_2 + t_a)}{E_1 I_1} + \frac{1}{E_1 A_1} + \frac{1}{E_2 A_2}]\tau^s(x) - \frac{K_T' y_1}{E_1 I_1} V_T(x) = 0 \tag{3-19}$$

By defining $\lambda'^2 = K_T' b_2[\frac{y_1(y_1+y_2+t_a)}{E_1 I_1} + \frac{1}{E_1 A_1} + \frac{1}{E_2 A_2}] = \frac{K_T'}{K_T}\lambda^2$, and $m_1' = \frac{1}{\lambda'^2}\left(\frac{K_T' y_1}{E_1 I_1}\right) = m_1$, Eq. (3-19) can be re-written as:

$$\frac{d^2\tau^s(x)}{dx^2} + \lambda'^2\tau^s(x) - m_1'\lambda'^2 V_T(x) = 0 \tag{3-20}$$

Subsequently, the general solution of interfacial shear stress distribution in the softening region can be expressed as:

$$\tau^s(x) = B_m\cos(\lambda' x) + B_n\sin(\lambda' x) + m_1' V_T(x) \tag{3-21}$$

where B_m and B_n are the integration constants. The corresponding interfacial slip in the softening region can be expressed as:

$$\delta_t^s(x) = \frac{1}{K_T'}[\tau_0 - B_m\cos(\lambda' x) - B_n\sin(\lambda' x) - m_1' V_T(x)] \tag{3-22}$$

3.2.4 Stages of Debonding Process

The entire deformation process of the interface can be divided into three stages, including elastic (*E*) stage, elastic-softening (*E-S*) stage, and elastic-softening-debonding (*E-S-D*) stage (De Lorenzis and Zavarise, 2009). During the *E* stage, the interfacial shear stresses stay lower than τ_p, and the interfacial stress/slip distributions are governed by Eqs. (3-16) and (3-17). At the end of the *E* stage, the plate end region enters into the softening stage. During the *E-S* stage, the softening region near the plate end tends to expand in length, while the regions far away from the plate end remain elastic. The interfacial stress/slip distributions at the softening region are governed by Eqs. (3-21) and (3-22). Once the interfacial slip at the plate end grows to δ_f, the debonding initiates at the plate end, and the deformation process of the interface enters into the *E-S-D* stage.

As experimentally observed by Deng and Lee (2007), the loading capacity drops suddenly once the debonding failure initiates at the plate end. That is because the debonding propagation is a dynamic process driven by the interfacial stresses and a sudden energy release can be expected during the debonding process (Teng *et al.*, 2015). Therefore, the load corresponding to the initiation of the plate-end debonding failure is usually defined as the load-carrying capacity (i.e., the debonding load) of the FRP-strengthened beam (Teng *et al.*, 2015; De Lorenzis *et al.*, 2013). Therefore, only the *E* and *E-S* stages are included in the analytical solution in order to predict the debonding load.

3.2.4.1 Elastic stage

At the elastic stage, the whole length of the interface behaves elastic and the interfacial shear stress distribution can be expressed as

$$\tau^e(x) = B_1 \cosh(\lambda x) + B_2 \sinh(\lambda x) + m_1 \frac{F}{2} \tag{3-23}$$

where F is the mechanical loading applied at the mid-span of the beam. Here, $V_T(x) = F/2$. The integration constants of B_1 and B_2 can be determined by applying suitable boundary conditions, including the shear force (Eq. 3-24) and the moment (Eq. 3-25) of the strengthened beam at the end of the FRP plate, while the axial forces of the beam and the plate soffit are zero (Eq. 3-26).

$$V_1(0) = V_T(0) = \frac{F}{2} \tag{3-24}$$

$$M_1(0) = M_T(0) = \frac{Fa}{2} \tag{3-25}$$

$$N_1(0) = N_2(0) = 0 \tag{3-26}$$

where a denotes the distance from the plate end to the supporting point (**Fig. 3-2**). Substituting Eqs. (3-9) and (3-10) into the first differentiation of Eq. (3-13) and applying the above boundary conditions, the following equation can be derived:

$$\left.\frac{d\tau^e(x)}{dx}\right|_{x=0} = -m_2 M_T(0) + m_3 \Delta T = -\frac{m_2 a}{2} F + m_3 \Delta T \tag{3-27}$$

where $m_3 = K_T(\alpha_2 - \alpha_1)$. The parameter m_2 is defined as:

$$m_2 = \frac{K_T y_1}{E_1 I_1} \tag{3-28}$$

By substituting Eq. (3-23) into Eq. (3-27), B_2 can be determined as:

$$B_2 = \frac{1}{\lambda}[-\frac{m_2 a}{2}F + m_3 \Delta T] \tag{3-29}$$

Considering the symmetry of the applied load on the FRP-strengthened beam, the interfacial shear stress at the mid-span is zero. That is,

$$\tau^e(L_P/2) = 0 \tag{3-30}$$

Therefore, B_1 can be determined as:

$$B_1 = \frac{1}{2}[\frac{m_2 a}{\lambda}\tanh\left(\frac{\lambda L_P}{2}\right) - \frac{m_1}{\cosh(\lambda L_P/2)}]F - \frac{\tanh(\lambda L_P/2)}{\lambda}m_3 \Delta T \tag{3-31}$$

In addition, the axial stress of the FRP plate (σ_P) at the position of x_0 ($0 \leq x_0 \leq L_P/2$) during the *E* stage can be calculated by integrating the shear stresses along the bond interface and applying the boundary condition (i.e., $\sigma_P(0) = 0$) at the plate end.

$$\begin{aligned} \sigma_P(x_0) &= \int_0^{x_0} \tau^e(x)/d_2\, dx \\ &= \frac{1}{d_2\lambda}[B_1 \sinh(\lambda x_0) + B_2 \cosh(\lambda x_0) - B_2] + \frac{m_1 F}{2d_2}x_0 \end{aligned} \tag{3-32}$$

3.2.4.2 Elastic-softening stage

At the *E-S* stage, both the softening region (near the plate end) and the elastic region (near the mid-span of the FRP plate) are considered, and the length of the softening region ($\bar{x}$) grows with the increasing applied load. The shear stress distributions in the two regions can be respectively expressed as follows:

$$\tau^s(x) = B_3 \cos(\lambda' x) + B_4 \sin(\lambda' x) + m_1 \frac{F}{2} \quad (0 \leq x < \bar{x}) \tag{3-33}$$

$$\tau^e(x) = B_5 \cosh(\lambda x) + B_6 \sinh(\lambda x) + m_1 \frac{F}{2} \quad (\bar{x} \leq x \leq L_P/2) \tag{3-34}$$

Similar to the methods adopted in the *E* stage, by applying the boundary conditions at the plate end, the integration constant B_4 can be determined as:

$$B_4 = \frac{1}{\lambda'}[\frac{m'_2 a}{2}F - m'_3\Delta T] \tag{3-35}$$

where $m'_2 = \frac{K'_T y_1}{E_1 I_1}$, and $m'_3 = K'_T(\alpha_2 - \alpha_1)$.

Also, at the mid-span the shear stress is equal to zero. That is

$$\tau^e(L_P/2) = B_5\cosh(\lambda L_P/2) + B_6\sinh(\lambda L_P/2) + m_1\frac{F}{2} = 0 \tag{3-36}$$

Apart from the boundary conditions at the plate end and the mid-span as mentioned above, the peak shear stress τ_p is achieved at the critical point $\bar{x}$ bridging the elastic and the softening regions (Eq. 3-37):

$$\tau^s(\bar{x}) = \tau^e(\bar{x}) = \tau_p \tag{3-37}$$

Substituting Eq. (3-37) into Eq. (3-33) and Eq. (3-34) and in combination with Eqs. (3-35) and (3-36), B_3, B_5 and B_6 can be determined as:

$$B_3 = \frac{1}{\cos(\lambda'\bar{x})}[\tau_p - \frac{F}{2}\left(\frac{m'_2 a}{\lambda'}\sin(\lambda'\bar{x}) + m'_1\right) + \frac{m'_3\Delta T}{\lambda'}\sin(\lambda'\bar{x})] \tag{3-38}$$

$$B_5 = \frac{1}{\sinh[\lambda(L_P/2-\bar{x})]}\left\{\tau_p\sinh(\lambda L_P/2)\ + \frac{m_1 F}{2}[\sinh(\lambda\bar{x}) - \sinh(\lambda L_P/2)]\right\} \tag{3-39}$$

$$B_6 = -\frac{1}{\sinh[\lambda(L_P/2-\bar{x})]}\left\{\tau_p\cosh(\lambda L_P/2)\ + \frac{m_1 F}{2}[\cosh(\lambda\bar{x}) - \cosh(\lambda L_P/2)]\right\} \tag{3-40}$$

As the determinations of the above integration constants include a variable $\bar{x}$, which is changed with the load levels. Using the same method adopted by De Lorenzis and Zavarise (2009), the relationship between $\bar{x}$ and F can be determined by considering that N_1, N_2, and M_1 are continuous at $x = \bar{x}$.

$$\frac{d\tau^s(\bar{x})}{dx} = -\frac{K'_T}{K_T}\frac{d\tau^e(\bar{x})}{dx} \tag{3-41}$$

$$-B_3\lambda'\sin(\lambda'\bar{x}) + B_4\lambda'\cos(\lambda'\bar{x}) = -\frac{K'_T}{K_T}[B_5\lambda\sinh(\lambda\bar{x}) + B_6\lambda\cosh(\lambda\bar{x})] \tag{3-42}$$

Therefore,

$$\frac{F}{2} = \frac{\tau_p\{\tan(\lambda'\bar{x}) + r\coth[\lambda(L_P/2-\bar{x})]\} + \frac{m'_3\Delta T}{\lambda'\cos(\lambda'\bar{x})}}{\frac{m_1\sin(\lambda'\bar{x}) + \frac{m'_2 a}{\lambda'}}{\cos(\lambda'\bar{x})} + m_1 r\frac{\cosh[\lambda(L_P/2-\bar{x})] - 1}{\sinh[\lambda(L_P/2-\bar{x})]}} \tag{3-43}$$

Here, $r = \frac{\lambda'}{\lambda} = \sqrt{\frac{K'}{K}}$ is introduced.

In addition, for the cases where $\lambda(L_P/2-\bar{x})>10$, Eq. (3-43) can be simplified as follows:

$$\frac{F}{2}=\{\tau_p[\tan(\lambda'\bar{x})+r]+\frac{m_3'\Delta T}{\lambda'\cos(\lambda'\bar{x})}\}/\{\frac{m_1\sin(\lambda'\bar{x})+\frac{m_2'a}{\lambda'}}{\cos(\lambda'\bar{x})}+m_1r\} \tag{3-44}$$

In the *E-S* stage, the tensile stress in the FRP plate at a distance x_0 can be derived as:

when $0\le x_0<\bar{x}$,

$$\begin{aligned}\sigma_P(x_0)&=\int_0^{x_0}\tau^s(x)/d_2\,dx\\&=\frac{1}{\lambda'd_2}[B_3\sin(\lambda'x_0)-B_4\cos(\lambda'x_0)+B_4]+\frac{m_1F}{2d_2}x_0\end{aligned} \tag{3-45}$$

when $\bar{x}\le x_0\le L_P/2$,

$$\begin{aligned}\sigma_P(x_0)&=\int_{\bar{x}}^{x_0}\frac{\tau^e}{d_2}dx+\sigma_P(\bar{x})\\&=\frac{1}{\lambda d_2}[B_5\sinh(\lambda x_0)+B_6\cosh(\lambda x_0)]+\frac{m_1F}{2d_2}x_0\\&-\frac{1}{\lambda d_2}[B_5\sinh(\lambda\bar{x})+B_6\cosh(\lambda\bar{x})]\\&+\frac{1}{\lambda'd_2}[B_3\sin(\lambda'\bar{x})-B_4\cos(\lambda'\bar{x})+B_4]\end{aligned} \tag{3-46}$$

3.2.4.3 Debonding load

The debonding load sustained by the FRP-strengthened beam is reached at the end of the *E-S* stage, when the interfacial shear stress at the plate end decreases to zero. Applying the boundary condition (i.e., $\tau^s(x)|_{x=0}=0$) and substituting Eq. (3-38) into Eq. (3-33), the corresponding load capacity F_{deb} at the initiation of debonding can be obtained as:

$$F_{deb}=\frac{2[\lambda'\tau_p+m_3'\Delta T\sin(\lambda'\bar{x}_{deb})]}{m_2'a\sin(\lambda'\bar{x}_{deb})+m_1'\lambda'+m_1'\lambda'\cos(\lambda'\bar{x}_{deb})} \tag{3-47}$$

The debonding load (F_{deb}) and the corresponding length of softening region ($\bar{x}_{deb}$) can be computed by combining Eqs. (3-43) and (3-47).

3.3. VALIDATION OF THE ANALYTICAL SOLUTION

3.3.1 Finite Element (FE) Model

The distributions of the interfacial stresses/slips and the axial stresses in the FRP plate obtained from the analytical solutions are verified against the numerical results from a finite element (FE) model. A simply supported beam as shown in **Fig. 3-2** is considered as an example. The geometrical dimensions of the beam are 76 mm in width, 86 mm in depth and 1100 mm in clear span. The beam is strengthened at its soffit with an 800 mm long FRP plate. The FRP plate has the same width as the beam and is 3 mm thick. The detailed parameters of the beam are provided in **Table 3-1**. The bond-slip parameters used to define the interfacial behavior between the FRP plate and the beam are also listed in **Table 3-1**. The bond-slip parameters used in the study are taken from De Lorenzis *et al.* (2013). All the FE results in this thesis are obtained using the general-purpose software Abaqus 6.14.

The FE modeling is implemented using the static general approach, based on full newton solution technic and system defined defaults convergence criteria. The beam was modeled by two-dimensional Euler-Bernoulli beam element with cubic interpolation (B23), which has 2 translational degrees of freedom and 1 rotational degree of freedom at each node. The FRP plate was modeled by two-dimensional two-node truss element (T2D2), which has 2 translational degrees of freedom at each node. In addition, the adhesive layer between the FRP plate and the beam is modeled by the two-dimensional 4-node cohesive element (COH2D4) with 2 translational degrees of freedom at nodes on top and bottom faces. In the interfacial normal direction, the stiffness of the element and mode I fracture energy were assumed as several orders of magnitude larger as compared to the mode II case, to ensure that neither penetration nor separation would occur in the interfacial normal direction.

In the initial step, the reference temperature (i.e., 0 ℃) was assigned for the entire specimen by predefined field variables. Then the temperature value was changed to the studied magnitude of temperature variation (i.e., -50 ℃, -25 ℃, 25 ℃ and 50 ℃) in the second step. The mechanical loading was applied in the third step using a displacement-control manner until the specimen failed.

Table 3-1 Parameters used in the FE model

Beam geometry parameters

b_1(mm)	d_1(mm)	b_2(mm)	d_2(mm)	L(mm)	L_P(mm)	t_a(mm)
76	86	76	3	1100	400	1

Material and interface parameters

E_1(N/mm^2)	E_2(N/mm^2)	τ_p(N/mm^2)	δ_t^0(mm)	δ_t^f(mm)	G_{IIc}(N/mm)	α_1(/℃)	α_2(/℃)
205000	212000	26.73	0.0526	0.1197	1.600	11×10^{-6}	1×10^{-6}

3.3.2 Mesh Sensitivity Analysis

A mesh sensitivity study was carried out to seek the most suitable size of FE meshes. The substrate beam, the FRP plate and the adhesive layer were simulated with the same mesh size. Such element size was varied from 0.1 mm to 6.4 mm. **Fig. 3-4** compares the interfacial shear stress distributions near the plate end predicted for the beam under a mechanical load of 80 kN with different element sizes, including 0.1 mm, 0.2 mm, 0.4 mm, 0.8 mm, 1.6 mm, 3.2 mm, and 6.4 mm. The comparisons in **Fig. 3-4** indicate that a mesh size of no larger than 0.4 mm is suitable to achieve an accurate FE prediction of the shear stress distribution near the plate end. Therefore, the element size of all constituents (i.e., both adherends and the adhesive layer) is taken as 0.2 mm in the FE model based on a tradeoff of accuracy and efficiency of the computation.

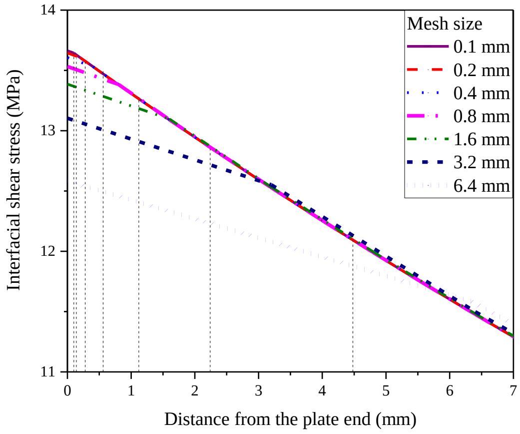

Fig. 3-4 Distribution of interfacail shear stress with different element sizes.

3.3.3 Comparisons with the FE Results

Fig. 3-5 and **Fig. 3-6** show the distributions of interfacial shear stresses/slips and the axial stresses in the FRP plate predicted by the analytical solution and the FE model under two different conditions, respectively: (a) the beam is subjected to mechanical loading only and the temperature variation is constant; (b) the beam is subjected to varying temperatures (from ΔT = -50 ℃ to ΔT = +50 ℃) while the mechanical load is constant. In these figures, the magnitudes of interfacial stresses/slips are normalized by the maximum interfacial shear stress and the corresponding slip (τ_p, δ_0). Also, only half of the laminate (i.e., from the plate end to the mid-span) is shown considering the symmetry of the strengthened beam. It is clearly seen that the analytical predictions are almost identical to those obtained from the FE model.

As shown in **Fig. 3-5**, the deformation process evolves gradually from the *E* stage to the *E-S* stage with the growth in the mechanical load. During the *E* stage (F = 80 kN or 130 kN and ΔT = 0 ^{o}C), the values of the shear stress/slip and the axial tensile stress of the FRP plate all increase with the load growth. After the peak shear stress (τ_p) is achieved at the plate end, the deformation process enters into the *E-S* stage, during which the softening of the bond interface starts at the plate end and the length of the softening region expands with the load growth. Meanwhile, the interfacial shear stresses near the plate end decrease with further load growth. Of course, the shear slips of the bond interface always increase during both the *E* and *E-S* stages. Once the interfacial slip increases to its maximum value (δ_f) and the shear stress drops to zero accordingly, the debonding initiates at the plate end and the debonding load of the strengthened beam is achieved.

In **Fig. 3-5c**, it is observed that the axial stresses of the FRP plate increase from the plate end to the middle region. Also, the axial stresses in the FRP plate are improved with the increasing mechanical load under low loading levels regardless of the plate location. During the *E-S* stage, the axial stresses near the plate end reduce because of the declined interfacial shear stresses as illustrated in **Fig. 3-5a**. Similar phenomena can be observed when the beam is subjected to a constant mechanical load and an increasing service temperature (**Fig. 3-6**). As shown in **Fig. 3-6**, the interfacial shear stresses change significantly with the temperature growth although the mechanical load remains constant. When the temperature variation is zero, the interface has already entered into the softening stage under the given load. Then the interface softening near the plate end becomes more significant as the temperature variation increases to 25 ℃ or 50 ℃. However, if the temperature variation is -25 ℃ or -50 ℃, the interface still lies in the elastic stage.

By comparing the behaviors of the FRP-strengthened beam under various temperatures, it is clear that the interfacial shear stresses/slips generated by the temperature increase are in the same direction as those induced by the mechanical loading. In other words, the maximum interfacial shear stress and the corresponding slip can be achieved at a relatively lower level of the applied mechanical load if the service temperature is increased, leading to a declined debonding load of the FRP-strengthened beam.

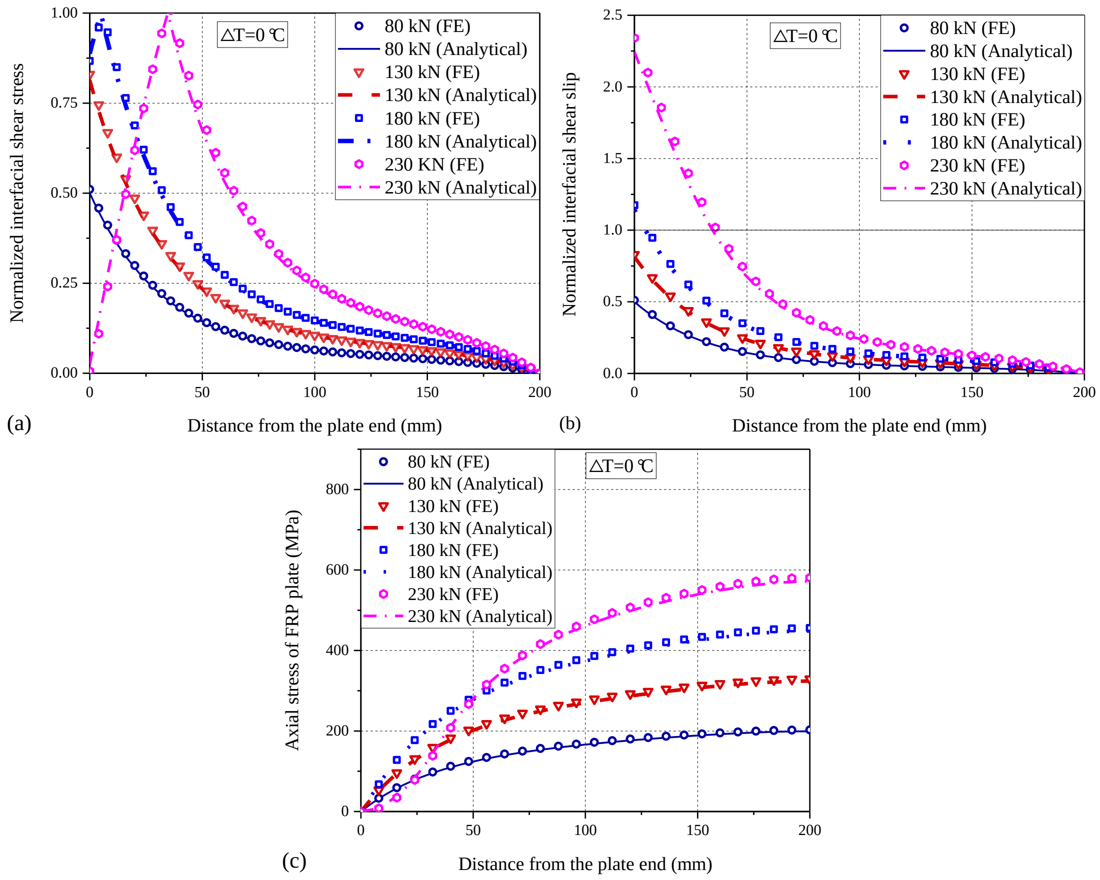

Fig. 3-5 Comparisons between analytical and FE results for the FRP-strengthened beam under various mechanical loadings: a) normalized interfacial shear stress distribution; b) normalized interfacial shear slip distribution; c) axial stress of the FRP plate.

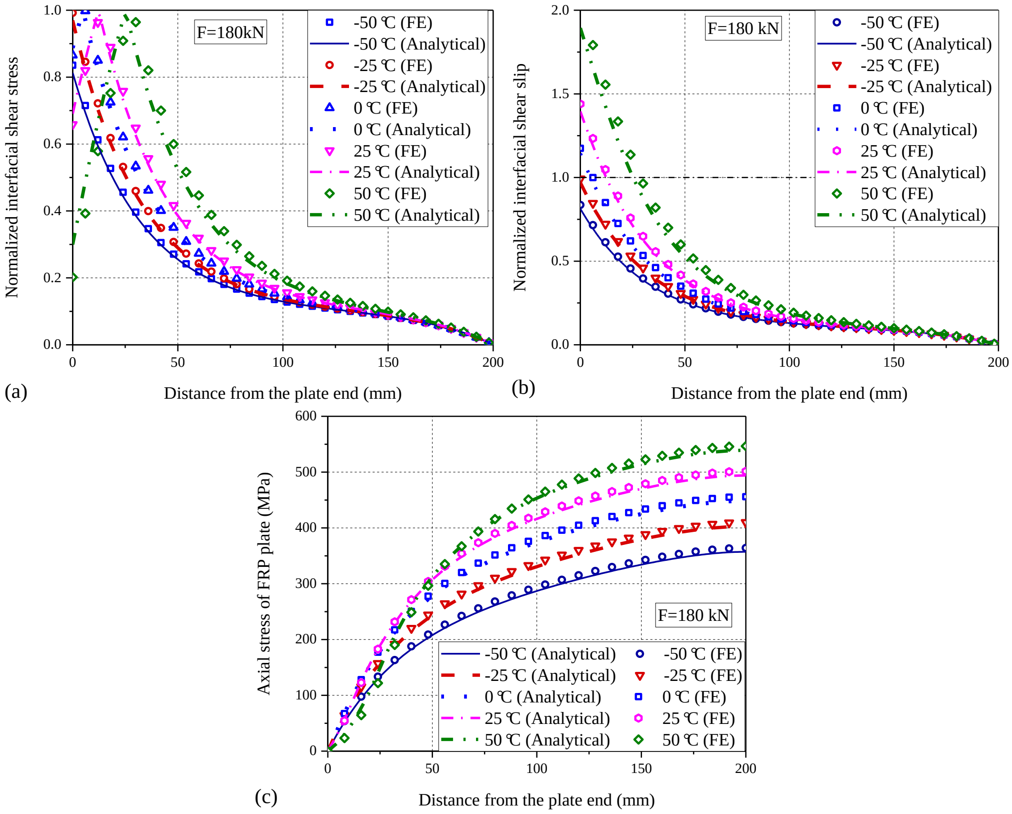

Fig. 3-6 Comparisons between analytical and FE results for the FRP-strengthened beam at various temperatures: a) normalized interfacial shear stress distributions; b) normalized interfacial shear slip distributions; c) axial stresses of the FRP plate.

3.4. PARAMETRIC STUDY

3.4.1 Effect of FRP Plate Properties

In this section, the analytically predicted debonding loads of the FRP-strengthened beam with different properties of the FRP plate are investigated to facilitate a good understanding of the thermal loading effect on the debonding load. The beam with the properties listed in **Table 3-1** is still taken as the benchmark. The key properties investigated herein are the length, thickness, and elastic modulus of the FRP plate.

Fig. 3-7 presents the changes of the debonding loads of the FRP-strengthened beam under various service temperatures in cases of different FRP plate lengths, thicknesses and elastic moduli, respectively. The predicted debonding loads at varying temperatures are all normalized by the value at the reference temperature (i.e., no temperature change, $\Delta T = 0$).

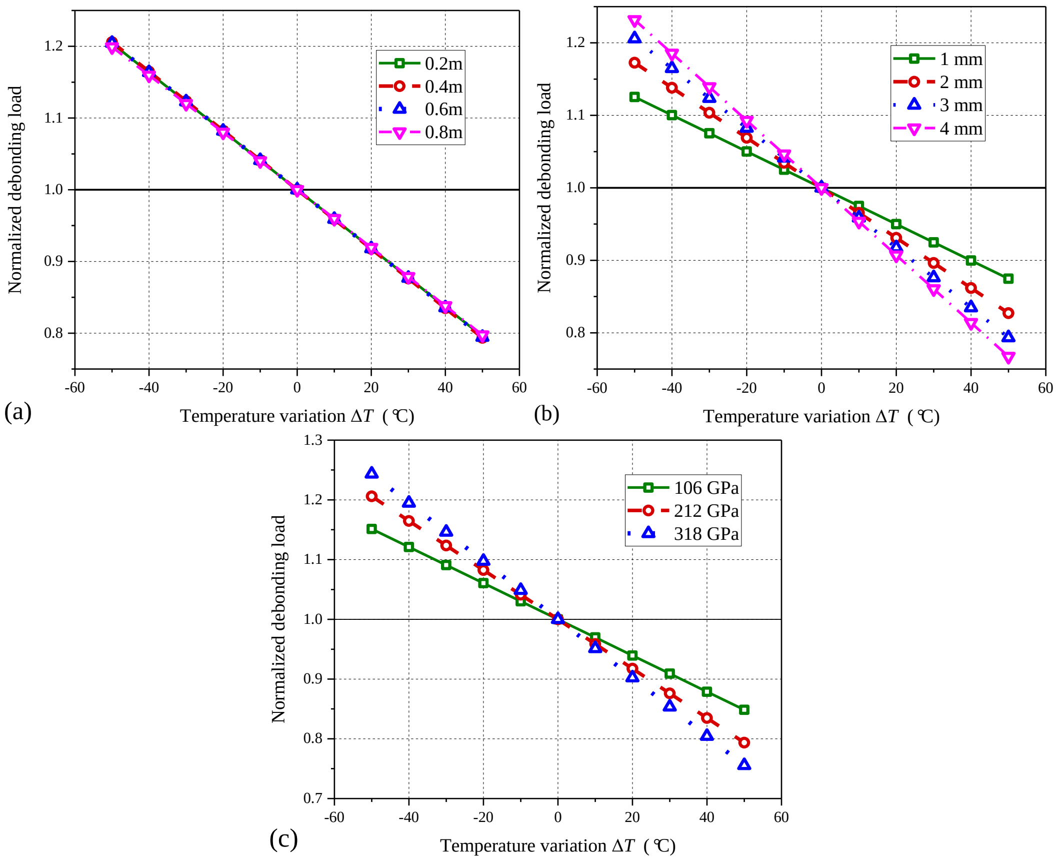

Fig. 3-7 Effect of temperature variation on the normalized debonding load for the strengthened beam with different FRP plate a) lengths; b) thicknesses; c) elastic moduli.

It is seen that the debonding load of the FRP-strengthened beam decreased with temperature increase regardless of the FRP plate properties (**Fig. 3-7**). The effect of the FRP plate length on the debonding load of the FRP-strengthened beam under various service temperatures is negligible, as shown in **Fig. 3-7a**. However, both the thickness and the elastic modulus of the FRP plate have significant effects on the changes of the debonding load with the temperature variation. The normalized debonding load of the FRP-strengthened beam at lower service temperatures increases with the increase in thickness and/or the elastic modulus of the FRP plate, while an opposite trend is found at higher service temperatures. This finding essentially means that higher reductions of the plate end debonding load are observed for the FRP-strengthened beam with higher elastic modulus and thickness of the FRP plate. Note here only the thermal stress effect is considered (i.e., the bond-slip relationship is assumed to have no change). The FRP plate thickness and the elastic modulus are expected to influence the debonding load as interfacial shear stresses are directly related to the axial stiffness values of the FRP plate. With a higher stiffness of the FRP plate, any thermal deformation can result in higher load transfer through the interface, thus causing a high rate of interfacial stress change. Even though this relationship cannot be clearly seen from the Eq. (3-47), the results from **Fig. 3-7b** and **7c** indicate that the higher rate of change due to the temperature variations at higher stiffness values of the FRP plate.

3.5. CONCLUSIONS

This chapter has presented a new and closed-form analytical solution for predicting the plate-end debonding failure of the FRP-strengthened steel/concrete beam under combined mechanical and thermal loading. The distributions of interfacial shear stresses/slips and the axial stresses of the FRP plate at different loading stages can be predicted using the proposed analytical solution. The analytical solution has been validated through the comparisons between analytical and FE results. The following conclusions can be drawn based on the analytical solution and the results presented in this chapter.

a) Although the FRP-to-steel/concrete interface remains elastic behavior, the interfacial shear stresses at the plate end grow with the increasing service temperature. The interfacial shear slip at the plate-end always increases with temperature growth.

b) The plate-end debonding load of the FRP-strengthened beam reduces with the increasing temperature.

c) The enhancement in the FRP plate stiffness results in an increasing rate of the debonding load reduction with the temperature.

3.6. REFERENCES

Abaqus 6.14 (2014) "Documentation." Providence, RI, USA: Dassault Systemes Simulia Corporation.

Ahmed, A., and Kodur, V.K.R. (2011). "Effect of bond degradation on fire resistance of FRP-strengthened reinforced concrete beams." *Composites Part B: Engineering* 42(2), 226-237.

Al Nuaimi, N., Sohail, M.G., Hawileh, R., Abdalla, J.A., and Douier, K. (2021). "Durability of Reinforced Concrete Beams Externally Strengthened with CFRP

Laminates under Harsh Climatic Conditions." *Journal of Composites for Construction*, 25(2).

Al-Shawaf, A, Al-Mahaidi, R and Zhao, X.L. (2009). "Effect of elevated temperature on bond behaviour of high modulus CFRP/steel double-strap joints." *Australian Journal of Structural Engineering* 10(1): 63-74.

Al-Shawaf, A.K. (2010). "Characterization of bonding behavior between wet lay-up carbon fibre reinforced polymer and steel plates in double-strap joints under extreme environmental temperatures." Monash University, Australia.

Al-Tamimi, A.K., Hawileh, R.A., Abdalla, J.A., Rasheed, H.A., and Al-Mahaidi, R. (2015). "Durability of the Bond between CFRP Plates and Concrete Exposed to Harsh Environments." *Journal of Materials in Civil Engineering* 27(9).

Bennati, S., Colonna, D. and Valvo, P.S. (2016). "A cohesive-zone model for steel beams strengthened with pre-stressed laminates." *Procedia Structural Integrity* 2: 2682-2689.

Biscaia, H.C. (2019). "The influence of temperature variations on adhesively bonded structures: A non-linear theoretical perspective." *International Journal of Non-Linear Mechanics* 113: 67-85.

Biscaia, H.C., Chastre, C. and Silva, M.A. (2017). "Analytical model with uncoupled adhesion laws for the bond failure prediction of curved FRP-concrete joints subjected to temperature. " *Theoretical and Applied Fracture Mechanics* 89: 63-78.

Biscaia, H.C. and Ribeiro, P. (2019). "A temperature-dependent bond-slip model for CFRP-to-steel joints." *Composite Structures* 217: 186-205.

Bocciarelli, M., Colombi, P., Fava, G., Sonzogni, L. (2016). "Energy-based analytical formulation for the prediction of end debonding in strengthened steel beams." *Composite Structures* 153: 212-221.

Bruno, D., Greco, F., Feudo, S.L., Blasi, P.N. (2016). "Multi-layer modeling of edge debonding in strengthened beams using interface stresses and fracture energies." *Engineering Structures* 109: 26-42.

Chandrathilaka, E., Gamage, J. and Fawzia, S. (2019). "Mechanical characterization of CFRP/steel bond cured and tested at elevated temperature." *Composite Structures* 207: 471-477.

Choobbor, S.S., Hawileh, R.A., Abu-Obeidah, A., and Abdalla, J.A. (2019). "Performance of hybrid carbon and basalt FRP sheets in strengthening concrete beams in flexure." *Composite Structures* 227.

Cornetti, P., Corrado, M., De Lorenzis, L. and Carpinteri, A. (2015). "An analytical cohesive crack modeling approach to the edge debonding failure of FRP-plated beams." *International Journal of Solids and Structures* 53: 92-106.

Dai, J.G., Gao, W.Y. and Teng, J.G. (2013). "Bond-Slip Model for FRP Laminates Externally Bonded to Concrete at Elevated Temperature." *Journal of Composites for Construction* 17(2): 217-228.

Dai, J.G., Ueda, T. and Sato, Y. (2005). "Development of the nonlinear bond stress–slip model of fiber reinforced plastics sheet–concrete interfaces with a simple method. " *Journal of Composites for Construction* 9(1): 52-62.

Dai, J.G., Ueda, T., Sato, Y. and Hasan, M. (2003). "Mode I fracture behavior of FRP-concrete interfaces. " *Proceedings of the Japan Concrete Institute* 25(1): 1577.

De Lorenzis, L., Fernando, D. and Teng, J.G. (2013). "Coupled mixed-mode cohesive zone modeling of interfacial debonding in simply supported plated beams." *International Journal of Solids and Structures* 50(14-15): 2477-2494.

De Lorenzis, L., and Zavarise, G. (2009). "Cohesive zone modeling of interfacial stresses in plated beams." *International Journal of Solids and Structures* 46(24): 4181-4191.

Deng, J. and Lee, M.M.K. (2007). "Behaviour under static loading of metallic beams reinforced with a bonded CFRP plate." *Composite Structures* 78(2): 232-242.

Deng, J., Lee, M.M.K. and Moy, S.S.J. (2004). "Stress analysis of steel beams reinforced with a bonded CFRP plate." *Composite Structures* 65(2): 205-215.

Dong, K. and Hu, K. (2016). "Development of bond strength model for CFRP-to-concrete joints at high temperatures." *Composites Part B: Engineering* 95: 264-271.

Fernando, D., Yu, T. and Teng, J.G. (2015). "Behavior and modeling of CFRP-strengthened rectangular steel tubes subjected to a transverse end bearing load." *International Journal of Structural Stability and Dynamics* 15(08): 1540031.

Ferrier, E., Rabinovitch, O. and Michel, L. (2016). "Mechanical behavior of concrete–resin/adhesive–FRP structural assemblies under low and high temperatures." *Construction and Building Materials* 127: 1017-1028.

Gao, W.Y., Dai, J.G. and Teng, J.G. (2015). "Analysis of Mode II debonding behavior of fiber-reinforced polymer-to-substrate bonded joints subjected to combined thermal and mechanical loading." *Engineering Fracture Mechanics* 136: 241-264.

Gao, W.Y., Teng, J.G., and Dai, J.G. (2012). "Effect of Temperature Variation on the Full-Range Behavior of FRP-to-Concrete Bonded Joints." *Journal of Composites for Construction*, 16(6), 671-683.

Ghous, Sohail, M., Al Nuaimi, N., Hawileh, R. A., Abdalla, J. A. and Douier, K. (2021). "Durability of plain concrete prism strengthened with galvanized steel mesh and CFRP laminates under harsh environmental conditions." *Construction and Building Materials* 286.

Haghani, R., Al-Emrani, M. and Kliger, R. (2009). "Interfacial stress analysis of geometrically modified adhesive joints in steel beams strengthened with FRP laminates." *Construction and Building Materials* 23(3): 1413-1422.

Hawileh, R.A., Abu-Obeidah, A., Abdalla, J.A. and Al-Tamimi, A. (2015). "Temperature effect on the mechanical properties of carbon, glass and carbon–glass FRP laminates." *Construction and Building Materials* 75, 342-348.

Idris, Y. and Ozbakkaloglu, T. (2014). "Flexural behavior of FRP-HSC-steel composite beams." *Thin-Walled Structures* 80: 207-216.

Ke, L., Li, C., He, J., Dong, S., Chen, C. and Jiao, Y. (2020). "Effects of elevated temperatures on mechanical behavior of epoxy adhesives and CFRP-steel hybrid joints." *Composite Structures* 235: 111789.

Korayem, A.H., Chen, S.J., Zhang, Q.H., Li, C.Y., Zhao, X.L. and Duan, W.H. (2016). "Failure of CFRP-to-steel double strap joint bonded using carbon nanotubes modified epoxy adhesive at moderately elevated temperatures." *Composites Part B: Engineering* 94: 95-101.

Lenwari, A., Thepchatri, T. and Albrecht, P. (2006). "Debonding strength of steel beams strengthened with CFRP plates." *Journal of Composites for Construction* 10(1): 69-78.

Liu, M. and Dawood, M. (2018). "A closed-form solution of the interfacial stresses and strains in steel beams strengthened with externally bonded plates using ductile adhesives." *Engineering Structures* 154: 66-77.

Lu, X., Teng, J., Ye, L., Jiang, J.J. (2005). "Bond–slip models for FRP sheets/plates bonded to concrete." *Engineering Structures* 27(6): 920-937.

Mohammadi, T., Wan, B., Harries, K.A., Sweriduk, M.E. (2017). "Bond Behavior of FRP–Concrete in Presence of Intermediate Crack Debonding Failure." *Journal of Composites for Construction* 21(5).

Nguyen, P.L., Vu, X.H. and Ferrier, E. (2019). "Elevated temperature thermomechanical behaviour of near surface mounted CFRP reinforced concrete specimens: Effect of adhesive at concrete/CFRP interface." *Engineering Structures* 197: 109361.

Nguyen, T.C., Bai Y., Zhao X.L., Al-Mahaidi R. (2011). "Mechanical characterization of steel/CFRP double strap joints at elevated temperatures." *Composite Structures* 93(6): 1604-1612.

Ouyang, Z. and Wan, B. (2009). "Nonlinear deterioration model for bond interfacial fracture energy of FRP-concrete joints in moist environments." *Journal of Composites for Construction* 13(1): 53-63.

Rizkalla, S., Dawood, M. and Schnerch, D. (2008). "Development of a carbon fiber reinforced polymer system for strengthening steel structures." *Composites Part a-Applied Science and Manufacturing* 39(2): 388-397.

Sahin, M.U. and Dawood, M. (2016). "Experimental Investigation of Bond between High-Modulus CFRP and Steel at Moderately Elevated Temperatures." *Journal of Composites for Construction* 20(6): 04016049.

Sauder, C., Lamon, J. and Pailler, R. (2004). "The tensile behavior of carbon fibers at high temperatures up to 2400 degrees C." *Carbon* 42(4): 715-725.

Schnerch, D., Dawood, M., Rizkalla, S., Sumner, E. (2007). "Proposed design guidelines for strengthening of steel bridges with FRP materials." *Construction and Building Materials* 21(5): 1001-1010.

Silva, M.A.G. and Biscaia, H. (2008). "Degradation of bond between FRP and RC beams." *Composite Structures* 85(2): 164-174.

Smith, S.T. and Teng, J.G. (2001). "Interfacial stresses in plated beams." *Engineering Structures* 23(7): 857-871.

Stratford, T. and Bisby, L. (2012). "Effect of warm temperatures on externally bonded FRP strengthening." *Journal of Composites for Construction* 16(3): 235-244.

Stratford, T. and Cadei, J. (2006). "Elastic analysis of adhesion stresses for the design of a strengthening plate bonded to a beam." *Construction and Building Materials* 20(1-2): 34-45.

Taljsten, B. (1997). "Strengthening of beams by plate bonding." *Journal of Materials*

Teng, J.G., Fernando, D., and Yu, T. (2015). Finite element modelling of debonding failures in steel beams flexurally strengthened with CFRP laminates. *Engineering Structures*, 86, 213-224.

Teng, J.G., Yu, T. and Fernando, D. (2012). "Strengthening of steel structures with fiber-reinforced polymer composites." *Journal of Constructional Steel Research* 78: 131-143.

Teng, J.G., Zhang, J.W. and Smith, S.T. (2002). "Interfacial stresses in reinforced concrete beams bonded with a soffit plate: a finite element study." *Construction and Building Materials* 16(1): 1-14.

Teng, R., Guo, Y., Wang, H., Zhao, Z., and Wang, X. (2021). "Experimental study of bending interface characteristics of CFRP-strengthened long-span steel main beams at different temperatures." *Engineering Structures* 235.

Wang, H.T. and Wu, G. (2018). "Crack propagation prediction of double-edged cracked steel beams strengthened with FRP plates." *Thin-Walled Structures* 127: 459-468.

Yu, B., and Kodur, V.K.R. (2014). "Effect of high temperature on bond strength of near-surface mounted FRP reinforcement." *Composite Structures* 110, 88-97.

Yu, T., Fernando D., Teng J.G., Zhao X.L. (2012). "Experimental study on CFRP-to-steel bonded interfaces." *Composites Part B-Engineering* 43(5): 2279-2289.

Yu, Y., Chiew, S.P. and Lee, C.K. (2011). "Bond failure of steel beams strengthened with FRP laminates - Part 2: Verification." *Composites Part B-Engineering* 42(5): 1122-1134.

Yuan, H., Lu, X., Hui, D. and Feo, L. (2012). "Studies on FRP-concrete interface with hardening and softening bond-slip law." *Composite Structures* 94(12): 3781-3792.

Yuan, H., Teng, J.G., Seracino, R., Wu, Z. S., and Yao, J. (2004). Full-range behavior of FRP-to-concrete bonded joints. *Engineering Structures*, 26(5), 553-565.

Zeng, J. J., Gao, W. Y., and Liu, F. (2018). "Interfacial behavior and debonding failures of full-scale CFRP-strengthened H-section steel beams." *Composite Structures*, 201, 540-552.

Zhang, S.S. and Teng, J.G. (2016). "End cover separation in RC beams strengthened in flexure with bonded FRP reinforcement: simplified finite element approach." *Materials and Structures* 49(6): 2223-2236.

Zhang, S.S., Yu, T. and Chen, G.M. (2017). "Reinforced concrete beams strengthened in flexure with near-surface mounted (NSM) CFRP strips: Current status and research needs." *Composites Part B: Engineering* 131: 30-42.

Zheng, J.J., Li, Q.B. and Dai, J.G. (2020). "Analytical solution for FRP-to-concrete bonded joints considering local unloading and reloading." *Engineering Fracture Mechanics* 235: 107185.

Zhou, H., Fernando, D., Torero, J.L., Maluk, C., Emberley, R. (2020). "Bond Behavior of CFRP-to-Steel Bonded Joints at Mild Temperatures: Experimental Study." *Journal of Composites for Construction* 24(6): 04020070.

Zhou, H., Torres, J.P., Fernando, D., Law, A., Emberley, R. (2019). "The bond behaviour of CFRP-to-steel bonded joints with varying bond properties at elevated temperatures." *Engineering Structures* 183: 1121-1133.

Zhang, H.Y., Kodur, V., Qi, S.L., and Wu, B. (2015). "Characterizing the bond strength of geopolymers at ambient and elevated temperatures." *Cement and Concrete Composites* 58, 40-49.

CHAPTER 4

EFFECT OF TEMPERATURE VARIATION ON THE PLATE-END DEBONDING OF FRP-STRENGTHENED STEEL BEAMS: COUPLED MIXED-MODE COHESIVE ZONE MODELING

4.1. INTRODUCTION

FRP composites have gained popularity in strengthening and retrofitting existing steel structures due to their many advantages such as the high strength-to-weight ratio, excellent durability performance and easy installation (e.g., Teng *et al.* 2012). Existing research has shown that the flexural capacity of externally bonded (EB) FRP-strengthened steel beams can be significantly improved (e.g., Deng and Lee 2007; Lenwari *et al.* 2006; Rizkalla *et al.* 2008; Yu *et al.* 2011; Zeng *et al.* 2018). The performance of an FRP-strengthened steel beam is largely determined by the effectiveness of stress transfer between the steel beam and the FRP plate. The dominant failure mode is the plate-end debonding (Colombi and Poggi 2006; Deng and Lee 2007; Linghoff *et al.* 2009; Sallam *et al.* 2006; Zeng *et al.* 2018), in which an interfacial crack initiates at the plate end and develops rapidly until the full debonding of the FRP plate. The plate-end debonding is generally attributed to the high interfacial stress concentration in both the mode II (i.e., tangential or shear) and mode I (i.e., normal) directions of the interface. Therefore, an accurate prediction on the bond behavior of FRP-strengthened steel beam is of great importance in determining its strengthening performance.

Due to the seasonal and diurnal temperature change, the service temperature of an FRP-strengthened steel beam could be changed from the installation temperature of FRP (i.e., the temperature at which the FRP is bonded to the steel). Such temperature change will lead to the thermal stress at the FRP-to-steel interface and consequently significantly affect the interfacial behavior and failure of FRP-strengthened steel beam. The thermal effect on the performance of FRP-strengthened steel beam was experimentally tested in previous studies at elevated temperatures (e.g., Stratford and Bisby 2012; Sahin and

Dawood 2016; Teng *et al.* 2021) and decreased temperatures (Yoshitake *et al.* 2014). The test results showed that, when the strengthened beam fails in plate-end debonding, both the interfacial stress distributions and debonding load change as temperature varies. The effect of temperature variation can be considered from two aspects: 1) the temperature-dependent properties of the adhesive layer (Silva and Biscaia 2008; Dai *et al.* 2013; Zhou *et al.* 2020); 2) the thermally induced interfacial stress (e.g., Gao *et al.* 2012, 2015). Specifically, as most of structural adhesives are ambient temperature cured ones, the mechanical properties of the adhesive layers are likely to be affected as the service temperature changes, especially when the temperature is close to or exceeds the glass transition temperature of the adhesive. As such, the bond behavior between the FRP and the substrate steel, including the interfacial stiffness, interfacial peak bond stress and interfacial fracture energy, can be deteriorated at elevated temperatures (e.g., Dai *et al.*, 2013; Korayem *et al.* 2016; Ferrier *et al.* 2016; Zhou *et al.* 2017, 2020; Biscaia and Ribeiro 2019; Chandrathilaka *et al.* 2019; Nguyen *et al.* 2019; Ke *et al.* 2020; Zhou *et al.* 2020). Meanwhile, the interfacial thermal stresses can be generated because of the discrepancy in coefficients of thermal expansions of steel and FRP materials. Depending on the direction of the initial thermal stress, the temperature variation may affect the bond strength between the FRP plate and steel substrate in different ways (e.g., Gao *et al.* 2012, 2015; Biscaia *et al.* 2015, 2017; Zhou *et al.* 2019).

The thermal stress effect on the distributions of interfacial stresses in both longitudinal and normal directions to the FRP-to-steel interface in FRP-strengthened steel beams have been analyzed by closed-form solutions proposed by Deng *et al.* (2004) and Stratford and Cadei (2006), which was based on linear elastic assumption for the bond-slip/separation laws, i.e., the interfacial stresses are linearly proportional to the deformation of the adhesive layer. According to these analyses, the magnitude of interfacial stresses at both normal and shear directions generated by thermal loading was found to be comparable to that generated by mechanical loading. The plate-end debonding load of FRP-strengthened beam can be approximated by comparing the maximum interfacial normal and shear stresses with the corresponding tensile and shear strengths of the adhesive layer (Deng and Lee 2004; Schnerch *et al.* 2007). However, such stress-based criterion may lead to underestimation of the plate-end debonding load due to the significant softening behavior of the interface, by which the interfacial fracture energy instead of the adhesive strength is a more dominant factor (Dai *et al.* 2005; Teng *et al.* 2012; Yu *et al.* 2012; Yuan *et al.*, 2012).

To overcome the shortcomings of stress-based approach, cohesive zone model (CZM) has been adopted to analyze the interfacial behaviors of FRP-bonded concrete/steel joints (Yuan *et al.* 2004) and FRP-strengthened concrete/steel beams (Wang 2006; De Lorenzis and Zavarise 2009) subjected to mechanical loading only. In these models, the interfacial debonding is assumed to occur when the critical interfacial energy release rate is reached. Based on the cohesive zone model, some analytical solutions have been proposed to consider the effect of combined mechanical and thermal loading on the full-range bond behaviors of FRP-bonded steel joints (Gao *et al.* 2012, 2015; Biscaia *et al.* 2015; Zhou *et al.* 2019, 2022) and curved FRP-concrete joints (Biscaia *et al.* 2017). For FRP-bonded joints subjected to mode II loading, it has been shown that the initial thermal stress induced by elevated temperatures improves the bond strength significantly. In contrast, it was found that the thermal stress induced by elevated temperature leads to reduced plate-end debonding load in FRP-strengthened steel beams in **Chapter 3**, based on the assumption that the FRP-to-steel interface is subjected to Mode II loading only. In reality, the Mode I stress in the normal direction of the interface may have a comparable magnitude as that in the shear direction (i.e., Mode II loading) in FRP-strengthened steel beams (Deng and Lee 2007).

The coupled mixed-mode cohesive zone model, which considers the interaction of both mode I and mode II stresses on the onset of plate-end debonding was presented by Camanho *et al.* (2003). Since then, three typical criteria governing the interface failure, including quadratic failure criterion (Cui *et al.* 1992), power law criterion (Wu and Reuter Jr 1965), and B-K criterion (Benzeggagh and Kenane 1996) were often adopted in analyzing the interfacial behaviors and predicting the debonding loads of FRP-strengthened steel beams in FE modeling (Fernando 2010; Teng *et al.* 2015; Zeng *et al.* 2018; Deng *et al.* 2018). In addition, based on coupled mixed-mode CZM, De Lorenzis *et al.* (2013) developed closed-form analytical solutions to predict the interfacial behavior of an FRP-strengthened steel beam under mechanical loading only, in which the quadratic failure criterion and power law criterion were utilized in predicting the onset of softening and debonding of the adhesive layer.

In view of the important effect of thermal stress on the plate-end debonding of the FRP-strengthened beam as well as the importance of coupled mode I and mode II analysis, this chapter aims to develop a closed-form solution based on coupled mixed-mode failure theory to analyze the interfacial behaviors and plate-end debonding failure of FRP-strengthened steel beams subjected to combined mechanical loading and temperature variation.

4.1.1 Problem Definition and Assumptions

Fig. 4-1 illustrates a simply supported FRP-strengthened steel beam subjected to three-point bending and temperature variation. As shown in the figure, the flange width of the I-beam is b_1 and the distance from its neutral axis to the bottom is y_1. An FRP plate with a width of b_2 and a length of $2l$ is bonded to the tension soffit of the I-beam by adhesive layer with thickness of t_a. y_2 is the distance between the neutral axis to the top surface of the FRP plate. a is the distance from the plate end to the support. The second moment of inertia, sectional area, and the elastic modulus of the adherend are noted as I, A, E, with the subscripts '1' and '2' representing the beam and FRP plate respectively. Due to the symmetry of the simply supported beam, only half of the strengthened beam with the x axis originating from the end of the FRP plate, is analyzed in this study.

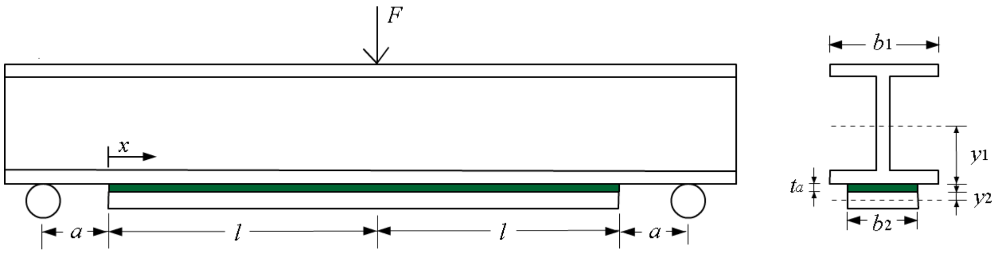

Fig. 4-1 Simply supported strengthened beam under three-point bending

To find a closed-form solution for predicting the interfacial behavior of the above FRP strengthened steel beam, several common assumptions are adopted in the present study:

1. Both the steel beam and the FRP plate are linearly elastic. The transverse shear deformation of the two adherends are ignored;

2. Magnitudes of interfacial shear and normal stresses are invariant across the thickness of the adhesive layer;

3. Sectional properties, the elastic moduli of steel beam and FRP plate are constant at varying temperatures;
4. The temperature variation and thermal deformation of the FRP-strengthened steel beam are uniformly distributed along axial direction.

4.2. COHESIVE ZONE MODEL

Before the introduction of coupled mixed-mode CZM analysis, the interfacial behavior under single mode CZM analysis is briefly introduced in this section.

4.2.1 Single Mode Interface Analysis

Fig. 4-2 illustrates the interfacial bond behavior between the steel substrate and FRP plate, including a bond-slip relationship under mode II loading (**Fig. 4-2a**) and a bond-separation relationship under mode I loading (**Fig. 4-2b**).

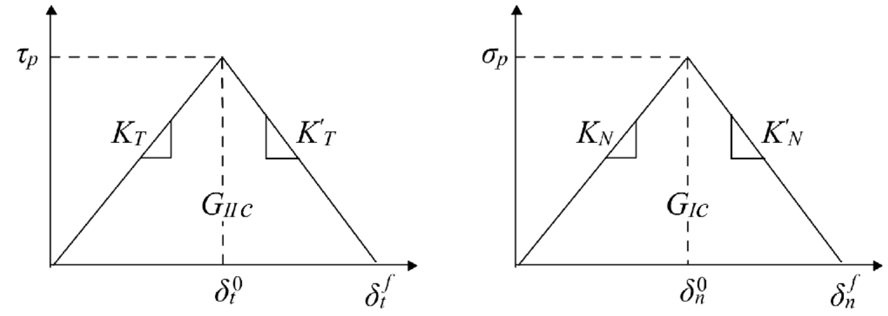

(a) (b)

Fig. 4-2 Bond-slip/separation relationship in CZM

Both the above two relationships are assumed to be bilinear and can be expressed as follows:

$$\tau = \begin{cases} K_T\delta_t & if\ \delta_t < \delta_t^0 \\ \tau_p - K'_T(\delta_t - \delta_t^0) & if\ \delta_t^0 < \delta_t < \delta_t^f \\ 0 & if\ \delta_t^f < \delta_t \end{cases}$$

$$\sigma = \begin{cases} K_N\delta_n & if\ \delta_n < \delta_n^0 \\ \sigma_p - K'_N(\delta_n - \delta_n^0) & if\ \delta_n^0 < \delta_n < \delta_n^f \\ 0 & if\ \delta_n^f < \delta_n \end{cases} \tag{4-1}$$

in which τ and σ represent the interfacial stress in shear and normal directions with subscript 'p' indicates the peak magnitude when softening initiates. δ is the interfacial deformation, with subscripts 't' and 'n' denoting the shear and normal directions, respectively. Superscripts '0' and 'f' represent the critical magnitude at onset of softening and debonding, respectively. K and K' are the slopes of the bilinear relationship in the elastic and softening branches, respectively, with the subscripts 'T' and 'N' indicating the tangential or normal direction, respectively.

The critical energy release rates, i.e., interfacial fracture energies under mode I and mode II (i.e., G_{Ic}, G_{IIc}) loadings, respectively, are defined as the areas enclosed beneath the relationship as follows:

$$G_{IIC} = \frac{1}{2}\tau_p \delta_t^f \text{ and } G_{IC} = \frac{1}{2}\sigma_p \delta_n^f \tag{4-2}$$

Based on the bond-slip relationship in mode II direction (**Fig. 4-2a)**, the interfacial bond behavior in FRP-strengthened steel beam subjected to coupled mechanical loading and temperature variation has been analyzed in **Chapter 3** on the assumption that only mode II loading is exerted at the FRP-to-steel interface. **Fig. 4-3** shows the obtained typical distributions of shear stresses and slips along the interface, in which the interfacial shear stresses and slips are normalized by the peak shear stress (τ_p) and the corresponding slip (δ_t^0), respectively. The deformation process of the interface evolves from *E* stage to *E-S* stage as the load or temperature increase. During *E* stage, the interfacial shear stress/slip is larger near the plate end and increases with increasing the mechanical loading or temperature. After the peak shear stress (τ_p) is reached at the plate end, the deformation process evolves to the elastic-softening (*E-S*) stage. During this stage, the softening first starts at the plate end and extends to the mid span of the beam gradually. As the load/temperature increases, the interfacial shear stress near the plate end increases first (i.e., *E* stage) and then decreases once the interface enters the softening (i.e., *E-S* stage). In comparison, the interfacial slip increases monotonically in both *E* and *E-S* stage with increasing of the mechanical or thermal loading. Finally, plate-end debonding occurs when the interface enters into the elastic-softening-debonding (*E-S-D*) stage, i.e., the interfacial shear stress at the plate end decreases to zero and the interfacial slip increases to δ_t^f.

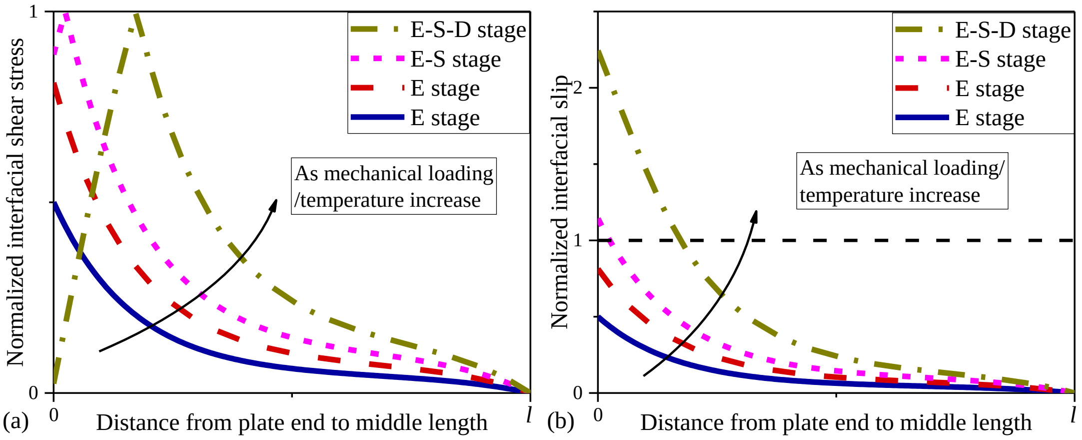

Fig. 4-3 Interfacial bond behavior in FRP-strengthened beam under increased mechanical or thermal loading: distributions of a) normalized interfacial shear stress; b) normalized interfacial slip.

It can be noted from **Fig. 4-3a**, as the load increases, both the increase and decrease of the interfacial shear stress can be observed at the plate end in *E* stage and *E-S* stage, respectively. But the interfacial slip increases monotonically with the increase of the applied mechanical or thermal loading (**Fig. 4-3b**). As such, it is easy to identify the deformation stage of the interface based on the magnitude of interfacial slip at the plate end [i.e., $\delta_t(0) < \delta_t^0$ in *E* stage; $\delta_t^0 < \delta_t(0) < \delta_t^f$ in *E-S* stage; $\delta_t(0) \geq \delta_t^f$ in *E-S-D* stage].

In addition, in single mode II analysis, the length of softening region ($\bar{x}$) in *E-S* stage is an essential parameter, when determining the distribution of interfacial stresses. That is because it corresponds to the turning point of the bilinear bond-slip relationship (i.e., the peak shear stress point in **Fig. 4-2a**). In **Chapter 3**, the length of the softening region can be determined for a given load F and temperature variation ΔT as follows:

$$\frac{F}{2} = \frac{\tau_p\{\tan(\lambda'\bar{x}) + r\coth[\lambda(l-\bar{x})]\} + \dfrac{m_3'\Delta T}{\lambda'\cos(\lambda'\bar{x})}}{\dfrac{m_1\sin(\lambda'\bar{x}) + \dfrac{m_2'a}{\lambda'}}{\cos(\lambda'\bar{x})} + m_1 r\dfrac{\cos[\lambda(l-\bar{x})]-1}{\sin[\lambda(l-\bar{x})]}} \tag{4-3}$$

where F is the applied mechanical load and ΔT is the temperature variation; λ, r, λ', m_3', m_1, m_2' are constants which can be calculated based on the inherent properties of the FRP plate and the steel beam.

4.2.2 *Coupled Mixed-Mode Cohesive Zone Model*

Fig. 4-4 shows the interfacial bond-slip/separation relationships between the FRP plate and the steel beam in coupled mixed-mode analysis. It can be observed that, the bond strengths in both mode I and mode II directions are compromised in the coupled mixed-mode analysis.

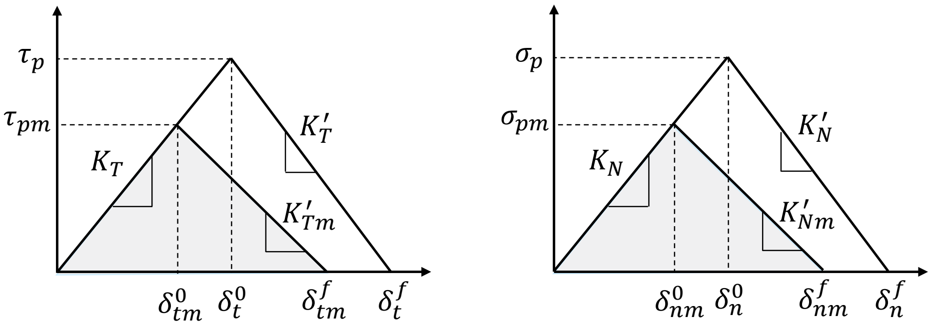

(a) **(b)**

Fig. 4-4 Interfacial CZ laws. (a) mode II. (b) mode I.

Similar to the single mode II analysis, the deformation stage of the interface can also be distinguished according to the mixed-mode interfacial deformation in the coupled mixed-mode analysis. The magnitude of mixed-mode deformation is defined as δ_m, which is the square root of the quadratic sum of relative displacements in both tangential (δ_t) and normal (δ_n) directions:

$$\delta_m = \sqrt{{\delta_t}^2 + \langle\delta_n\rangle^2} \tag{4-4}$$

where the Macaulay bracket ($\langle\ \ \rangle$) indicates that the compressive deformation (i.e., $\delta_n < 0$) in normal direction does not generate any damage to the interface (also adopted in Eq. 4-7).

In addition, when $\delta_n > 0$, the displacement-based mode-mixity ratio is defined as,

$$\gamma = \frac{\delta_t}{\delta_n} \tag{4-5}$$

Considering that the distributions of interfacial slip and separation along the bondline [i.e., $\delta_t(x)$ and $\delta_n(x)$] change with the applied mechanical loading, γ is function of x and F.

With Eqs. (4-4) and (4-5), the tangential and normal components of the relative displacement can be expressed as follows:

$$\delta_t = \frac{\gamma \delta_m}{\sqrt{1+\gamma^2}};\ \delta_n = \frac{\delta_m}{\sqrt{1+\gamma^2}} \tag{4-6}$$

4.2.2.1 Criterion for onset of softening

The initiation of softening is defined by the quadratic stress failure criterion, as follows:

$$(\frac{\tau}{\tau_p})^2 + (\frac{\langle \sigma \rangle}{\sigma_p})^2 = 1 \tag{4-7}$$

To satisfy this equation, the corresponding maximum interfacial stresses in both shear and normal directions, which are termed as τ_{pm} and σ_{pm}, should be less than or at maximum equal to the interfacial strength in single-mode conditions (i.e., τ_p and σ_p).

Substituting the mixed-mode displacement at onset of softening (δ_m^0) into Eq. (4-6) yields

$$\delta_{tm}^0 = \frac{\gamma \delta_m^0}{\sqrt{1+\gamma^2}};\ \delta_{nm}^0 = \frac{\delta_m^0}{\sqrt{1+\gamma^2}} \tag{4-8}$$

where δ_{tm}^0 and δ_{nm}^0 are the interfacial slip and separation at onset of softening in mixed-mode analysis, respectively.

Correspondingly, the mixed-mode displacement at the onset of softening (δ_m^0) can be calculated by δ_{tm}^0 and δ_{nm}^0. By considering the bond-slip/separation relationship in elastic stage (Eq. 4-1) and substituting Eq. (4-8) into Eq. (4-7), δ_m^0 can be expressed as

$$\delta_m^0 = \begin{cases} \delta_t^0 \delta_n^0 \sqrt{\frac{1+\gamma^2}{{\delta_t^0}^2+\gamma^2}} & if\ \delta_n^0 > 0 \\ \delta_t^0 & if\ \delta_n^0 \leq 0 \end{cases} \tag{4-9}$$

4.2.2.2 Criterion for onset of debonding

The criterion for the initiation and propagation of debonding was assumed to follow the power-law mixed-mode fracture criterion:

$$(\frac{G_I}{G_{Ic}})^{\alpha} + (\frac{G_{II}}{G_{IIc}})^{\alpha} = 1 \tag{4-10}$$

where G_{Ic} and G_{IIc} are the critical fracture energies in single mode I and mode II conditions, respectively (Eq. 4-2). While the power factor (α) is taken as 1 as suggested in previous studies (De Lorenzis *et al.* 2013; Teng *et al.* 2015; Zeng *et al.* 2018).

When Eq. (4-10) is satisfied,

$$G_I = \frac{1}{2}\tau_{pm}\delta_{tm}^{f} \text{ and } G_{II} = \frac{1}{2}\sigma_{pm}\delta_{nm}^{f} \tag{4-11}$$

where δ_{tm}^{f} and δ_{nm}^{f} are the interfacial displacements in shear and normal directions in coupled mixed-mode analysis when debonding occurs (**Fig. 4-4**). In an analogy to Eq. (4-6), δ_{tm}^{f} and δ_{nm}^{f} can be expressed as functions of δ_{m}^{f} and γ, i.e.,

$$\delta_{tm}^{f} = \frac{\gamma\delta_{m}^{f}}{\sqrt{1+\gamma^2}};\ \delta_{nm}^{f} = \frac{\delta_{m}^{f}}{\sqrt{1+\gamma^2}} \tag{4-12}$$

By substituting Eqs. (4-11) and (4-12) into Eq. (4-10), mixed-mode displacement at onset of debonding (δ_{m}^{f}) can be obtained as

$$\delta_{m}^{f} = \frac{2(1+\gamma^2)}{\delta_{m}^{0}}[\left(\frac{K_N}{G_{Ic}}\right)^{\alpha} + \left(\frac{\gamma^2 K_T}{G_{IIc}}\right)^{\alpha}]^{-1/\alpha} \tag{4-13}$$

From Eqs. (4-9) and (4-13), it can be seen that for given interfacial bond-slip/separation relationships, the magnitudes of δ_{m}^{0} and δ_{m}^{f} only depend on the mode-mixity ratio (γ).

Similar to the mode II analysis, the deformation stage of the interface can be distinguished by the mixed-mode deformation at plate end [$\delta_m(0)$]. When $\delta_m(0)$ is smaller than δ_{m}^{0}, the interface is in *E* stage. Then it evolves to *E-S* stage, when $\delta_m(0)$ is greater than δ_{m}^{0} and smaller than δ_{m}^{f}. Finally, the debonding occurs while $\delta_m(0)$ increases to δ_{m}^{f}.

4.2.2.3 Cohesive zone model at softening stage

In *E-S* stage, the interface near plate end enters the softening stage, thus the slopes of the softening branches in the bond-slip/separation relationships can be computed as follows:

$$K'_{Tm} = \frac{K_T \delta^0_{tm}}{\delta^f_{tm} - \delta^0_{tm}}; \; K'_{Nm} = \frac{K_N \delta^0_{nm}}{\delta^f_{nm} - \delta^0_{nm}} \tag{4-14}$$

And the following definition is introduced

$$r_m = \sqrt{\frac{K'_{Tm}}{K_T}} \tag{4-15}$$

And r_m tends to be a constant value when the mode-mixity ratio (γ) is sufficiently large (De Lorenzis *et al.* 2013).

In coupled mixed-mode analysis, the damage evolution in softening region is described through a single scalar damage variable (d), which is defined as follows,

$$d = \frac{\delta^f_m (\delta_m - \delta^0_m)}{\delta_m (\delta^f_m - \delta^0_m)} \tag{4-16}$$

Thus, the interfacial stresses in the entire deformation stages can be calculated as:

$$\tau = \begin{cases} K_T \delta_t & \delta_m \le \delta^0_m \\ (1-d) K_T \delta_t & \delta^0_m \le \delta_m \le \delta^f_m \\ 0 & \delta^f_m \le \delta_m \end{cases} \tag{4-17}$$

$$\sigma = \begin{cases} K_N \delta_n & \delta_m \le \delta^0_m \\ (1-d) K_N \delta_n & \delta^0_m \le \delta_m \le \delta^f_m \\ 0 & \delta^f_m \le \delta_m \end{cases} \tag{4-18}$$

4.3. INTERFACIAL BEHAVIOR AT ELASTIC STAGE

In this section, an analytical solution is proposed based on elastic mechanics theory to derive the interfacial behavior in *E* stage, in which the thermal deformation of both adherends and the interfacial thermal stress is considered.

4.3.1 Interfacial Shear Stress

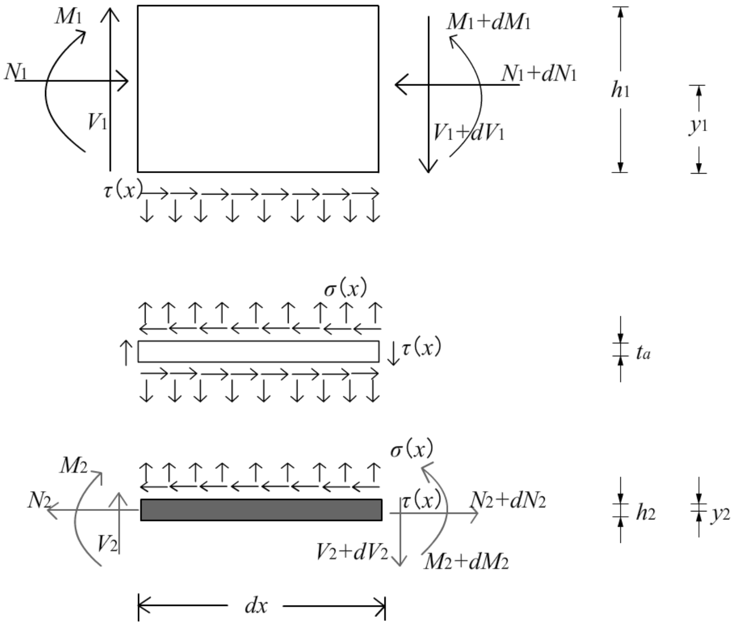

Fig. 4-5 Differential element of the strengthened beam

Fig. 4-5 illustrates a differential segment of the FRP-strengthened steel beam with a length of dx. Both adherends are subjected to axial force, shear force, bending moment and interfacial stresses in shear and normal directions. And the following equilibrium equations can be established.

$$\frac{dN_1(x)}{dx} = \tau(x)b_2 \qquad \frac{dN_2(x)}{dx} = \tau(x)b_2 \tag{4-19}$$

$$N_1 = N_2 \tag{4-20}$$

$$\frac{dM_1(x)}{dx} = V_1(x) - \tau(x)b_2y_1 \qquad \frac{dM_2(x)}{dx} = V_2(x) - \tau(x)b_2y_2 \tag{4-21}$$

where M, V, N are the bending moment, axial and shear force sustained by each adherend, with subscript ‘1’ and ‘2’ representing the steel beam and FRP plate.

For the FRP-strengthened steel beam illustrated in **Fig. 4-1**, the overall moment equilibrium of the differential element in the strengthened beam yields,

$$\frac{dM_T(x)}{dx} = V_T(x) = \frac{F}{2} \tag{4-22}$$

$M_T(x)$ and $V_T(x)$ are the bending moment and shear force acting on the FRP-strengthened beam at x. Considering the flexural stiffness of both adherends, the moment equilibrium can be expressed as follows:

$$M_T = M_1 + M_2 + N_1(y_1 + y_2 + t_a) \tag{4-23}$$

To uncouple the differential equations, the curvatures of the FRP plate and steel beam are assumed to be equal in deriving the distribution of the interfacial shear stress (Smith and Teng 2001). As such, the relationship of moment in both adherends can be expressed as:

$$M_1 = RM_2; \quad R = \frac{E_1 I_1}{E_2 I_2} \tag{4-24}$$

By substituting Eq. (4-24) into Eq. (4-23), the bending moment acting on the steel beam and the FRP plate can be expressed as function of M_T and the axial force N_1:

$$M_1 = \frac{R}{R+1} M_T - \frac{R}{R+1} N_1(y_1 + y_2 + t_a) \tag{4-25}$$

$$M_2 = \frac{1}{R+1} M_T - \frac{1}{R+1} N_1(y_1 + y_2 + t_a) \tag{4-26}$$

For a temperature change as ΔT, the strain on tension soffit of the steel beam (ε_1) and top of FRP plate (ε_2) can be expressed as follows:

$$\varepsilon_1(x) = \frac{du_1}{dx} = \frac{y_1}{E_1 I_1} M_1(x) - \frac{1}{E_1 A_1} N_1(x) + \alpha_1 \Delta T \tag{4-27}$$

$$\varepsilon_2(x) = \frac{du_2}{dx} = -\frac{y_2}{E_2 I_2} M_2(x) + \frac{1}{E_2 A_2} N_2(x) + \alpha_2 \Delta T \tag{4-28}$$

where α_1 and α_2 are the thermal expansion coefficients of the steel beam and the FRP, respectively.

The interfacial slip in tangential direction can be expressed as:

$$\delta_t(x) = u_2(x) - u_1(x) \tag{4-29}$$

In E stage, the interfacial shear stress can be obtained by substituting Eq. (4-29) into Eq. (4-1) and described as:

$$\tau^e(x) = K_T[u_2(x) - u_1(x)] \tag{4-30}$$

where superscripts ‘e’ indicates the E stage.

Differentiating Eq. (4-30) twice and substituting the differentiation of Eqs. (4-27) and (4-28) yield:

$$\frac{d^2\tau^e(x)}{dx^2} = K_T[\frac{y_1}{E_1I_1}\frac{dM_1(x)}{dx} + \frac{y_2}{E_2I_2}\frac{dM_2(x)}{dx} - \frac{1}{E_1A_1}\frac{dN_1(x)}{dx} - \frac{1}{E_2A_2}\frac{dN_2(x)}{dx}] \tag{4-31}$$

Furthermore, substituting Eqs. (4-25) and (4-26) into the above equation gives the following governing equation for the distribution of interfacial shear stress:

$$\frac{d^2\tau^e(x)}{dx^2} - K_Tb_2[\frac{(y_1+y_2)(y_1+y_2+t_a)}{E_1I_1+E_2I_2} + \frac{1}{E_1A_1} + \frac{1}{E_2A_2}]\tau^e(x) + K_T\left(\frac{y_1+y_2}{E_1I_1+E_2I_2}\right)V_T(x) = 0 \tag{4-32}$$

The general solutions of Eq. (4-32) is given by

$$\tau^e(x) = B_1\cosh(\lambda x) + B_2\sinh(\lambda x) + m_1\frac{F}{2} \tag{4-33}$$

where $\lambda^2 = K_Tb_2[\frac{(y_1+y_2)(y_1+y_2+t_a)}{E_1I_1+E_2I_2} + \frac{1}{E_1A_1} + \frac{1}{E_2A_2}]$ and $m_1 = \frac{K_T}{\lambda^2}\left(\frac{y_1+y_2}{E_1I_1+E_2I_2}\right)$.

B_1 and B_2 are the integration constants and can be calculated by applying suitable boundary conditions.

At the plate end ($x = 0$), the axial force of either the steel beam or the FRP plate is zero. And the moment resisted by FRP plate is zero at the plate end. As such, the following boundary conditions can be obtained as follows,

$$N_1(0) = 0;\ N_2(0) = 0;\ M_2(0) = 0 \tag{4-34}$$

Substituting Eqs. (4-27) and (4-28) into differentiation of Eq. (4-30) obtains

$$\left.\frac{d\tau^e(x)}{dx}\right|_{x=0} = K_T[-\frac{y_2}{E_2I_2}M_2(x) - \frac{y_1}{E_1I_1}M_1(x) + \frac{1}{E_2A_2}N_2(x) + \frac{1}{E_1A_1}N_1(x) + (\alpha_2 - \alpha_1)\Delta T)] \tag{4-35}$$

Furthermore, by applying the preceding boundary conditions, Eq. (4-35) can be derived as:

$$\left.\frac{d\tau^e(x)}{dx}\right|_{x=0} = -m_2M_1(0) + K_T(\alpha_2 - \alpha_1)\Delta T \tag{4-36}$$

where, $m_2 = \frac{K_T y_1}{E_1 I_1}$, $M_1(0) = M_T(0) = \frac{Fa}{2}$.

By comparing the first derivative of Eq. (4-33) with Eq. (4-36), B_2 can be determined as

$$B_2 = \frac{1}{\lambda}[-\frac{m_2 a}{2}F + K_T(\alpha_2 - \alpha_1)\Delta T] \tag{4-37}$$

Due to the symmetry of the FRP-strengthened steel beam, the interfacial shear stress at mid-span is zero [i.e., $\tau^e(l) = 0$]. Then B_1 can be determined as follows:

$$B_1 = \frac{1}{2}[\frac{m_2 a}{\lambda}\tanh(\lambda l) - \frac{m_1}{\cosh(\lambda l)}]F - \frac{\tanh(\lambda l)}{\lambda}K_T(\alpha_2 - \alpha_1)\Delta T \tag{4-38}$$

4.3.2 Interfacial Normal Stress

Similar to Eq. (4-30), the interfacial normal stress in *E* stage can be expressed as:

$$\sigma^e(x) = K_N[v_2(x) - v_1(x)] \tag{4-39}$$

where $v_1(x)$ and $v_2(x)$ are the vertical components of the displacements at the bottom of the steel beam and top of the FRP plate, respectively. And the difference between $v_1(x)$ and $v_2(x)$ represents the interfacial separation.

The vertical shear force applied on each adherend is balanced by interfacial normal stress.

$$\frac{dV_1(x)}{dx} = -b_2\sigma(x);\ \frac{dV_2(x)}{dx} = b_2\sigma(x) \tag{4-40}$$

According to the Euler-Bernoulli beam theory,

$$\frac{d^2v_1(x)}{dx^2} = -\frac{1}{E_1I_1}M_1(x);\ \frac{d^2v_2(x)}{dx^2} = -\frac{1}{E_2I_2}M_2(x) \tag{4-41}$$

Differentiate Eq. (4-39) four times and substituting the twice derivation of Eq. (4-41), the following equation can be obtained:

$$\frac{d^4\sigma^e(x)}{dx^4} = K_N[\frac{1}{E_1I_1}\frac{d^2M_1(x)}{dx^2} - \frac{1}{E_2I_2}\frac{d^2M_2(x)}{dx^2}] \tag{4-42}$$

By substituting the differentiations of Eqs. (4-21) and (4-40), the final governing differential equation of normal stress is given as:

$$\frac{d^4\sigma^e(x)}{dx^4} - K_N b_2\left(\frac{1}{E_1I_1} + \frac{1}{E_2I_2}\right)\sigma^e(x) + K_N b_2\left(\frac{y_1}{E_1I_1} - \frac{y_2}{E_2I_2}\right)\frac{d\tau^e(x)}{dx} = 0 \tag{4-43}$$

With $d^5\tau^e(x)/dx^5$ neglected (Smith and Teng, 2001), the general solution to this four-order differential equation is

$$\sigma^e(x) = e^{-\beta x}[C_1\cos(\beta x) + C_2\sin(\beta x)] + e^{\beta x}[C_3\cos(\beta x) + C_4\sin(\beta x)] - n_1\frac{d\tau^e(x)}{dx} \tag{4-44}$$

Where $\beta = \sqrt[4]{\frac{K_N b_2}{4}\left(\frac{1}{E_1I_1} + \frac{1}{E_2I_2}\right)}$, $n_1 = \frac{y_1E_2I_2 - y_2E_1I_1}{E_1I_1 + E_2I_2}$, $n_3 = K_N b_2[\frac{y_1}{E_1I_1} - \frac{y_2}{E_2I_2}]$.

C_1 to C_4 are integrity constants. By noting that when $x \to \infty$, $\sigma \to 0$, therefore, C_3, C_4 are eliminated.

Then Eq. (4-44) evolves to the following simple form:

$$\sigma^e(x) = e^{-\beta x}[C_1\cos(\beta x) + C_2\sin(\beta x)] - n_1\lambda[B_1\sinh(\lambda x) + B_2\cosh(\lambda x)] \tag{4-45}$$

Substituting Eq. (4-41) into the second derivative of Eq. (4-39) and applying the boundary condition at plate end [i.e., $M_1(0) = Fa$] lead to

$$\left.\frac{d^2\sigma^e(x)}{dx^2}\right|_{x=0} = K_N\left[\frac{1}{E_1I_1}M_1(0) - \frac{1}{E_2I_2}M_2(0)\right] = \frac{K_N a}{2E_1I_1}F \tag{4-46}$$

Substituting Eq. (4-41) into the third derivative of Eq. (4-39) yields

$$\left.\frac{d^3\sigma^e(x)}{dx^3}\right|_{x=0} = K_N[\frac{1}{E_1I_1}V_1(0) + \frac{1}{E_2I_2}V_2(0)] + K_N b_2\left(\frac{y_1}{E_1I_1} - \frac{y_2}{E_2I_2}\right)\tau^e(0) \tag{4-47}$$

Considering the boundary condition of shear force at the plate end [i.e., $\mathrm{V}_2(0) = 0; \mathrm{V}_1(0) = \mathrm{V}_\mathrm{T}(0) = \frac{\mathrm{F}}{2}$], the above equation can be rewritten as follows:

$$\left.\frac{d^3\sigma^e(x)}{dx^3}\right|_{x=0} = \frac{K_N}{E_1I_1}\frac{F}{2} + n_3\left(B_1 + m_1\frac{F}{2}\right) \tag{4-48}$$

where

$$n_3 = K_N b_2 \left(\frac{y_1}{E_1 I_1} - \frac{y_2}{E_2 I_2}\right) \tag{4-49}$$

By substituting second and third derivative of Eq. (4-45) into Eqs. (4-46) and (4-48), C_1 and C_2 can be determined as follows:

$$C_1 = \frac{K_N}{4\beta^3}\frac{F}{E_1 I_1}(1+\beta a) + \frac{n_1 \lambda^3}{2\beta^3}(\lambda B_1 + \beta B_2) - \frac{n_3}{2\beta^3}(B_1 + m_1 \frac{F}{2}) \tag{4-50}$$

$$C_2 = -\frac{K_N}{4\beta^2}\frac{Fa}{E_1 I_1} - \frac{n_1}{2\beta^2}\lambda^3 B_2 \tag{4-51}$$

With the above constants, the distributions of relative displacements in both shear and normal directions along the bondline in E stage can be expressed as

$$\delta_t^e(x) = \frac{1}{K_T}[B_1 \cosh(\lambda x) + B_2 \sinh(\lambda x) + m_1 \frac{F}{2}] \tag{4-52}$$

$$\delta_n^e(x) = \frac{1}{K_N}\{e^{-\beta x}[C_1 \cos(\beta x) + C_2 \sin(\beta x)] - n_1 \lambda [B_1 \sinh(\lambda x) + B_2 \cosh(\lambda x)]\} \tag{4-53}$$

4.3.3 The Mechanical Load at Onset of Softening

According to the interfacial behavior of FRP-strengthened steel beam in E stage (**Fig. 4-3a**), the maximum interfacial stresses is located at the plate end. Consequently, the softening and debonding initiate at the plate end. Using Eqs. (4-33) and (4-45), the magnitude of interfacial stresses at softening initiation ($F = F_{sof}$) at the plate end ($x = 0$) can be expressed as

$$\tau^e(0) = B_1 + m_1 \frac{F_{sof}}{2} \qquad \sigma^e(0) = C_1 - n_1 \lambda B_2 \tag{4-54}$$

Substituting Eq. (4-54) into Eq. (4-7), and considering a positive σ^e at the plate end gives,

$$(\frac{B_1 + m_1 \frac{F_{sof}}{2}}{\tau_p})^2 + (\frac{C_1 - n_1 \lambda B_2}{\sigma_p})^2 = 1 \tag{4-55}$$

As B_1, B_2, C_1 are functions of F and ΔT, for a given temperature variation ΔT, the mechanical loading at onset of softening (F_{sof}) can be obtained by solving Eq. (4-55).

4.4. INTERFACIAL BEHAVIOR IN ELASTIC-SOFTENING STAGE

After interfacial softening occurs at the plate end, the interfacial behavior should be interpreted by the softening branches in the mixed-mode CZ law in both mode I and mode II directions. In coupled mixed-mode analysis, the parameters in softening branches (i.e., peak stresses and slopes of softening branches) are changed compared with the single mode analysis (**Fig. 4-4**). And these parameters are dependent on the coupling and mutual influence of the interfacial displacements in both mode I and mode II directions.

In De Lorenzis *et al.*'s analysis (2013), an 'effective tangential cohesive zone (CZ) law' was proposed for describing the interfacial bond behavior in mode II direction in *E-S* stage. By adopting the 'effective tangential CZ law', the distributions of interfacial shear stress and magnitude of the single scalar damage variable (d) can be determined based on mode II analysis. Then the interfacial bond behavior in mode I direction can be obtained based on Eq. (4-18). The proposed analytical solution in this chapter generally follows this method.

4.4.1 Effective Tangential Cohesive Zone Law

Fig. 4-6 shows the 'effective tangential CZ law' used in the mixed-mode analysis. The effect of Mode I loading (i.e., the interfacial normal stress and separation) on the Mode II bond behavior in the coupled mixed-mode analysis is considered by decreasing the peak shear stress ($\tau_{p,eff}$) and varied slope of softening branch ($K'_{T,eff}$) in the bond-slip relationship. In the 'effective tangential CZ law', the bond-slip relationship in softening branch is still assumed to be linear. The softening branch is determined by the instantaneous bond-slip data at two points, including the point with the peak shear stress at $x = \bar{x}$ [i.e., $\delta_t^{es}(\bar{x})$, $\tau_{p,eff}$] and the point with maximum shear slip at $x = 0$ [i.e., $\delta_t^{es}(0)$, $\tau_t^{es}(0)$]. Considering that these parameters change as the variation of applied mechanical loading in *E-S* stage, the ‘effective tangential CZ law’ also varies at different levels of thermal and mechanical loading.

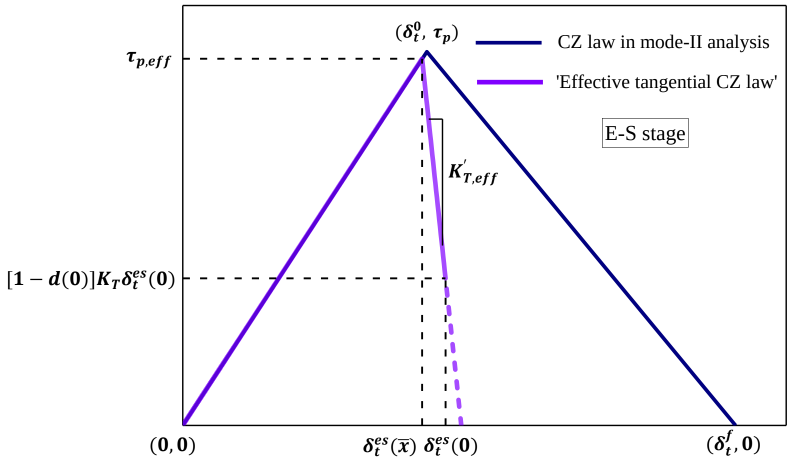

Fig. 4-6 ‘Effective tangential CZ law’ under mixed-mode conditions (De Lorenzis *et al.* 2013).

Following the above-mentioned approach, the distributions of interfacial shear stress in the coupled mixed-mode analysis can be simplified as a mode II analysis with replacing the bond-slip relationship as the “effective tangential CZ law”. Thus, the governing equations and boundary conditions in *E-S* stage in single mode II analysis are still hold for the coupled mixed-mode analysis. And the relationship between the length of the softening region ($\bar{x}$) and the applied mechanical and thermal loading (F and ΔT) is still applicable in the coupled mixed-mode analysis, but with different input parameters (i.e., from ‘τ_p’ to $\tau_{p,eff}$, from ‘K'_T’ to ‘$K'_{T,eff}$’). As a consequence, the length of the softening zone ($\bar{x}$) can be calculated by the following function (refer to Eq. 4-3):

$$F = 2\{\tau_{p,eff}\{\tan(\lambda'_{eff}\bar{x}) + r_{eff}\coth[\lambda(l-\bar{x})]\} + \frac{m'_{3,eff}\Delta T}{\lambda'_{eff}\cos(\lambda'_{eff}\bar{x})}\}$$
$$/\{\frac{m_1\sin(\lambda'_{eff}\bar{x}) + \frac{m'_{2,eff}a}{\lambda'_{eff}}}{\cos(\lambda'_{eff}\bar{x})} + m_1 r_{eff}\frac{\cosh[\lambda(l-\bar{x})]-1}{\sinh[\lambda(l-\bar{x})]}\} \tag{4-56}$$

where,

$$\lambda_{eff}'^{\,2} = \frac{K'_{T,eff}}{K_T}\lambda^2,\ m'_{2,eff} = \frac{K'_{T,eff}y_1}{E_1I_1},\ r_{eff} = \frac{\lambda'_{eff}}{\lambda} = \sqrt{\frac{K'_{T,eff}}{K_T}},\ m'_{3,eff} = K'_{T,eff}(\alpha_2-\alpha_1)$$

Then the problem turns into the determination of the parameters in the ‘effective tangential CZ law’, including $\tau_{p,eff}$ and $K'_{T,eff}$.

In *E-S* stage, the maximum interfacial shear stress ($\tau_{p,eff}$) is located at the connection point between the softening and elastic region (i.e., $x = \bar{x}$) and can be calculated by multiplying the interfacial slip [i.e., $\delta_t^{es}(\bar{x})$] with the interfacial shear stiffness (K_T):

$$\tau_{p,eff} = K_T \delta_t^{es}(\bar{x}) \leq \tau_p \tag{4-57}$$

In addition, the stiffness in the softening branch ($K'_{T,eff}$) can be calculated as the slope between the two points in **Fig. 4-6**, including $[\delta_t^{es}(\bar{x}),\ \tau_{p,eff}]$ and $\{\delta_t^{es}(0),\ [1 - d(0)]K_T\delta_t^{es}(0)\}$.

$$K_{T,eff}^{'} = K_T \frac{\delta_t^{es}(\bar{x}) - [1 - d(0)]\delta_t^{es}(0)}{\delta_t^{es}(0) - \delta_t^{es}(\bar{x})} = K_T \frac{1 - [1 - d(0)]\dfrac{\delta_t^{es}(0)}{\delta_t^{es}(\bar{x})}}{\dfrac{\delta_t^{es}(0)}{\delta_t^{es}(\bar{x})} - 1} \tag{4-58}$$

According to Eqs. (4-57) and (4-58), $\tau_{p,eff}$ and $K'_{T,eff}$ depend on the damage variable at plate end [$d(0)$], the interfacial slip at both the plate end [$\delta_t^{es}(0)$] and the connection point between the elastic and softening region [$\delta_t^{es}(\bar{x})$], and the length of softening zone ($\bar{x}$).

In *E-S* stage, $d(0)$ can be calculated by substituting the interfacial slip at plate end [$\delta_m^{es}(0)$] into Eq. (4-16),

$$d(0) = \frac{\delta_m^f[\delta_m^{es}(0) - \delta_m^0]}{\delta_m^{es}(0)(\delta_m^f - \delta_m^0)} \tag{4-59}$$

In which, the mixed-mode deformation at onset of softening and debonding (i.e., δ_m^0 and δ_m^f) can be calculated by substituting the mode-mixity ratio in *E-S* stage at plate end and the junction point [i.e., $\gamma^{es}(0)$ and $\gamma^{es}(\bar{x})$] into Eqs. (4-9) and (4-13) as follows,

$$\delta_m^0 = \begin{cases} \delta_t^0 \delta_n^0 \sqrt{\frac{1 + \gamma^{es}(\bar{x})^2}{{\delta_t^0}^2 + \gamma^{es}(\bar{x})^2}} & if\ \delta_n^0 > 0 \\ \delta_t^0 & if\ \delta_n^0 \leq 0 \end{cases} \tag{4-60}$$

$$\delta_m^f = \frac{2[1+\gamma^{es}(0)^2]}{\delta_m^0}[\left(\frac{K_N}{G_{IC}}\right)^\alpha + \left(\frac{\gamma^{es}(0)^2 K_T}{G_{IIC}}\right)^\alpha]^{-1/\alpha} \tag{4-61}$$

According to the equations from (4-57) to (4-61), the dominant parameters in ‘effective tangential CZ law’, including $\tau_{p,eff}$ and $K'_{T,eff}$, can be solved provided that the magnitudes of interfacial slip and damage variable at plate end and the connection point [i.e., $\delta_t^{es}(0)$, $\delta_t^{es}(\bar{x})$, $\gamma^{es}(0)$, $\gamma^{es}(\bar{x})$] are known. The subsequent sections focus on the derivation process of these unknown parameters. De Lorenzis *et al.*'s model (2013) adopted two assumptions for simplifying the derivation process of the above-mentioned four parameters for the mixed-mode analysis under mechanical loading only: (1) the normalized Mode II slip/Mode I seperation distributions along the inteface at different load levels are constant. Dai *et al.* (2006) also proved theoretically that the normalized strain distriubtions of FRP (i.e., by the maximum FRP strain value) along an FRP-to-concrete interface are unique under different load levels if the bond-stress slip relationship at different location is constant. (2) a constant mode-mixity at the plate-end for *E* stage and *E-S* stages. To investigate if the above two assumptions are applicable for the mixed-mode analysis under combined mechanical loading and temperature variation, the FE analyses are conducted. The previous experimentally studied beam (i.e., specimen S304) by Deng and Lee (2007) is taken as an example. The FE results will be first presented, while the detailed information about the FE model will be presented in the later sections.

4.4.2 Constant Normalized Interfacial Shear Slip/Separation Assumption

Fig. 4-7 compares the distributions of interfacial shear slip/separation under single mechanical loading (i.e., 80 kN, 0 ℃; 120 kN, 0 ℃) and combined mechanical loading and temperature variation (i.e., 60 kN, 40 ℃; 110 kN, 40 ℃) over the bond length obtained from the FE modeling. Both *E* and *E-S* stages are included in these figures. The magnitudes of interfacial shear slip/separation along the bondline are normalized by their magnitudes at the plate end [i.e., $\delta_t^{e}(0)$ and $\delta_n^{es}(0)$]. It is clear that all the normalized distributions converge to a single curve. In other words, the normalized interfacial slip/separation in both *E* stage and *E-S* stage are identical regardless of the load level and the magnitude of temperature variation. And the absolute magnitudes of interfacial slip/separation along the bondline in *E-S* stage can be obtained by multiplying the interfacial slip/separation in *E* stage [i.e., Eq. (4-52) and Eq. (4-53)] with a coefficient φ_T, and φ_N, respectively.

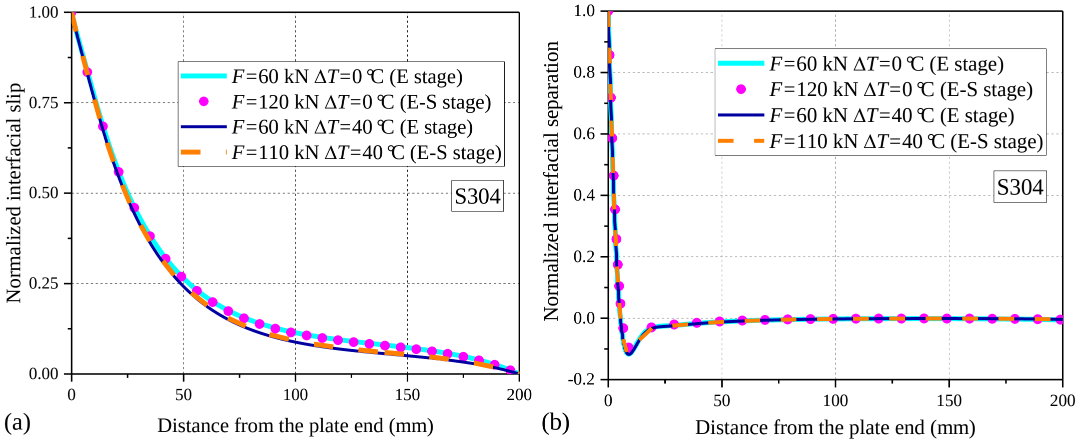

Fig. 4-7 Distribution of normalized a) interfacial slip $[\delta_t^{es}(x)/\delta_t^{es}(0)]$ and b) separation $[\delta_n^{es}(x)/\delta_n^{es}(0)]$ under various loadings.

Thus, the distributions of interfacial slip and separation in *E-S* stage can be expressed as follows,

$$\delta_t^{es}(x) = \frac{\varphi_T}{K_T}[B_1\cosh(\lambda x) + B_2\sinh(\lambda x) + m_1\frac{F}{2}];\ 0 < x < l \tag{4-62}$$

$$\delta_n^{es}(x) = \frac{\varphi_N}{K_N}\{e^{-\beta x}[C_1\cos(\beta x) + C_2\sin(\beta x)] - n_1\lambda[B_1\sinh(\lambda x) + B_2\cosh(\lambda x)]\}; 0 < x < l \tag{4-63}$$

where φ_T and φ_N are the amplification factors.

By substituting $x = 0$ into the above equation, the magnitudes of interfacial slip and separation at plate end can be expressed as

$$\delta_t^{es}(0) = \frac{\varphi_T}{K_T}\left(B_1 + m_1\frac{F}{2}\right) \quad \delta_n^{es}(0) = \frac{\varphi_N}{K_N}(C_1 - n_1\lambda B_2) \tag{4-64}$$

In addition, the interfacial stresses at the conjunction point between elastic and softening regions ($x = \bar{x}$) should satisfy the quadratic stress failure criterion [Eq. (4-7)] as follows:

$$\begin{aligned}&\{\frac{\varphi_T}{\tau_p}\left[B_1\cosh(\lambda\bar{x}) + B_2\sinh(\lambda\bar{x}) + m_1\frac{F}{2}\right]\}^2\\ &\quad + \{\frac{\varphi_N}{\sigma_p}\langle e^{-\beta x}[C_1\cos(\beta\bar{x}) + C_2\sin(\beta\bar{x})] - n_1\lambda[B_1\sinh(\lambda\bar{x})\\ &\quad + B_2\cosh(\lambda\bar{x})]\rangle\}^2 = 1\end{aligned} \tag{4-65}$$

And for a given $\bar{x}$, the amplification factors can be solved as,

$$\frac{1}{{\varphi_T}^2} = \frac{1}{{\varphi_N}^2} = \left[\frac{1}{\tau_p}\left(B_1\cosh(\lambda\bar{x}) + B_2\sinh(\lambda\bar{x}) + m_1\frac{F}{2}\right)\right]^2 +$$

$$\{\frac{1}{\sigma_p}\langle \mathrm{e}^{-\beta x}[C_1\cos(\beta\bar{x}) + C_2\sin(\beta\bar{x})] - n_1\lambda[B_1\sinh(\lambda\bar{x}) + B_2\cosh(\lambda\bar{x})]\rangle\}^2 \qquad (4\text{-}66)$$

Here, $\varphi_N = \varphi_T$ is assumed and the reason will be discussed in next section.

4.4.3 Mode-Mixity Ratio Assumption

Fig. 4-8 shows the variation of mode-mixity ratio (γ) at two different locations (i.e., *x* = 0 mm and 4 mm) under increasing levels of mechanical loading in the FE results. It is clear that the mode-mixity ratio reduces significantly at locations away from the plate end (e.g., *x*=4 mm) during the *E-S* stage. However, at the plate end location (i.e., *x* = 0), the reduction of the mode-mixity ratio is marginal from the *E* stage to *E-S* stage and only becomes very significant after the interface enters into debonding stage. The temperature variation changes the load when the interface starts entering into the *E-S* stage (i.e., onset of the softening in **Fig. 4-8**), but does not change the above-mentioned trend.

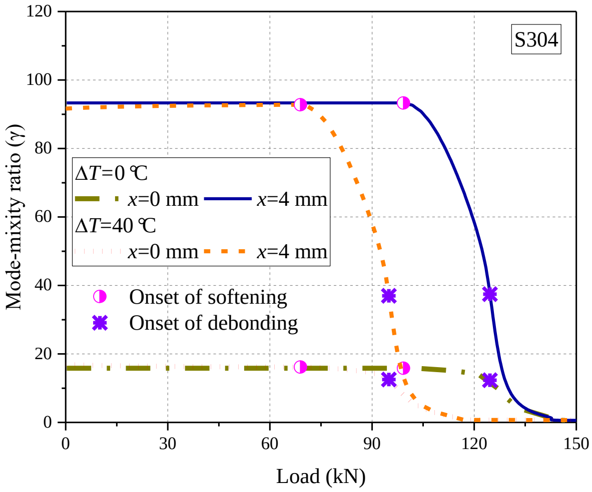

Fig. 4-8 Variation of mode-mixity ratio (γ) at different locations under increasing mechanical loading.

To further investigate how the mode-mixity ratio (γ) changes at different locations during the interfacial debonding failure process, **Fig. 4-9** compares the mode-mixity ratio (γ) at different locations at the *E* stage and end of the *E-S* stage (i.e., γ^{deb} at the debonding load). Again, it is shown that the mode-mixity change is independent of temperature variation at any location. However, the mode-mixity ratios during both *E* stage (represent by γ^{e} at the end of *E* stage) and *E*-*S* stage (represent by γ^{deb} at the end of *E*-*S* stage) increase with the distance from the plate end. At the plate end, the difference between $\gamma^{e}$and $\gamma^{deb}$is the minimum while at a distance the γ^{deb}value is usually smaller than the γ^{e} value, indicating that the mode-mixity ratio reduces when the bond interface shifts from *E* stage to *E*-*S* stage. while the reduction seems to be more significant when the location is further away from the plate end.

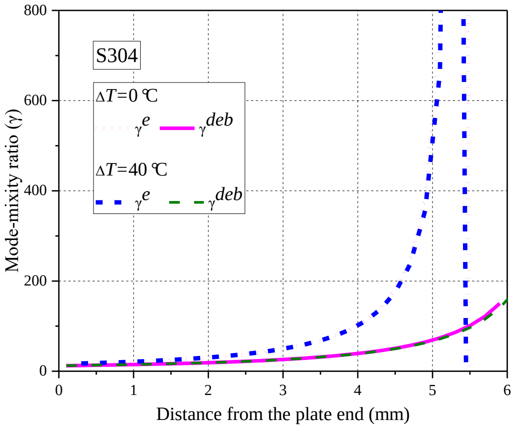

Fig. 4-9 Distributions of mode-mixity ratio (γ) at different locations near the plate end

Following De Lorensis *et al.* (2013), here it is also assumed that the magnitude of mode-mixity ratio in *E*-*S* stage is equal to that in *E* stage at the plate end and [i.e., $\gamma^{es}(0) = \gamma^{e}(0)$].

Accordingly, the mode-mixity ratio at the plate end in *E*-*S* stage can be calculated as

$$\gamma^{es}(0) = \frac{\delta_t^{es}(0)}{\delta_n^{es}(0)} = \frac{\varphi_T}{\varphi_N}\frac{\delta_t^{e}(0)}{\delta_n^{e}(0)} \tag{4-67}$$

In *E* stage, $\gamma^{e}(0) = \frac{\delta_t^{e}(0)}{\delta_n^{e}(0)}$. Therefore, $\varphi_T = \varphi_N$.

Apart from the magnitude of γ^{es} at the plate end (i.e., *x* = 0 mm), the magnitude of γ^{es} at the connection point between elastic and softening region ($x = \bar{x}$) should be paid special attention, because it determines the key parameters of the softening branch in the 'effective tangential CZ law' (i.e., $\tau_{p,eff}$ and $K_{T,eff}^{'}$).

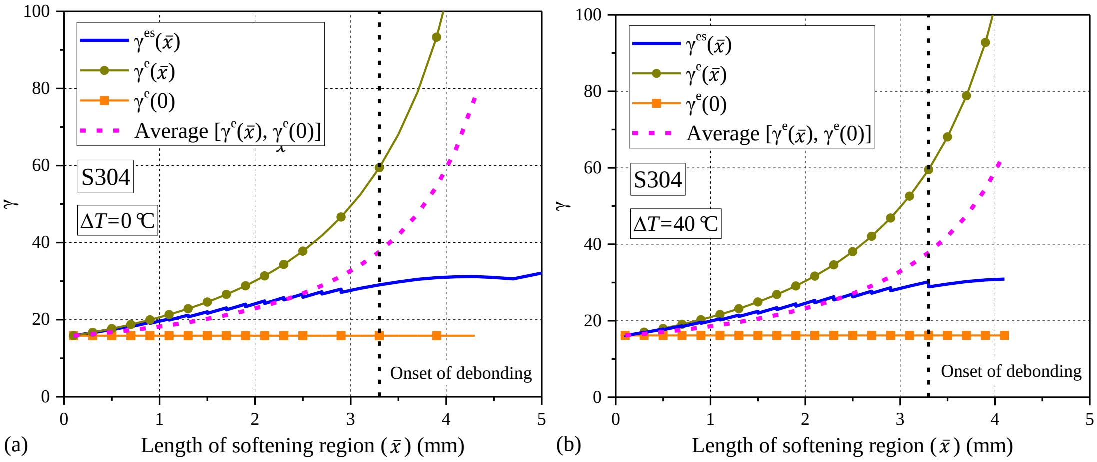

Fig. 4-10 Variation of mode-mixity ratio (γ) with $\bar{x}$: a) ΔT = 0 ℃; b) ΔT = 40 ℃.

When the interface changes from *E* stage to *E-S* stage, there is a location $\bar{x}$, representing the connection point of elastic and softening regions. **Fig. 4-10** presents the mode-mixity ratios of the location $\bar{x}$ at the ends of *E*-stage (i.e., $\gamma^{e}(\bar{x})$ in **Fig. 4-10**) and *E-S* stage (i.e., $\gamma^{es}(\bar{x})$ in **Fig. 4-10**), respectively. **Fig. 4-10a** and **Fig. 4-10b** represent FRP-strengthened steel beams under mechanical loading and combined themal and mechanical loading, respectively. The mode-mixity ratio at the plate end ($\gamma^{e}(0)$) is also provided in the figure as a reference. The vertical line indicates that the interface starts debonding when $\bar{x}$ reaches that value. In De Lorenzis *et al.* (2013), it was assumed $\gamma^{es}(\bar{x}) = \gamma^{es}(0) = \gamma^{e}(0)$ for FRP-strengthened steel beam at mechanical loading in the *E-S* stage. It seems such approximation is a bit rough considering the obvious difference between $\gamma^{es}(\bar{x})$ and $\gamma^{e}(0)$ (see **Fig. 4-10a**). Instead, it is more rational to approximate $\gamma^{es}(\bar{x})$ as the average of $\gamma^{e}(0)$ and $\gamma^{e}(\bar{x})$ (see the pink dotted lines in both **Fig. 4-10a** and **Fig. 4-10b**), since it is difficult to obtain the explicit solution for $\gamma^{es}(\bar{x})$. Accordingly,

$$\gamma^{es}(\bar{x}) = \frac{\gamma^{e}(0) + \gamma^{e}(\bar{x})}{2} \tag{4-68}$$

In *E-S* stage, for deriving the interfacial behavior of FRP-strengthened steel beam, $\bar{x}$ should be calculated in advance based on the given parameters, the applied loading, and the boundary condition, since the bond-slip equations are different at the two sides of $\bar{x}$. When adopting the ‘effective tangential CZ law’, both the $\tau_{p,eff}$ and $K_{T,eff}^{'}$ are also dependent on the magnitude of $\bar{x}$, which is unknown before the calculation. In this chapter, an iteration process (realized through Matlab) is deployed to solve this problem as explained in the next section.

4.4.4 Analytical Flowchart for Obtaining the Interfacial Behavior in E-S Stage

Fig. 4-11 presents the calculation procedure of the interfacial stresses of FRP-strengthened steel beam. When the interface is in the *E* stage, the distributions of interfacial stresses can be determined by Eqs. (4-33) and (4-45). Once the interface enters the *E-S* stage, the interfacial behavior can be determined iteratively as follows:

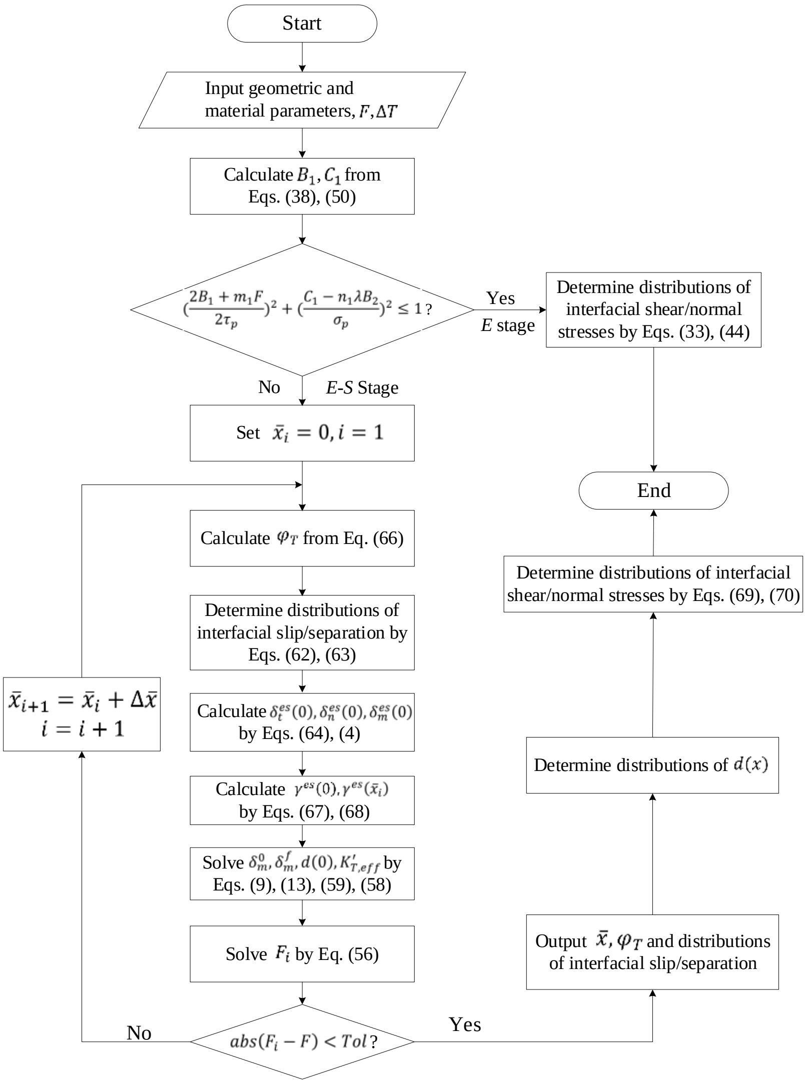

Fig. 4-11 Analytical Flow Chart for Obtaining the Interfacial Behavior in *E-S* Stage (Noting that all the equations in **Fig. 4-11** are shown in this chapter, thus the chapter number is not included in the equation numbers.)

1. Set $\bar{x}_i = 0$, the corresponding value of magnification factor (φ_T) can be calculated by Eq. (4-66). Based on which, the distributions of interfacial slip/separation can be obtained by Eq. (4-62) and Eq. (4-63). Then, the magnitude of $\delta_t^{es}(\bar{x}_i)$ and $\tau_{p,eff}$ can be calculated by Eq. (4-62) and Eq. (4-57), respectively. In addition, the magnitudes of $\delta_t^{es}(0)$ and $\delta_n^{es}(0)$ at plate end can be calculated by Eq. (4-64), then $\delta_m^{es}(0)$ can be calculated by Eq. (4-4).

2. Then the mode-mixity ratio at plate end, $\gamma^{es}(0)$, and the assumed location, $\gamma^{es}(\bar{x}_i)$, can be calculated by Eqs. (4-67) and (4-68). Once $\gamma^{es}(0)$ and $\gamma^{es}(\bar{x}_i)$ are available, δ_m^0 and δ_m^f can be calculated through Eq. (4-9) and Eq. (4-13), respectively. Based on δ_m^0, δ_m^f and $\delta_m^{es}(0)$, $d(0)$ can be calculated by Eq. (4-59).

3. When $d(0)$ is determined, the slope of effective softening branch ($K'_{T,eff}$) can be calculated by Eq. (4-58). Then the parameters in 'effective tangential CZ law', including the slope of elastic branch (K_T), peak shear strength ($\tau_{p,eff}$) and the slope of softening branch ($K'_{T,eff}$) are given at $\bar{x}_i$.

4. The magnitude of F_i corresponding to the trial $\bar{x}_i$ can be calculated by Eq. (4-56). Initially, F_i is smaller than the applied load. Then, the magnitude of $\bar{x}_i$ is slightly increased and Step 1~3 is repeated until the convergence is reached. Substituting the determined $\bar{x}$, φ_T into the Eqs. (4-62) and (4-63), the distributions of interfacial slip/separation in *E-S* stage [i.e., $\delta_t^{es}(x)$ and $\delta_n^{es}(x)$] can be derived.

5. At last, the distribution of $d(x)$ in Eq. (4-70) can be derived through Eq. (4-16), to which the $\delta_t^{es}(x)$ and $\delta_n^{es}(x)$ are substituted. Then, based on the obtained interfacial slip/separation [$\delta_t^{es}(x)$ and $\delta_n^{es}(x)$] and damage variable [$d(x)$], the distributions of interfacial bond/normal stresses in *E* stage and *E-S* stage can be obtained as follows:

$$\tau^{es}(x) = K_T\delta_t^{es}(x);\ \sigma^{es}(x) = K_N\delta_n^{es}(x)\ (\bar{x} < x < l) \tag{4-69}$$

$$\tau^{es}(x) = [1 - d(x)]K_T\delta_t^{es}(x);\ \sigma^{es}(x) = [1 - d(x)]K_N\delta_n^{es}(x)\ (0 < x < \bar{x}) \tag{4-70}$$

4.4.5 Prediction of the Debonding Load

The debonding load is achieved at end of the *E-S* stage, when $\delta_m^{es}(0) = \delta_m^f$ and $\tau^{es}(0) = 0$. Therefore, at a given ΔT, set $F = F_{sof}$ and gradually increase the magnitude of F. For each trial value of F, check the magnitude of shear stress at plate end [$\tau^{es}(0)$] that resultant from the iteration calculation in the previous section. $\tau^{es}(0)$

decreases as the increase of trial magnitude of F, and the debonding load is achieved when $\tau^{es}(0)$ decreases to zero.

4.5. RESULTS AND DISCUSSION

4.5.1 Validation of the Analytical Solution

The FE modeling are conducted by using the general-purpose software Abaqus 6.14. In the FE model, both the steel beam and FRP plate are modeled by 2-node cubic beam element (B23), and the adhesive layer is modeled by 4-node two-dimensional cohesive element (COH2D4). As shown in **Fig. 4-12**, the steel beam and FRP plate are tied by cohesive element at the reference line of both adherends and the adhesive layer, rather than their centroidal axes (Zhang and Teng 2010).

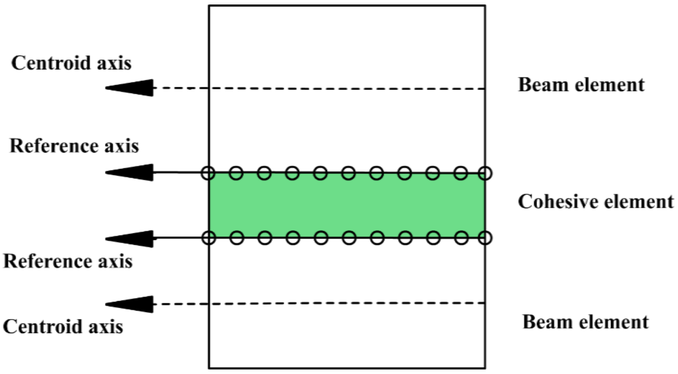

Fig. 4-12 Schematic of the element types and reference axes of the beam and FRP plate

According to the mesh convergence study in **Chapter 3**, the length of the beam element is taken as 0.2 mm for both steel beam and FRP plate. The size of the elements at the adhesive layer is 0.2*1 mm (with 1 mm in thickness).

The beams S303 and S304 (i.e., steel beam under three-point bending and strengthened by 0.3 m or 0.4 m FRP plate) presented in Deng and Lee (2007) were selected as the studied case in this chapter. The layout and the loading condition of the strengthened beam are shown in **Fig. 4-1**. And the mechanical parameters of both adherends and the interface are summarized in **Table 4-1**.

Table 4-1 Parameters used in the FE model

Geometry data				S304	S303
y_1 (mm)	A_1 (mm^2)	I_1 (mm^4)	b_2 (mm)	l (mm)	l (mm)
63.5	1602	4.59*10^6	76	200	150
y_2 (mm)	A_2 (mm^2)	I_2 (mm^4)	t_a (mm)	a (mm)	a (mm)
1.5	228	171	1.0	350	400

Material and interface bond behavior data					
E_1 (N/mm^2)	α_1 (/℃)	τ_p (N/mm^2)	δ_t^0 (mm)	δ_t^f (mm)	G_{II} (N/mm)
205000	11*10^{-6}	26.7	0.0526	0.1191	1.59
E_2 (N/mm^2)	α_2 (/℃)	σ_p (N/mm^2)	δ_n^0 (mm)	δ_n^f (mm)	G_I (N/mm)
212000	6*10^{-7}	29.7	0.00371	0.004	0.0594

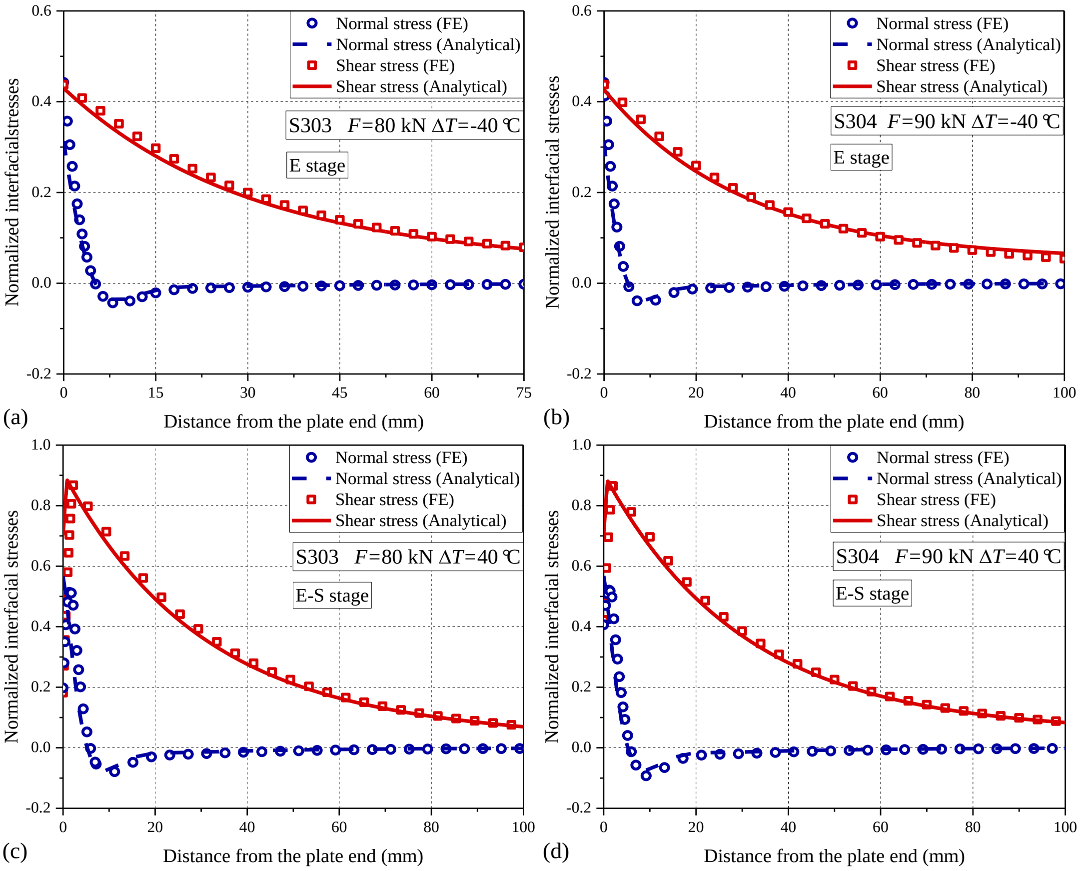

Fig. 4-13 Comparison of interfacial stresses from FE and analytical solution: a) S303 at 80 kN and -40 ℃; b) S304 at 90 kN and -40 ℃; c) S303 at 80 kN and 40 ℃; d) S304 at 90 kN and -40 ℃.

Fig. 4-13 compares the distributions of interfacial shear and normal stresses with the magnitude normalized by τ_p and σ_p, respectively. The dotted lines represent analytical results, while the continuous lines represent FE modeling results. To clearly show the interfacial behavior near the plate end, only a quarter length of FRP plate starting from the plate end is shown in **Fig. 4-13**. Both the mechanical loading (i.e., 80 kN for S303; 90 kN for S304) and temperature variation (i.e., -40 ℃ and 40 ℃) are considered. It can be observed that the distributions of interfacial shear/normal stresses from the analytical solutions are in good agreement with the FE results. Therefore, the validity of the proposed analytical approach for predicting the interfacial bond behavior of FRP-strengthened beam under combined mechanical and thermal loading is confirmed.

As shown in **Fig. 4-13**, the deformation stages of two beams are *E* stage at -40 ℃ and *E-S* stage at 40 ℃ respectively, although the load level is the same. This phenomenon is resulted from the interfacial thermal stress as discussed below.

In the ΔT = -40 ℃ case (**Fig. 4-13a, b**), the maximum shear stresses can be observed at the plate end, and the magnitude of shear stress decreases with the distance to the plate end. The direction of the interfacial shear stress remains unchanged from the plate end to the middle span of the FRP plate. In comparison, the interfacial normal stress is tensile (positive value) at the plate end while turns to compressive (negative value) at locations away from the plate end. Besides, the magnitudes of both shear and normal interfacial stresses decrease to zero at the middle length of FRP plate. While at ΔT = 40 ℃ (**Fig. 4-13c, d**), the interface is in *E-S* stage, with the softening region occurs near the plate end. In comparison to the distribution of interfacial stress derived by mode II analysis only (**Fig. 4-3**), the peak interfacial stress in the mix-mode analysis is less than τ_p.

4.5.2 Comparison with Previous Results

Table 4-2 compares the load at onset of softening and debonding at normal temperatures obtained from the analytical solutions proposed in this chapter, the coupled mixed-mode analysis (De Lorenzis *et al.* 2013), and FE modeling (Teng *et al.*, 2015) with the experimental (Deng and Lee, 2007) results. It can be observed that both the FE modeling and analytical solutions provide closer predictions of the experimental results. Specifically, the FE results give almost the identical predictions with the experimental data, because of the consideration of the geometric imperfection and nonlinear constitutive law of the steel beam (Teng *et al.*, 2015). In comparison, a slightly larger difference can be observed between the experimental data and analytical results, which can be attributed to the simplified assumptions on the mode-mixty ratio at $\bar{x}$ in *E-S* stage [i.e., $\gamma^{es}(\bar{x})$] as mentioned above. In addition, in experiments, the steel beam already exhibited some yielding at the ultimate failure.

Table 4-2 The loads at the onset of softening and debonding at normal temperature

At normal temperature (ΔT=0)	Debonding load (kN)				Softening onset load (kN)	
	Experimental results (Deng and Lee, 2007)	FE results (Teng *et al.*, 2015)	Analytical solution (De Lorenzis *et al.*, 2013)	Proposed analytical solution	FE results (Teng *et al.*, 2015)	Proposed analytical solution
S303	120	118	138	127	84	98
S304	135	132	155	143	117	111

Table 4-3 and **Table 4-4** compare the predicted mechanical loading at the onset of softening and debonding that predicted by the single mode II and proposed coupled mixed-mode analyses. Despite the same bond-slip relationship in mode II directions being adopted in both analytical solutions, the single mode II analysis tends to overestimate the debonding load at all temperature levels, because of the neglection of the interfacial normal stress effect. For both S303 and S304 under mechanical loading, the debonding load is increased by about 45% from the onset of softening till the debonding in mode II analysis, while such increase is 29% only in the mixed-mode analysis. The length of softening region at debonding load is around 32.0 mm in mode II analysis but 3.9 mm only in coupled mixed-mode analysis. The differences in the bond behaviors and resultant debonding loads can be attributed to the different local bond behaviors adopted in both analytical solutions. As summarized in **Table 4-5**, in the coupled mixed-mode analysis, the local bond behavior follows the 'effective tangential CZ law', in which the interfacial fracture energy and peak shear stress are lower than that in mode II analysis, because of the consideration of normal stress effect.

Table 4-3 The loads at the onset of softening at changed temperature

Softening onset load (kN)	Temperature variation (ΔT)	-40 ℃	-20 ℃	0 ℃	20 ℃	40 ℃
S303	Single mode II analysis (Chapter 3)	148	134	120	105	91
	Proposed analytical solution	126	112	98	84	70
S304	Single mode II analysis (Chapter 3)	168	151	135	119	103
	Proposed analytical solution	142	127	111	95	79

Table 4-4 The loads at the onset of debonding at changed temperature

Debonding load (kN)	Temperature variation (ΔT)	-40 ℃	-20 ℃	0 ℃	20 ℃	40 ℃

S303	Single mode II analysis (Chapter 3)	201	187	174	160	146
	Proposed analytical solution	154	140	127	113	99
S304	Single mode II analysis (Chapter 3)	226	210	195	180	164
	Proposed analytical solution	174	159	143	127	112

In addition, the mechanical loading at the onset of softening and debonding of FRP-strengthened steel beam are dramatically affected by the temperature variation. For beams S303 and S304, the increase of service temperature from -40 ℃ lower (i.e., ΔT=-40 ℃) to 40 ℃ higher (i.e., ΔT=40 ℃) than the ambient temperature (which could happen by seasonal temperature change) leads to a decrease of about 35% of the debonding load, and thus would lead to the premature failure of the structure. Therefore, an in-depth understanding of the thermal effect on the debonding behavior of the FRP-strengthened steel beam is essential for the safe strengthening design.

Table 4-5 Comparison of the mode II and coupled mixed-mode analyses

	Effect of interfacial normal stress	Interfacial behavior in mode II direction	Peak shear stress	Fracture energy in mode II direction
Mode II analysis	Not considered	Entire bilinear bond-slip relationship	τ_p	Larger
Coupled mixed-mode analysis	Considered	Effective tangential cohesive zone law	$\tau_{p,eff} \leq \tau_p$	Smaller

4.5.3 Interfacial Stress Distribution under Combined Mechanical and Thermal Loading

Fig. 4-14 shows the distributions of interfacial stresses in both shear and normal directions of the FRP-strengthened steel beam S304 under combined mechanical (110 kN) and thermal loading (ΔT ranges from -40 ℃ to 40 ℃). It can be observed that the interface evolves from *E* stage to *E-S* stage as the temperature increases.

When $\Delta T \leq 0$ ℃, the entire bond length is in the elastic stage and the magnitude of the interfacial stresses at each point increase with ΔT. After the softening criterion (Eq. 4-17) is satisfied, the softening occurs at the plate end and the shear stress in the softening region decreases subsequently as the temperature increase. It can be expected that the plate-end debonding will happen with the further increase of temperature.

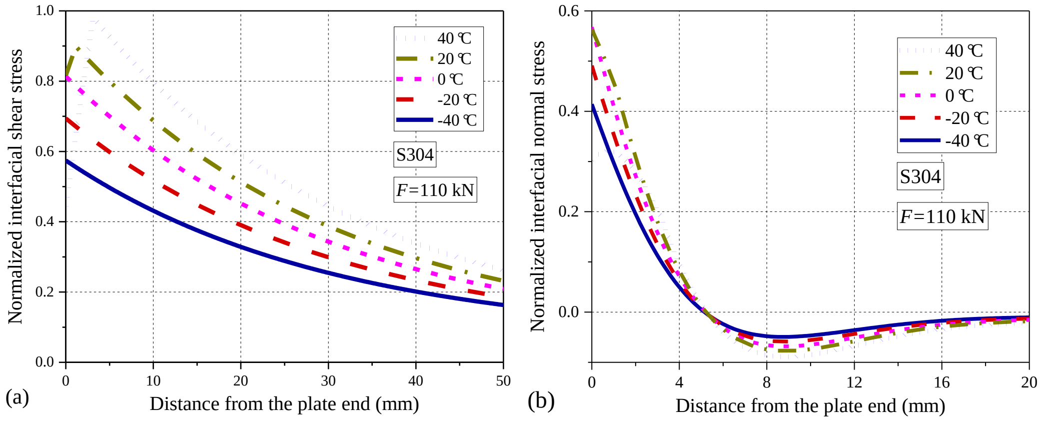

Fig. 4-14 Interfacial stress distributions of FRP-strengthened steel beam under combined mechanical and thermal loading: a) normalized interfacial shear stress; b) normalized interfacial normal stress.

To better explain this phenomenon, the interfacial behavior under mechanical or thermal loading is separately investigated in **Fig. 4-15** and **Fig. 4-16**.

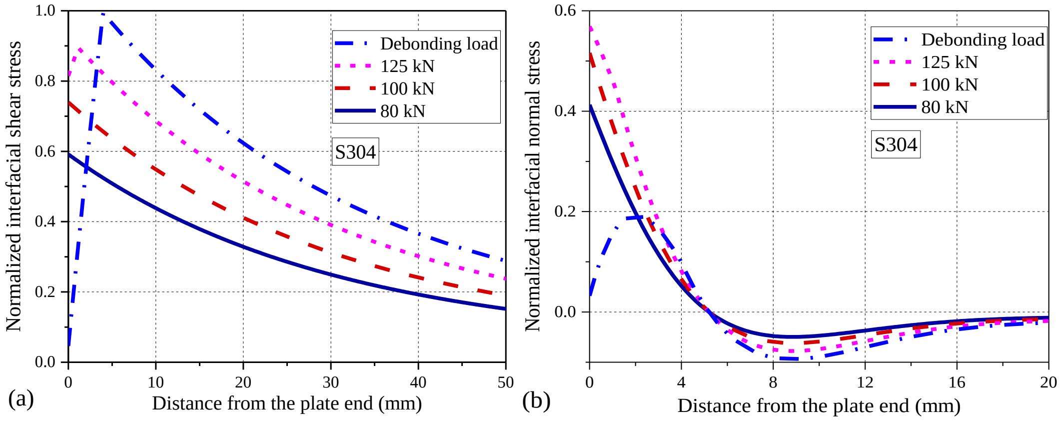

Fig. 4-15 Interfacial stress distributions of FRP-strengthened steel beam under various mechanical loading: a) normalized interfacial shear stress; b) normalized interfacial normal stress.

Fig. 4-15 presents the distributions of interfacial shear and normal stresses in beam S304 under increasing mechanical loading. As the load increases, the bonding interface evolves from *E* stage (80 kN and 100 kN) to *E*-*S* stage (125 kN) and the trend is similar to that under constant loading and increasing temperature (**Fig. 4-14**). In addition, despite the different deformation stages experienced by the interface, the magnitude of interfacial stress in both directions are all positive near the plate end.

Fig. 4-16 shows the distributions of interfacial stresses under single thermal loading. When a temperature decrease is applied to the FRP-strengthened steel beam, negative interfacial stresses are generated at the bond interface (**Fig. 4-16**) near plate end. And the directions of interfacial stresses in shear and normal directions are opposite to those generated by the mechanical loading (**Fig. 4-15**). The interfacial stresses from both mechanical and thermal loading can be superimposed on each other. As such, the magnitudes of interfacial stresses that caused by the mechanical loading (**Fig. 4-15**) are reduced near the plate end. Because of the lower interfacial stresses at ΔT = -40 ℃ and ΔT = -20 ℃ as comparing to the ambient temperature (ΔT = 0 ℃) case under same mechanical loading, a higher level of mechanical load is needed at onset of softening and debonding.

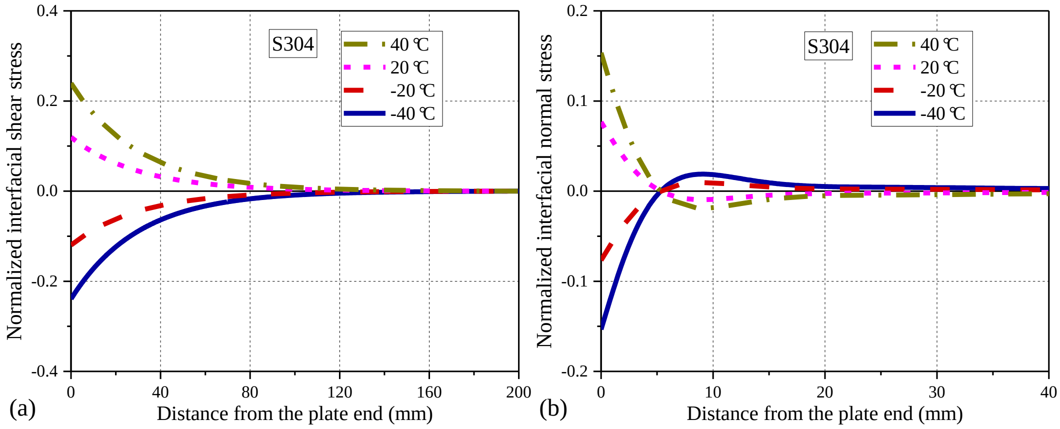

Fig. 4-16 Interfacial stress distributions of FRP-strengthened steel beam under single thermal loading: a) normalized interfacial shear stress; b) normalized interfacial normal stress.

On the contrary, the interfacial stresses caused by a temperature elevation (**Fig. 4-16**) are in the same direction as that caused by the mechanical loading (**Fig. 4-15**). Thus, a higher level of damage of interface can be achieved at elevated temperature given the same mechanical loading (**Fig. 4-14**). As a consequence, the required mechanical loading at onset of softening and debonding should be lower. In summary, the onset of softening and debonding is delayed at decreased temperatures while accelerated at increased temperatures.

4.5.4 *Parametric Study*

To investigate the effect of the FRP geometry on the plate-end debonding load under temperature variations, a parametric study was further conducted using the proposed analytical approach.

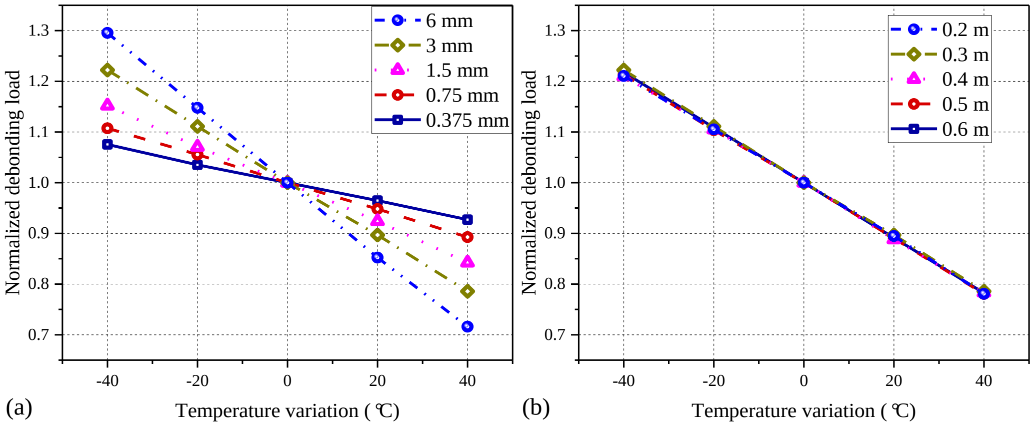

Fig. 4-17 Effect of temperature variation on normalized debonding load of the FRP-strengthened steel beam at different plate (a) thicknesses and (b) lengths.

Fig. 4-17 presents the changes of plate-end debonding load with the temperature variation of the same steel beam strengthened by different FRP plates, in terms of plate thickness (**Fig. 4-17a**) and plate length (**Fig. 4-17b**). In this figure, the plate-end debonding load at various temperatures is normalized by the value at ambient temperature (i.e., ΔT = 0 ℃). Regardless of the FRP thickness and length, the debonding load of the FRP-strengthened steel beam decreases linearly with the temperature increase. According to **Fig. 4-17a**, the steel beams strengthened with thicker FRP plates are more sensitive to the temperature elevation. For an extreme case, when an 80 ℃ (i.e., from ΔT = -40 ℃ to ΔT = 40 ℃) temperature increase was applied, 60% decrease of the debonding load can be observed for the steel beam strengthened with a 6 mm thick FRP plate. In comparison, the effect of the FRP length on the change of debonding load is negligible (**Fig. 4-17b**). However, in view of that a shorter bond length usually leads to a lower debonding loading, longer and thinner FRP plates are preferred to minimize the negative thermal stress effect on the safety of FRP-strengthened steel beams. If the use of a thicker FRP plate is not avoidable, additional mechanical anchorages are needed to suppress the debonding failure.

4.6. CONCLUSIONS

This chapter presents a closed-form analytical solution based on coupled mixed-mode cohesive zone model to analyze the interfacial behavior of FRP-strengthened steel beam under combined mechanical loading and thermal loading. The interfacial stresses in both tangential and normal directions are considered in predicting the loads at onset of softening and debonding of the FRP-to-steel interface. Based on the results of this study, several conclusions can be drawn as follows:

a) The proposed coupled mixed-mode analysis can provide an accurate prediction of the interfacial behavior and debonding load of FRP-strengthened steel beams under combined mechanical and thermal loading;

b) The interfacial behavior between the steel beam and FRP plate can be seriously affected by the temperature variation. The interfacial stress at elevated temperatures is in same direction as that generated by mechanical loading and thus accelerates the deformation process of the interface.

c) The debonding load of FRP-strengthened steel beam is significantly decreased by the temperature elevation. As such, special attention should be paid to the design of FRP-strengthened beams when the service temperature increase is expected.

d) The thermal stress is more significant when a thicker FRP plate is adopted in strengthening the steel beam, for which case use of longer FRP plate and additional anchorages are preferred to reduce the negative effect of temperature increase.

4.7. REFERENCES

Abaqus 6.14 (2014) "Documentation." Providence, RI, USA: Dassault Systemes Simulia Corporation.

Benzeggagh, M.L., and Kenane, M. (1996). Measurement of mixed-mode delamination fracture toughness of unidirectional glass/epoxy composites with mixed-mode bending apparatus. *Composites Science and Technology*, 56(4), 439-449.

Biscaia, H.C., Chastre, C., Viegas, A., and Franco, N. (2015). Numerical modelling of the effects of elevated service temperatures on the debonding process of FRP-to-concrete bonded joints. *Composites Part B: Engineering*, 70, 64-79.

Biscaia, H.C., Chastre, C., and Silva, M. A. (2017). Analytical model with uncoupled adhesion laws for the bond failure prediction of curved FRP-concrete joints subjected to temperature. *Theoretical and Applied Fracture Mechanics*, 89, 63-78.

Biscaia, H.C., and Ribeiro, P. (2019). A temperature-dependent bond-slip model for CFRP-to-steel joints. *Composite Structures*, 217, 186-205.

Camanho, P.P., Davila, C.G., and de Moura, M.F. (2003). Numerical simulation of mixed-mode progressive delamination in composite materials. *Journal of Composite Materials,* 37(16), 1415-1438.

Chandrathilaka, E., Gamage, J., and Fawzia, S. (2019). Mechanical characterization of CFRP/steel bond cured and tested at elevated temperature. *Composite Structures*, 207, 471-477.

Colombi, P., and Poggi, C. (2006). An experimental, analytical and numerical study of the static behavior of steel beams reinforced by pultruded CFRP strips. *Composites Part B-Engineering,* 37(1), 64-73.

Cui, W., Wisnom, M., and Jones, M. (1992). A comparison of failure criteria to predict delamination of unidirectional glass/epoxy specimens waisted through the thickness. *Composites*, 23(3), 158-166.

Dai, J.G., Ueda, T. and Sato, Y. (2006). Unified Analytical Approaches for Determining Shear Bond Characteristics of FRP-Concrete Interfaces through Pullout Tests, *Journal of Advanced Concrete Technology*, 4(1), 133-145.

Dai, J.G., Gao, W.Y. and Teng, J.G. (2013) Bond-Slip Model for FRP Laminates Externally Bonded to Concrete at Elevated Temperature. *Journal of Composites for Construction*, 17(2): 217-228.

Dai, J.G., Ueda, T. and Sato, Y. (2005) Development of the nonlinear bond stress–slip model of fiber reinforced plastics sheet–concrete interfaces with a simple method. *Journal of Composites for Construction*, 9(1): 52-62.

De Lorenzis, L., Fernando, D., and Teng, J.G. (2013). Coupled mixed-mode cohesive zone modeling of interfacial debonding in simply supported strengthened beams. *International Journal of Solids and Structures*, 50(14-15), 2477-2494.

De Lorenzis, L., and Zavarise, G. (2009). Cohesive zone modeling of interfacial stresses in strengthened beams. *International Journal of Solids and Structures*, 46(24), 4181-4191.

Deng, J., and Lee, M.M.K. (2007). Behaviour under static loading of metallic beams reinforced with a bonded CFRP plate. *Composite Structures,* 78(2), 232-242.

Deng, J., Lee, M. M.K., and Moy, S.S.J. (2004). Stress analysis of steel beams reinforced with a bonded CFRP plate. *Composite Structures*, 65(2), 205-215.

Deng, J., Li, J.H., Wang, Y., and Xie, W.Z. (2018). Numerical study on notched steel beams strengthened by CFRP plates. *Construction and Building Materials,* 163, 622-633.

Fernando, N.D. (2010). Bond behaviour and debonding failures in CFRP-strengthened steel members. The Hong Kong Polytechnic University.

Ferrier, E., Rabinovitch, O., and Michel, L. (2016). Mechanical behavior of concrete–resin/adhesive–FRP structural assemblies under low and high temperatures. *Construction and Building Materials*, 127, 1017-1028.

Gao, W.Y., Dai, J.G. and Teng, J.G. (2015) Analysis of Mode II debonding behavior of fiber-reinforced polymer-to-substrate bonded joints subjected to combined thermal and mechanical loading. *Engineering Fracture Mechanics* 136: 241-264.

Gao, W.Y., Teng, J.G., and Dai, J.G. (2012). Effect of Temperature Variation on the Full-Range Behavior of FRP-to-Concrete Bonded Joints. *Journal of Composites for Construction*, 16(6), 671-683.

Ke, L., Li, C., He, J., Dong, S., Chen, C., and Jiao, Y. (2020). Effects of elevated temperatures on mechanical behavior of epoxy adhesives and CFRP-steel hybrid joints. *Composite Structures*, 235, 111789.

Korayem, A.H., Chen, S.J., Zhang, Q.H., Li, C.Y., Zhao, X.L., and Duan, W.H. (2016). Failure of CFRP-to-steel double strap joint bonded using carbon nanotubes modified epoxy adhesive at moderately elevated temperatures. *Composites Part B: Engineering*, 94, 95-101.

Lenwari, A., Thepchatri, T., and Albrecht, P. (2006). Debonding strength of steel beams strengthened with CFRP plates. *Journal of Composites for Construction*, 10(1), 69-78.

Linghoff, D., Haghani, R., and Al-Emrani, M. (2009). Carbon-fibre composites for strengthening steel structures. *Thin-Walled Structures*, 47(10), 1048-1058.

Nguyen, P.L., Vu, X.H., and Ferrier, E. (2019). Elevated temperature thermomechanical behaviour of near surface mounted CFRP reinforced concrete specimens: Effect of adhesive at concrete/CFRP interface. *Engineering Structures*, 197, 109361.

Rizkalla, S., Dawood, M., and Schnerch, D. (2008). Development of a carbon fiber reinforced polymer system for strengthening steel structures. *Composites Part A: Applied Science and Manufacturing*, 39(2), 388-397.

Sahin, M. U., and Dawood, M. (2016). Experimental Investigation of Bond between High-Modulus CFRP and Steel at Moderately Elevated Temperatures. *Journal of Composites for Construction*, 20(6), 04016049.

Sallam, H.E.M., Ahmad, S.S.E., Badawy, A.A.M., and Mamdouh, W. (2006). Evaluation of steel I-beams strengthened by various plating methods. *Advances in Structural Engineering*, 9(4), 535-544.

Schnerch, D., Dawood, M., Rizkalla, S., and Sumner, E. (2007). Proposed design guidelines for strengthening of steel bridges with FRP materials. *Construction and Building Materials*, 21(5), 1001-1010.

Silva, M.A.G., and Biscaia, H. (2008). Degradation of bond between FRP and RC beams. *Composite Structures*, 85(2), 164-174.

Smith, S.T., and Teng, J.G. (2001). Interfacial stresses in strengthened beams. *Engineering Structures*, 23(7), 857-871.

Stratford, T., and Cadei, J. (2006). Elastic analysis of adhesion stresses for the design of a strengthening plate bonded to a beam. *Construction and Building Materials*, 20(1-2), 34-45.

Stratford, T.J., and Bisby, L.A. (2012). Effect of Warm Temperatures on Externally Bonded FRP Strengthening. *Journal of Composites for Construction*, 16(3), 235-244.

Teng, J.G., Fernando, D., and Yu, T. (2015). Finite element modelling of debonding failures in steel beams flexurally strengthened with CFRP laminates. *Engineering Structures*, 86, 213-224.

Teng, J.G., Yu, T., and Fernando, D. (2012). Strengthening of steel structures with fiber-reinforced polymer composites. *Journal of Constructional Steel Research*, 78, 131-143.

Teng, R., Guo, Y., Wang, H., Zhao, Z., and Wang, X. (2021). Experimental study of bending interface characteristics of CFRP-strengthened long-span steel main beams at different temperatures. *Engineering Structures*, 235.

Wang, J.L. (2006). Cohesive zone model of intermediate crack-induced debonding of FRP-strengthened concrete beam. *International Journal of Solids and Structures*, 43(21), 6630-6648.

Wu, E.M., and Reuter Jr, R. (1965). Crack extension in fiberglass reinforced plastics. T. & AM Report No. 275, University of Illinois.

Yoshitake, I., Tsuda, H., Itose, J., and Hisabe, N. (2014). Effect of discrepancy in thermal expansion coefficients of CFRP and steel under cold temperature. *Construction and Building Materials*, 59, 17-24.

Yu, T., Fernando, D., Teng, J.G., and Zhao, X.L. (2012). Experimental study on CFRP-to-steel bonded interfaces. *Composites Part B-Engineering*, 43(5), 2279-2289.

Yu, Y., Chiew, S.P., and Lee, C.K. (2011). Bond failure of steel beams strengthened with FRP laminates - Part 2: Verification. *Composites Part B-Engineering*, 42(5), 1122-1134.

Yuan, H., Teng, J.G., Seracino, R., Wu, Z. S., and Yao, J. (2004). Full-range behavior of FRP-to-concrete bonded joints. *Engineering Structures*, 26(5), 553-565.

Yuan, H., Lu, X., Hui, D., and L., Feo. (2012) Studies on FRP-concrete interface with hardening and softening bond-slip law. *Composite Structures* 94(12): 3781-3792.

Zeng, J.J., Gao, W.Y., and Liu, F. (2018). Interfacial behavior and debonding failures of full-scale CFRP-strengthened H-section steel beams. *Composite Structures*, 201, 540-552.

Zhang, L., and Teng, J.G. (2010). Simple General Solution for Interfacial Stresses in Strengthened Beams. *Journal of Composites for Construction*, 14(4), 434-442.

Zhou, A., Qiu, Q., Chow, C.L., and Lau, D. (2020). Interfacial performance of aramid, basalt and carbon fiber reinforced polymer bonded concrete exposed to high temperature. *Composites Part A: Applied Science and Manufacturing*, 131, 105802.

Zhou, H., Fernando, D., Torero, J.L., Torres, J.P., Maluk, C., and Emberley, R. (2020). Bond Behavior of CFRP-to-Steel Bonded Joints at Mild Temperatures: Experimental Study. *Journal of Composites for Construction*, 24(6), 04020070.

Zhou, H., Gao, W.Y., Biscaia, H.C., Wei, X.J., and Dai, J.G. (2022). Debonding analysis of FRP-to-concrete interfaces between two adjacent cracks in plated beams under temperature variations. *Engineering Fracture Mechanics*, 263.

Zhou, H., Torres, J.P., Fernando, D., Law, A., and Emberley, R. (2019). The bond behaviour of CFRP-to-steel bonded joints with varying bond properties at elevated temperatures. *Engineering Structures*, 183, 1121-1133.

Zhou, H., Urgel, J.M., Emberley, R., Maluk, C., and Fernando, D. (2017). "Behaviour of the FRP-to-steel bonded joints under elevated temperature." In Proceeding of 6th Asia-Pacific Conference on FRP in Structures, At: Singapore.

CHAPTER 5

THERMAL EFFECT ON INTERMEDIATE CRACK-INDUCED DEBONDING AND STRESS INTENSITY FACTOR IN FRP-RETROFITTED CRACKED STEEL BEAMS: A THEORETICAL STUDY

5.1. INTRODUCTION

Externally bonded fiber-reinforced polymer (FRP) plates are effective in retrofitting and strengthening aging steel beams due to the superior properties of FRP composites, such as their high strength-to-weight ratio and corrosion resistance. If an FRP-retrofitted beam is loaded, the interfacial debonding between the steel beam and the FRP plate is among the most common failure modes (Teng *et al.* 2012). When the interfacial debonding occurs, the load-carrying capacity of the FRP-retrofitted steel beam mainly depends on the axial load carried by the externally bonded FRP plate, which in turn relies on the interfacial stress transferred from the steel beam to the FRP plate through the bonding adhesive layer (Teng *et al.* 2015). For an FRP-retrofitted steel beam without a crack or notch, interfacial debonding commonly initiates at the plate end, known as the plate-end debonding (PE debonding). However, for an FRP-retrofitted notched or cracked steel beam, the FRP debonding failure usually initiates near the notched or cracked section and propagates towards the two plate ends. This type of debonding is termed as the intermediate crack-induced debonding (IC debonding). In spite of the two above-mentioned different modes of debonding failure, the failure in both cases is induced by the high interfacial stresses between the FRP and the substrate beam. Therefore, accurate prediction of the interfacial stress distribution is essential for understanding the interfacial debonding mechanism in the FRP-retrofitted steel beam.

An FRP-retrofitted steel beam is likely to experience significant temperature variations (e.g., seasonal and diurnal service temperature changes) (Gholami *et al.* 2013; Stratford and Bisby 2012) during its service life. Such temperature variations may influence the interfacial stress distribution at the bondline and the associated debonding failure of the externally bonded FRP plate (Biscaia and Ribeiro 2019; Gao *et al.* 2012; Gao *et al.* 2015; Gholami *et al.* 2013; Sahin and Dawood 2016; Stratford and Bisby 2012). The temperature variation (i.e., thermal loading) has two different effects on the interfacial bond behavior of the FRP-retrofitted steel beam. The first effect is related to the thermal stress at the bondline induced by the thermal incompatibility between the two adherends (i.e., FRP and steel) (Gao *et al.* 2012; Gao *et al.* 2015). The second effect is the interfacial bond deterioration due to the softening of the adhesive layer at elevated service temperatures (Dai *et al.* 2012; Silva and Biscaia 2008; Zhou *et al.* 2020). For the thermal stress effect, the thermal expansion of the steel beam due to the service temperature variation is usually larger than that of the FRP plate. This is because the steel usually has a coefficient of thermal expansion (CTE) of about 12×10^{-6}/ ℃, while the carbon FRP (CFRP) plates widely used for the strengthening of steel structures have a longitudinal CTE close to zero (ACI 440.2R-08; Klamer *et al.* 2008). As a result, the interfacial stress/slip caused by the thermal loading may be in the same direction as that caused by the mechanical loading, which may accelerate the propagation of FRP debonding, leading to a decrease in the debonding load.

The bond deterioration of the FRP-to-steel interface (i.e., the adhesive layer) at elevated service temperatures has been widely studied in existing literature using the bonded joint tests (e.g., Sahin and Dawood 2016; Zhou *et al.* 2020). The test results have indicated that the bond properties, including the interfacial shear stiffness, peak shear strength and interfacial fracture energy, are significantly reduced at elevated service temperatures, especially when the temperatures are close or higher than the glass transition temperature (T_g) of the adhesive layer. In contrast, limited experimental studies have been conducted to investigate the debonding behavior and the load-carrying capacity of FRP-retrofitted steel beams at different service temperatures (Hassein Abed 2012; Sahin and Dawood 2016; Stratford and Bisby 2012). Indeed, it is challenging to monitor the thermal stress distributions along the bondline due to the changes in the service temperatures because a complex measurement apparatus is usually required (Hassein Abed 2012). Therefore, the thermal stress effect is usually studied through theoretical and finite element (FE) analyses.

The thermal stress effects on the full-range behavior of FRP-to-steel/concrete bonded joints subjected to combined thermal and mechanical loading were analytically studied by Gao *et al.* (2012, 2015). The analytical solution provides a rigorous interpretation of the thermal stress effect on the debonding load of the bonded joint and can be used to isolate the above two different effects of temperature variation. However, there is a lack of research on the thermal stress effect on the IC debonding propagation in FRP-retrofitted steel beams. Most of the analytical solutions in the existing literature only involve the debonding process of the FRP-retrofitted steel beam under mechanical loading (Chen and Qiao 2009; Teng *et al.* 2006; Wang 2006). Limited analytical studies (Deng *et al.* 2004; Stratford and Cadei 2006) have been carried out, based on linear elastic mechanics, to study the thermal stress effect on the interfacial stress distribution along the bondline in the FRP-retrofitted steel beam subjected to combined thermal and mechanical loading. However, the derived interfacial stress distribution in fact cannot be used directly to predict IC debonding failure and related load carrying capacity (i.e., debonding load). That is because the IC debonding propagation of the FRP plate is mainly controlled by the interfacial fracture energy rather than the maximum stress value (Teng *et al.* 2012). To this end, this chapter aims to develop a new analytical solution for predicting the bond behavior and the related full-range IC debonding process in the FRP-retrofitted notched steel beam under combined thermal and mechanical loading. The thermal stress effects on the interfacial stress distribution, the IC debonding load and the stress intensity factor (SIF) at the notch tip are examined.

5.2. ANALYTICAL SOLUTION

The analytical solution in elastic stage is proposed following the previous analytical solutions that proposed by Deng *et al.* (2016). Comparing with the previous analytical solution, the softening and debonding of the interface is considered in this analytical solution.

5.2.1 Assumptions and Notation

Similar to the assumptions adopted in the previous chapters, the following assumptions are also adopted in this chapter, including: (a) both the beam and the FRP plate are assumed to be linear elastic, (b) shear deformations of the beam and the FRP plate are neglected, and (c) interfacial shear stresses are assumed to be invariant across the thickness of the adhesive layer. In addition, the temperature variation and the associated thermal deformations of the FRP and the substrate are assumed to be uniformly distributed along the full length of the beam.

The present research only focuses on the thermal stress effect and ignores the bond deterioration effect, i.e., in the analysis process, it is assumed that the bond-slip model remains unchanged at different service temperatures. It is hypothesised that the derived analytical solution can be extended to consider possible bond deterioration effects by replacing the assumed bond-slip model with a temperature-dependent one, once it is calibrated through experimental tests.

5.2.2 Mode II Cohesive Law

The analytical solution is based on a pure mode II interfacial stress analysis, and the bilinear bond-slip model, which was adopted in previous chapters, is also used to describe the interfacial bond behavior between the FRP and the retrofitted steel beam as depicted in **Fig. 5-1**. Before the maximum shear stress (τ_p) is achieved, the bondline remains elastic, and the interfacial shear stress increases linearly with the growth of the interfacial slip. After τ_p is attained at an interfacial slip δ_t^0, the shear stress decreases linearly with the interfacial slip. At last, the shear stress reduces to zero when the relative slip increases to δ_t^f, which leads to the initiation of Mode II debonding at the bondline.

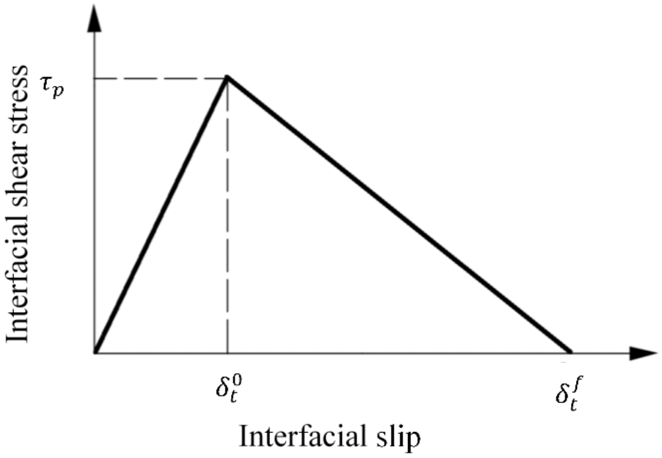

Fig. 5-1 Bilinear bond-slip relationship

Fig. 5-2 shows a typical FRP-retrofitted steel beam under four-point bending loading with a notch in the mid-span section. The FRP plate is bonded to the tension soffit of the steel beam. It is worth noting that the FRP plates, especially high modulus CFRP plates, are increasingly used for the fatigue strengthening of in-service cracked steel beams (Wang and Wu 2018; Yu and Wu 2018; Yu and Wu 2017). Therefore, the design configuration shown in **Fig. 5-2** has been adopted by some existing studies to investigate the fatigue behavior and strength enhancement of cracked steel beams retrofitted with CFRP plates (e.g., Colombi and Fava 2015; Colombi and Fava 2016; Wang and Wu 2018). The steel beam is made of S275J0 steel with an elastic modulus of 208 GPa and has a clear span (L) of 1 m. The depth (d_1) and width (i.e., the length of the flanges, b_1) of the beam are 120 mm and 64 mm, respectively. The thicknesses of the web (t_w) and the flange (t_f) are 4.4 mm and 6.3 mm, respectively. Therefore, the cross-sectional area (A_1) and the second moment of area (I_1) for the steel beam are calculated as 1278.96 mm^2 and 3.06 $\times 10^6$ mm^4, respectively.

The CFRP plate is 0.8 m long (L_P), 60 mm wide (b_2) and 1.4 mm thick (d_2), which has an elastic modulus (E_2) of 195 GPa. The sectional area of the CFRP plate (A_2) is 84 mm^2. The CFRP plate is bonded to the soffit of the steel beam with a 2.5 mm thick (t_a) adhesive layer, which is made of Sikadur 30 epoxy resin. As shown in **Fig. 2**, the distance between the FRP plate end and the support (a) is 0.1 m.

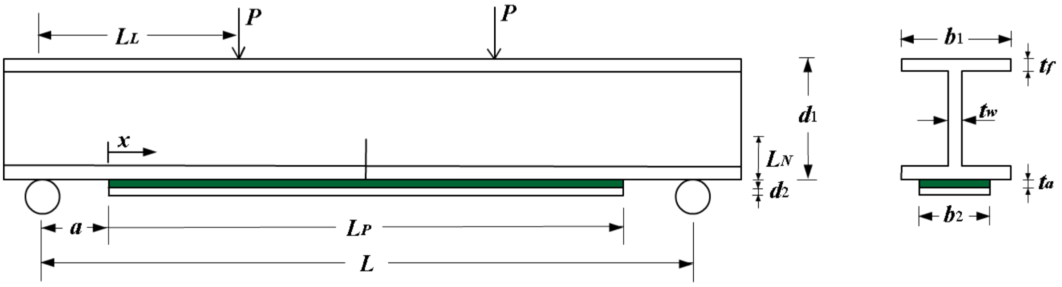

Fig. 5-2 FRP-retrofitted notched steel beam under four-point bending

The notch is located at the mid-span of the steel beam with a depth (L_N) of 50 mm and a width (b_N) of 2.5 mm, and it divides the steel beam into two symmetrical parts. The two-point loads are applied on the top surface of the steel beam, which are symmetrically located about the mid-span section with an 0.25 m distance between the loading point and the adjacent support (L_L). Due to the symmetrical behavior, only the left part of the beam is considered in the analytical solution. **Fig. 5-3** illustrates the stress condition of a differential element of the FRP-retrofitted steel beam under combined thermal and mechanical loading (with a constant temperature profile over the beam depth). The differential element is subjected to axial loading (N), vertical shear force (V), bending moment (M) and interfacial shear stress (τ). The superscripts 1 and 2 in this figure represent the steel beam and the FRP plate, respectively. As shown in **Fig. 5-3**, these parameters vary along the bondline, and therefore, their values are functions of x, where the variable x is defined as the distance from the differential element to the left end of the FRP plate.

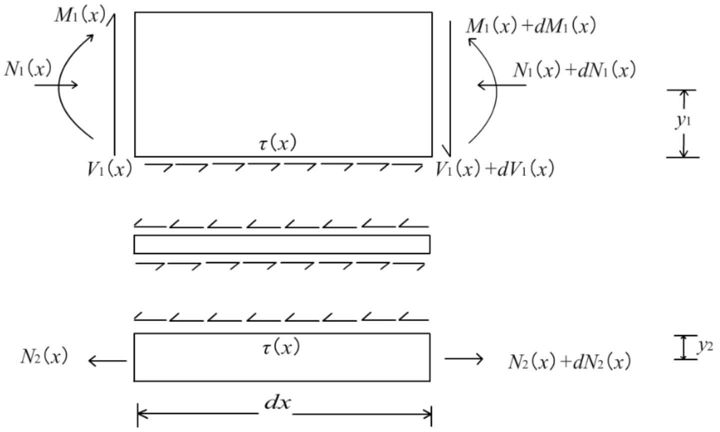

Fig. 5-3 Differential element of the FRP-retrofitted steel beam

When the force equilibriums of the beam and the differential element along the bondline are considered, Eqs. (5-1) and (5-2) can be obtained. Also, the moment equilibriums of the beam and the element can be expressed by Eqs. (5-3) and (5-4) as follows:

$$N_1 = -N_2 \tag{5-1}$$

$$\frac{1}{b_2}\frac{dN_1}{dx} = -\tau \tag{5-2}$$

$$M_1 + N_2(y_1 + t_a + y_2) = M_T \tag{5-3}$$

$$\frac{dM_1}{dx} = V_1 - \tau b_2 y_1 \tag{5-4}$$

where N_1 and N_2 are the axial forces sustained by the steel beam and the FRP plate, respectively. M_1 and M_T are the bending moment sustained by the steel beam and the overall retrofitted structure, respectively. y_1 is the distance from the centroid of the steel beam to the beam bottom surface, and y_2 is the distance from the centroid of the FRP plate to its top surface, as depicted in **Fig. 5-3**.

5.2.3 Governing Equations

At the elastic stage, the local bond-slip relationship of the FRP-to-steel interface (i.e., the adhesive layer) is linearly elastic, and the interfacial shear stress can be described as:

$$\tau^e = \frac{\tau_p}{\delta_t^0}\delta_t \tag{5-5}$$

where the interfacial shear slip (δ_t) can be calculated by the displacement difference between the bottom of the steel beam (u_1) and the top of the FRP plate (u_2) (i.e., $\delta_t = u_2 - u_1$). τ is the interfacial shear stress, and those with the superscripts e and s denote the stress values in the elastic and softening stages.

Since the bending stiffness of the FRP plate is negligible compared with that of the steel beam, the bending moment sustained by the FRP plate and the related bending deformation are not considered in the analytical solution. Therefore, the strain at the bottom surface of the steel beam (ε_1) and that at the top surface of the FRP plate (ε_2) can be computed as follows:

$$\varepsilon_1 = \frac{M_1 y_1}{E_1 I_1} + \frac{N_1}{E_1 A_1} + \alpha_1 \Delta T \tag{5-6}$$

$$\varepsilon_2 = \frac{N_2}{E_2 A_2} + \alpha_2 \Delta T \tag{5-7}$$

where α_1 and α_2 are the CTEs of steel and FRP respectively, ΔT is the value of temperature variation, A_1 and I_1 are the sectional area and the second moment of area of the steel beam, and A_2 is the sectional area of the FRP plate.

Differentiating Eq. (5-2) with respect to x and then substituting Eqs. (5-3), (5-5), (5-6) and (5-7) into it, the governing equation of the axial force distribution in the FRP plate at elastic stage can be derived as

$$\frac{d^2 N_2}{dx^2} - \lambda^2 N_2 + \lambda^2 \frac{\Delta\varepsilon_{sf}}{f_2} = 0 \tag{5-8}$$

where

$$\lambda = \sqrt{\frac{f_2}{f_1}} \tag{5-9}$$

$$f_1 = \frac{\delta_t^0}{\tau_p b_2} \tag{5-10}$$

$$f_2 = \frac{(y_1+y_2)y_1}{E_1 I_1} + \frac{1}{E_1 A_1} + \frac{1}{E_2 A_2} \tag{5-11}$$

$$\Delta\varepsilon_{sf} = \frac{M_T y_1}{E_1 I_1} + (\alpha_1 - \alpha_2)\Delta T \tag{5-12}$$

$\Delta\varepsilon_{sf}$ is the strain difference between the bottom of steel beam and the top of CFRP plate, and the thermal strain $(\alpha_1 - \alpha_2)\Delta T$ is induced by the thermal incompatibility between steel and FRP.

The above governing equation (i.e., Eq. 5-8) has a general solution as follows:

$$N_2(x) = C_m e^{-\lambda x} + C_n e^{\lambda x} + \frac{\Delta\varepsilon_{sf}}{f_2} \tag{5-13}$$

where C_m and C_n are two integration constants, and the subscripts m and n will be subsequently replaced with different numbers at various loading stages.

The interfacial shear stress at elastic stage can be derived from Eq. (5-13) as follows:

$$\tau^e(x) = \frac{1}{b_2}\frac{dN_2(x)}{dx} = -\frac{\lambda}{b_2}C_m e^{-\lambda x} + \frac{\lambda}{b_2}C_n e^{\lambda x} + \frac{1}{b_2 f_2}\frac{d\Delta\varepsilon_{sf}}{dx} \tag{5-14}$$

Substituting Eq. (5-12) into Eq. (5-14) gives

$$\tau^e(x) = -\frac{\lambda}{b_2}C_m e^{-\lambda x} + \frac{\lambda}{b_2}C_n e^{\lambda x} + \frac{y_1}{b_2 f_2 E_1 I_1}V_T(x) \tag{5-15}$$

where $V_T(x)$ is the shear force applied on the steel beam.

At the softening branch of the shear stress-slip curve shown in **Fig. 5-1**, the relationship between the interfacial shear stress and the interfacial slip can be described as:

$$\tau^s = \tau_0 - \frac{\tau_p}{\delta_t^f - \delta_t^0}\delta \tag{5-16}$$

where $\tau_0 = \tau_p \delta_f / (\delta_t^f - \delta_t^0)$, and $\frac{\tau_p}{\delta_t^f - \delta_t^0}$ denotes the slope of the softening branch of the bond-slip curve.

Using the same procedure as adopted for the elastic stage analysis, the governing equation of the axial force distribution in the FRP plate at the softening stage can be deduced as:

$$\frac{d^2 N_2}{dx^2} + {\lambda'}^2 N_2 + {\lambda'}^2 \frac{\Delta\varepsilon_{sf}}{f_2} = 0 \tag{5-17}$$

where $\lambda' = \sqrt{\frac{f_2}{f_1'}}$, and $f_1' = \frac{\delta_t^f - \delta_t^0}{\tau_p b_2}$.

Correspondingly, the general solution of Eq. (5-17) is:

$$N_2(x) = C_p \cos(\lambda' x) + C_q \sin(\lambda' x) + \frac{\Delta\varepsilon_{sf}}{f_2} \tag{5-18}$$

where C_p and C_q are two integration constants. Therefore, the distribution of interfacial shear stress can be solved as

$$\tau^s(x) = \frac{1}{b_2}\frac{dN_2(x)}{dx} = -\frac{\lambda'}{b_2}C_p \sin(\lambda' x) + \frac{\lambda'}{b_2}C_q \cos(\lambda' x) + \frac{y_1}{b_2 f_2 E_1 I_1}V_T(x) \tag{5-19}$$

5.2.4 Solutions of Full-range Deformation Behavior

The full-range bond behavior of the FRP-to-steel interface in the FRP-retrofitted steel beam under combined thermal and mechanical loading includes the elastic (*E*) stage, elastic-softening (*E-S*) stage, elastic-softening-debonding (*E-S-D*) stage, and softening-debonding (*S-D*) stage. In the current study, all these stages are analyzed to obtain the detailed solutions of the interfacial shear stresses. In addition, the debonding load (i.e., the load-capacity corresponding to the initiation of IC debonding) of the FRP-retrofitted steel beam is determined at the end of the *E-S* stage.

The integration constants (i.e., C_m, C_n, C_p, C_q) in Eqs. (5-13), (5-15), (5-18) and (5-19) can be solved using the boundary conditions at the *E* and *E-S* stages. The boundary conditions include the axial forces in the FRP plate at two locations, i.e., zero and N_{2l_2} at the FRP plate end ($x = 0$) and at the left side of the notch ($x = l_2 = \frac{L_P}{2} - \frac{b_N}{2}$), respectively.

5.2.4.1 Elastic stage

At the elastic stage, the axial force in the FRP plate and the interfacial shear stress can be described by Eqs. (5-20) and (5-21), respectively. Note that the integration constants C_m and C_n in Eq. (5-13) are denoted as C_1 and C_2 in Eq. (5-20).

$$N_2(x) = C_1 e^{-\lambda x} + C_2 e^{\lambda x} + \frac{\Delta\varepsilon_{sf}}{f_2} \tag{5-20}$$

$$\tau^e(x) = \frac{1}{b_2}\frac{dN_2(x)}{dx} = -\frac{\lambda}{b_2}C_1 e^{-\lambda x} + \frac{\lambda}{b_2}C_2 e^{\lambda x} + \frac{y_1}{b_2 f_2 E_1 I_1}V_T(x) \tag{5-21}$$

Substituting the axial forces in the FRP plate at the plate end ($x = 0$) and at the notched section ($x = l_2$) into Eq. (5-20), the following equations can be obtained:

$$0 = C_1 + C_2 + \frac{\Delta\varepsilon_{sf0}}{f_2} \tag{5-22}$$

$$N_{2l_2} = C_1 e^{-\lambda l_2} + C_2 e^{\lambda l_2} + \frac{\Delta\varepsilon_{sfl_2}}{f_2} \tag{5-23}$$

The constants C_1 and C_2 can be solved from Eqs. (5-22) and (5-23) as follows:

$$C_1 = \frac{-\frac{\Delta\varepsilon_{sf0}}{f_2} e^{\lambda l_2} - N_{2l_2} + \frac{\Delta\varepsilon_{sfl_2}}{f_2}}{e^{\lambda l_2} - e^{-\lambda l_2}} \tag{5-24}$$

$$C_2 = \frac{-\frac{\Delta\varepsilon_{sf0}}{f_2} e^{-\lambda l_2} - N_{2l_2} + \frac{\Delta\varepsilon_{sfl_2}}{f_2}}{e^{-\lambda l_2} - e^{\lambda l_2}} \tag{5-25}$$

where $\Delta\varepsilon_{sf0} = \frac{Pay_1}{E_1 I_1} + (\alpha_1 - \alpha_2)\Delta T$, and $\Delta\varepsilon_{sfl_2} = \frac{PL_L y_1}{E_1 I_1} + (\alpha_1 - \alpha_2)\Delta T$.

5.2.4.2 Elastic-softening stage

As the shear stress propagates along the FRP-to-steel interface, the adhesive layer begins to soften at the notched section. In the *E-S* stage, the softening region is located near the notched section, while the elastic region is located near the plate end. These two regions are connected at the location $x = \bar{x}$, and the length of softening region is then determined as $l_2 - \bar{x}$.

During the *E-S* stage, the axial force in the FRP plate and the interfacial shear stress in the softening region can be expressed as:

$$N_2(x) = C_3 \cos(\lambda' x) + C_4 \sin(\lambda' x) + \frac{\Delta\varepsilon_{sf}}{f_2} \tag{5-26}$$

$$\tau^s(x) = \frac{1}{b_2}\frac{dN_2(x)}{dx} = -\frac{\lambda'}{b_2} C_3 \sin(\lambda' x) + \frac{\lambda'}{b_2} C_4 \cos(\lambda' x) + \frac{y_1}{b_2 f_2 E_1 I_1} V_T(x) \tag{5-27}$$

The boundary conditions of the softening region in the *E-S* stage consist of the maximum shear stress ($\tau = \tau_p$) at $x = \bar{x}$ and the axial force in the FRP plate ($N_2 = N_{2l_2}$) at the notched section ($x = l_2$), which can be described as follows:

$$\tau_p = -\frac{\lambda'}{b_2} C_3 \sin(\lambda' \bar{x}) + \frac{\lambda'}{b_2} C_4 \cos(\lambda' \bar{x}) + \frac{y_1}{b_2 f_2 E_1 I_1} V_T(\bar{x}) \tag{5-28}$$

$$N_{2l_2} = C_3 \cos(\lambda' l_2) + C_4 \sin(\lambda' l_2) + \frac{\Delta\varepsilon_{sfl_2}}{f_2} \tag{5-29}$$

where $V_T(\bar{x}) = 0$ when the softening region locates in the pure bending zone ($L_L - a < \bar{x} < l_2$), and $V_T(\bar{x}) = P$ when the softening region is beyond the pure bending zone ($0 < \bar{x} < L_L - a$).

By combining Eq. (5-28) and Eq. (5-29), the integration constants C_3 and C_4 can be computed as follows:

$$C_3 = \frac{\left(\lambda' N_{2l_2} - \frac{\Delta\varepsilon_{sf} l_2 \lambda'}{f_2}\right)\cos(\lambda'\bar{x}) + \frac{y_1 \sin(\lambda' l_2)}{f_2 E_1 I_1} V_T(\bar{x}) - b_2 \tau_p \sin(\lambda' l_2)}{\lambda' \cos[\lambda'(l_2 - \bar{x})]} \tag{5-30}$$

$$C_4 = \frac{\left(\lambda' N_{2l_2} - \frac{\Delta\varepsilon_{sf} l_2 \lambda'}{f_2}\right)\sin(\lambda'\bar{x}) - \frac{y_1 \cos(\lambda' l_2)}{f_2 E_1 I_1} V_T(\bar{x}) + b_2 \tau_p \cos(\lambda' l_2)}{\lambda' \cos[\lambda'(l_2 - \bar{x})]} \tag{5-31}$$

According to the above equations, the axial force in the FRP plate at the notched section (N_{2l_2}) and the location of the connection point ($\bar{x}$) are required for determining the values of the integration constants C_3 and C_4. Meanwhile, the elastic region is located between $x = 0$ and $x = \bar{x}$ at the *E*-*S* stage, and the axial force in the FRP plate and the interfacial shear stress can be depicted by

$$N_2(x) = C_5 e^{-\lambda x} + C_6 e^{\lambda x} + \frac{\Delta\varepsilon_{sf}}{f_2} \tag{5-32}$$

$$\tau^e(x) = \frac{1}{b_2}\frac{dN_2(x)}{dx} = -\frac{\lambda}{b_2} C_5 e^{-\lambda x} + \frac{\lambda}{b_2} C_6 e^{\lambda x} + \frac{y_1}{b_2 f_2 E_1 I_1} V_T(x) \tag{5-33}$$

The boundary conditions of the elastic region in the *E*-*S* stage are $\tau^e = \tau_p$ at $x = \bar{x}$ and $N_2 = 0$ at $x = 0$. Substituting the boundary conditions into Eqs. (5-32) and (5-33), they can be rewritten as

$$\tau_p = -\frac{\lambda}{b_2} C_5 e^{-\lambda\bar{x}} + \frac{\lambda}{b_2} C_6 e^{\lambda\bar{x}} + \frac{y_1}{b_2 f_2 E_1 I_1} V_T(\bar{x}) \tag{5-34}$$

$$0 = C_5 + C_6 + \frac{\Delta\varepsilon_{sf0}}{f_2} \tag{5-35}$$

Therefore, the detailed values of the integration constants C_5 and C_6 can be derived from Eq. (5-34) and Eq. (5-35) as follows:

$$C_5 = \frac{-b_2\tau_p + \frac{y_1 V_T(\bar{x})}{f_2 E_1 I_1} - \frac{\Delta\varepsilon_{sf0}}{f_2}\lambda e^{\lambda\bar{x}}}{\lambda(e^{\lambda\bar{x}} + e^{-\lambda\bar{x}})} \tag{5-36}$$

$$C_6 = \frac{b_2\tau_p - \frac{y_1 V_T(\bar{x})}{f_2 E_1 I_1} - \frac{\Delta\varepsilon_{sf0}}{f_2}\lambda e^{-\lambda\bar{x}}}{\lambda(e^{\lambda\bar{x}} + e^{-\lambda\bar{x}})} \tag{5-37}$$

Moreover, the location of the connection point between the elastic region and the softening region ($\bar{x}$) in the *E*-*S* stage is an essential parameter to determine the integration constants ($C_3 \sim C_6$). The value of $\bar{x}$ can be solved by considering the continuity of the bending moments and the axial forces of the two adherends at $x = \bar{x}$ (Wang 2006).

By differentiating Eqs. (5-5) and (5-16) with respect to x and substituting Eqs. (5-6) and (5-7), the following two equations can be obtained at two different regions:

In the elastic region,

$$\frac{d\tau^e(x)}{dx} = -\frac{\tau_p}{\delta_t^0}\left[(\alpha_1 - \alpha_2)\Delta T + \frac{M_1 y_1}{E_1 I_1} + \frac{N_1}{E_1 A_1} - \frac{N_2}{E_2 A_2}\right] \tag{5-38}$$

while in the softening region,

$$\frac{d\tau^s(x)}{dx} = \frac{\tau_p}{\delta_t^f - \delta_t^0}\left[(\alpha_1 - \alpha_2)\Delta T + \frac{M_1 y_1}{E_1 I_1} + \frac{N_1}{E_1 A_1} - \frac{N_2}{E_2 A_2}\right] \tag{5-39}$$

At the location $x = \bar{x}$, the axial forces and the bending moments of the two adherends are continuous. Therefore, the relationship between τ_e and τ_s can be expressed as

$$\frac{d\tau^e(\bar{x})}{dx} = -\frac{\delta_t^f - \delta_t^0}{\delta_t^0}\frac{d\tau^s(\bar{x})}{dx} \tag{5-40}$$

Substituting Eqs. (5-27) and (5-33) into Eq. (5-40), and considering that the magnitude of shear force $V_T(\bar{x})$ is constant (i.e., $dV_T(\bar{x})/dx = 0$), the following equation can be derived:

$$C_5 e^{-\lambda\bar{x}} + C_6 e^{\lambda\bar{x}} = C_3\cos(\lambda'\bar{x}) + C_4\sin(\lambda'\bar{x}) \tag{5-41}$$

In the above equation, the value of the integration constants (i.e., C_3~C_6) are functions of the unknown location of the connection point ($\bar{x}$) and the axial force at the notched section (N_{2l_2}). Therefore, $\bar{x}$ can be determined based on the given mechanical and thermal loads (F, ΔT) by substituting Eqs. (5-30), (5-31), (5-36) and (5-37) into Eq. (5-41), once the axial force of the FRP plate (N_{2l_2}) in the notched section is determined.

5.2.4.3 Debonding load

For FRP retrofitted notched steel beam, the total loss of the load-carrying capacity happens when the debonding propagates to the plate ends. However, before that, the irreversible damage has been generated when the interfacial debonding occurs near the notched section. Then the debonding will propagate rapidly because of the suddenly release of energy and the load-carrying capacity barely increases in *E-S* and *E-S-D* stages (Gao *et al.* 2016). Therefore, when making the design scheme, it is rational to define the load-carrying capacity analytically at onset of debonding.

When interfacial debonding occurs at the FRP-to-steel interface at the notched section, the corresponding shear stress reduces to zero, that is

$$\tau^s(l_2) = 0 \tag{5-42}$$

Substituting Eq. (5-27) into Eq. (5-42), the following equation can be obtained:

$$\tau^s(l_2) = -\frac{\lambda'}{b_2}C_3\sin(\lambda' l_2) + \frac{\lambda'}{b_2}C_4\cos(\lambda' l_2) + \frac{y_1}{b_2 f_2 E_1 I_1}V_T(l_2) = 0 \tag{5-43}$$

As illustrated in **Fig. 5-2**, the notch is located in constant moment region, and therefore, $V_T(l_2)$ = 0. Eq. (5-43) can be simplified as follows

$$C_3\tan(\lambda' l_2) = C_4 \tag{5-44}$$

Considering that C_3 and C_4 are all dependent on P and ΔT, the above equation has established the relationship among the debonding load (P), the thermal loading (ΔT) and the length of the softening region ($\bar{x}$) at the initiation of FRP debonding. When the FRP-retrofitted steel beam under a given temperature variation (ΔT) is considered, the two unknown variables (i.e., P and $\bar{x}$) can be calculated by combination of Eqs. (5-41) and (5-44).

5.2.4.4 Elastic-softening-debonding stage

After the onset of debonding, the deformation stage evolves to the *E-S-D* stage. Hereby, set the location of the conjunction point between softening and debonding region as $\bar{\bar{x}}$. Then the lengths of the elastic, softening and deboned regions are $\bar{x}, \bar{\bar{x}} - \bar{x}$ and $l_2 - \bar{\bar{x}}$, respectively.

During the *E-S-D* stage, the axial force of FRP plate in debonded region is identical to the force of FRP plate at the notched section (N_{2l_2}) and the interfacial shear stress in the debonded region (τ^d) is zero.

$$N_2(x) = N_{2l_2};\ \tau^d(x) = 0 \tag{5-45}$$

And the axial force in the FRP plate and the interfacial shear stress within the softening region can be described as follows:

$$N_2(x) = C_7\cos(\lambda' x) + C_8\sin(\lambda' x) + \frac{\Delta\varepsilon_{sf}}{f_2} \tag{5-46}$$

$$\tau^s(x) = \frac{1}{b_2}\frac{dN_2(x)}{dx} = -\frac{\lambda'}{b_2}C_7\sin(\lambda' x) + \frac{\lambda'}{b_2}C_8\cos(\lambda' x) + \frac{y_1}{b_2 f_2 E_1 I_1}V_T(\bar{\bar{x}}) \tag{5-47}$$

The boundary conditions of the softening region at the *E-S-D* stage consist of the maximum shear stress at $x = \bar{x}$ (i.e., $\tau = \tau_p$), and the axial force in the FRP plate at connection point between softening and debonding areas [i.e., $N_2(\bar{\bar{x}}) = N_{2l_2}$], which can be depicted as follows:

$$\tau_p = -\frac{\lambda'}{b_2} C_7 \sin(\lambda' \bar{x}) + \frac{\lambda'}{b_2} C_8 \cos(\lambda' \bar{x}) + \frac{y_1}{b_2 f_2 E_1 I_1} V_T(\bar{x}) \tag{5-48}$$

$$N_{2l_2} = C_7 \cos(\lambda' \bar{\bar{x}}) + C_8 \sin(\lambda' \bar{\bar{x}}) + \frac{\Delta\varepsilon_{sfl_2}}{f_2} \tag{5-49}$$

Then the integration constants C_7 and C_8 can be computed as follows:

$$C_7 = \frac{\left(\lambda' N_{2l_2} - \frac{\Delta\varepsilon_{sfl_2}\lambda'}{f_2}\right)\cos(\lambda'\bar{x}) + \frac{y_1 \sin(\lambda'\bar{\bar{x}})}{f_2 E_1 I_1} V_T(\bar{x}) - b_2 \tau_p \sin(\lambda' \bar{\bar{x}})}{\lambda' \cos[\lambda'(\bar{\bar{x}} - \bar{x})]} \tag{5-50}$$

$$C_8 = \frac{\left(\lambda' N_{2l_2} - \frac{\Delta\varepsilon_{sfl_2}\lambda'}{f_2}\right)\sin(\lambda'\bar{x}) - \frac{y_1 \cos(\lambda'\bar{\bar{x}})}{f_2 E_1 I_1} V_T(\bar{x}) + b_2 \tau_p \cos(\lambda' \bar{\bar{x}})}{\lambda' \cos[\lambda'(\bar{\bar{x}} - \bar{x})]} \tag{5-51}$$

Meanwhile, the FRP axial force and interfacial shear stress in elastic region at *E-S-D* stage can be expressed as follows:

$$N_2(x) = C_9 e^{-\lambda x} + C_{10} e^{\lambda x} + \frac{\Delta\varepsilon_{sf}}{f_2} \tag{5-52}$$

$$\tau^e(x) = \frac{1}{b_2}\frac{dN_2(x)}{dx} = -\frac{\lambda}{b_2} C_9 e^{-\lambda x} + \frac{\lambda}{b_2} C_{10} e^{\lambda x} + \frac{y_1}{b_2 f_2 E_1 I_1} V_T(x) \tag{5-53}$$

The boundary conditions of the elastic region at *E-S* stage are $\tau^e = \tau_p$ at $x = \bar{x}$ and $N_2 = 0$ at $x = 0$, which is identical to the boundary conditions in elastic region in *E-S* stage. Therefore,

$$C_9 = C_5 = \frac{-b_2 \tau_p + \frac{y_1 V_T(\bar{x})}{f_2 E_1 I_1} - \frac{\Delta\varepsilon_{sf0}}{f_2} \lambda e^{\lambda \bar{x}}}{\lambda(e^{\lambda\bar{x}} + e^{-\lambda\bar{x}})} \tag{5-54}$$

$$C_{10} = C_6 = \frac{b_2 \tau_p - \frac{y_1 V_T(\bar{x})}{f_2 E_1 I_1} - \frac{\Delta\varepsilon_{sf0}}{f_2} \lambda e^{-\lambda \bar{x}}}{\lambda(e^{\lambda\bar{x}} + e^{-\lambda\bar{x}})} \tag{5-55}$$

According to Eqs. (5-50), (5-51), (5-54) and (5-55), the integration constants are dependent on the location of the conjunction points between the elastic, softening and debonding regions (i.e., $\bar{x}$ and $\bar{\bar{x}}$). Considering that the continuity axial forces and the bending moments of both adherends are still hold in *E-S-D* stage, the $\bar{x}$ can be solved by Eq. (5-41) with replacing $C_3 \sim C_6$ as $C_7 \sim C_{10}$. And $\bar{\bar{x}}$ can be solved by considering that the interfacial shear stress at $\bar{\bar{x}}$ is zero.

$$\tau^s(\bar{\bar{x}}) = -\frac{\lambda'}{b_2}C_7\sin(\lambda'\bar{\bar{x}}) + \frac{\lambda'}{b_2}C_8\cos(\lambda'\bar{\bar{x}}) + \frac{y_1}{b_2 f_2 E_1 I_1}V_T(\bar{\bar{x}}) = 0 \qquad (5\text{-}56)$$

5.2.4.5 Softening-debonding stage

As the propagation of the debonded region from the notched section to the plate end, the length of elastic region decreases. After the length of elastic region decreases to zero (i.e., $\bar{x} = 0$), then only softening region and debonded region remain at the interface.

And the axial force in the FRP plate and the interfacial shear stress within the softening region can be described as follows:

$$N_2(x) = C_{11}\cos(\lambda' x) + C_{12}\sin(\lambda' x) + \frac{\Delta\varepsilon_{sf}}{f_2} \qquad (5\text{-}57)$$

$$\tau^s(x) = \frac{1}{b_2}\frac{dN_2(x)}{dx} = -\frac{\lambda'}{b_2}C_{11}\sin(\lambda' x) + \frac{\lambda'}{b_2}C_{12}\cos(\lambda' x) + \frac{y_1}{b_2 f_2 E_1 I_1}V_T(x) \qquad (5\text{-}58)$$

The axial force in the FRP plate is zero at plate end and N_{2l_2} at $(x = \bar{\bar{x}})$, therefore,

$N_2(0) = 0; N_2(\bar{\bar{x}}) = N_{2l_2}.$

$$0 = C_{11} + \frac{\Delta\varepsilon_{sf0}}{f_2} \qquad (5\text{-}59)$$

$$N_{2l_2} = C_{11}\cos(\lambda'\bar{\bar{x}}) + C_{12}\sin(\lambda'\bar{\bar{x}}) + \frac{\Delta\varepsilon_{sf\bar{\bar{x}}}}{f_2} \qquad (5\text{-}60)$$

where $\Delta\varepsilon_{sf\bar{\bar{x}}} = \frac{P\bar{\bar{x}}y_1}{E_1 I_1} + (\alpha_1 - \alpha_2)\Delta T$, when $0 < \bar{\bar{x}} < L_L - a$; $\Delta\varepsilon_{sf\bar{\bar{x}}} = \frac{PL_L y_1}{E_1 I_1} + (\alpha_1 - \alpha_2)\Delta T$ when $L_L - a < \bar{\bar{x}} < l_2$.

By combining Eqs. (5-59) and (5-60), C_{11} and C_{12} can be determined as:

$$C_{11} = -\frac{\Delta\varepsilon_{sf0}}{f_2} \qquad (5\text{-}61)$$

$$C_{12} = \frac{1}{\sin(\lambda'\bar{\bar{x}})}\left[N_{2l_2} - \frac{\Delta\varepsilon_{sf\bar{\bar{x}}}}{f_2} - C_{11}\cos(\lambda'\bar{\bar{x}})\right] \qquad (5\text{-}62)$$

Similar to *E*-*S* stage, $\bar{\bar{x}}$ can be solved by considering the interfacial shear stress is zero.

$$-\frac{\lambda'}{b_2}C_{11}\sin(\lambda'\bar{\bar{x}}) + \frac{\lambda'}{b_2}C_{12}\cos(\lambda'\bar{\bar{x}}) + \frac{y_1}{b_2 f_2 E_1 I_1}V_T(\bar{\bar{x}}) = 0 \qquad (5\text{-}63)$$

5.2.5 *Axial Force in the FRP Plate at the Notched Section*

The interfacial shear stress distributions can be determined by Eq. (5-21) at the *E* stage; by Eqs. (5-27) and (5-33) at the *E-S* stage, by Eqs. (5-47) and (5-53) at *E-S-D* stage; by Eq. (5-58) at *S-D* stage. The integration constants (i.e., C_1~C_{12}) in these equations need to be firstly determined to obtain the detailed stress distributions along the bondline. As stated above, the magnitude of axial force in the FRP plate at the notched section (i.e., N_{2l_2}) is an essential parameter in determination of the location of the connection points between different regions $(\bar{x}, \bar{\bar{x}})$ in *E-S* stage and the integration constants (i.e., C_1~C_4, C_7, C_8) in all deformation stages.

5.2.5.1 At E and E-S stages

In the previous studies conducted by Deng *et al.* (2016) and Colombi and Fava (2015), the axial force in the FRP plate at the notched section was derived using the deformation compatibility of the FRP-retrofitted steel beam based on the plane section assumption:

$$\frac{M_{1l_2}(y_1'+t_a+y_2)}{E_1 I_1'} - \frac{N_{2l_2}}{E_1 A_1'} = \frac{N_{2l_2}}{E_2 A_2} \tag{5-64}$$

where y_1' is the distance from the neutral axis of the notched section to the bottom surface of the steel beam, I_1' and A_1' are the moment of inertia and the area of the notched section, respectively. M_{1l_2}, N_{2l_2} are the moment sustained by the steel beam and the axial force sustained by the FRP plate at the notched section, with subscript l_2 indicates the location.

It should be noted that in Eq. (5-64), only the deformations induced by the mechanical loading are considered. If the deformations of the FRP-retrofitted steel beam under combined thermal and mechanical loading are considered, Eq. (5-64) can be re-written as follows:

$$\frac{M_{1l_2}(y_1'+t_a+y_2)}{E_1 I_1'} - \frac{N_{2l_2}}{E_1 A_1'} + \alpha_1 \Delta T = \frac{N_{2l_2}}{E_2 A_2} + \alpha_2 \Delta T \tag{5-65}$$

By multiplying the original crack width of the steel beam (b_N) to both sides of Eq. (5-65), it can be rewritten as,

$$\left[\frac{M_{1l_2}(y_1'+t_a+y_2)}{E_1 I_1'} - \frac{N_{2l_2}}{E_1 A_1'} + \alpha_1 \Delta T\right] b_N = \left(\frac{N_{2l_2}}{E_2 A_2} + \alpha_2 \Delta T\right) b_N \tag{5-66}$$

The left side of Eq. (5-66) is the deformation of the cracked beam section at middle thickness of the FRP plate in *x*-axis. And the right side of Eq. (5-66) is the axial deformation of the FRP plate beneath the notch (with original length of b_N) after loading.

Also, the sectional moment equilibrium of the FRP-retrofitted steel beam at the notched section can be expressed as follows:

$$N_{2l_2}(y_1' + t_a + y_2) + M_{1l_2} = M_{Tl_2} \tag{5-67}$$

where M_{Tl_2} is the moment sustained by the FRP retrofitted steel beam at $(x = l_2)$ and $M_{Tl_2} = P \times L_L$.

By combining Eqs. (5-67) and (5-65), the axial force in the FRP plate can be computed as

$$N_{2l_2} = \frac{\Delta\varepsilon'_{sfl_2}}{f_2'} \tag{5-68}$$

where

$$f_2' = \frac{(y_1' + t_a + y_2)^2}{E_1 I_1'} + \frac{1}{E_1 A_1'} + \frac{1}{E_2 A_2} \tag{5-69}$$

$$\Delta\varepsilon'_{sfl_2} = \frac{PL_L(y_1' + t_a + y_2)}{E_1 I_1'} + (\alpha_1 - \alpha_2)\Delta T \tag{5-70}$$

5.2.5.2 At E-S-D and S-D stages

At *E-S-D* and *S-D* stage, the interfacial debonding firstly occurs near the notched section and propagates gradually from the notched section to the plate ends, with total length of $(L_P - 2\bar{\bar{x}})$. Within the debonded region, the axial strain in the FRP plate is constant and the deformation of the FRP plate can be derived as $\left(\frac{N_{2l_2}}{E_2 A_2} + \alpha_2 \Delta T\right)(L_P - 2\bar{\bar{x}})$. In comparison, the axial deformation of the notched steel beam can be considered from two parts, one is the deformation of the steel beam at the notch, which can be calculated by same method as *E* and *E-S* stage. The other is the deformation of the steel beam with intact section which can be derived by integrating the tensile strain along the debonded interface.

Then the deformation compatibility of the FRP retrofitted steel beam can be expressed as follows,

$$\left[\frac{M_{1l_2}(y_1'+t_a+y_2)}{E_1I_1'}-\frac{N_{2l_2}}{E_1A_1'}+\alpha_1\Delta T\right]b_N+2\int_{\bar{\bar{x}}}^{l_2}\left[\frac{M_1(x)(y_1+t_a+y_2)}{E_1I_1}-\frac{N_2}{E_1A_1}+\alpha_1\Delta T\right]dx-2\delta_{\mathrm{f}}=\left(\frac{N_{2l_2}}{E_2A_2}+\alpha_2\Delta T\right)(L_P-2\bar{\bar{x}}) \tag{5-71}$$

Considering the sectional moment equilibrium at intact section (Eq. 5-3) and notched section (Eq. 5-67), the equation can be written as,

$$\frac{PL_L(y_1'+t_a+y_2)}{E_1I_1'}b_N+2\frac{(y_1+t_a+y_2)}{E_1I_1}\int_{\bar{\bar{x}}}^{l_2}[M_T(x)]dx-(\alpha_2-\alpha_1)\Delta T(L_P-2\bar{\bar{x}})-2\delta_{\mathrm{f}} \tag{5-72}$$

$$=N_{2l_2}\beta_1$$

where $\beta_1=\frac{(y_1'+t_a+y_2)^2}{E_1I_1'}b_N+\frac{1}{E_1A_1'}b_N+2\frac{(y_1+t_a+y_2)^2}{E_1I_1}(l_2-\bar{\bar{x}})+2\frac{(l_2-\bar{\bar{x}})}{E_1A_1}+\frac{1}{E_2A_2}(L_P-2\bar{\bar{x}})$.

When the debonded region locates in the pure bending region ($L_L-a<\bar{\bar{x}}<l_2$),

$$\int_{\bar{\bar{x}}}^{l_2}[M_T(x)]dx=PL_Ll_2-PL_L\bar{\bar{x}} \tag{5-73}$$

When the debonded region extends beyond the pure bending region ($0<\bar{\bar{x}}<L_L-a$),

$$\int_{\bar{\bar{x}}}^{l_2}M_{\mathrm{T}}(x)dx=\int_{\bar{\bar{x}}}^{L_L-a}M_{\mathrm{T}}(x)dx+\int_{L_L-a}^{l_2}M_{\mathrm{T}}(x)dx \tag{5-74}$$

$$=P(L_Ll_2-a\bar{\bar{x}}-\frac{1}{2}\bar{\bar{x}}^2)-\frac{1}{2}P(L_L-a)^2$$

5.2.6 Stress Intensity Factor at the Notch Tip

For steel structure with notches, the fatigue failure is also a commonly observed failure mode. And the effectiveness of strengthening with FRP plate on increasing the lifetime of cracked steel beam members have been proved by numerous analyses, based on experiments (Bocciarelli *et al.* 2018; Colombi and Fava 2015; Colombi and Fava 2016; Colombi *et al.* 2015; Jones and Civjan 2003; Wang and Wu 2018; Yu and Wu 2018; Yu and Wu 2017) and numerical modeling (Hosseini *et al.* 2021; Yu *et al.* 2014a). And further research shows that the retrofitting effect can be highly enhanced by applying prestress on the FRP plate (Ghafoori *et al.* 2012). However, little attention has been paid on the thermal effect on the retrofitting effect of the FRP strengthened steel beam.

The thermal stress effect on the stress intensity factor (SIF) at the notch tip in the FRP-retrofitted steel beam is studied herein since under fatigue loading the IC debonding in the FRP retrofitted notched steel beam is strongly related to the notch SIF. SIF has been widely used to quantify the degree of stress intensity and to predict the fatigue behavior of FRP-retrofitted steel beams in previous studies (e.g., Bocciarelli *et al.* 2018; Colombi and Fava 2016; Colombi *et al.* 2015; Doroudi *et al.* 2021; Dunn *et al.* 1997; Jones and

Civjan 2003; Yu and Wu 2017; Yu *et al.* 2014b). some analytical solutions are proposed to calculate the magnitude of SIF of notched steel beam before and after FRP retrofitting based on fracture mechanics (Ghafoori and Motavalli 2011; Hosseini *et al.* 2021). The comparison of SIF values at various temperatures can reflect the thermal stress effect on the fatigue behavior of FRP-retrofitted steel beams. More importantly, once the SIF is obtained, the fatigue life of FRP-retrofitted steel beams can be estimated using the modified Paris law following the approach proposed by Yu *et al.* (2014b). After applying the FRP retrofitting, the notched steel beam is under the bending moment induced by the mechanical loading and the axial force from the FRP plate. Therefore, the SIF value at the notch tip can be computed by considering the effects of bending moment and axial load (Colombi and Fava 2016; Yu and Wu 2017).

For the notched I-section steel beam under bending moment (as shown in **Fig. 5-2**), the SIF value can be calculated as (Dunn *et al.* 1997):

$$K_I^M = M_{1l_2}\sqrt{\frac{\beta_M}{I_1 t_w}\left(\frac{I_1}{I_1'} - 1\right)} \tag{5-75}$$

Also, the SIF value induced by the axial force can be calculated as

$$K_I^N = N_{1l_2}\sqrt{\frac{\beta_N}{A_1 t_w}\left(\frac{A_1}{A_1'} - 1\right)} \tag{5-76}$$

β_M and β_N in Eqs. (5-75) and (5-76) are non-dimensional coefficients, which are defined as functions of the crack length and the beam geometry. The two coefficients can be estimated using the method proposed by Colombi and Fava (2016):

$$\beta_N = \beta_M = \frac{1.16}{\psi^{0.374}} \tag{5-77}$$

where the parameter ψ in the above equation is defined as $\psi = \frac{L_N}{d_1}$, while L_N and d_1 are the length of crack and the depth of the steel beam, respectively.

Before the FRP retrofitting, the overall bending moment induced by the mechanical loading at the notched section (M_{Tl_2}) is sustained by the steel beam, which yields

$$M_{1l_2} = M_{Tl_2} \tag{5-78}$$

After the FRP retrofitting, the moment resisted by the steel beam can be determined as

$$M_{1l_2} = M_{Tl_2} - N_{1l_2} * y_1' \tag{5-79}$$

Note that in Eq. (5-79), the axial load applied on the steel beam at notched section (N_{1l_2}) equals to the axial force in the FRP plate (N_{2l_2}).

Substituting Eq. (5-79) into Eq. (5-75) and combining with (5-76), the SIF value at the notch tip induced by the bending moment and the axial force can be calculated as

$$K_I = K_I^M - K_I^N = \left(M_{Tl_2} - N_{2l_2} * y_1'\right)\sqrt{\frac{\beta_M}{I_1 t_w}\left(\frac{I_1}{I_1'} - 1\right)} - N_{2l_2}\sqrt{\frac{\beta_N}{A_1 t_w}\left(\frac{A_1}{A_1'} - 1\right)} \tag{5-80}$$

From Eq. (5-80), it is clearly seen that the FRP retrofitting yields a decrease in the SIF value due to the combined effects of a moment reduction from M_{Tl_2} to $M_{Tl_2} - N_{2l_2} * y_1'$ and a compressive axial force (N_{2l_2}) applied on the steel beam.

To further illustrate the beneficial effects of the FRP retrofitting, the SIF values of the steel beam with various notch depths under a constant applied load (i.e., P = 15 kN in **Fig. 5-2**) are investigated. **Fig. 5-4** shows the SIF values computed by the proposed analytical solution, which are compared with the predictions by an FE model to verify the reliability of the analytical solution. The details of the FE model are provided in the following section. It is seen that the SIF at the notch tip increases with the notch depth for the steel beam without FRP retrofitting, mainly due to the reduced moment of inertia at the notched section. However, after the steel beam is retrofitted with the FRP plate, the SIF at the tip decreases with the notch depth for the beam under the same mechanical loading. That is, the SIF values reduce with the growth in the notch depth and the increasing restraint of the externally bonded FRP plate for the FRP-retrofitted steel beam under the same applied load.

As shown in **Fig. 5-4**, a relatively large deviation (i.e., 24%) is observed between the analytical result and the FE prediction for the FRP-retrofitted steel beam with a notch depth of 20 mm (i.e., ψ = L_N/d_1 = 1/6), and such deviation decreases with the growth in the notch depth. The relatively large deviation for the beam with a 20 mm deep notch may be due to the constant of 0.374 adopted to define the function of β_M and β_N in Eqs. (5-75) and (5-76), which should actually be a variable relevant to the parameters of the two adherends. To achieve a more reliable prediction of SIF values using the proposed analytical solution, a notch depth of 50 mm instead of 20 mm that was used in Colombi and Fava (2015) is adopted in the present study, yielding a depth ratio of around 0.42. With this notch depth, the FE model prediction and analytical solution lead to almost identical results, so that Eq. (5-80) still can be utilized to quantify the thermal stress effect on the SIF values of the FRP-retrofitted steel beam.

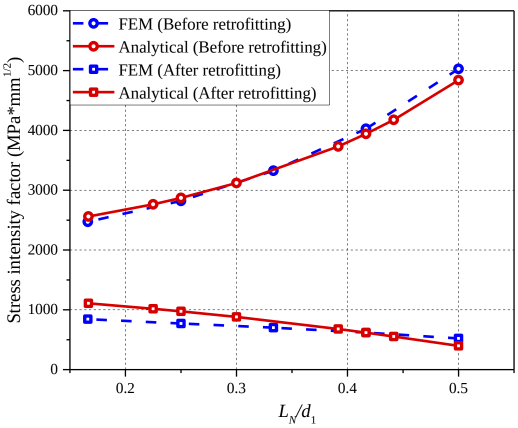

Fig. 5-4 Comparison of the SIF values from the analytical solution and the FE model

In addition, by substituting the function of the axial force in the FRP plate (i.e., Eq. (5-68)) into Eq. (5-80), the relationship among the SIF at the notch tip (K_I), the applied bending moment (M_T) and the temperature variation (ΔT) at E and E-S stages can be derived as

$$K_I = M_{Tl_2}[\theta_1 - \frac{(y_1'+t_a+y_2)}{E_1 I_1'}\frac{\theta_2+y_1'\theta_1}{f_2'}] - \frac{\theta_2+y_1'\theta_1}{f_2'}(\alpha_1-\alpha_2)\Delta T \qquad (5\text{-}81)$$

where $\theta_1 = \sqrt{\frac{\beta_M}{I_1 t_w}\left(\frac{I_1}{I_1'}-1\right)}$, and $\theta_2 = \sqrt{\frac{\beta_N}{A_1 t_w}\left(\frac{A_1}{A_1'}-1\right)}$.

In Eq. (5-81), it is clearly seen that the thermal stress-induced change in the SIF value is $\frac{\theta_2+y_1'\theta_1}{f_2'}(\alpha_1-\alpha_2)\Delta T$, when the FRP-retrofitted steel beam is subjected to combined thermal and mechanical loading. Since the values of θ_1, θ_2, f_2', and $(\alpha_1-\alpha_2)$ are all positive, a service temperature increase (i.e., with a positive value of ΔT) leads to a decrease in K_I.

5.3. FINITE ELEMENT MODELING

A two-dimensional finite element (FE) model was developed within the Abaqus 6.14 software framework to verify the proposed analytical solution. The design configuration shown in **Fig. 5-2** has been adopted as the studied case. And the geometric and material parameters of the steel and CFRP are given in are given in **Table 5-1**. It should be noted that the geometrical dimensions and the elastic moduli of steel and CFRP considered in the analytical solution are assumed as the same as those used in Colombi and Fava (2015). The CTEs of the steel beam and the FRP plate are defined as 1.1×10^{-5}/℃ and 0.6×10^{-6}/℃ respectively, which are the typical values of steel and CFRP at ambient temperature according to Stratford and Bisby (2012).

Table 5-1 Geometrical and material properties used in the case study

Geometrical dimensions of the intact section

d_1 (mm)	b_1 (mm)	t_w (mm)	t_f (mm)	A_1 (mm^2)	I_1 (mm^4)	y_1(mm)
120	64	4.4	6.3	1.28×10^3	3.06×10^6	60

Geometrical dimensions of the notched section

L_N (mm)	b_N (mm)	A_1' (mm^2)	I_1' (mm^4)	y_1' (mm)	E_1 (MPa)
50	2.5	6.84×10^2	2.99×10^5	102.5	208000

Geometrical dimensions of adhesive layer and FRP plate

t_a (mm)	d_2 (mm)	b_2 (mm)	A_2 (mm^2)	L_P (mm)
2.5	1.4	60	84	800

Material properties

E_1 (MPa)	E_2 (MPa)	α_1 (/℃)	α_2 (/℃)
208000	195000	11×10^{-6}	6×10^{-7}

The steel beam and the externally bonded FRP plate are both modeled using 4-node plane stress quadrilateral elements (CPS4), while the adhesive layer is modeled using 4-node cohesive elements (COH2D4). In addition, for the I section beam, the different widths at the flanges and web are modeled by adopting different out-of-plane thicknesses (i.e., 4.4 mm for the web and 64 mm for the flanges).

In the analytical solution, the shear deformations of the steel beam and the FRP plate are ignored. Only the deformations induced by the bending moment and the axial force are considered for the steel beam, while only the axial force deformation is considered for the FRP plate. For the proposed FE model, however, none of the above-mentioned assumptions are employed in the model due to the more accurate simulation using the plane stress elements. Therefore, the comparisons between analytical and FE results are capable of verifying the rationality of these assumptions for the interfacial stress analysis of the FRP-retrofitted steel beams under combined thermal and mechanical loading.

The failure criterion of the bond interface is defined by the coupled mixed-mode cohesive law, which is the most accurate failure criterion and presented by Camanho *et* *al.* (2003) and then modified by De Lorenzis *et al.* (2013) and Teng *et al.* (2015). In coupled-mixed mode cohesive law, the interfacial stresses in both normal (mode I) and shear (mode II) directions are considered. The shape of the bond-separation relationship in pure mode I analysis is same with the interfacial bond behavior in mode II analysis, with linear elastic and softening branches. At elastic stage, the interfacial normal stress (σ) increases with the interfacial separation (δ_n) until peak shear stress (σ_p) at separation of δ_n^0. Then in softening stage, the interfacial normal stress decreases to zero at separation of δ_n^f.

In particular, the onset of softening is defined by a quadratic stress criterion as follows:

$$\left\{\frac{\langle\sigma\rangle}{\sigma_p}\right\}^2 + \left\{\frac{\tau}{\tau_p}\right\}^2 = 1 \tag{5-82}$$

where σ and σ_p are the interfacial normal stress and the peak normal stress when the interface is subjected to a pure mode I loading. The Macaulay bracket used in the above equation indicates that the compressive stress does not cause the initial damage.

After onset of softening, the interfacial behavior is defined as a linear softening bond-slip/separation response and a scalar damage variable *D* is introduced to quantify the degree of damage. *D* is zero at the damage initiation and equal to one at complete interfacial debonding. And the local interfacial behavior in softening stage is described by the following equation:

$$\begin{Bmatrix}\sigma\\ \tau\end{Bmatrix} = \begin{bmatrix}(1-D^*)K_n & 0\\ 0 & (1-D)K_t\end{bmatrix}\begin{Bmatrix}\delta_n\\ \delta\end{Bmatrix} \tag{5-83}$$

where K_n and K_t are the elastic stiffness of the cohesive law in normal and shear directions and $K_n = \sigma_p/\delta_n^0$, $K_t = \tau_p/\delta_t^0$. δ_n and δ are the interfacial separation and slip in both normal and shear directions. In addition, the symbol '$*$' denotes that D^* is equal to zero when σ and δ_n are compressive.

The debonding of the externally bonded FRP plate initiates when the interfacial fracture energy exceeds the critical fracture energy under a pure mode condition. That is, the FRP debonding in a mixed-mode analysis is controlled by the power-law fracture criterion as shown in Eq. (5-84), while the power factor (α) is taken as one according to the suggestions in the previous studies (De Lorenzis *et al.* 2013; Teng *et al.* 2015; Zeng *et al.* 2018)

$$\left\{\frac{G_I}{G_{Ic}}\right\}^{\alpha} + \left\{\frac{G_{II}}{G_{IIc}}\right\}^{\alpha} = 1 \qquad (5\text{-}84)$$

where G_I and G_{II} are the energy release rates in the shear and normal directions. G_{Ic} and G_{IIc} are the critical fracture energies in the shear and normal directions, which are determined and utilized in pure mode I and mode II analyses. The adopted interfacial bond behavior in both directions is shown in **Table 5-2**.

Table 5-2 Interfacial properties used in the analytical and FE analyses

Mode I	σ_p (MPa)	δ_n^0 (mm)	δ_n^f (mm)	G_I (N/mm)
	25	0.0139	0.0277	0.347
Mode II	τ_p (MPa)	δ_t^0 (mm)	δ_t^f (mm)	G_{II} (N/mm)
	20	0.0289	0.0578	0.578

The mesh sizes are chosen as 1 mm*1 mm for the steel beam and 1 mm*0.7 mm (in thickness) for the FRP plate in the FE model. Meanwhile, the adhesive layer is modeled by the cohesive elements with a mesh size of 1 mm along the span direction. It is noteworthy that the sizes of element meshes adopted in the current study are more refined in comparison with those used in the previous FE simulations (e.g., Dai *et al.* 2015; Stratford and Cadei 2006; Teng *et al.* 2015) in order to achieve better predictions with higher accuracy. In addition, 3-node linear plane stress triangle elements are adopted around the crack tip to avoid the strain localization and determine the SIF values (**Fig. 5-5**).

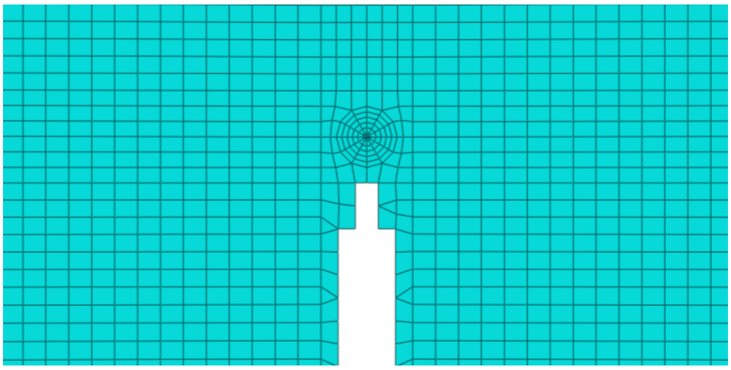

Fig. 5-5 Schematic of the mesh sizes near the crack tip of the steel beam

In the proposed analytical solution, only the shear stress-slip behavior (i.e., the mode II behavior) of the FRP-to-steel interface is considered, which is different from the coupled mixed-mode cohesive law defined in the FE model. In order to examine whether or not the mode II behavior controls the debonding propagation in the FRP-retrofitted notched steel beam, **Fig. 5-6** compares the bond stress-slip/separation relationships adopted for the definition of the mixed-mode cohesive law and those generated from the FE predictions at the notched section and the FRP plate end. The FE predictions have demonstrated that the FRP debonding is predominately controlled by the mode II behavior of the FRP-to-steel interface at the notched section. Therefore, the mode II analysis adopted in the analytical solution is reasonable, which is simple but yields appropriate predictions for the interfacial stress distributions and the associated IC debonding propagation in the FRP-retrofitted notched steel beam. It should be noted that the FE predictions indicate that a mixed-mode cohesive law may be more suitable for analyzing the PE debonding failure near the FRP plate end (**Fig. 5-6b**). However, the PE debonding is not a common failure mode for the FRP-retrofitted cracked or notched steel beam under bending loading, and therefore, the thermal stress effect on the PE debonding in the FRP-retrofitted cracked steel beam is beyond the scope of the current study.

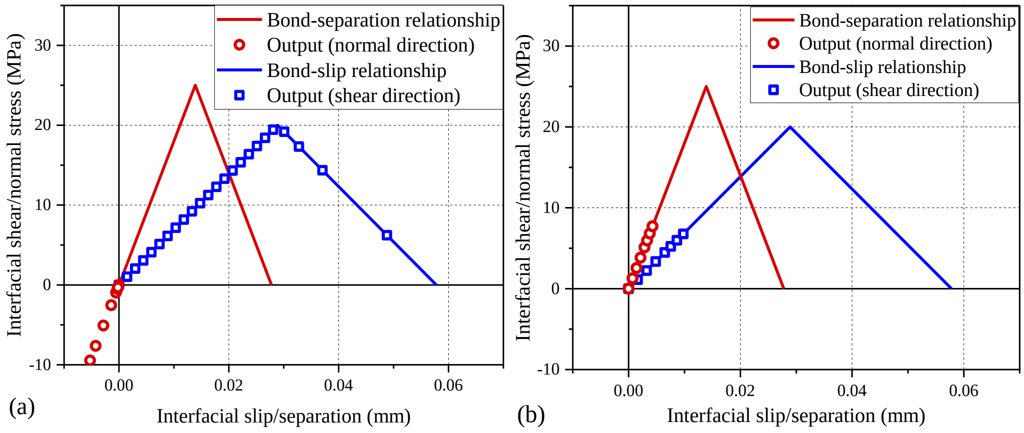

Fig. 5-6 The input and output of interfacial shear stress-slip/separation relationships: a) at the notched section; b) at the FRP plate end.

5.4. RESULTS AND DISCUSSION

5.4.1 Debonding Propagation in the FRP-retrofitted Steel Beam

Fig. 5-7 shows the axial force distributions in the FRP plate and the interfacial shear stresses along the bondline obtained from the analytical solution and the FE model. The FRP-retrofitted steel beam is assumed to sustain different levels of applied loads without the consideration of thermal loading. It is seen that the analytical results are in good agreement with the FE predictions. The axial force in the FRP plate grows from zero at the plate end until the maximum value achieved at the notched section (**Fig. 5-7a**). Moreover, the axial force value at each point improves with the increase in the applied load (i.e., the mechanical loading). **Fig. 5-7b** illustrates that when the mechanical loading level is low, the interface deformation is in the *E* stage. When the shear stress at the notched section increases to the maximum shear stress, the interface enters into the *E-S* stage. After that, the shear stresses in the softening region decreases subsequently with the increase of the mechanical loading, until the interfacial shear stress reduces to zero at the notch section, which leads to the occurrence of the IC debonding. With further increase in the applied loading, the debonded region propagates from the notched section to the plate ends.

Fig. 5-8 compares the analytical and FE results for the FRP-retrofitted steel beam under various levels of thermal loading while a constant mechanical loading (i.e., P = 18 kN). Although the mechanical loading maintains at a constant value, the axial force in the FRP plate increases along the bond length with the temperature increase (**Fig. 5-8**).

According to **Fig. 5-8b**, the direction of the interfacial shear stress at plate end is opposite to that generated by mechanical loading given a temperature decrease (i.e., $\Delta T < 0$). At elevated temperatures ($\Delta T > 0$), the direction of interfacial shear stress is changed. The magnitude of the interfacial shear stress at plate end increases with the increase of temperature. This is similar to the interfacial behavior of FRP strengthened intact steel beam, which suffers from the plate-end debonding failure. But the effect of temperature increase on the interface near the notched section is opposite. When the temperature is decreased, the interface near the notch is in *E-S* stage. However, when the temperature increase is higher than 25 ℃, the deformation stage of the interface evolves back to *E* stage. That is, the magnitude of interfacial shear stress near the notch decreases with the further temperature increase. In summary, the thermal stress effect on the stress evolution near the notched section may be alleviated or accelerated depending on the temperature increase or decrease.

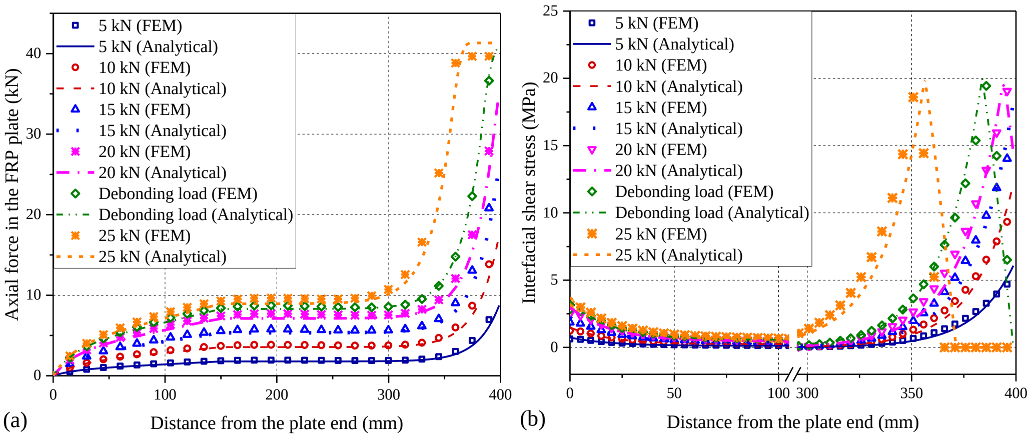

Fig. 5-7 Comparisons of analytical and FE results for the FRP-retrofitted steel beam under various mechanical loading levels: a) axial forces in the FRP plate; b) interfacial shear stresses.

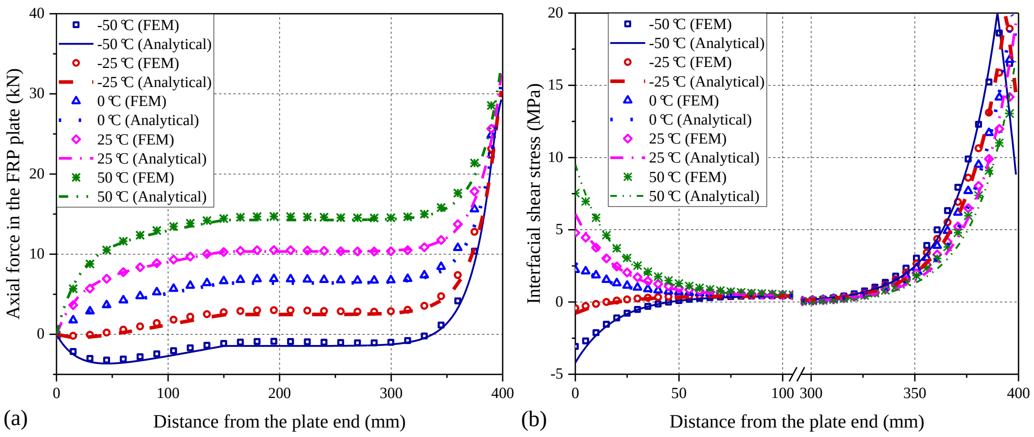

Fig. 5-8 Comparisons of analytical and FE results for the FRP-retrofitted steel beam under various levels of thermal loading: a) axial force in the FRP plate; b) interfacial shear stresses.

Fig. 5-9 further compares the IC debonding loads of the FRP-retrofitted steel beam at various temperature variations. It is seen that the debonding load is improved with the temperature increase. This observation is similar to the finding reported by (Gao *et al.* 2012, 2015), in which the debonding load of the FRP-to-concrete bonded joint is increased with the service temperature increase. In addition, the good agreement in the debonding loads between the analytical results and the FE predictions demonstrates that the assumptions adopted in the present analytical solution are appropriate.

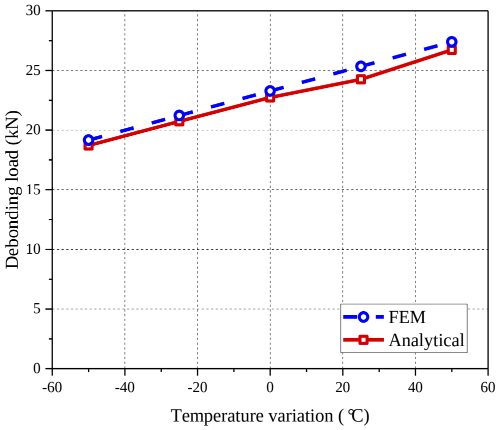

Fig. 5-9 The debonding loads obtained at various service temperatures

5.4.2 Axial Force in the FRP Plate and the SIF at the Notch Tip

Fig. 5-10 shows the changes in the axial force and the SIF with the increase in the applied mechanical loading. The continuous curves in **Fig. 5-10a** and **Fig. 5-10b** represent the analytical results of the axial force in the FRP plate and the SIF at the notch tip with the mechanical loading increase, while the scatters are the corresponding FE predictions. Before the IC debonding, the axial force in the FRP plate and the SIF increase approximately linearly with the applied mechanical loading. After the FRP debonding initiates at the notched section, the FE predicted axial force in the FRP plate increases in a much lower rate, while the FE-predicted SIF increases dramatically. It shows that the onset of interfacial debonding leads to larger possibility of crack propagation in the steel beam. According to the analytical results, the load sustained by the FRP retrofitted steel beam increases dramatically after the onset of debonding, which is not the case in experiments (Deng *et al.* 2016). That is because at larger mechanical loading, the steel beam near the notch is possibly yielded because of the stress concentration. Such that, the elastic adherends assumption may not still hold. Therefore, the analysis in this chapter focuses the bond behavior before and around the onset of debonding.

Overall, the analytical results and the FE predictions agree with each other satisfactorily before the FRP debonding, which demonstrates that the analytical solution is capable of predicting the axial force in the FRP plate and the SIF at the notch tip during the *E* and *E*-*S* stages.

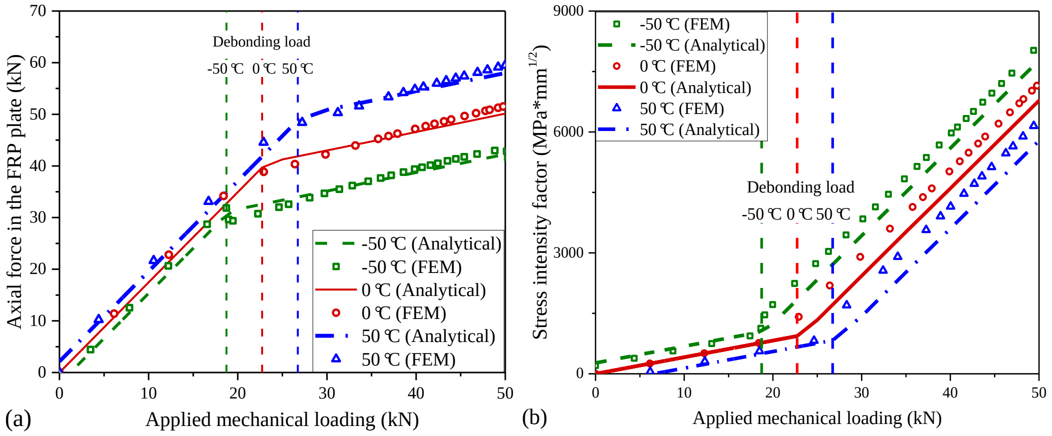

Fig. 5-10 Changes in the axial force and the SIF value: a) the axial force in the FRP plate at the notched section; b) the SIF value at the notch tip.

Fig. 5-11 illustrates the effects of thermal stress on the axial force in the FRP plate and the SIF for the beam under a constant mechanical loading of 15 kN at elastic stage, when the service temperature is changed from 50 ℃ lower (ΔT = -50 ℃) to 50 ℃ higher (ΔT = +50 ℃) than the ambient temperature. The axial force in the FRP plate at the notched section increases slightly with the temperature increase. A total 17.7% increase in the axial force is seen when the temperature variation ranges from -50 ℃ to 50 ℃. However, the corresponding SIF at the notch tip decreases almost 50%. The above observations lead to a conclusion that the thermal stresses induced by elevated temperatures have positive effects on the IC debonding load as well as the fatigue resistance of the FRP-retrofitted cracked steel beam. Furthermore, the FE predictions of the axial force in the FRP plate and the SIF at various service temperatures are also provided in **Fig. 5-11** to further verify the analytical solution. Only slight differences exist between the analytical and FE results, demonstrating the applicability of the analytical solution for predicting the debonding load and the SIF at the notch tip for the FRP-retrofitted steel beam subjected to various thermal loadings.

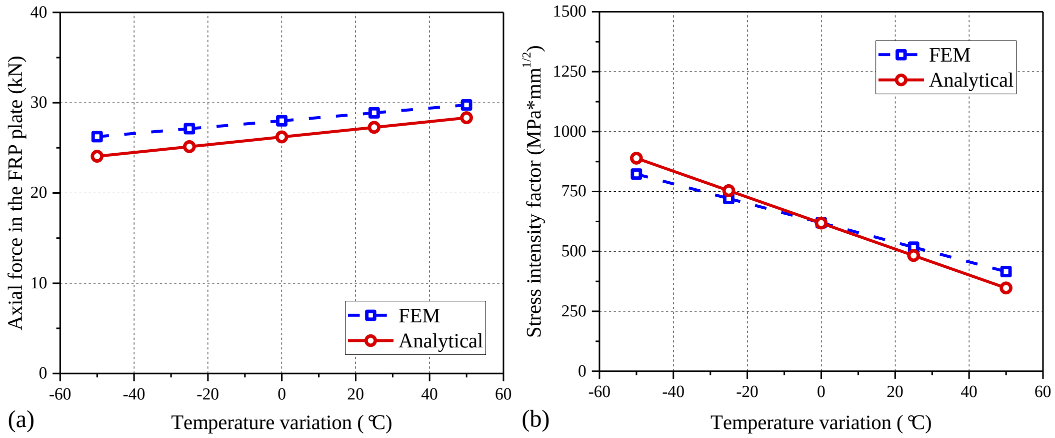

Fig. 5-11 Effects of temperature variation on the analytical results: (a) effect on the axial force in the FRP plate; (b) effect on the SIF at the notch tip.

5.5. PARAMETRIC STUDY

The proposed analytical solution is further used to carry out a parametric study, to investigate how the thickness and elastic modulus of FRP plate influence the IC debonding load and the SIF value at the notch tip in the FRP-retrofitted notched steel beam exposed to various service temperatures. **Fig. 5-12** and **Fig. 5-13** present the analytical results, which are normalized with the corresponding values obtained at ambient temperature (i.e., with a temperature variation equal to zero). The other parameters considered in the parametric study are assumed the same as those adopted in **Fig. 5-2** and the preceding sections.

Fig. 5-12 presents the effects of the thickness and the elastic modulus of the FRP plate on the IC debonding load of the FRP-retrofitted steel beam at various service temperatures. The debonding load increases with the service temperature elevation due to the thermal stress effect and vice versa. Moreover, a larger increase/decrease in the debonding load is observed when a thicker FRP plate with a higher elastic modulus is applied given the same temperature increase/decrease. For instance, the IC debonding load is decreased by 74% when the steel beam is retrofitted by a 2.8 mm thick FRP plate with an elastic modulus of 210 GPa and experiences a 50 ℃ temperature decrease. Such significant reduction should be approximately considered in practical FRP retrofit design of cracked steel beams. Unfortunately, there is a lack of proper design provisions to account for the thermal stress effect in the current codes of practice (e.g., ACI 440.2R-08 and the Chinese technical code GB-50608). The findings arisen from the current study may provide a theoretical background for future modification of the code provisions to account for the thermal stress effect.

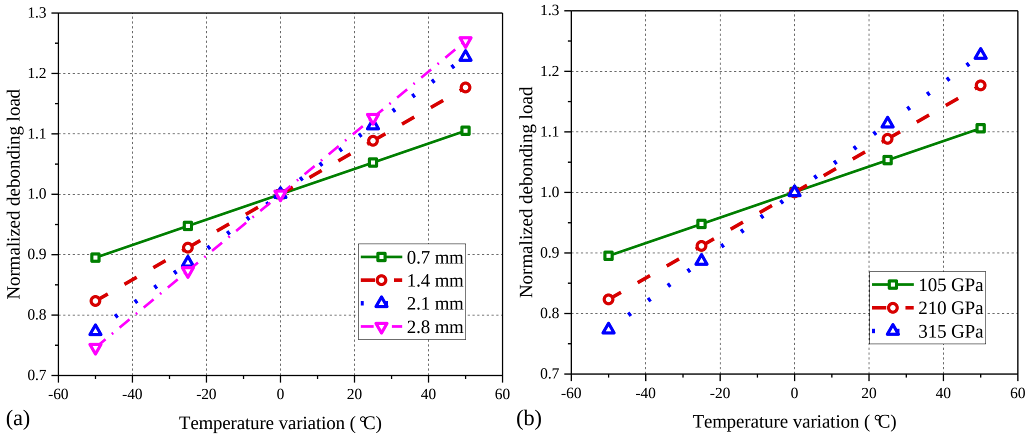

Fig. 5-12 Normalized debonding loads of FRP-retrofitted beams subjected to various thermal loadings: a) effect of the FRP plate thicknesses; b) effect of the FRP plate elastic modulus.

As shown in **Fig. 5-13**, the SIF at the notch tip of FRP-retrofitted steel beam decreases with the service temperature increase, when the mechanical loading applied on the beam is kept at a constant of 15 kN, at which the FRP-to-steel interface is found to be still in the *E* stage by checking the shear stress distributions along the bondline. Three different thicknesses (i.e., 0.7 mm, 1.4 mm and 2.1 mm) and three different elastic moduli (i.e., 105 GPa, 210 GPa and 315 GPa) of the FRP plate are considered in the parametric study. It is seen that the temperature increase leads to a decrease in the SIF value at the notch tip and thus an improvement of the fatigue behavior of the steel beam, especially when a thicker and stiffer FRP plate is used.

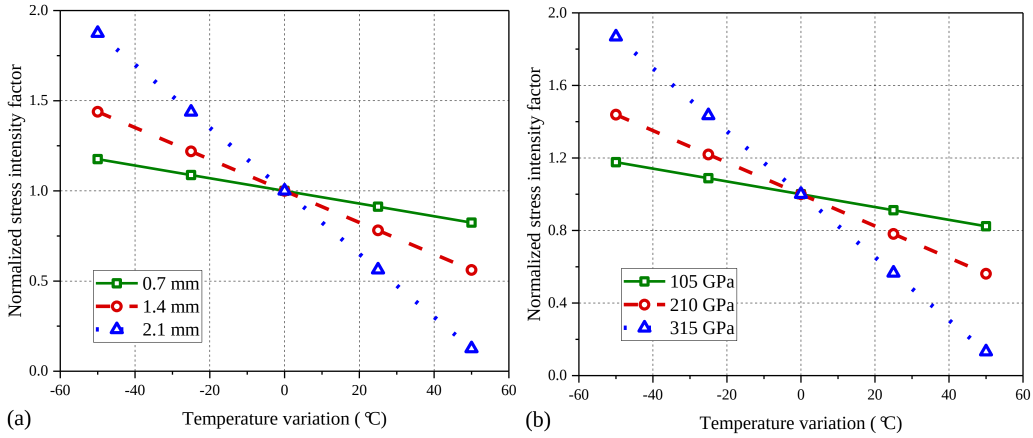

Fig. 5-13 Normalized SIF values for the beam subjected to various thermal loadings: a) effect of the FRP plate thicknesses; b) effect of the FRP elastic modulus.

5.6. CONCLUSIONS

This chapter presents a new analytical solution for investigating the thermal stress effects on the interfacial stress distribution, the IC debonding load and the SIF at the notch tip in an FRP-retrofitted notched steel beam subjected to combined thermal and mechanical loading. The analytical solution is validated through comparisons between the analytical and FE results. Based on the results presented in this chapter, the following conclusions can be drawn:

a) The thermal stress effects on the interfacial stress distributions and the SIF at the notch tip are significant, while they are neglected in current codes of practice of FRP-strengthened structures.

b) Regarding the IC debonding process occurred in the FRP-retrofitted steel beam under a specific level of mechanical loading, a temperature increase/decrease may alleviate or accelerate the interfacial stress concentrations, leading to an enhanced or declined IC debonding load, respectively.

c) The analytical results revealed that the SIF value at the notch tip decreases with the service temperature increase and vice versa, which should be appropriately considered in the fatigue strengthened of FRP-retrofitted cracked steel beams.

d) The thermal stress effects are more pronounced when a thicker and stiffer FRP plate is applied for the retrofitting purpose.

It should be noted that all the above observations in **Chapter 3, 4** and **5** are achieved upon the assumption of a constant bond-slip model of the FRP-to-steel interface. In reality, such a bond-slip model may vary with the service temperature (e.g., when the service temperature approaches the glass transition temperature of the bond adhesive). Further studies are recommended to calibrate the bond-slip models for FRP-to-steel interfaces, and then the proposed analytical solutions can be implemented with updated model parameters.

5.7. REFERENCES

Abaqus 6.14 (2014) "Documentation." Providence, RI, USA: Dassault Systemes Simulia Corporation.

American Concrete Institute (ACI). Guide for the design and construction of externally bonded FRP systems for strengthening concrete structures. ACI 440.2R-08, Farmington Hills, MI; 2008.

Chinese Technical Code. Technical code for infrastructure application of FRP composites. GB-50608, China Planning Press, Beijing; 2010.

Biscaia, H.C., and Ribeiro, P. (2019). "A temperature-dependent bond-slip model for CFRP-to-steel joints." *Composite Structures*, 217, 186-205.

Bocciarelli, M., Colombi, P., D'Antino, T., and Fava, G. (2018). "Intermediate crack induced debonding in steel beams reinforced with CFRP plates under fatigue loading." *Engineering Structures*.

Camanho, P.P., Davila, C.G., and de Moura, M.F. (2003). "Numerical simulation of mixed-mode progressive delamination in composite materials." *Journal of Composite Materials*, 37(16), 1415-1438.

Chen, F.L., and Qiao, P.Z. (2009). "Debonding analysis of FRP-concrete interface between two balanced adjacent flexural cracks in plated beams." *International Journal of Solids and Structures*, 46(13), 2618-2628.

Colombi, P., and Fava, G. (2015). "Experimental study on the fatigue behaviour of cracked steel beams repaired with CFRP plates." *Engineering Fracture Mechanics*, 145, 128-142.

Colombi, P., and Fava, G. (2016). "Fatigue crack growth in steel beams strengthened by CFRP strips." *Theoretical and Applied Fracture Mechanics*, 85, 173-182.

Colombi, P., Fava, G., and Sonzogni, L. (2015). "Fatigue crack growth in CFRP-strengthened steel plates." *Composites Part B-Engineering*, 72, 87-96.

Dai, J.G., Gao, W.Y., and Teng, J.G. (2015). "Finite element modeling of insulated FRP-strengthened RC beams exposed to fire." *Journal of Composites for Construction*, 19(2), 04014046.

Dai, J.G., Gao, W.Y., and Teng, J.G. (2012). "Bond-slip model for FRP laminates externally bonded to concrete at elevated temperature." *Journal of Composites for Construction*, 17(2), 217-228.

De Lorenzis, L., Fernando, D., and Teng, J.G. (2013). "Coupled mixed-mode cohesive zone modeling of interfacial debonding in simply supported plated beams." *International Journal of Solids and Structures*, 50(14-15), 2477-2494.

Deng, J., Jia, Y.H., and Zheng, H.Z. (2016). "Theoretical and experimental study on notched steel beams strengthened with CFRP plate." *Composite Structures*, 136, 450-459.

Deng, J., Lee, M.M.K., and Moy, S.S.J. (2004). "Stress analysis of steel beams reinforced with a bonded CFRP plate." *Composite Structures*, 65(2), 205-215.

Doroudi, Y., Fernando, D., Hosseini, A., and Ghafoori, E. (2021). "Behavior of cracked steel plates strengthened with adhesively bonded CFRP laminates under fatigue Loading: Experimental and analytical study." *Composite Structures*, 266.

Dunn, M.L., Suwito, W., and Hunter, B. (1997). "Stress intensity factors for cracked I-beams." *Engineering Fracture Mechanics*, 57(6), 609-615.

Gao, W., Teng, J., and Dai, J.G. (2012). "Effect of temperature variation on the full-range behavior of FRP-to-concrete bonded joints." *Journal of composites for construction*, 16(6), 671-683.

Gao, W.Y., Dai, J.G., and Teng, J.G. (2015). "Analysis of Mode II debonding behavior of fiber-reinforced polymer-to-substrate bonded joints subjected to combined thermal and mechanical loading." *Engineering Fracture Mechanics*, 136, 241-264.

Gao, W.Y., Dai, J.G., and Teng, J.G. (2016). "Fire resistance design of un-protected FRP-strengthened RC beams." *Materials and Structures*, 49(12), 5357-5371.

Ghafoori, E., and Motavalli, M. (2011). "Analytical calculation of stress intensity factor of cracked steel I-beams with experimental analysis and 3D digital image correlation measurements." *Engineering Fracture Mechanics*, 78(18), 3226-3242.

Ghafoori, E., Motavalli, M., Botsis, J., Herwig, A., and Galli, M. (2012). "Fatigue strengthening of damaged metallic beams using prestressed unbonded and bonded CFRP plates." *International Journal of Fatigue*, 44, 303-315.

Gholami, M., Sam, A.R.M., Yatim, J.M., and Tahir, M.M. (2013). "A review on steel/CFRP strengthening systems focusing environmental performance." *Construction and Building Materials*, 47, 301-310.

Hassein Abed, G. (2012). "Effects of temperature on the adhesive bonding in steel beams reinforced with CFRP composites." University of Southampton.

Hosseini, S.M., Melchior, J., Izadi, M., and Ghafoori, E. (2021). "Fatigue crack arrest in steel beams using FRP composites." *Engineering Failure Analysis*.

ACI 440.2R (2008). "Guide for the Design and Construction of Externally Bonded FRP Systems for Strengthening Concrete Structures." Structures Congress: 2008, 1-8.

Jones, S.C., and Civjan, S.A. (2003). "Application of fiber reinforced polymer overlays to extend steel fatigue life." *Journal of Composites for Construction*, 7(4), 331-338.

Klamer, E.L., Hordijk, D.A., and Hermes, M.C.J.H. (2008). "The influence of temperature on RC beams strengthened with externally bonded CFRP reinforcement." *Heron*, 53(3), 157-185.

Sahin, M.U., and Dawood, M. (2016). "Experimental Investigation of Bond between High-Modulus CFRP and Steel at Moderately Elevated Temperatures." *Journal of Composites for Construction*, 20(6), 04016049.

Silva, M.A.G., and Biscaia, H. (2008). "Degradation of bond between FRP and RC beams." *Composite Structures*, 85(2), 164-174.

Stratford, T., and Cadei, J. (2006). "Elastic analysis of adhesion stresses for the design of a strengthening plate bonded to a beam." *Construction and Building Materials*, 20(1-2), 34-45.

Stratford, T.J., and Bisby, L.A. (2012). "Effect of Warm Temperatures on Externally Bonded FRP Strengthening." *Journal of Composites for Construction*, 16(3), 235-244.

Teng, J.G., Fernando, D., and Yu, T. (2015). "Finite element modelling of debonding failures in steel beams flexurally strengthened with CFRP laminates." *Engineering Structures*, 86, 213-224.

Teng, J.G., Yu, T., and Fernando, D. (2012). "Strengthening of steel structures with fiber-reinforced polymer composites." *Journal of Constructional Steel Research*, 78, 131-143.

Teng, J.G., Yuan, H., and Chen, J.F. (2006). "FRP-to-concrete interfaces between two adjacent cracks: Theoretical model for debonding failure." *International Journal of Solids and Structures*, 43(18-19), 5750-5778.

Wang, H.T., and Wu, G. (2018). "Crack propagation prediction of double-edged cracked steel beams strengthened with FRP plates." *Thin-Walled Structures*, 127, 459-468.

Wang, J.L. (2006). "Cohesive zone model of intermediate crack-induced debonding of FRP-plated concrete beam." *International Journal of Solids and Structures*, 43(21), 6630-6648.

Yu, Q.Q., and Wu, Y.F. (2018). "Fatigue retrofitting of cracked steel beams with CFRP laminates." *Composite Structures*, 192, 232-244.

Yu, Q.Q., and Wu, Y.F. (2017). "Fatigue Strengthening of Cracked Steel Beams with Different Configurations and Materials." *Journal of Composites for Construction*, 21(2).

Yu, Q.Q., Zhao, X.L., Chen, T., Gu, X.L., and Xiao, Z.G. (2014a). "Crack propagation prediction of CFRP retrofitted steel plates with different degrees of damage using BEM." *Thin-Walled Structures*, 82, 145-158.

Yu, Q.Q., Zhao, X.L., Xiao, Z.G., Chen, T., and Gu, X.L. (2014b). "Evaluation of Stress Intensity Factor for CFRP Bonded Steel Plates." *Advances in Structural Engineering*, 17(12), 1729-1746.

Zeng, J. J., Gao, W. Y., and Liu, F. (2018). "Interfacial behavior and debonding failures of full-scale CFRP-strengthened H-section steel beams." *Composite Structures*, 201, 540-552.

Zhou, H., Fernando, D., Torero, J.L., Torres, J.P., Maluk, C., and Emberley, R. (2020). "Bond Behavior of CFRP-to-Steel Bonded Joints at Mild Temperatures: Experimental Study." *Journal of Composites for Construction*, 24(6), 04020070.

CHAPTER 6

BOND BEHAVIOR OF CFRP-TO-STEEL BONDED JOINTS AT DIFFERENT SERVICE TEMPERATURES: EXPERIMENTAL STUDY AND FE MODELING

6.1. INTRODUCTION

Externally bonded (EB) carbon fiber-reinforced polymer (CFRP) composites are widely used to strengthen and retrofit steel structures using wet layup techniques. The composite action between EB CFRP plates and steel substrates is heavily dependent on their bond behavior. Since the strengths of the adherends (steel and CFRP) are much higher than that of the bonding adhesive, the failure of the strengthening system always occurs at the bond interface, which is referred to as debonding failure (Teng *et al.* 2012; Zhao and Zhang 2007). Therefore, the structural behaviors of EB CFRP-strengthened steel structures depend on the mechanical properties of the adhesives used to bond the CFRP plates to the existing steel structures.

Another key issue of CFRP-strengthened steel structures is their durability and resistance to harsh environments. Among the environmental factors that may adversely affect the behaviors of CFRP-strengthened steel structures, temperature effects should be appropriately considered during the strengthening design and highlighted in the existing literature (Gholami *et al.* 2013). This is because the service temperatures of CFRP-strengthened steel structures may vary significantly due to seasonal and diurnal temperature changes. Sometimes, when the surface of the CFRP plate is directly exposed to solar radiation (such as in the strengthened steel structures used in outdoor applications), it is possible to obtain relatively high service temperatures (i.e., around 60 ℃) at the bond interface, which are much higher than the room temperature of the air (Stratford and Bisby 2012). In addition, the EB CFRP-strengthened steel structures may suffer from severe cold environments in winter, especially when used in high latitudes (Green *et al.* 2006; Yoshitake *et al.* 2014).

The adhesives widely used to bond CFRP plates to steel structures are usually epoxy resins, mainly because of their excellent mechanical properties and workability. Apart from the preceding advantages, however, the material properties of conventional epoxy adhesives are sensitive to service temperature variations. At relatively high service temperatures, epoxy adhesives may change from a solid-state to a softened and viscous state. For commercially available epoxy resins used in the strengthening applications, the reported glass transition temperature is typically 40~60 ℃ (Heshmati *et al.* 2015; Ke *et al.* 2020). When the epoxy adhesives are subjected to service temperatures close to the glass transition temperature, their strength and stiffness may be significantly reduced. Also, epoxy adhesives may become brittle at low service temperatures, possibly leading to stress concentrations at the bond interface due to the increased stiffness and reduced deformability of epoxy adhesives. Therefore, the debonding load (also referred to as "bond strength" or "ultimate load" in the literature) of the EB CFRP plate and the steel substrate can be severely affected by the service temperature variations. In addition to the mechanical property changes of epoxy resins, interfacial thermal stresses may be generated during service temperature variations due to the different coefficients of thermal expansion (CTEs) of steel and CFRP materials. The existing studies have only investigated the thermal stress effects through analytical solutions and finite element (FE) modelings (Gao *et al.* 2012; Gao *et al.* 2015; Zhou *et al.* 2019). The results have indicated that the interfacial thermal stresses were possibly in the same or opposite directions with that generated by the mechanical loading and consequently decrease or increase the debonding load of the bond interface.

6.2. EXISTING EXPERIMENTAL AND ANALYTICAL STUDIES

A few CFRP-to-steel bonded joints (Al-Shawaf *et al.* 2009; Biscaia and Ribeiro 2019; Chandrathilaka *et al.* 2019; He *et al.* 2020; Ke *et al.* 2020; Li *et al.* 2016; Liu *et al.* 2014; Nguyen *et al.* 2011; Zhou *et al.* 2020) were tested under combined pull-out loads and high temperature variations (i.e., thermal loadings) in the literature, aiming to study the temperature-dependent bond properties of the CFRP-to-steel interface. For example, Zhou *et al.* (2020) carried out CFRP-to-steel single-lap shear tests at service temperatures from 25 ℃ to 55 ℃. The test results showed that the initial stiffness and peak shear stress of the bond interface decreased at high service temperatures. However, the interfacial fracture energy increased with the temperatures up to 47.5 ℃ and then reduced with the further temperature increase. Biscaia *et al.* (2019) reported an average

65.9% reduction in the debonding load for the bonded joints tested at high temperatures of 80 ℃ and 95 ℃ compared to the results obtained at 20 ℃. Meanwhile, a 90.1% decrease in the peak shear stress and a 61.0% decrease in the ultimate slip were observed. Similar phenomena were also reported in other single- or double-lap shear tests (Al-Shawaf *et al.* 2009; Chandrathilaka *et al.* 2019; He *et al.* 2020; Ke *et al.* 2020; Li *et al.* 2016; Liu *et al.* 2014; Nguyen *et al.* 2011).

Heshmati *et al.* (2015) collected the results from some previous bonded joint tests (Al-Shawaf *et al.* 2009; Al-Shawaf 2010; Nguyen *et al.* 2011), which showed that the initial (elastic) stiffnesses of the bond interface decreased from room temperature to T_g-5 ℃ (T_g was the glass transition temperature of the bonding adhesive), while the debonding loads maintained almost unchanged within the temperature range. However, when the exposure temperatures were higher than T_g-5 ℃, the debonding loads and elastic stiffnesses of the bond interface gradually decreased with average rates of 3.3% and 4.4% per degree Celsius, respectively. In contrast, the CFRP-to-steel double- or single-lap shear tests at decreased temperatures (i.e., low service temperatures changed from curing temperature under ambient conditions) are limited (Al-Shawaf and Zhao 2013). The results of the double- or single-lap shear tests showed that the elastic stiffness and peak shear stress of the bond interface remained nearly constant or increased slightly at decreased temperatures. Similar observations were also reported for the bond interface between EB FRP and concrete or other substrates when epoxy resins were used as the bonding adhesives (Di -Tommaso *et al.* 2001; Park *et al.* 2010; Yao *et al.* 2016; Zhang *et al.* 2010). Moreover, the debonding load of the joint was related to the interfacial fracture energy (defined as the area enclosed by the shear stress versus the interfacial slip relationship) if the bond length was sufficiently long and larger than the effective bond length (i.e., the length beyond which the debonding load of the joint would not increase any further). However, it was observed that the deformability of epoxy resins decreased significantly at low service temperatures, resulting in brittle bond failures (Al-Shawaf and Zhao 2013; Park *et al.* 2010; Zhang *et al.* 2010) and reduced interfacial fracture energy (Zhang *et al.* 2010). In addition to the experimental studies, some analytical solutions were proposed to predict the full-range deformation behavior of FRP-to-concrete bonded joints under combined thermal and mechanical loadings (Biscaia 2019; Gao *et al.* 2012; Gao *et al.* 2015). These analytical approaches are also applicable to CFRP-to-steel bonded joints and can help to isolate the effect of interfacial thermal stresses from changes in bond properties, since only the latter should be appropriately taken into account when developing temperature-dependent bond-slip models of the bond interfaces (Dong and Hu 2016; Jia *et al.* 2021).

From the literature review work described above, it is clear that the majority of the bonded joint tests are carried out at increased temperatures (i.e., representing ambient conditions where the service temperatures are much higher than the curing temperature), while there is lacking bonded joint tests of the CFRP-to-steel interface at decreased temperatures (i.e., lower winter service temperatures). More importantly, reliable bond-slip models for CFRP-to-steel interfaces at different service temperatures are lacking in the literature, mainly because the local bond-slip relationships of the bond interfaces tested in previous studies have not been reported in detail. This chapter presents a comprehensive experimental study on the CFRP-to-steel double-lap shear tests at increased and decreased service temperatures. The experimental results of debonding loads and strain distributions of the CFRP plate at different service temperatures are investigated and compared. The latter is used to derive the local bond-slip model of the CFRP-to-steel interface at different service temperatures. Then, a finite element (FE) model is developed to predict the bond behavior of the CFRP-to-steel interface under mechanical loading and temperature variations, in which the preceding bond-slip model is used to define the local shear stress versus the interfacial slip relationships of the interface at different service temperatures. The proposed FE model is validated by the double-lap shear tests in this chapter and then used to further study the temperature effects on the interfacial shear stress distributions and the debonding loads of the bonded joints at different service temperatures.

6.3. EXPERIMENTAL PROGRAM

6.3.1 Material Properties

A series of CFRP-to-steel double-lap bonded joint tests were carried out at five different service temperatures of -20 ℃, 0 ℃, 30 ℃, 45 ℃ and 60 ℃, and accordingly, the specimens were named as JT-20, JT0, JT30, JT45 and JT60, respectively. At each service temperature, three duplicated specimens were prepared and identified by a letter of “A”, “B” or “C” after the specimen designation. These five different temperatures were determined to reflect possible service temperature variations that CFRP-strengthened steel structures may encounter in different regions of China (Zhou *et al.* 2022). **Fig. 6-1** shows the geometric dimensions of the double-lap bonded joint, which consists of two separate steel plates jointly bonded with CFRP plates on both surfaces. The length of the two CFRP plates was 340 mm and the bond lengths were 150 mm on each steel plate, leaving a gap of 40 mm between the two ends of the steel plates (see **Fig. 6-1** for more details).

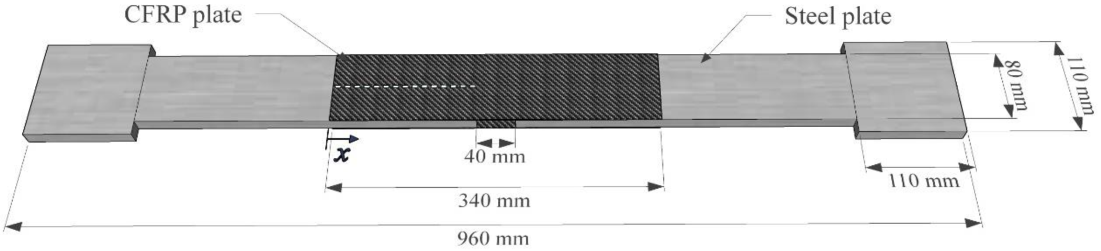

Fig. 6-1 Geometric dimensions of the double-lap bonded joint

The steel plates were made of Q235 steel with a thickness of 15 mm, and the width of the bonding area was 80 mm. The two ends of the steel plate were wider (i.e., 110 mm) and used to apply the pull-out force from the grip by friction. The nominal thickness of the CFRP plate was 1.5 mm. The elastic modulus and ultimate strain were measured as 141.9±0.9 GPa and 13050±26 με as per ASTM D3039 (2017). In addition, the elastic modulus, yielding stress and tensile strength of the steel were determined to be 204.6±3.2 GPa, 225.9±2.9 MPa and 370.5±7.6 MPa as per ASTM A370 (2017), with the dimensions shown in **Fig. 6-2**. The thermal expansion coefficients of CFRP plate and steel were measured as $4.2\times10^{-6}/℃$ and $10.4\times10^{-6}/℃$ according to the test standard of ISO 11359 (1999).

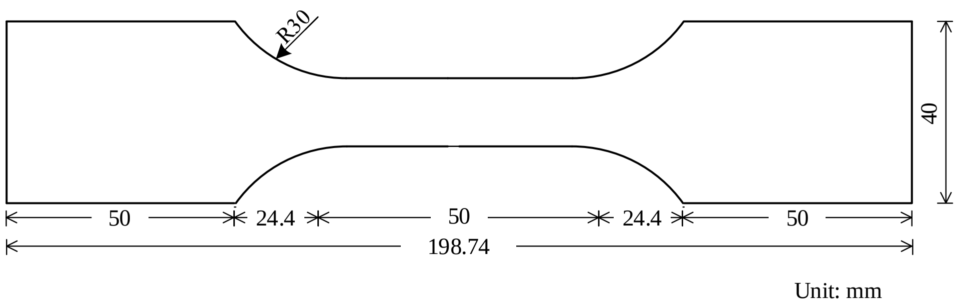

Fig. 6-2 The dimensions of the steel coupons

The bonding adhesive used in the double-lap shear tests was Sikadur-330CN adhesive. According to the brochure provided by the manufacturer, the tensile strength and elastic modulus of the adhesive at room temperature were 49.7 MPa and 2.55 GPa, respectively. The T_g value of the adhesive was measured by dynamic mechanical analysis (DMA) as per ASTM D7028 (2007). It is noteworthy that there are three different methods usually used to define the T_g value, including the T_g-onset method, the peak in the loss modulus curve and the peak in the tan(δ) curve. A full description of these definitions is beyond the scope of the current study and more details can be found in Gao *et al.* (2018) and Maluk *et al.* (2011). The T_g values using the T_g-onset method, the peak in the loss modulus curve and the peak in the tan(δ) curve are determined as 56.25 ℃, 60.2 ℃ and 69.7 ℃, respectively.

6.3.2 Strengthening Applications

The surface of the steel plate was prepared following the procedures given by standard SSPC-SP5. First, the surfaces of the steel plates were smoothened using a steel grinder, in order to remove the surface imperfections. Then, the steel surfaces were degreased with acetone in accordance with SSPC-SP1. Thereafter, the sandblasting method was adopted to remove the oxide coating (**Fig. 6-3a**). According to the suggestion specified in Fernando *et al.* (2013), angular alumina grits with a diameter of 0.25 mm were used for sandblasting to ensure the chemical compatibility of the steel surfaces with the bonding adhesive. In addition, the blasting angle was controlled at about 75 ° (Amada 2000), and the pressure was maintained at around 0.4-0.6 MPa. After sandblasting, the residual surface dust was cleaned by using compressed air. Before bonding to the steel surfaces, the CFRP plates were carefully washed with acetone using gauze. Then, the CFRP plates were bonded to the steel surfaces within half an hour to avoid oxidation of the steel surfaces. As Deng and Lee (2007) recommended, more adhesives were laid along the center than the outer edges, which allowed air trapped between the adherends to be easily escaped when they were pushed together. The excess adhesives along the edges of the plate were scraped off, collected and weighted. The average epoxy weight per side of the bonded joint was 11.4 g, and the average thickness was determined as 0.37 mm by dividing the weight by the epoxy density. The bonded joints were cured at room temperature for at least two weeks after the strengthening application was completed. During the curing process, the uniform thickness of the adhesive layer was maintained by applying consistent compressive stress of approximately 4.2 kPa on the top surface of the CFRP plate (by applying a weight as shown in **Fig. 6-3b**). Such a curing method was also used by Zeng *et al.* (2018) and Colombi *et al.* (2015) for the preparation of the CFRP-strengthened steel beams.

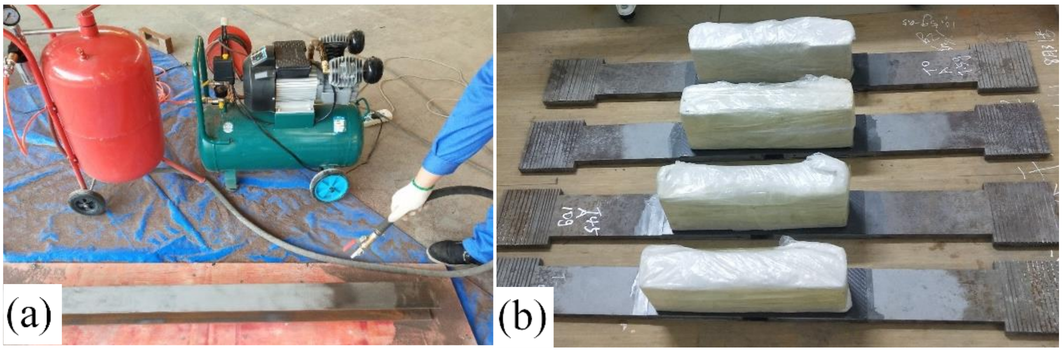

Fig. 6-3 Preparation of the specimens: (a) sandblasting; (b) curing.

6.3.3 Loading Scheme and Instrumentation

Fig. 6-4 shows the test setup and environmental chamber used for the double-lap shear tests. The environmental chamber was equipped with several internal insulation panels to reduce possible heat exchange between it and the surrounding air. During the tests, high service temperatures were achieved by the heating pipes, while low service temperatures were obtained using liquid nitrogen. Three thermocouples were mounted at various locations on each bonded joint, including two end zones of each specimen and mid-height of the CFRP plate, to ensure that the bonded joint reached a uniform temperature equal to the target service temperature.

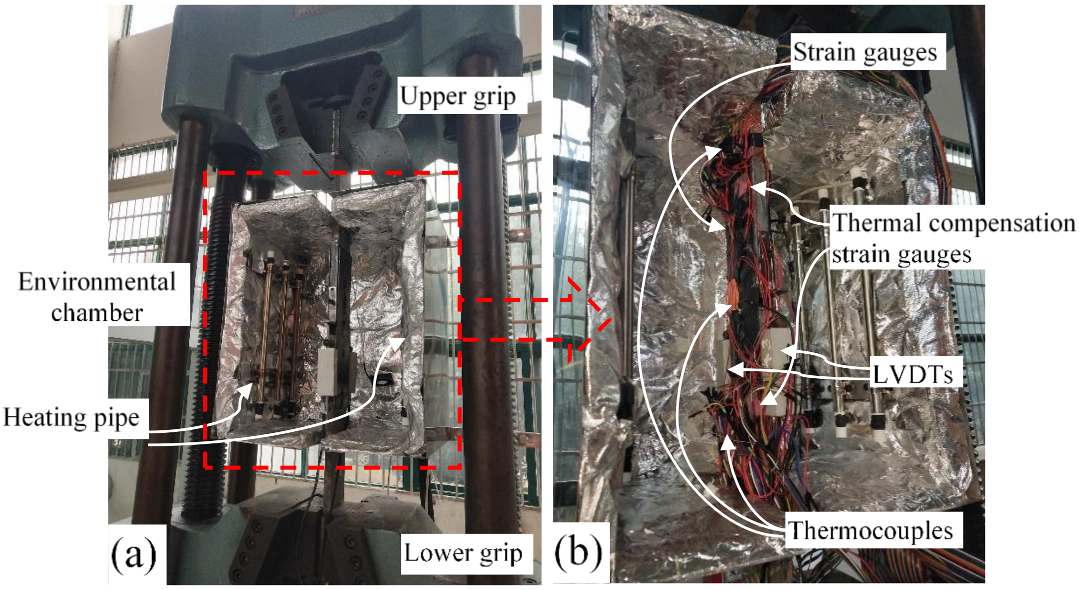

Fig. 6-4 Test setup and environmental chamber: a) overview; b) inside view.

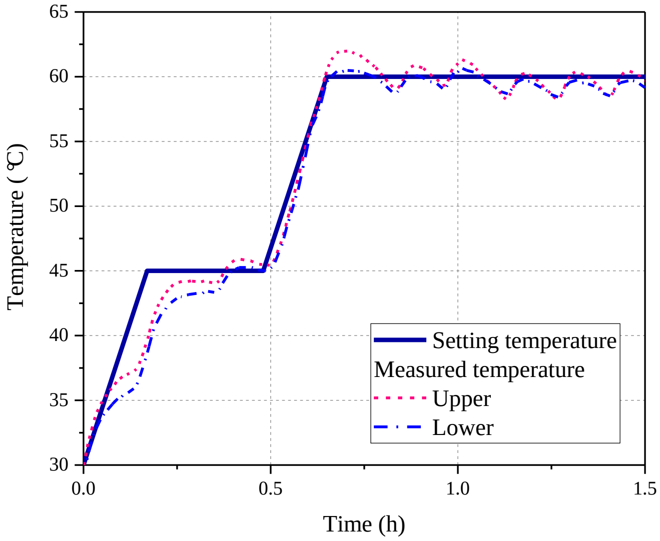

Fig. 6-5 Measured temperature history of the CFRP-retrofitted steel beam during the heating process.

Fig. 6-5 shows the variation of temperatures for the specimen tested at 60 ℃, which were measured at different locations of specimens. It can be seen that the temperatures measured by both upper and lower thermal couples were quite close to each other and changed gradually following the set temperature. After the measured temperatures reached the target value, the air temperature inside the chamber was regulated at a nearly constant value for at least 30 minutes, to ensure that the temperature was uniformly distributed in the specimen.

At each service temperature, a number of strain gauges were bonded to the surfaces of the CFRP plate in the first specimen of three duplicates to measure the strain distributions in the CFRP plate. The arrangement and detailed locations of the strain gauges are shown in **Fig. 6-6**. The first strain gauge was located 5 mm from the plate end, and the others were spaced at 10 mm intervals apart (**Fig. 6-6**). The other two strain gauges from the same batch were bonded to TiS glasses and placed near the joint to account for thermal compensation. As shown in **Fig. 6-6**, two LVDTs were attached to the adjacent ends of two steel plates with a gap of 40 mm to measure the relative displacement. Therefore, the measured displacements consisted of two parts, including the sum of the interfacial shear slips at the two loaded ends and the axial deformation of the 40 mm unbonded length of the CFRP plate. Therefore, half of the measured relative displacement minus the axial deformation of the 20 mm CFRP plate was considered to be the slip at the loaded end of the bonded joint under combined thermal and mechanical loadings.

The testing procedure was divided into two steps. First, the bonded joint was placed in the environmental chamber with the upper end held by the loading grip. Then the heating pipe or liquid nitrogen pump was started to increase or decrease the chamber temperature to the target service temperature. The pull-out loading was applied within 30 min after the measured temperatures were stabilized at the target temperature and evenly distributed across the different positions recorded by the thermocouples. The pull-out load was applied by the lower grip at a speed of 2 mm/min.

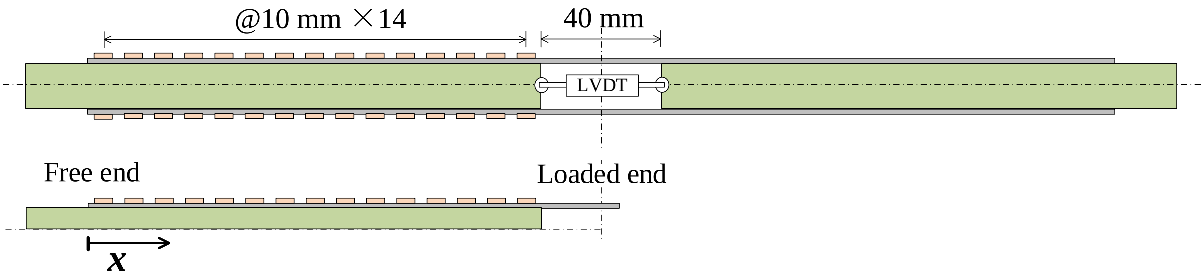

Fig. 6-6 Locations of strain gauges and LVDTs

6.4. RESULTS AND DISCUSSION

6.4.1 Failure Modes

Fig. 6-7 shows a typical failure mode of the bonded joints tested at different service temperatures from -20^{o}C to 45^{o}C, which was caused by the debonding failure at the bond interface and the localized delamination of the CFRP plate. This failure mode has demonstrated an excellent surface preparation of the steel substrate. However, when the service temperature was increased to 60^{o}C, the delamination zone of the CFRP plate became negligible, mainly due to the softening of the bonding adhesive at the high service temperature close to the glass transition temperature of the adhesive. Similar observations were also reported in the previous single- or double-lap shear tests of CFRP-to-steel bonded joints at high service temperatures (He *et al.* 2020; Nguyen *et al.* 2011). **Fig. 6-8** further compares the difference between the failure modes of JT0-A and JT60-A after the tests. It can be seen that a large number of burrs and adhesive fragments were attached to the debonded interface of JT0-A, and the observed failure progress was very brittle. In contrast, the debonded surface of JT60-A was relatively smooth because of the reduced elastic stiffness and softening behavior of the adhesive layer at 60^{o}C.

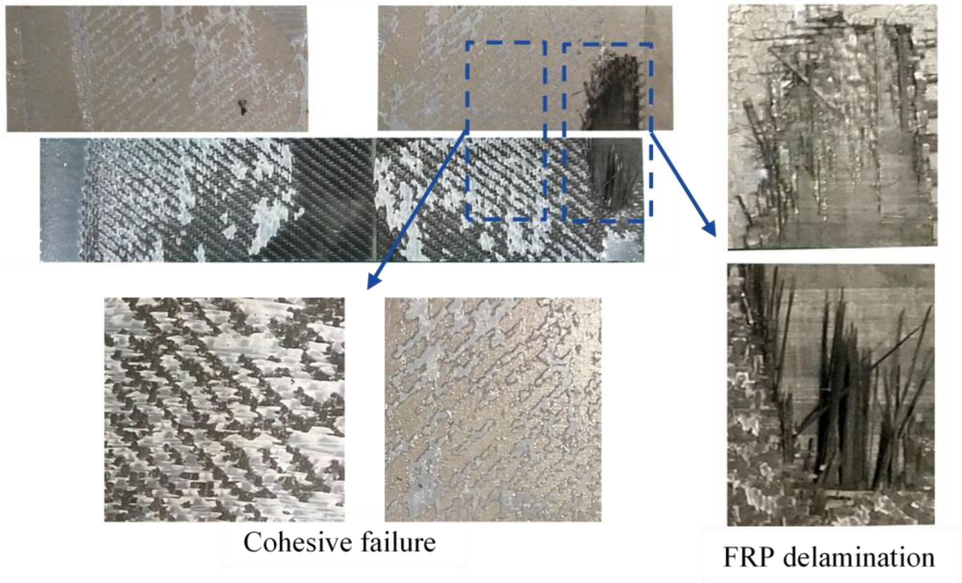

Fig. 6-7 Debonded interface of JT-20-A.

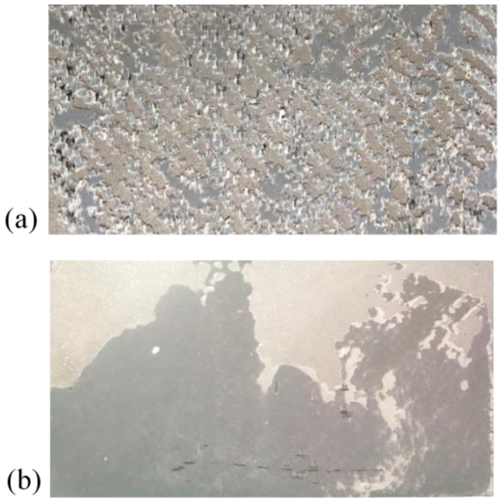

Fig. 6-8 Difference between the failure modes of: (a) JT0-A; and (b) JT60-A.

6.4.2 Results

Fig. 6-9 shows the changes of debonding loads for the CFRP-to-steel bonded joints tested at different service temperatures. In this figure, the existing single- or double-lap shear test results of CFRP-to-steel bonded joints reported in the literature (Al-Shawaf *et al.* 2009; Al-Shawaf and Zhao 2013; Biscaia and Ribeiro 2019; Chandrathilaka *et al.* 2019; He *et al.* 2020; Li *et al.* 2016; Nguyen *et al.* 2011; Zhou *et al.* 2020) are also presented for comparison. In addition, the glass transition temperatures of the bonding adhesives adopted in the literature are indicted in the figure. It can be seen that most of the existing tests were conducted at high service temperatures, as mentioned earlier. All the debonding loads are normalized by the corresponding average value measured at room temperature for a clear comparison. In **Fig. 6-9**, since different types of bonding adhesives were used in the tests of He *et al.* (2020) and Al-Shawaf *et al.* (2009, 2013), the debonding loads at different service temperatures are normalized by the average value of the joints obtained at room temperature for each type of adhesive, and the results of different types of adhesives are denoted by various symbols. In addition, only the specimens cured at room temperature in Chandrathilaka *et al.* (2019) are included in the figure for comparison. In addition, the glass transition temperatures of the bonding adhesives adopted in the literature are shown in the figure.

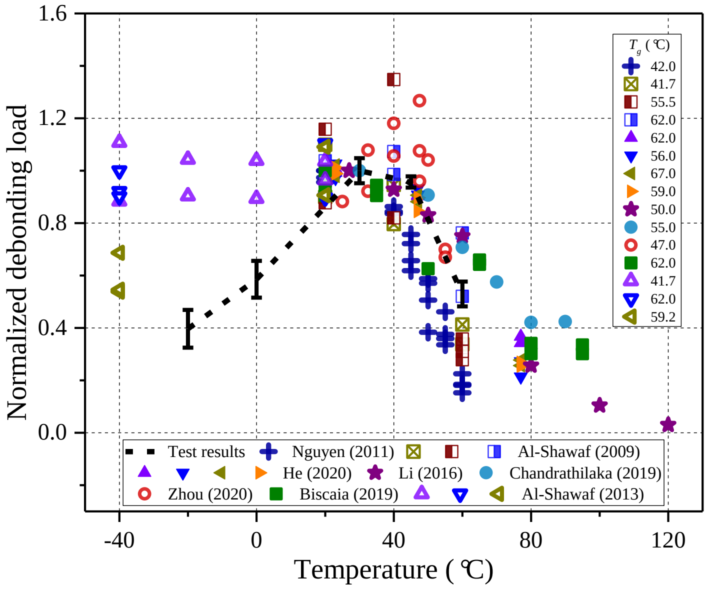

Fig. 6-9 Comparison of the normalized debonding loads at different service temperatures

In the present study, the debonding loads increased from -20 ℃ to 30 ℃ and then decreased with the further service temperature increase. The average debonding loads were reduced only slightly (i.e., 4.3%) from 30 ℃ to 45 ℃ and more significantly (i.e., 44.7%) from 45 ℃ to 60 ℃. The latter significant reduction of the debonding loads is attributed to the softening behavior of the adhesive layer at high service temperatures close to its glass transition temperature. Similar observations about the significant reduction of the debonding loads for the bonded joints tested at high service temperatures were also reported by other researchers (Al-Shawaf *et al.* 2009; Biscaia and Ribeiro 2019; Chandrathilaka *et al.* 2019; He *et al.* 2020; Li *et al.* 2016; Nguyen *et al.* 2011; Zhou *et al.* 2020), in which epoxy resins were used as the bonding adhesives. In comparison, the ultimate loads of CFRP-to-steel double-lap joints tested by Al-Shawaf and Zhao (2013) were quite different at decreased temperatures. Specifically, the ultimate loads of specimens bonded by Araldite*420 A/B and Sikadur*-30 displayed negligible bond strength differences between subzero and ambient exposures. While the bond strength showed around 69% decrease as the temperature decreased from 20 ℃ to -40 ℃. It was attributed to the different properties of the bonding adhesive. In the present test, the debonding loads of the joints decreased significantly from the room temperature (i.e., 30 ℃ in this study) to low service temperatures (i.e., 0 ℃ and -20 ℃), which was very similar to the joints which are bonded by MBrace*Saturant bonding adhesive (Shawaf and Zhao, 2013). Therefore, the debonding load decrease was due to the reduction of the interfacial fracture energy and the effect of the interfacial thermal stresses. Such combined effects will be further examined and discussed in the following sections to clarify how they affect the bond behaviors of CFRP-to-steel bonded joints under combined mechanical and thermal loadings (i.e., service temperature variations).

Furthermore, current design guidelines recommend that the maximum service temperature (i.e., temperature limit) specified for FRP-strengthened structures should be less than T_g-15 ℃ (ACI 440.2R; Concrete society 2012). According to the above design guidance, the allowable maximum service temperature of the adhesive used in the present study should be 41^{o}C, 45^{o}C or 55^{o}C according to the T_g value determined by the T_g-onset method, the peak value of the loss modulus curve or the peak value of the tan(δ) curve, as described in **Section 6.3.1**. The test results in **Fig. 6-9** have indicated that the recommended maximum service temperature for practical FRP strengthening applications is generally safe when the T_g value is determined using the T_g-onset method or the peak in the loss modulus curve method. However, since the debonding loads were significantly reduced at 55^{o}C, this design guidance may not be conservative for practical FRP strengthening applications when the T_g value is determined as the peak in the tan(δ) curve (i.e., 55^{o}C in the current study). This suggests that more attention should be paid to the method used for determining the T_g value for practical strengthening applications. In addition, the significant reduction of the debonding loads at low service temperatures raise safety concerns for the applications of FRP-strengthened steel structures in cold regions.

Fig. 6-10 compares the load-displacement curves of the bonded joints tested at different service temperatures. Since the measured curves for the three duplicates tested at each temperature are similar (see **Fig. 6-19** for more details), only the results of the first specimen are included herein for a clear comparison. At low service temperatures of 0 ℃ and -20 ℃, the load-displacement curve exhibits an almost linear elastic response until the debonding failure of the CFRP plate. At service temperatures of 30 ℃ and 45 ℃, theload initially grows linearly with the displacement in the elastic stage. With a further increase in the displacement, a nonlinear load-displacement response appears and reaches a short load plateau and the load increase converges at the debonding failure. This load plateau indicates that the bond length used in the study was longer than the “effective bond length” of the bonded joint. However, this load plateau was not observed at 60 ℃, because such temperature led to the increase in the effective bond length (i.e., longer than 150 mm used in this study). The increase in the effective bond length at high service temperatures is mainly attributed to the decrease in elastic stiffness and the associated softening behavior of the bonding adhesive (Stratford and Bisby 2012; Zhou *et al.* 2020). Another reason for the increase in the effective bond length at high service temperatures is the effect of interfacial thermal stresses caused by the different CTEs of CFRP and steel plate, which requires a longer bond length to reach the load capacity (i.e., debonding load) as revealed by the analytical solution proposed by Gao *et al.* (2015). In addition, the initial slopes of the load-displacement curves were slightly larger at low service temperatures due to the increased elastic stiffness of the bond interface.

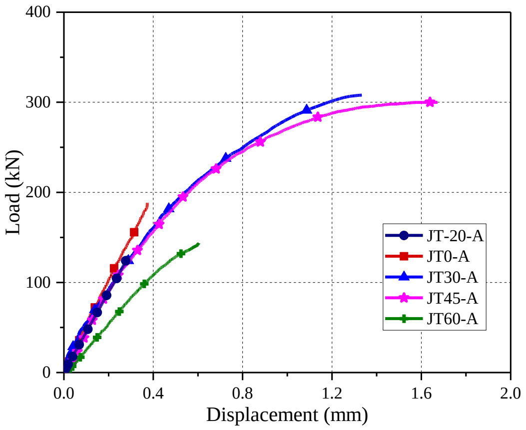

Fig. 6-10 Load-displacement curves of the bonded joints tested at different service temperatures

Fig. 6-11 shows the strain distributions in the CFRP plate of the bonded joint tested at 30 ℃, in which the x-axis originates from the free end (**Fig. 6-6**). It is evident that the strain values at each location grow with the applied pull-out loads. Furthermore, the CFRP strains increase monotonically from the free end (x=0 mm) to the loaded end (x=150 mm). At the ultimate state, the strain distribution curve is almost flat near the loaded end, indicating that the interfacial debonding of the CFRP plate occurred in the loaded end region. **Fig. 6-12** further compares the strain distributions in the CFRP plate for the joints tested at different service temperatures under the same load (i.e., 100 kN). It can be seen that the recorded CFRP strains near the loaded end (at x =145 mm) are very close, while the variation trends of the strain distributions along the bond length are dissimilar at different service temperatures. At low service temperatures, the strain distributions grow slowly from the free end and increase abruptly near the loaded end, whereas at 60 ℃ the CFRP strains are increased almost linearly from the free end to the loaded end. The different strain distributions should be due to diverse local bond-slip relationships of the bond interface at different service temperatures, which will be further examined in the next section.

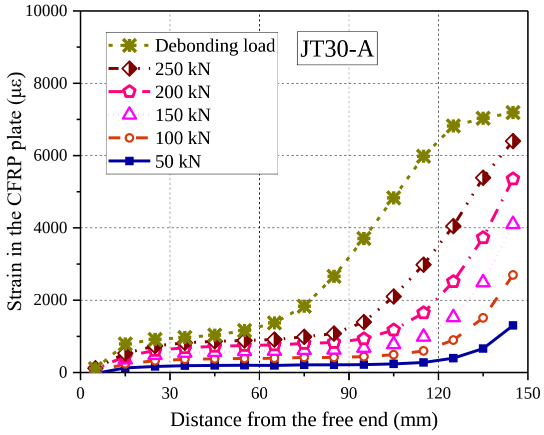

Fig. 6-11 Strain distributions in the CFRP plate of JT30-A.

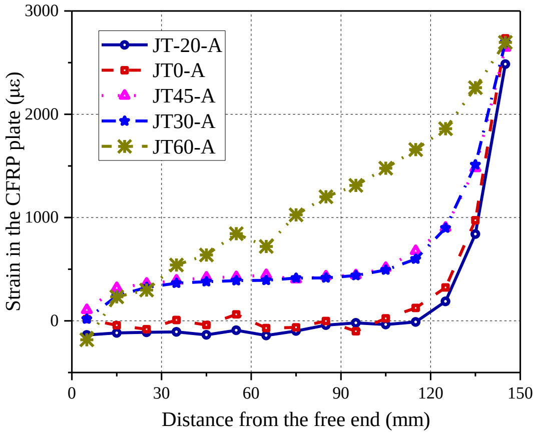

Fig. 6-12 Strain distributions in the CFRP plate at 100 kN.

6.4.3 Local Bond-slip Relationships

The interfacial bond stress ($\tau_{i+\frac{1}{2}}$) (i starts from the free end) between two subsequent strain gauges at the locations of x_i and x_{i+1} can be derived from the difference of the measured strains (i.e., $\varepsilon_{i+1} - \varepsilon_i$) by the following equation (Barris *et al.* 2018; Ko *et al.* 2014; Yang *et al.* 2017; Yu *et al.* 2012).

$$\tau_{i+\frac{1}{2}} = \frac{\varepsilon_{i+1}-\varepsilon_i}{x_{i+1}-x_i} E_f t_f \tag{6-1}$$

where E_f and t_f are the elastic modulus and thickness of the CFRP plate. The corresponding local interfacial slip can be calculated by integrating the CFRP strain from the zero point (where the measured CFRP strains of the two adjacent strain gauges are almost identical) to the relevant location as follows:

$$\delta_{i+\frac{1}{2}} = \sum_1^i \varepsilon_{f,i}(1+\alpha)\,(x_{i+1}-x_i) \tag{6-2}$$

Fig. 6-13 shows the local bond-slip relationships obtained from the double-lap shear tests at normal temperature. The dotted lines represent the results recorded at various locations along the CFRP plate, while the dashed lines are based on nonlinear regression analysis using the curve fitting toolbox provided by MATLAB software. The same data treatment approach was also used by the previous study to derive the local bond-slip relationships of the CFRP-to-steel interface (Zhou *et al.* 2020).

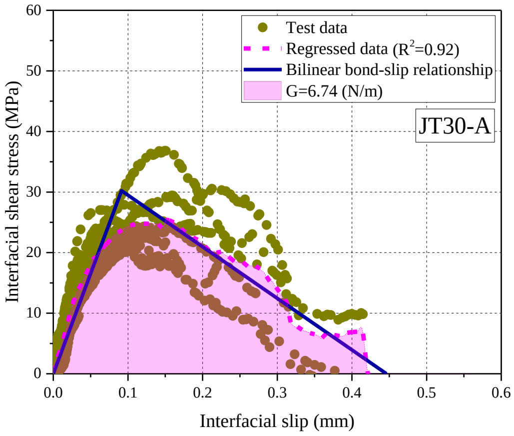

Fig. 6-13 Local bond-slip relationships obtained from the bonded joint tests of JT30-A.

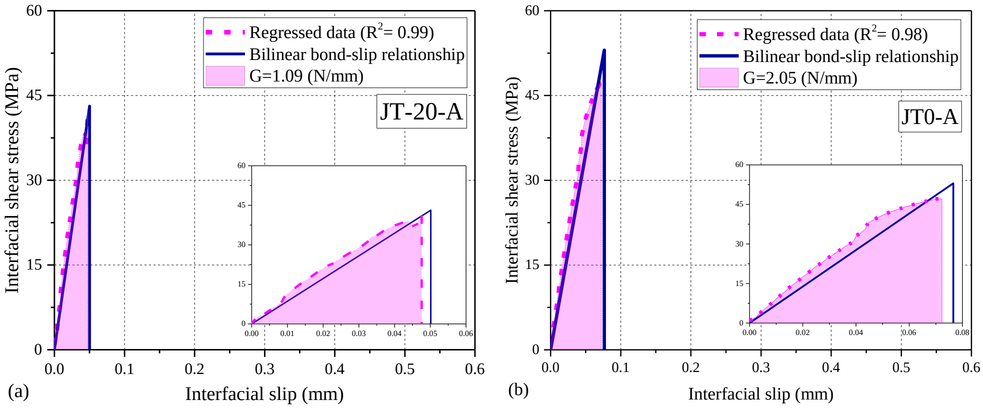

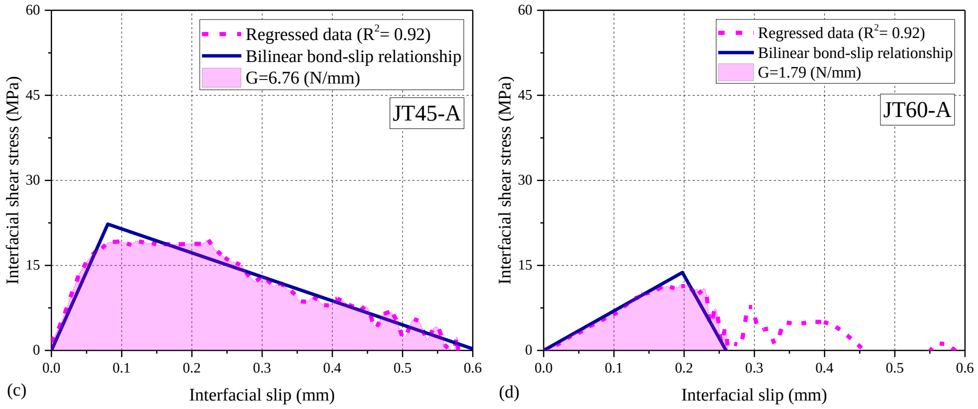

Fig. 6-14 Local bond-slip relationships obtained from the bonded joint tests: (a) JT-20-A; (b) JT0-A; (c) JT45-A; (d) JT60-A.

From the regressed curves shown in **Fig. 6-13** and **Fig. 6-14**, a bilinear relationship can be used approximately to describe the local bond-slip responses at different service temperatures. Indeed, due to the increased elastic stiffness of the bonding adhesive at low service temperatures, the local bond-slip relationships of the joints tested at -20 ℃ and 0 ℃ exhibit a very brittle behavior with an abruptly descending portion. That is, the bilinear bond-slip model can be simplified to an elastic-brittle model, as illustrated in **Fig. 6-14a** and **Fig. 6-14b**. **Fig. 6-15** depicts the bilinear bond-slip model used to describe the relationship between the shear stress and the interfacial slip, including elastic and softening portions (**Fig. 6-15a**). In the elastic stage (i.e., $\delta<\delta_0$ and $\tau<\tau_p$), the shear stress increases linearly with the interfacial slip with a constant slope of K_T. After reaching the peak shear stress (τ_p), the interfacial shear stress decreases linearly with the interfacial slip with a slope of K_T' until the interfacial debonding occurs at the slip δ_f.The interfacial fracture energy is defined as the area underneath the bond-slip curve (i.e., $G_f = \tau_p \delta_f / 2$). As mentioned earlier, at -20 ℃ and 0 ℃, the interfacial shear stress is observed to increase linearly to τ_p, followed by the CFRP debonding failure (i.e., $\delta_0 = \delta_f$), and thus the bond-slip model can be approximately described by the elastic-brittle model as shown in **Fig. 6-15b**.

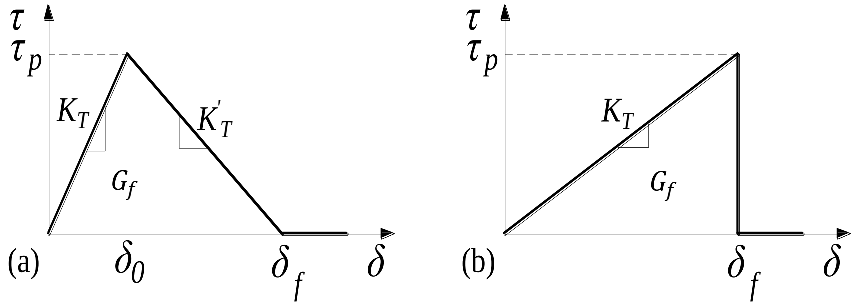

Fig. 6-15 Local bond-slip relationships: a) bilinear; b) elastic-brittle.

The area enclosed by the regressed shear stress-interfacial slip curve in **Fig. 6-14** is used to define the interfacial fracture energy for the local bond-slip model, while the slopes of the elastic and softening portions (K_T and K_T') are determined from the least-squares curve fitting of the regressed curve at each service temperature. For the joints tested at -20°C and 0°C, only the elastic stiffness (K_T) needs to be determined. **Table 6-1** summarizes all the bond properties of the CFRP-to-steel interface at different service temperatures obtained from the test results presented in **Fig. 6-14**. It can be seen that the elastic stiffness and peak shear stress are generally reduced with the service temperature increase, while the interfacial fracture energies at 30 ℃ and 45 ℃ are much higher than those obtained at other service temperatures.

Table 6-1 Bond properties of the interface at different service temperatures

Temperature (°C)	Elastic stiffness (MPa/mm)	Peak shear stress (MPa)	Interfacial fracture energy (N/mm)
-20	861	43.1	1.09
0	693	53.0	2.05
30	331	30.2	6.74
45	278	22.3	6.76
60	69.6	13.8	1.79

6.5. FINITE ELEMENT (FE) MODEL

6.5.1 Description of the FE Model

To gain insight into the temperature effects on the bond behavior of CFRP-to-steel bonded joints at different service temperatures, a two-dimensional finite element (FE) model was developed within the framework of Abaqus 6.14. The CFRP and steel plates were modeled by 4-node plane stress quadrilateral elements (CPS4R), while the adhesive layer was modeled by a 4-node cohesive element (COH2D4). The element sizes of the CFRP and steel plates as well as the adhesive layer were set as 0.2 mm. Due to the symmetry of the bonded joint, only a quarter of the joint was modeled (**Fig. 6-16**). The symmetrical boundary conditions in the vertical and horizontal directions were set on the right and bottom of the FE model, respectively. The room temperature was set to 30 ℃ as the initial step. The service temperature was defined as a second loading step using the predefined field variable, in which the entire joint was set as the same service temperature without considering the temperature gradient within the joint. This assumption was established corresponding to the final state after completing the service temperature change. Then, pull-out loads were applied using a displacement-controlled manner at the end of the steel plate. It should be noted that in the following chapters, the defined temperatures in the second and third steps were the experimental temperatures, rather than the magnitude of temperature variation (ΔT) as stated in previous chapters. While the temperature variation should be equal to the experimental temperature minus normal temperature.

In the FE model, the CFRP and steel plates were assumed to be isotropically elastic with the stiffnesses of 141.9 GPa and 204.6 GPa, respectively. The local bond-slip relationships of the CFRP-to-steel interface at different service temperatures were defined by the bond properties provided in **Table 6-1**. It is worth noting that for the FE modeling process of the joints tested at -20°C and 0°C, the stiffness of the softening portion (i.e., K_T') was defined by a sufficiently large value (i.e., 100 times of K_T) to avoid possible numerical convergence problems.

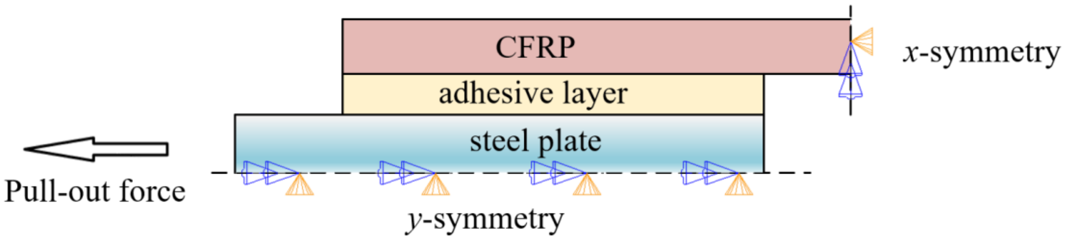

Fig. 6-16 FE model of the CFRP-to-steel bonded joint

6.5.2 *Validation of the FE Model*

6.5.2.1 Distribution of CFRP strains

Fig. 6-17 compares the CFRP strain distributions obtained from the double-lap shear tests and the FE predictions for the joints under different load levels and service temperatures. The excellent agreement between them has demonstrated the accuracy and reliability of the proposed local bond-slip model that can be used to describe the bond properties of the CFRP-to-steel interface at different service temperatures. At low service temperatures (e.g., -20°C and 0°C), the CFRP strains grow slowly from the free end and increase abruptly near the loaded end, mainly due to the high shear stiffness and elastic-brittle behavior of the bond interface at low service temperatures. At high service temperatures (e.g., 45°C and 60°C), the CFRP strains increase faster from the free end to the loaded end, and eventually a strain plateau is observed near the loaded end corresponding to the debonding failure of the CFRP plate. The strain distributions have indicated the nonlinear local bond-slip behavior of the bond interface at high service temperatures.

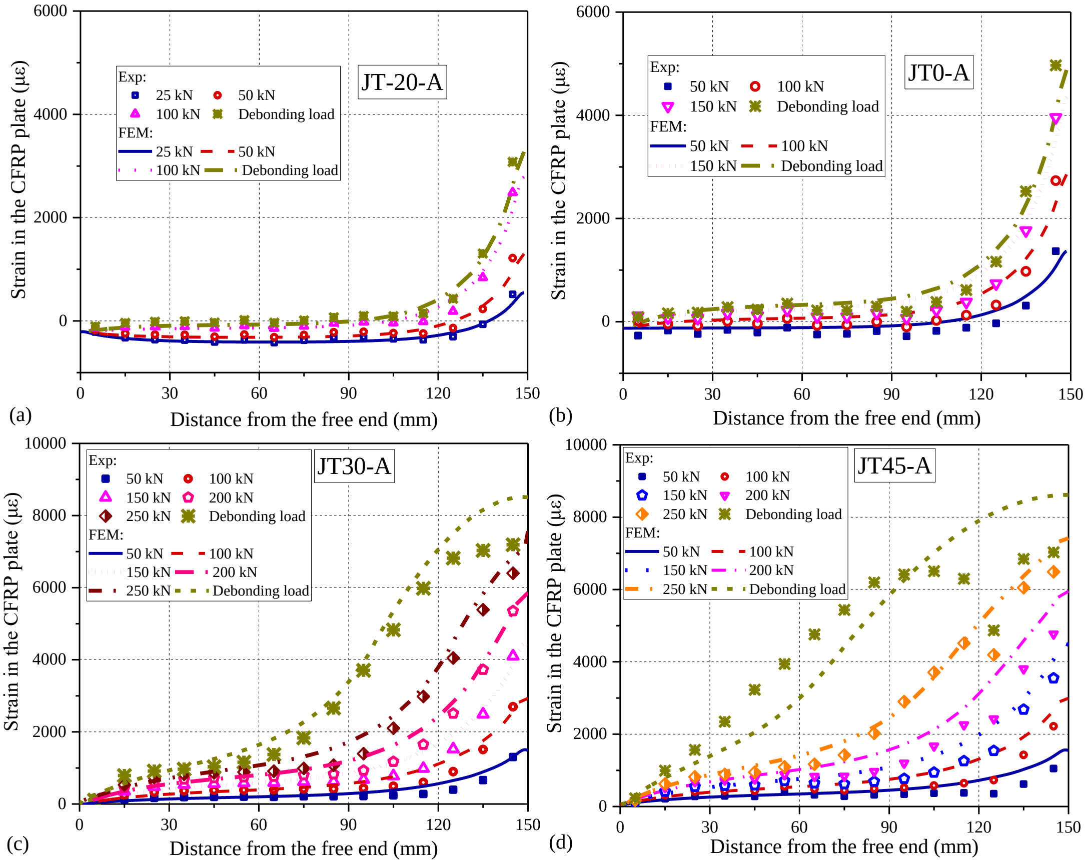

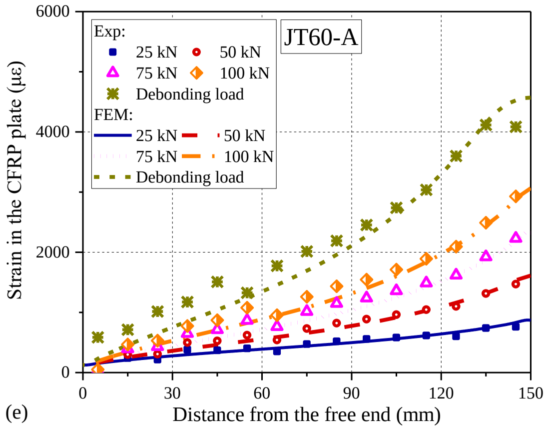

Fig. 6-17 Comparisons of CFRP strain distributions at different load levels obtained from the double-lap shear tests and the FE predictions: a) JT-20-A; b) JT0-A; c) JT30-A; d) JT45-A; e) JT60-A.

6.5.2.2 Distribution of interfacial shear stresses

Fig. 6-18 further compares the distributions of the interfacial shear stresses obtained from the double-lap shear tests and the FE model predictions. With the growth of the pull-out load, the bond interface undergoes two stages before the debonding failure, including elastic and elastic-softening stages. At low load levels, the interfacial shear stresses are increased monotonically from the free end to the loaded end, and the entire bond length is in the elastic stage. With the further increase of the pull-out load, the shear stress at the loaded end reaches the peak value and then decreases accordingly, and thus the bond interface enters the elastic-softening stage. Under the ultimate state, the debonding failure occurs at the loaded end of the CFRP plate. Overall, the FE predictions agree well with the test results, although the dispersion between them becomes relatively significant after the bond interface enters the softening stage. It is worth noting that before the pull-out load is applied (i.e., 0 kN), the interfacial shear stresses are distributed almost symmetrically due to the imposition of the service temperature (**Fig. 6-18 a,b,d and e**). The thermal stresses generated near the loaded end at low service temperatures are positive and vice versa, resulting in significant effects on the bond behavior and the associated debonding loads of the joint at different service temperatures, which will be further discussed in the next section.

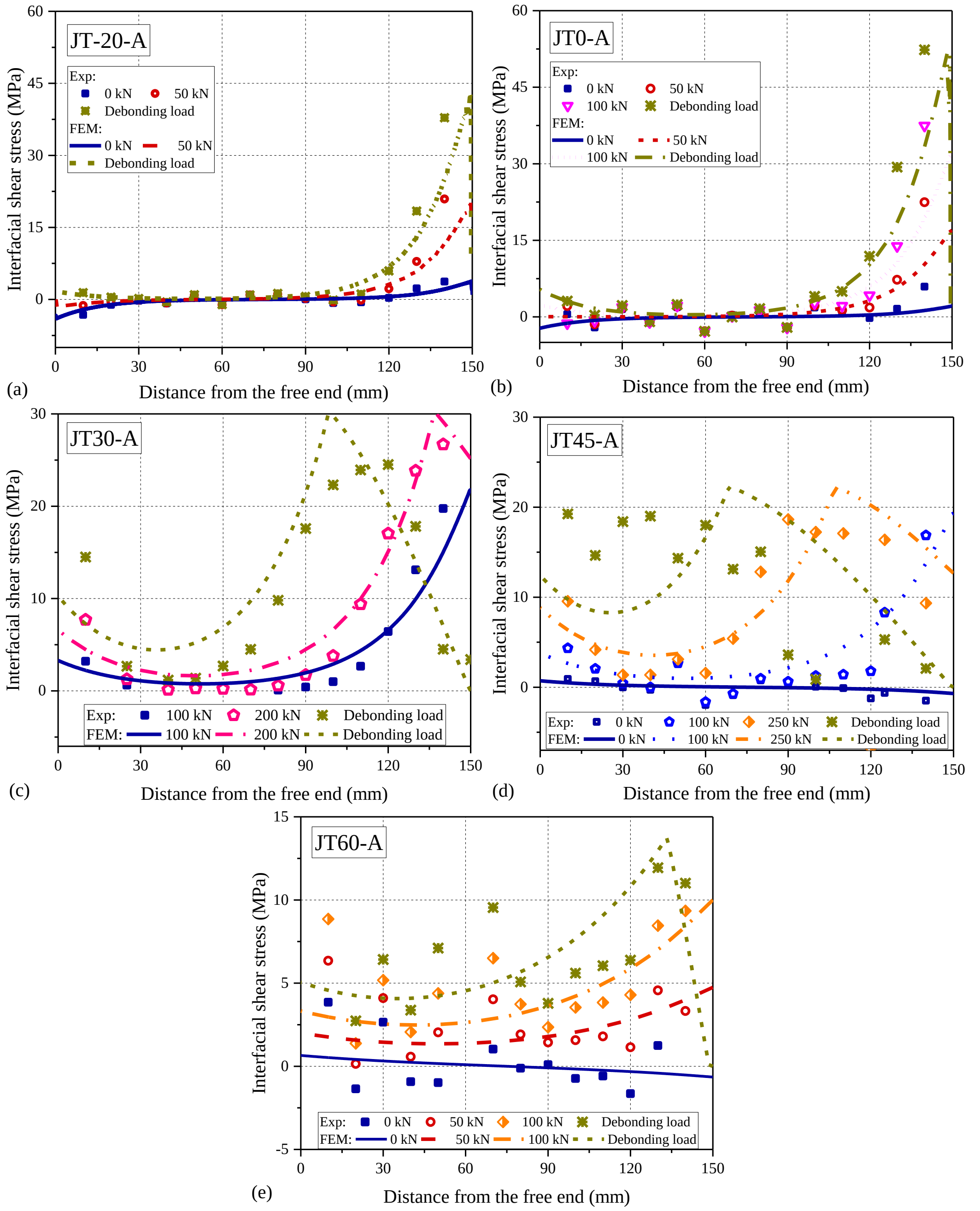

Fig. 6-18 Comparisons of interfacial shear stress distributions at different load levels obtained from the double-lap shear tests and the FE predictions: a) JT-20-A; b) JT0-A; c) JT30-A; d) JT45-A; e) JT60-A.

6.5.2.3 Load-displacement curves

Fig. 6-19 depicts the comparisons of the load-displacement curves between the double-lap shear test results and the corresponding FE predictions. All the test results for three duplicate specimens tested at each service temperature are presented, and the debonding loads predicted by the FE model are marked in the figure. It can be observed that in the elastic stage, the load increases linearly with the displacement. At room and high service temperatures, the interfacial deformation process evolves from an elastic stage to an elastic-softening stage, and finally CFRP debonding occurs at the end of the elastic-softening stage. In contrast, at -20 ℃ and 0 ℃, the elastic stage is approximately terminated at the occurrence of the CFRP debonding, indicating that the elastic-softening stage is negligible due to the increased elastic stiffness of the bond interface at low temperatures. The FE model can accurately predict the load-displacement responses at different service temperatures. Each predicted load-displacement curve is almost the average of the measured results of the three duplicates at each service temperature.

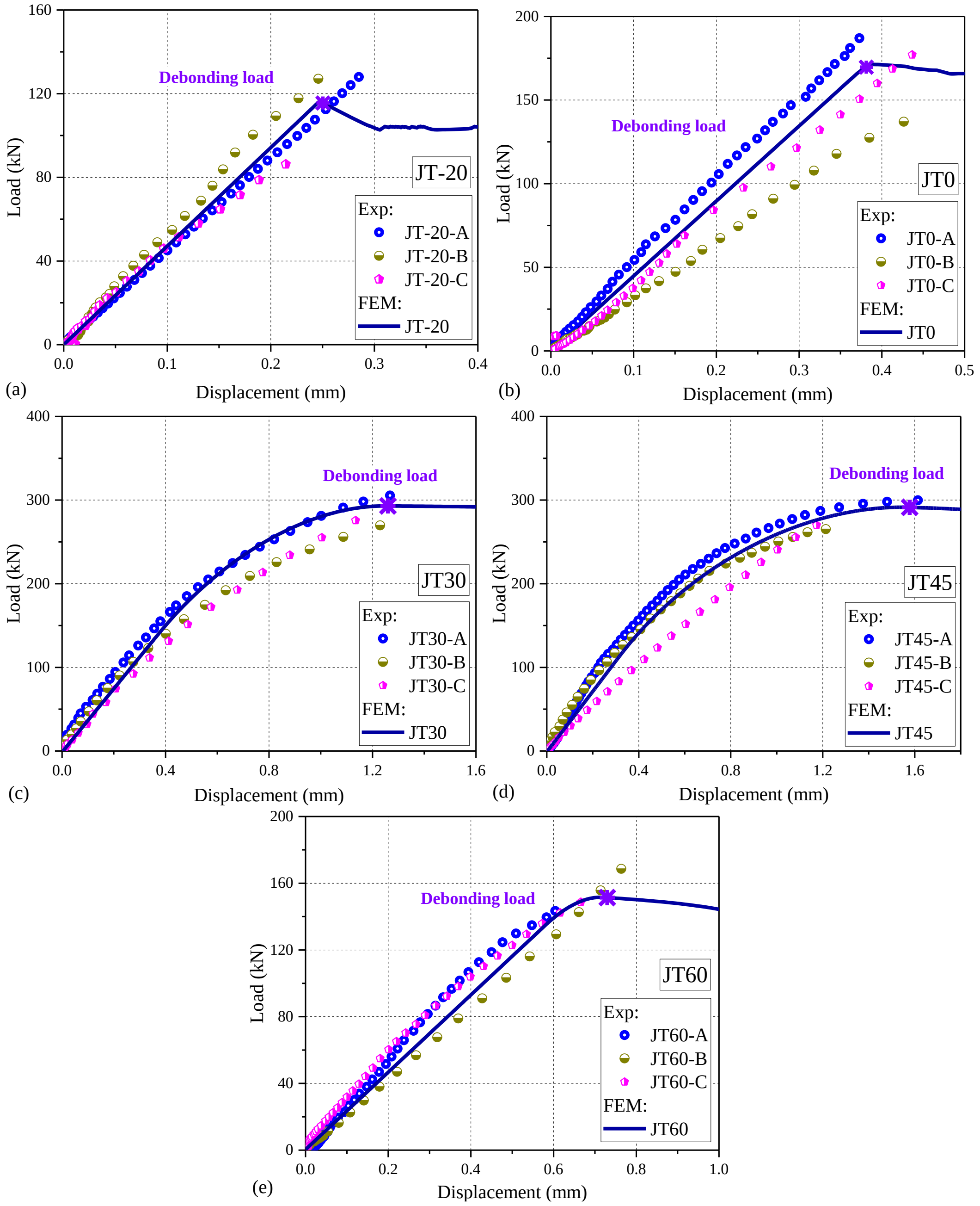

Fig. 6-19 Comparison of load-displacement curves obtained from the double-lap shear tests and the FE predictions: a) JT-20; b) JT0; c) JT30; d) JT45; e) JT60.

Table 6-2 summarizes the debonding loads obtained from the double-lap shear tests and the FE predictions for the joints tested at different service temperatures. The tested debonding load at each temperature is averaged from the results of three duplicate specimens. The percentage difference between the test result and the corresponding FE prediction is determined by dividing the difference by the tested debonding load. The comparison in **Table 6-2** shows that the percentage differences are all less than 8%, indicating that the FE model is capable of predicting the debonding loads of the bonded joints tested at different service temperatures.

Table 6-2 Comparison of debonding loads at different service temperatures

Temperature (℃)	Test results (kN)				FE predictions (kN)	Difference
	A	B	C	Average		
-20	129.4	133.4	86.6	116.5	117.8	1.1%
0	187.5	146.3	181.9	171.9	169.7	-1.3%
30	309.1	281.0	290.4	293.5	289.6	-1.3%
45	277.7	265.1	300.0	280.9	291.3	0.4%
60	143.5	171.2	151.6	155.5	151.4	-2.6%

6.6. DISCUSSION OF TEMPERATURE EFFECTS

6.6.1 Temperature Effect on the Bond Behavior

Fig. 6-20 shows the strain distributions in the CFRP plate after the imposition of the service temperature (i.e., before applying the pull-out load as described in **Section 6.5.1**), in which the measured CFRP strains and the FE predictions are both included for comparison. Since the applied service temperature at different locations exhibits slight variations along the bond length, the CFRP strain distributions measured by the strain gauges show small fluctuations. Nevertheless, the trends of the measured strain distributions in the CFRP plate at different service temperatures are well captured by the FE model. **Fig. 6-21** depicts the interfacial shear stress distributions predicted by the FE model. It can be seen that the interfacial shear stresses near the loaded end due to the imposition of the decreased service temperature are in the same direction as the pull-out load. In particular, the maximum value of the thermally-induced interfacial shear stresses is about 3.8 MPa when the service temperature is -20 ℃. This shear stress is approximately 8.9% of the peak shear stress (i.e., 42.9 MPa) obtained during the double-lap shear test. In addition, the maximum value of the thermally-induced shear stresses depends on the range of service temperature variation and the elastic stiffness of the bond interface, as also revealed by the analytical studies proposed by the Gao *et al.* (2012, 2015).

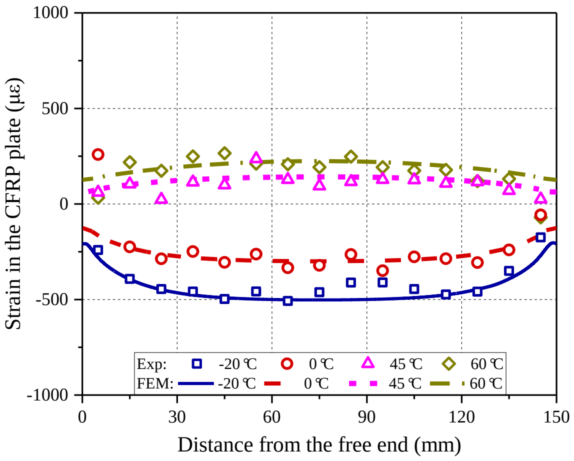

Fig. 6-20 CFRP strain distributions after the imposition of different service temperatures

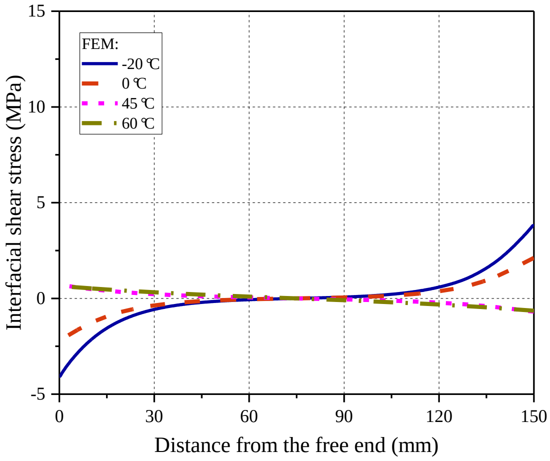

Fig. 6-21 Shear stress distributions after the imposition of different service temperatures

Fig. 6-22 and **Fig. 6-23** illustrate the CFRP strain distributions and the corresponding interfacial shear stresses for the bonded joints under a constant pull-out load of 25 kN. Such a load level corresponds to the elastic stage of the bond interface at different service temperatures (as shown in **Fig. 6-19**). The results obtained at different service temperatures have indicated that they are significantly influenced by the combined effects of mechanical and thermal loadings (i.e., temperature variations). In addition, the comparisons between the measured results and the FE predictions shown in **Fig. 6-22** have further demonstrated the reliability of the FE model in predicting the CFRP strain distributions of the joints tested at different service temperatures.

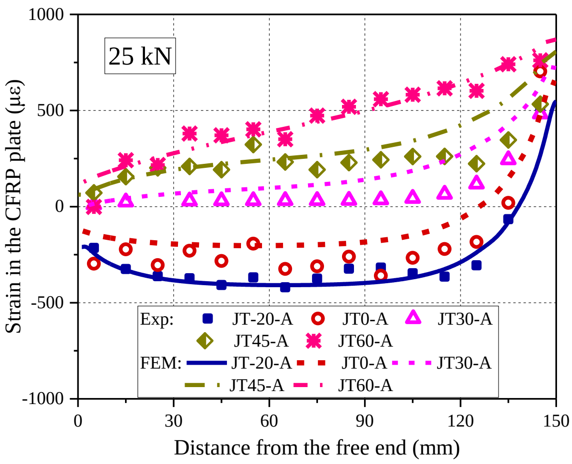

Fig. 6-22 CFRP strain distributions after applying a pull-out load of 25 kN

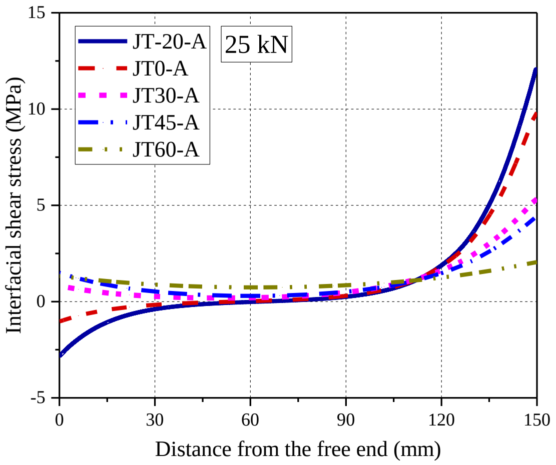

Fig. 6-23 Shear stress distributions after applying a pull-out load of 25 kN

As shown in **Fig. 6-23**, the interfacial shear stresses at the loaded end are affected by the temperature variations. That is, higher shear stresses are obtained at low service temperatures (i.e., -20°C and 0°C), while the minimum shear stress occurs at 60 ℃. The latter is attributed to the combined effects of interfacial thermal stress and reduced elastic stiffness of the bond interface. The observations in **Fig. 6-23** also suggest that the decreased temperature variations may lead to an earlier occurrence of the debonding failure, and thus more attention should be paid to the CFRP debonding of the strengthened steel beams at low service temperatures.

6.6.2 Temperature Effect on the Debonding Load

In the analytical solution previously proposed by the Gao *et al.* (2012), the effect of interfacial thermal stress on the debonding load of the bonded joint was theoretically analyzed in the case of single-lap shear tests. From the analytical solution, the increase in the debonding load (ΔP_{deb}) due to the presence of interfacial thermal stress can be calculated by the following equation:

$$\Delta P_{deb} = -\frac{E_p t_p b_p}{1+\alpha}(\alpha_p - \alpha_c)\Delta T \tag{6-3}$$

where α is the stiffness ratio defined as $\alpha = E_p t_p b_p / E_s t_s b_s$. E, t, b are the elastic modulus, thickness and width of the adherend with the subscripts "p" or "s" representing the CFRP plate or the steel substrate, respectively. According to Eq. 3, the increase in the debonding load induced by the thermal stress depends on the properties of the CFRP plate and the steel substrate; however, it is irrelevant to the local bond-slip behavior of the bond interface.

The present FE model can be used to investigate the temperature effects on the debonding load of bonded joints at different service temperatures, in which the combined effects of thermal stresses and local bond-slip behavior (i.e., bond properties) can be properly considered for different temperatures. Therefore, the advantage of the present FE model over the previous analytical solution is that the former can be used to distinguish the above two different effects on the debonding loads. **Fig. 6-24** compares the change in the debonding load at different service temperatures predicted by the FE model and the analytical solution. Note that the increases in the debonding load are determined by normalizing the load values at different service temperatures by the corresponding analytical or FE result obtained at 30°C. It can be seen that the analytical results are almost increased linearly with the temperature growths, while the FE results show that the debonding load is reduced significantly at 0 ℃, -20 ℃ and 60 ℃. The difference between the analytical results and the FE predictions is mainly due to the changes in the local bond-slip behavior (i.e., bond properties) of the CFRP-to-steel interface at different service temperatures. In other words, the difference is mainly induced by the bond degradation of the interface at low and high service temperatures. In addition, the comparison between the FE predictions and the test results has demonstrated the accuracy and reliability of the proposed FE model.

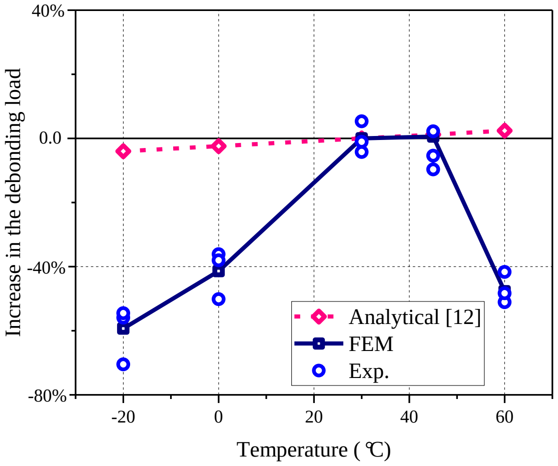

Fig. 6-24 Temperature effects on the debonding loads: analytical vs. FE results

6.7. CONCLUSIONS

This chapter presents the results from the double-lap shear tests of CFRP-to-steel bonded joints at different service temperatures from -20 ℃ to 60 ℃. The test results including the failure modes, debonding loads, load-displacement curves, CFRP strain distributions and interfacial shear stress and slip responses were examined and compared. Also, a bilinear local bond-slip model was established to describe the shear stress versus the interfacial slip relationships of the bond interface at different service temperatures. An FE model was proposed to predict the bond behavior and the debonding loads of the bonded joint at different service temperatures, and was validated through the comparisons between the experimental and FE results. The validated FE model was then used to further investigate the temperature effects on the CFRP strain distributions, interfacial shear stresses and the debonding loads of the bonded joints at different service temperatures. Based on the results and discussions presented in this chapter, the following conclusions can be drawn:

a) The service temperature variations have two different effects on the bond behavior and the related debonding loads of the bonded joint at different service temperatures, including the effect of interfacial thermal stresses and the changes in the local bond-slip behavior.

b) The debonding loads of the bonded joint are increased from a low service temperature to room temperature and then decrease at a high service temperature close to the glass transition temperature of the bonding adhesive.

c) The bilinear bond-slip model can describe the relationships between the shear stress and the interfacial slip at different service temperatures. At low service temperatures, the softening portion of the bilinear model can be neglected, and thus the bond-slip model can be simplified as the elastic-brittle model.

d) The elastic stiffness and the peak shear stress of the local bond-slip model are generally reduced with the service temperature increase, while the interfacial fracture energy decreases at both low and high service temperatures.

e) The good agreement between the test results and the corresponding FE predictions has demonstrated the reliability and accuracy of the proposed FE model. The advantage of this FE model over the previous analytical solution is that the former can be used to distinguish the above two different effects on the debonding loads.

The experimental and FE results have demonstrated that the debonding loads of the CFRP-to-steel interface are significantly reduced at both low and high service temperatures. This observation raises an important issue: the temperature effects must be appropriately considered in practical strengthening design. However, the design guidance on how to consider the temperature effects is lacking in current design guidelines. Therefore, more research is needed to account for the temperature effects on the bond behavior and the associated debonding loads of CFRP-strengthened flexural steel members under different service temperature conditions.

6.8. REFERENCES

Abaqus 6.14 (2014) "Documentation." Providence, RI, USA: Dassault Systemes Simulia Corporation.

ACI-440.2R (2008). "Guide for the Design and Construction of Externally Bonded FRP Systems for Strengthening Concrete Structures." Structures Congress, 1-8.

Al-Shawaf, A.K., Al-Mahaidi, R., and Zhao, X.L. (2009). "Effect of elevated temperature on bond behaviour of high modulus CFRP/steel double-strap joints." *Australian Journal of Structural Engineering*, 10(1), 63-74.

Al-Shawaf, A.K., and Zhao, X.L. (2013). "Adhesive rheology impact on wet lay-up CFRP/steel joints’ behaviour under infrastructural subzero exposures." *Composites Part B: Engineering*, 47, 207-219.

Al-Shawaf, A.K. (2010). "Characterization of bonding behavior between wet lay-up carbon fibre reinforced polymer and steel plates in double-strap joints under extreme environmental temperatures." PhD Thesis, Monash University, Australia.

Amada, S., and Satoh, A. (2000). "Fractal analysis of surfaces roughened by grit blasting." *Journal of Adhesion Science and Technology*, 14(1), 27-41.

ASTM-D7028 (2007). "Standard Test Method for Glass Transition Temperature (DMA Tg) of Polymer Matrix Composites by Dynamic Mechanical Analysis (DMA)." West Conshohocken, Philadelphia (PA): ASTM International.

ASTM-D3039 (2017). "Standard Test Method for Tensile Properties of Polymer Matrix Composite Materials." West Conshohocken, Philadelphia (PA): ASTM International.

ASTM-A370 (2017). "Standard Test Methods and Definitions for Mechanical Testing of Steel Products." West Conshohocken, Philadelphia (PA): ASTM International.

Barris, C., Correia, L., and Sena-Cruz, J. (2018). "Experimental study on the bond behaviour of a transversely compressed mechanical anchorage system for externally bonded reinforcement." *Composite Structures*, 200, 217-228.

Biscaia, H.C. (2019). "The influence of temperature variations on adhesively bonded structures: A non-linear theoretical perspective." *International Journal of Non-Linear Mechanics*, 113, 67-85.

Biscaia, H.C., and Ribeiro, P. (2019). "A temperature-dependent bond-slip model for CFRP-to-steel joints." *Composite Structures*, 217, 186-205.

Chandrathilaka, E., Gamage, J., and Fawzia, S. (2019). "Mechanical characterization of CFRP/steel bond cured and tested at elevated temperature." *Composite Structures*, 207, 471-477.

Colombi, P., Fava, G., and Sonzogni, L. (2015). "Fatigue crack growth in CFRP-strengthened steel plates." *Composite Part B-Engineering*, 72, 87-96.

Concrete Society (2012). "Design Guidance for Strengthening Concrete Structures Using Fibre Composite Materials — A Review." Technical Report 55, 3rd ed. Camberley, UK.

Deng, J., and Lee, M.M.K. (2007). "Behaviour under static loading of metallic beams reinforced with a bonded CFRP plate." *Composite Structures*, 78(2), 232-242.

Di Tommaso, A., Neubauer, U., Pantuso, A., and Rostasy, F. (2001). "Behavior of adhesively bonded concrete-CFRP joints at low and high temperatures." *Mechanics of Composite Materials*, 37(4), 327-338.

Dong, K., and Hu, K. (2016). "Development of bond strength model for CFRP-to-concrete joints at high temperatures." *Composites Part B: Engineering*, 95, 264-271.

Fernando, D., Teng, J.G., Yu, T., and Zhao, X.L. (2013). "Preparation and Characterization of Steel Surfaces for Adhesive Bonding." *Journal of Composites for Construction*, 17(6).

Gao, W.Y., Teng, J.G., and Dai, J.G. (2012). "Effect of temperature variation on the full-range behavior of FRP-to-concrete bonded joints." *Journal of Composites for Construction*, 16(6), 671-683.

Gao, W.Y., Dai, J.G., and Teng, J.G. (2015). "Analysis of Mode II debonding behavior of fiber-reinforced polymer-to-substrate bonded joints subjected to combined thermal and mechanical loading." *Engineering Fracture Mechanics*, 136, 241-264.

Gao, W.Y., Dai, J.G., and Teng, J.G. (2018). "Three-level fire resistance design of FRP-strengthened RC beams." *Journal of Composites for Construction*, 22(3), 05018001.

Gholami, M., Sam, A.R.M., Yatim, J.M., and Tahir, M.M. (2013). "A review on steel/CFRP strengthening systems focusing environmental performance." *Construction and Building Materials*, 47, 301-310.

Green, M.F., Bisby, L.A., Fam, A.Z., and Kodur, V.K. (2006). "FRP confined concrete columns: Behaviour under extreme conditions." *Cement and Concrete Composites*, 28(10), 928-937.

He, J., Xian, G., and Zhang, Y.X. (2020). "Effect of moderately elevated temperatures on bond behaviour of CFRP-to-steel bonded joints using different adhesives." *Construction and Building Materials*, 241, 118057.

Heshmati, M., Haghani, R., and Al-Emrani, M. (2015). "Environmental durability of adhesively bonded FRP/steel joints in civil engineering applications: State of the art." *Composites Part B: Engineering*, 81, 259-275.

ISO-11359 (1999). "Plastics–thermomechanical analysis (TMA)–part 2: determination of coefficient of linear thermal expansion and glass transition temperature." International Standard Switzerland.

Jia, D.G., Gao, W.Y., Duan, D. X., Yang, J., and Dai, J.G. (2021). "Full-range behavior of FRP-to-concrete bonded joints subjected to combined effects of loading and temperature variation." *Engineering Fracture Mechanics*, 254, 107928.

Ke, L., Li, C., He, J., Dong, S., Chen, C., and Jiao, Y. (2020). "Effects of elevated temperatures on mechanical behavior of epoxy adhesives and CFRP-steel hybrid joints." *Composite Structures*, 235, 111789.

Ko, H., Matthys, S., Palmieri, A., and Sato, Y. (2014). "Development of a simplified bond stress–slip model for bonded FRP–concrete interfaces." *Construction and Building Materials*, 68, 142-157.

Li, S., Zhu, T., Lu, Y., and Li, X. (2016). "Effect of Temperature Variation on Bond Characteristics between CFRP and Steel Plate." *International Journal of Polymer Science*, 2016, 5674572.

Liu, H.B., Zhao, X.L., Bai, Y., Singh, R.K., Rizkalla, S., and Bandyopadhyay, S. (2014). "The Effect of Elevated Temperature on the Bond Between High Modulus Carbon Fibre-Reinforced Polymer Sheet and Steel." *Australian Journal of Structural Engineering*, 15(4), 355-366.

Maluk, C., Bisby, L., Terrasi, G., and Green, M. "Bond strength degradation for CFRP and steel reinforcing bars in concrete at elevated temperature." American Concrete Institute, Farmington Hills, MI, 2011; 41–75.

Nguyen, T.C., Bai, Y., Zhao, X.L., and Al-Mahaidi, R. (2011). "Mechanical characterization of steel/CFRP double strap joints at elevated temperatures." *Composite Structures*, 93(6), 1604-1612.

Park, Y.B., Song, M.G., Kim, J.J., Kweon, J.H., and Choi, J.H. (2010). "Strength of carbon/epoxy composite single-lap bonded joints in various environmental conditions." *Composite Structures*, 92(9), 2173-2180.

Stratford, T.J., and Bisby, L.A. (2012). "Effect of Warm Temperatures on Externally Bonded FRP Strengthening." *Journal of Composites for Construction*, 16(3), 235-244.

Teng, J.G., Yu, T., and Fernando, D. (2012). "Strengthening of steel structures with fiber-reinforced polymer composites." *Journal of Constructional Steel Research*, 78, 131-143.

Yang, Y., Biscaia, H., Chastre, C., and Silva, M. (2017). "Bond characteristics of CFRP-to-steel joints." *Journal of Constructional Steel Research*, 138, 401-419.

Yao, M.X., Zhu, D.J., Yao, Y.M., Zhang, H.A., and Mobasher, B. (2016). "Experimental study on basalt FRP/steel single-lap joints under different loading rates and temperatures." *Composite Structures*, 145, 68-79.

Yoshitake, I., Tsuda, H., Itose, J., and Hisabe, N. (2014). "Effect of discrepancy in thermal expansion coefficients of CFRP and steel under cold temperature." *Construction and Building Materials*, 59, 17-24.

Yu, T., Fernando, D., Teng, J.G., and Zhao, X.L. (2012). "Experimental study on CFRP-to-steel bonded interfaces." *Composites Part B-Engineering*, 43(5), 2279-2289.

Zeng, J.J., Gao, W.Y., and Liu, F. (2018). "Interfacial behavior and debonding failures of full-scale CFRP-strengthened H-section steel beams." *Composite Structures*, 201, 540-552.

Zhang, Y., Vassilopoulos, A.P., and Keller, T. (2010). "Effects of low and high temperatures on tensile behavior of adhesively-bonded GFRP joints." *Composite Structures*, 92(7), 1631-1639.

Zhao, X.L., and Zhang, L. (2007). "State-of-the-art review on FRP strengthened steel structures." *Engineering Structures*, 29(8), 1808-1823.

Zhou, H., Fernando, D., Torero, J.L., Torres, J.P., Maluk, C., and Emberley, R. (2020). "Bond Behavior of CFRP-to-Steel Bonded Joints at Mild Temperatures: Experimental Study." *Journal of Composites for Construction,* 24(6), 04020070.

Zhou, H., Gao, W.Y., Biscaia, H.C., Wei, X.J., and Dai, J.G. (2022). "Debonding analysis of FRP-to-concrete interfaces between two adjacent cracks in plated beams under temperature variations." *Engineering Fracture Mechanics*, 263.

Zhou, H., Torres, J.P., Fernando, D., Law, A., and Emberley, R. (2019). "The bond behaviour of CFRP-to-steel bonded joints with varying bond properties at elevated temperatures." *Engineering Structures*, 183, 1121-1133.

CHAPTER 7

STRUCTURAL BEHAVIOR OF CFRP-STRENGTHENED STEEL BEAMS AT DIFFERENT SERVICE TEMPERATURES: EXPERIMETNTAL STUDY AND FE MODELING

7.1. INTRODUCTION

Externally bonded carbon fiber-reinforced polymer (CFRP) composites have been widely used to strengthen existing steel structures (Teng *et al.* 2012). A number of experimental results have proved that at normal ambient temperature, the load-carrying capacity and post-yielding stiffness of steel beams flexurally strengthened by CFRP plates can be significantly improved (Zeng *et al.* 2018; Colombi and Poggi 2006). High-strength epoxy resins are often used as adhesives to bond CFRP plates to the substrate steel beams. Therefore, the structural performance of CFRP-strengthened steel beams depends on the stress transfer between the CFRP plate and the steel beam. The presence of high interfacial stress concentration at the interface will lead to interfacial debonding failure, which may occur at the crack locations (i.e., termed as "intermediate crack-induced debonding") or initiates at the plate ends (i.e., termed as "plate-end debonding"), depending on whether the strengthened steel beam has a notch/crack in its tensile soffit (Colombi and Poggi 2006; Deng and Lee 2007; Sahin and Dawood 2016). The existing experimental studies in the literature have demonstrated that the plate-end debonding can be effectively suppressed by extending the length of the CFRP plate (Deng and Lee 2007; Sahin and Dawood 2016) to the beam supports. In these cases, the strengthened steel beams may fail due to web buckling (Zeng *et al.* 2018) or CFRP rupture (Deng and Lee 2007; Sahin and Dawood 2016), as illustrated in **Fig. 7-1**.

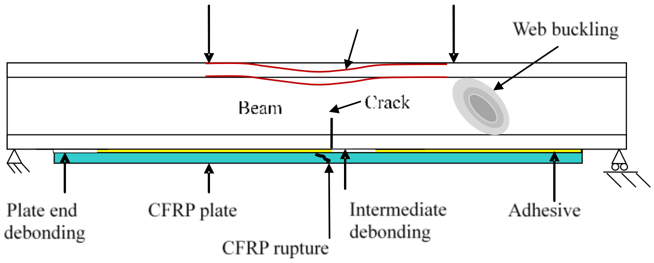

Fig. 7-1 Typical failure modes of CFRP-strengthened steel beams (Teng *et al.* 2012).

An important concern in the applications of EB-CFRP in strengthening steel structures is the temperature sensitivity of the bond interface, which is due to seasonal or daily temperature variations (Gholami *et al.* 2013). Both the interfacial bond strength and stiffness may be significantly degraded at high service temperatures, especially when the glass transition temperature (T_g) of the bonding adhesive is exceeded.

To investigate the thermally induced bond degradation between CFRP plates and steel, the double-lap shear tests on 15 CFRP-to-steel double-lap bonded joints were conducted at temperatures from -20 ℃ to 60 ℃, and the changes in the interfacial bond-slip relationships with the service temperature variations were investigated in **Chapter 6**. The results showed that the interfacial shear stiffness, peak shear stress and interfacial fracture energy decrease as the temperature increases. Similar phenomena were also reported in other studies (Zhou *et al.* 2020; Biscaia and Ribeiro 2019;Yang *et al.* 2017). In addition to the temperature-dependent interfacial bond-slip behavior, thermally-induced interfacial stresses were also generated during the temperature variations due to the much higher coefficient of thermal expansion (CTE) of steel than CFRP plates (Gao *et al.* 2012, 2015). These thermally-induced interfacial stresses might occur in the same or opposite direction as the mechanical loading, thus reducing or increasing the debonding load.

A few experiments have been conducted to examine the flexural performance of CFRP-strengthened steel beams at moderately elevated (Sahin and Dawood 2016; Stratford and Bisby 2012; Teng *et al.* 2021) and decreased (Yoshitake 2014) temperatures. Stratford and Bisby (2012) performed sustained loading tests on CFRP-strengthened steel beams under the condition of increasing temperatures. Substantial slips were found at the plate end when the temperatures were higher than 40 ℃, and the debonding loads were significantly reduced at elevated temperatures. Teng *et al.* (2021) reported that an elevated temperature up to 60 ℃ deteriorated the interfacial stress transfer and the flexural stiffness of CFRP-strengthened steel beams. However, Sahin and Dawood (2016) reported that the plate-end debonding load of CFRP-strengthened steel beam was increased at 50 ℃ compared to the test result at 25 ℃, and attributed this increase to the enhanced toughness of the bonding adhesive at increased temperatures. Yoshitake *et al.* (2014) studied the effect of cold temperature (i.e., -20 ℃) on the structural performance of CFRP-strengthened steel beams. However, the strengthened beams failed due to CFRP rupture rather than interfacial debonding. Under such a circumstance, the load-carrying capacity of the strengthened steel beam should be dependent on the tensile strength of the CFRP plate, which is believed to be insensitive to the service temperature variations.

In view of the differences in the reported experimental results of CFRP-strengthened steel beams and the lack of a systematic investigation into the interfacial bond behaviors, this study aims to conduct a comprehensive experimental study on CFRP-strengthened steel beams at a wider temperature range from -20 ℃ to 60 ℃, including both cold and elevated service temperatures, to better understand how the temperature variations affect the interfacial bond behavior and structural performance.

7.2. EXPERIMENTAL PROGRAM

Three-point bending tests were conducted on a series of CFRP-strengthened steel beams at different temperatures, including -20 ℃, 0 ℃, 30 ℃, 45 ℃ and 60 ℃. **Fig. 7-2** shows a schematic of the geometrical dimensions and loading scheme of the tested specimens. The steel beams had an overall length of 1.5 m and were strengthened by a 300 mm or 600 mm long CFRP plate through adhesive bonding. Stiffeners were provided for the steel beams strengthened with the 600 mm CFRP plate to avoid local buckling of the beam web. The beams were simply supported with a clear span of 1.3 m and implemented with a concentrated load at the mid-span location.

The specimens were nominated according to the length of the CFRP plate and the experimental temperature. For example, BP600T30 represents the steel beam strengthened with the 600 mm CFRP plate and tested under 30 ℃. To ensure the reliability of the experimental data, two duplicate specimens were tested at two extreme temperatures -20 ℃ and 60 ℃. (BP600T-20 and BP600T-20-R; BP300T60 and BP300T60-R). In addition, two un-strengthened reference beams were prepared, including one with stiffeners and the other without stiffeners (denoted as Bs and B). The details of all tested specimens are summarized in **Table. 7-1**.

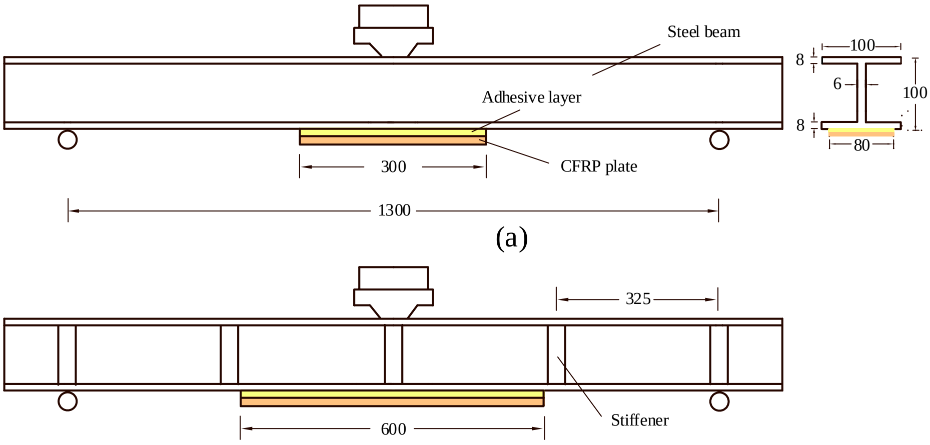

(a)

(b)

Fig. 7-2 Schematic of CFRP-strengthened steel beams: a) BP300; b) BP600.

Table 7-1 Details of specimens

Series number	Specimens name	CFRP plate length (mm)	Stiffeners	Temperature (℃)
Reference	B	-	No	30
	Bs	-	Yes	30
BP300	BP300T-20	300	No	-20
	BP300T0		No	0
	BP300T30		No	30
	BP300T45		No	45
	BP300T60		No	60
	BP300T60-R		No	60
BP600	BP600T-20	600	Yes	-20
	BP600T-20-R		Yes	-20
	BP600T30		Yes	30
	BP600T45		Yes	45
	BP600T60		Yes	60

7.2.1 Materials

The steel was hot rolled and the beams had an H-shaped cross-section. The height and flange width of the beam were 100 mm, and the thicknesses of the flange and web were 6 mm and 8 mm, respectively. Accordingly, the sectional area and moment of inertia of the beams were 2.19×10^3 mm^2 and 3.83×10^7 mm^4, respectively. The stress-strain relationship of the steel material was obtained by direct tensile tests of three coupon samples cut from the flange and three others cut from the web as per ISO 6892-1 (2016). **Fig. 7-3** shows all obtained stress-strain relationships and their average. The elastic modulus and yielding strength of the steel were 199.1±4.3 GPa and 371.6±8.0 MPa, respectively.

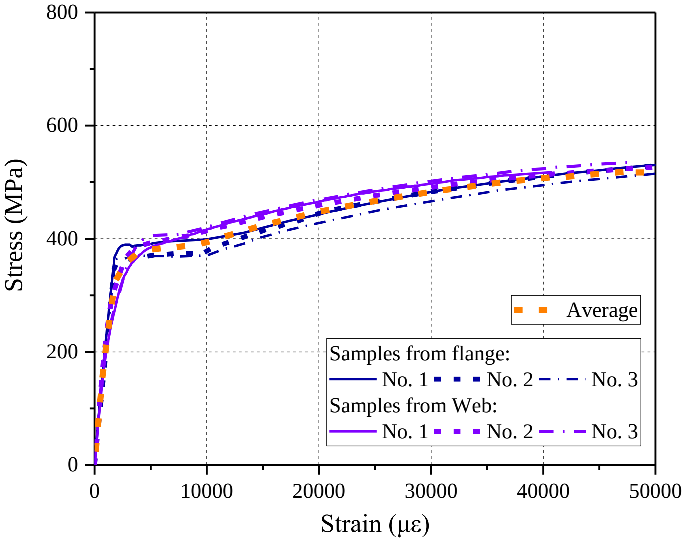

Fig. 7-3 Stress-strain relationship of steel.

The externally bonded CFRP plates and the bonding adhesive were the same as those used in previous bonded joint tests (**Chapter 6**). The elastic modulus and ultimate strain of the CFRP plate were measured as 141.9±0.9 GPa and 13050±26 με as per ASTM D3039 (2017) based on a nominal thickness of 1.5 mm. The thermal expansion coefficients of CFRP plate and steel were measured in the investigated temperature range (i.e., -20 ℃ to 60 ℃) by the thermomechanical analysis (TMA) test according to ISO 11359 (1999). The measured CTEs of steel and CFRP plate were 1.2491×10^{-5}/ ℃ and 4.18×10^{-6}/ ℃, respectively. Sikadur-330CN adhesive was adopted as the bonding adhesive. The mechanical properties of the bonding adhesive at normal temperature including the tensile strength and the elastic modulus were 49.7 MPa and 2.55 GPa, respectively, as provided by the manufacturer. In addition, its allowable service temperature range was specified as -40 ℃ to 45 ℃.

7.2.2 Preparation of Specimens

The preparation of CFRP-strengthened steel beam specimens followed the same procedure reported in the previous experiment (**Chapter 6**). Specifically, the steel beam surface was firstly degreased with acetone and then sandblasted with 0.25 mm diameter angular alumina grit to ensure its chemical compatibility with the adhesive (Fernando *et al.* 2013). The blasting angle was controlled at about 75 ° (Amada and Satoh 2000), and the pressure was controlled at 0.4-0.6 MPa. After sandblasting, the surface dust was cleaned away by compressed air. Prior to being bonded to the steel surface, the CFRP plate was carefully cleaned with acetone using gauze. Afterwards, the CFRP plate was adhesively bonded to the steel surface within half an hour to avoid oxidation of the steel surface. After the CFRP plates were bonded to the surface of the steel beam, a uniform compressive stress of 4.2 kPa was applied on the top surface of the CFRP plate to ensure that the CFRP plate was tightly bonded to the steel surface during the curing process. Before the bending tests, the specimens were cured at room temperature for at least two weeks.

7.2.3 Testing Procedure and Instrumentations

The design of the heating and cooling facilities was based on the same working mechanism as previously employed the tests of CFRP-to-steel bonded joints at different temperatures (**Chapter 6**), but with stronger power for increasing and decreasing the experimental temperatures. An environmental chamber with a larger size (i.e., 3.4 m × 1.9 m × 1.2 m) was built with heat insulation boards to reduce possible heat exchange between the specimens and the out-chamber air during the tests. Some thermocouples were installed at various locations of the CFRP-strengthened steel beams, including the surface of the CFRP plate, at the central location of the beam web, and at the two ends of the top flange. During the experiment, the beam specimens were firstly conditioned inside the environmental chamber until the temperatures measured at different locations reached the target temperature, which was held at a nearly constant value for at least thirty minutes to load the strengthened steel beams until failure. The mechanical loading was applied by an electrohydraulic loading and controlling system at a constant loading rate of 5 mm/min.

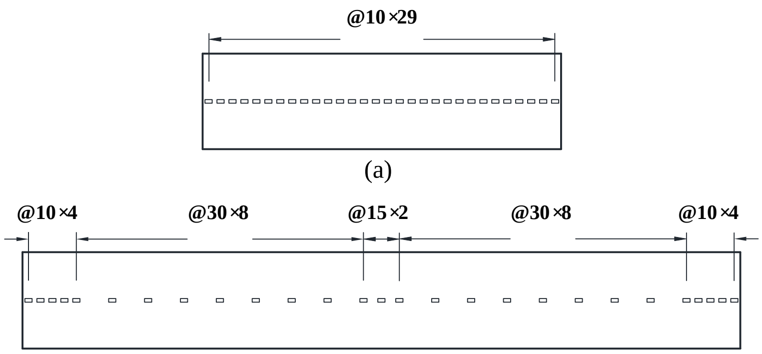

(a)

(b)

Fig. 7-4 Locations of strain gauges on the CFRP plate: a) BP300; b) BP600.

During the loading process, the mid-span deflection, load, the longitudinal strain distribution along the CFRP plate (**Fig. 7-4**), and the strains on the beam web at the mid-span location (**Fig. 7-5**) were acquired at a frequency of 5 Hz. The strain gauges were bonded using the NP-50B adhesive, which is applicable for the service temperature ranging from -30 ℃ to 300 ℃. In addition, strain gauges from the same batch were attached to the TiS glass and placed near the strain measurement locations for thermal compensation purposes. As shown in **Fig. 7-4**, for BP300 and BP600, the first and last strain gauges were located at 5 mm away from the two plate ends, respectively. For BP300, the spacing of the strain gauges was set as 10 mm along the entire length. While for BP600, the spacing of the strain gauges was set as 30 mm in the middle length and 10 mm near the plate ends, considering the higher interfacial shear stress concentration before the plate-end debonding (Smith and Teng 2001).

As shown in **Fig. 7-5**, six strain gauges were bonded onto the beam web at the mid-span of the beam at different heights. At each beam height, there were two strain gauges on two opposite sides of the beam web, and their values were used to illustrate the sectional strain profile. The difference between the two strain values at the same height could be used to monitor the local buckling of the web. In addition, two LVDTs were installed to measure the interfacial slips between the CFRP plate and the steel beam at the two plate ends (**Fig. 7-6**).

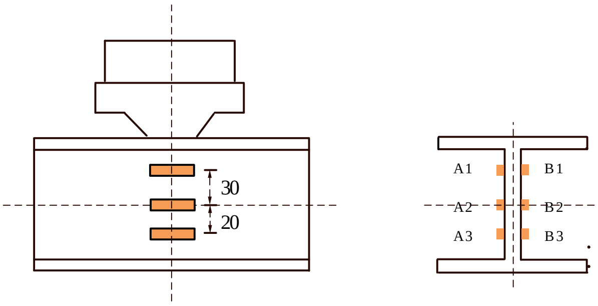

(a) (b)

Fig. 7-5 Strain gauges on the beam web: a) front view; b) side view.

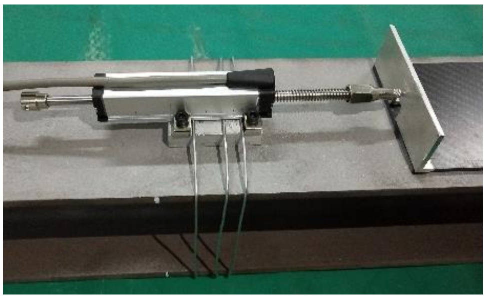

Fig. 7-6 LVDT on each end of the specimen

7.3. EXPERIMENTAL RESULTS

7.3.1 Failure Observation

Fig. 7-7 shows the typical failure mode of steel beams strengthened by the shorter CFRP plates (BP300). All steel beams in the BP300 series were failed due to interfacial debonding. Some residual deformation in the steel beam can be observed in this figure, indicating the yielding in steel materials.

Fig. 7-7 Typical failure mode of BP300 beam series at various temperatures.

Fig. 7-8 shows the debonded interface of the beams in the BP300 series. It can be observed that the cohesive failure, which occurred inside the adhesive layer, was the dominant failure mode. The interfacial debonding suddenly occurred at both ends of the CFRP plate at lower and normal temperatures (i.e., from -20 ℃ to 30 ℃) because of the relatively brittle property of the bonding adhesive at such temperatures. In addition, numerous burrs and debris of adhesive were seen at the debonded interface. In contrast, the interfacial debonding only occurred at one end of the CFRP plate at the higher temperatures of 45 ℃ and 60 ℃ (i.e., the upper side of BP300T45 and BP300T60 in **Fig. 7-8**). Meanwhile, the debonded interface was much smoother, which should be attributed to the increased ductility of the bonding adhesive at elevated temperatures.

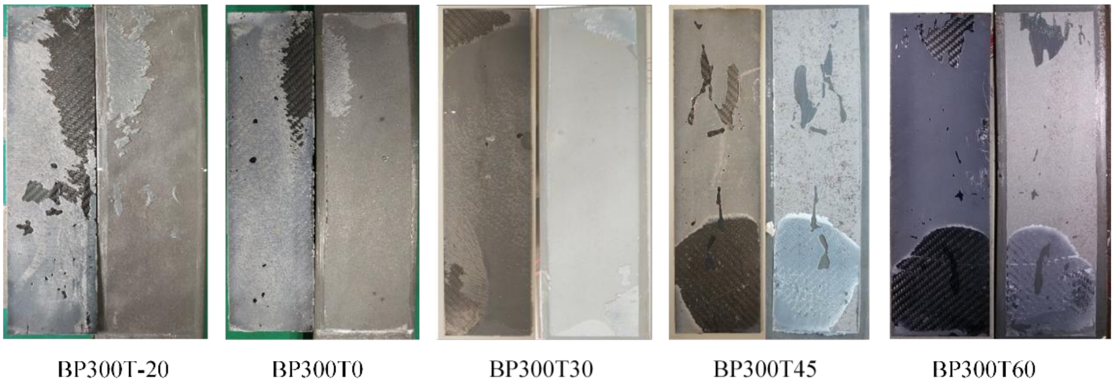

Fig. 7-8 Debonded interface of the CFRP-strengthened steel beams (BP300 series).

Fig. 7-9 shows the failure modes of steel beams strengthened by the longer CFRP plates (BP600). Unlike the BP300 series, which failed due to plate-end debonding at all temperatures, the beams strengthened by longer CFRP plates (BP600) failed by plate-end debonding only at 60 ℃, while the CFRP rupture was observed at all other temperatures (i.e., -20 ℃ to 45 ℃).

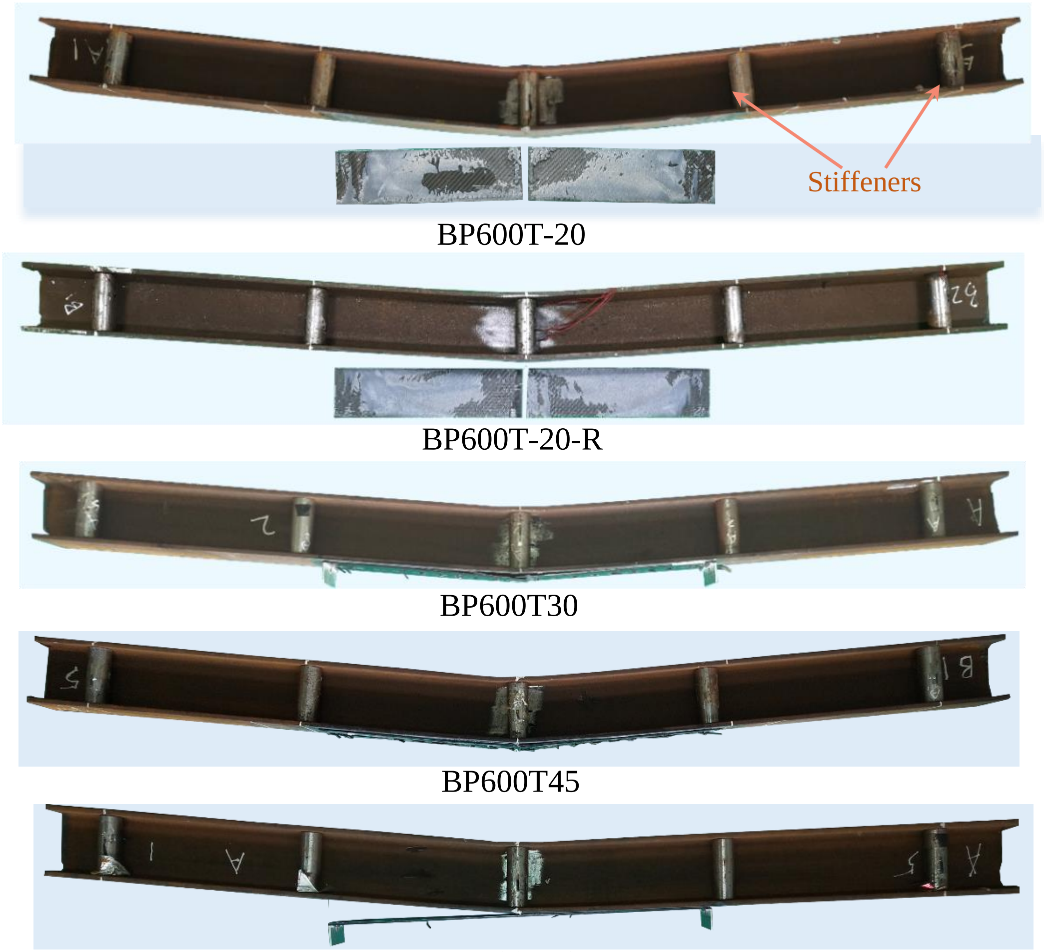

Fig. 7-9 Failure modes of BP600 beam series at various temperatures.

7.3.2 Structural Performance at Room Temperature

Fig. 7-10 compares the load-deflection curves of steel beams with and without CFRP strengthening and tested at 30 ℃. It can be seen that for all specimens, at low levels of mechanical loading, the load increases linearly with the deflection, indicating that the material response was elastic. At this stage, the difference in the flexural stiffness of the beams was negligible due to the much lower sectional stiffness of the CFRP plate as compared to the steel beam.

At higher load levels, the load-deflection curves of the un-strengthened steel beams exhibited nonlinearity because of the steel yielding. After steel yielding, the load increased almost linearly until a deflection of 40 mm occurred in the un-strengthened steel beam with the stiffeners. However, the un-strengthened steel beams without stiffeners exhibited a lower load resistance at a deflection larger than 20 mm, mainly due to the web buckling.

In addition, after the yielding of the steel, the flexural stiffnesses of CFRP-strengthened steel beams were higher than those of un-strengthened steel beams. Finally, the interfacial debonding or CFRP rupture occurred suddenly and the load dropped to the level of un-strengthened steel beams. The ultimate load and deflection of steel beams strengthened with the longer CFRP plate (i.e., BP600T30) were much higher than those of beams strengthened with the shorter CFRP plate (i.e., BP300T30).

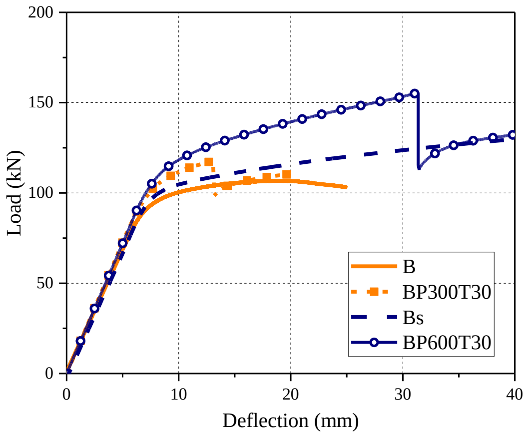

Fig. 7-10 Comparison of the load-deflection curves of steel beam with and without CFRP strengthening at 30 ℃.

Fig. 7-11 shows the strain distributions in the CFRP plate under different levels of mechanical loading at 30 ℃. It is seen that the strains in the CFRP plate were symmetrically distributed around its middle span, where the maximum strain value was read. The local CFRP strain increased with the applied mechanical load. The maximum values of CFRP strains recorded at the mid-span for BP300T30 and BP300T60 were very close at the same level of mechanical loading (e.g., 40 kN and 100 kN), while the shapes of the strain distributions were quite different (see **Fig. 7-11**) due to the different bond lengths. The CFRP strain increase rate with the mechanical loading became much higher after the yielding of the steel beam (i.e., under a load higher than 100 kN), explaining why the flexural stiffness enhancement became more significant after the yielding of the steel beam in the load-deflection curves (**Fig. 7-10**).

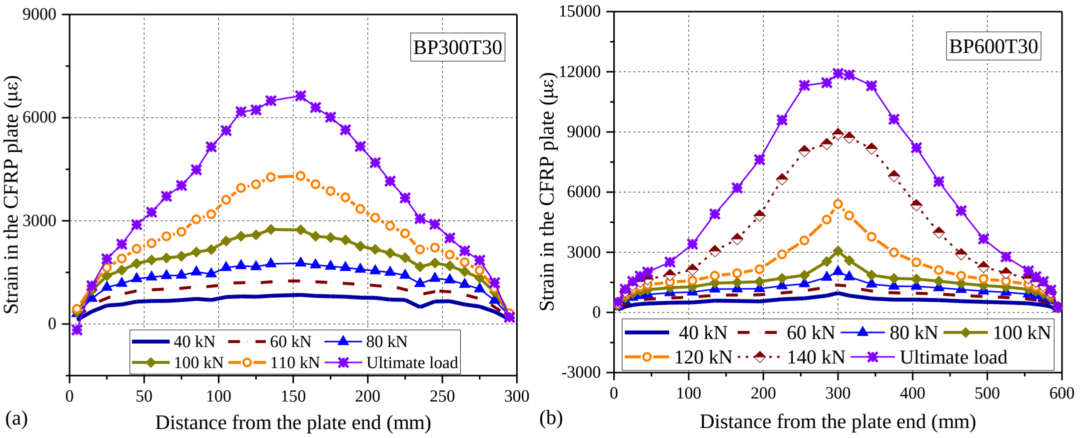

(a) (b)

Fig. 7-11 Distributions of CFRP strain under different mechanical loading: a) BP300T30; b) BP600T30.

The local interfacial shear stress ($\tau_{i+\frac{1}{2}}$) (i starts from the plate end) can be computed based on the two adjacent CFRP strains (ε_i, ε_{i+1}) measured at the locations of x_{i+1} and x_i by the following equation (Yang *et al.* 2017; Yu *et al.* 2012; Barris *et al.* 2018; Ko *et al.* 2014).

$$\tau_{i+\frac{1}{2}} = \frac{\varepsilon_{i+1}-\varepsilon_i}{x_{i+1}-x_i} E_f t_f \tag{7-1}$$

where E_f and t_f are the elastic modulus and thickness of the CFRP plate, respectively.

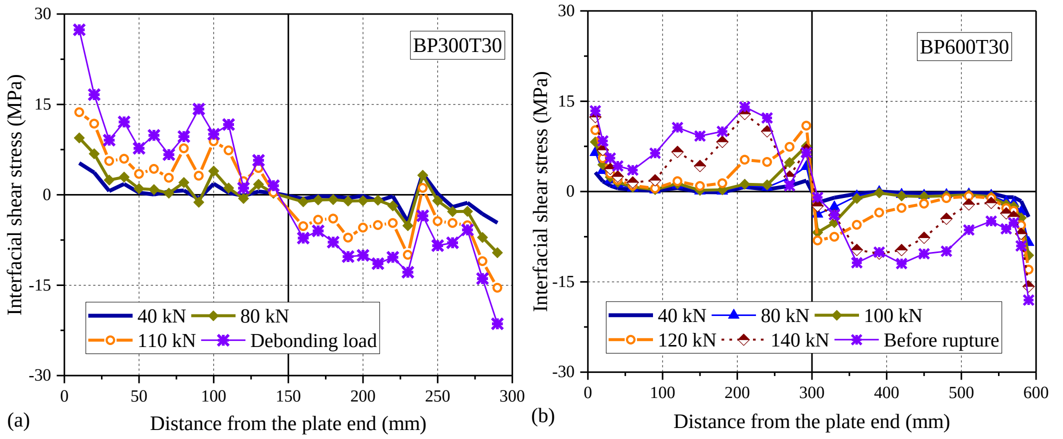

(a) (b)

Fig. 7-12 The distributions of interfacial shear stresses at 30 ℃: a) BP300T30; b) BP600T30.

Fig. 7-12 shows the distributions of interfacial shear stresses for the two CFRP-strengthened steel beams (BP300T30 and BP600T30) at different levels of mechanical loading. Overall, the interfacial stress was generally higher at the two plate ends of the

CFRP plate and lower in the middle span. After the yielding of the steel beam (i.e., load higher than 100 kN), the magnitudes of interfacial shear stress near the middle length (i.e., *x*=100 mm and 200 mm for BP300T30 and *x*=200 mm and 400 mm for BP600T30) also became higher. In addition, the plate-end interfacial shear stress in BP30030 was higher than that in BP60030, suggesting that the use of the longer CFRP plate could delay the plate-end debonding.

In the tests of the CFRP-to-steel double-lap bonded joints (**Chapter 6**), there existed significant localized stress softening at the loaded end at 30 ℃. This phenomenon was not clearly seen in the flexural tests of CFRP-strengthened steel beams (**Fig. 7-12**), despite using the same bonding material, CFRP length and curing conditions. The difference was due to the reduced mode II interfacial fracture energy because of the coupling effect from the interfacial stress in the mode I direction (De Lorenzis 2013). The length of the softening region before debonding was significantly reduced and especially the softening could not be captured near the plate end (e.g., *x* = 10 mm).

7.3.3 Comparison of Structural Performance at Different Temperatures

7.3.3.1 Load-deflection behaviors

Fig. 7-13 compares the load-deflection curves of the reference and strengthened steel beams at different temperatures. All the beams exhibited a similar trend, i.e., the load increased with the deflection almost linearly before the steel yielding. The post-yielding slope of the curve was much lower than the value in the elastic stage and depended on the magnitude of service temperature. The effect of service temperature on the post-yielding slope of the load-deflection curves seemed to be more significant in the case of the shorter CFRP plate (i.e., 300 mm). At the ultimate failure, the loads and deflections of the strengthened steel beams also varied significantly at different service temperatures. For the shorter CFRP plate case, the deflections at plate-end debonding failure reached the maximum value at 45 ℃ but decreased as the temperature was further increased to 60 ℃ (**Fig. 7-13a**). For the longer CFRP plate case, the loads and deflections at the ultimate state were very similar for all the strengthened beams tested in the temperature range of -20 ℃ to 45 °, except for the one at 60 ℃ (**Fig. 7-13b**), which had significantly low values.

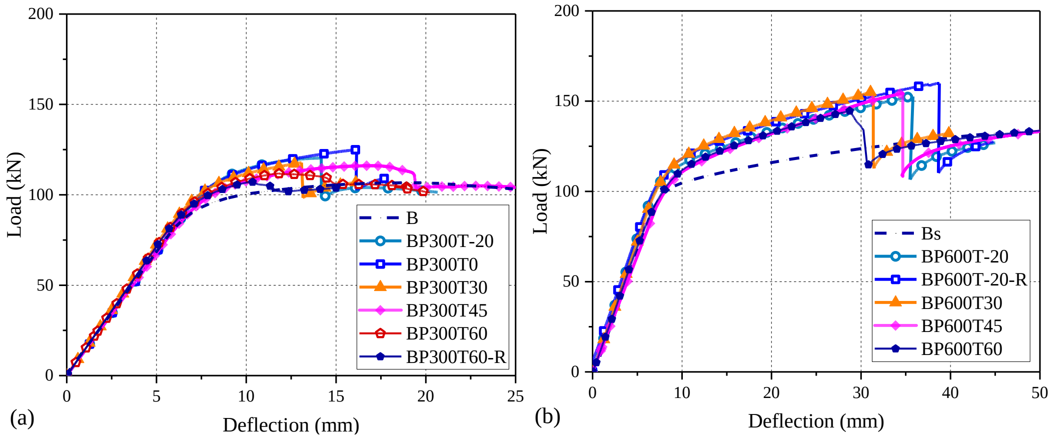

Fig. 7-13 The load-deflection behavior of CFRP-strengthened steel beams: a) BP300; b) BP600.

Fig. 7-14 indicates the change in the ultimate load of the strengthened beams with the temperature. The use of the longer CFRP plate led to a higher load-carrying capacity at all temperature levels. In addition, compared to that at ambient temperature, the ultimate load was slightly changed at the lowest temperature but decreased significantly at 60 ℃. Specifically, compared with 30 ℃, the plate-end debonding load of the steel beam strengthened by the shorter CFRP plate was increased by 6.1% and 2.1% at 0 ℃ and -20 ℃, respectively, but decreased by 7.1% at 60 ℃. In addition, the ultimate loads of the steel beams strengthened by the longer CFRP plates were almost constant (i.e., with changes less than 0.8%) in the temperature range from -20 ℃ to 45 ℃ since they were all failed due to CFRP rupture, which tensile strength was insensitive to the concerned temperature variations. In comparison, the ultimate load decreased by 6.3% at 60 ℃, indicating that the temperature increase to this level would lead to a significant reduction in the plate-end debonding load, which should be paid special attention in the practical design.

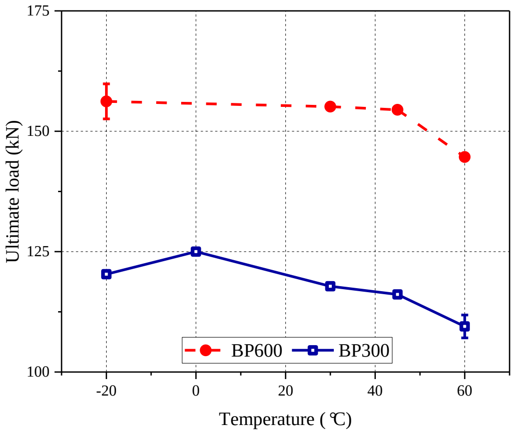

Fig. 7-14 The ultimate loads of CFRP-strengthened steel beams at different temperatures.

7.3.3.2 Distributions of CFRP strains

The distributions of CFRP strains under the ultimate loads are compared in **Fig. 7-15**. The magnitudes of CFRP strains in the BP300 series were generally higher in the specimens with higher ultimate loads. In comparison, the distributions of CFRP strains were quite close for the beams in the BP600 series in the temperature range of -20 ℃ to 45 ℃ (**Fig. 7-15b**). For both series of specimens, the maximum CFRP strains recorded in the beam at 60 ℃ were significantly lower compared to the other temperatures.

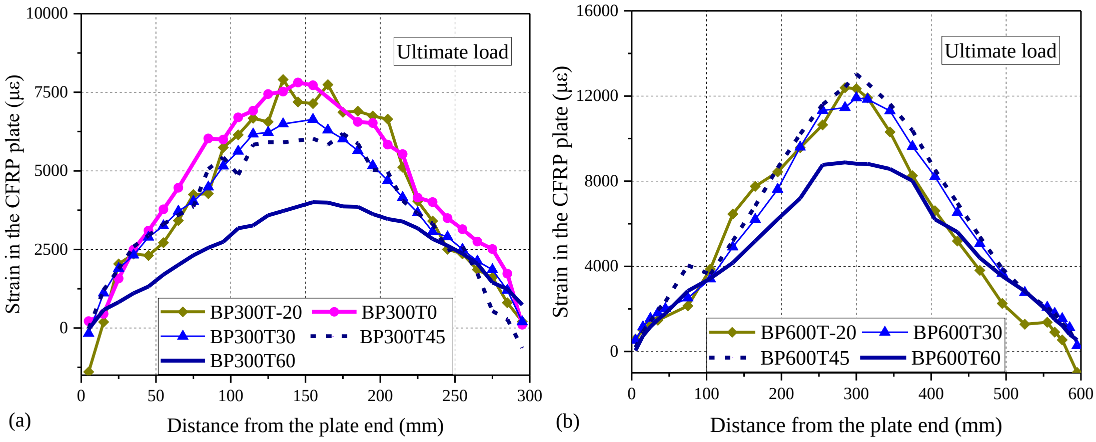

Fig. 7-15 Comparison of CFRP strains at the ultimate states under different temperatures: a) BP300 series; b) BP600 series.

7.3.3.3 Sectional strain profile

Fig. 7-16 shows the sectional strain profiles of CFRP-strengthened steel beams over the height at their midspan, which were measured on the steel web (both sides named as

"A" and "B" in **Fig. 7-16**) and the CFRP plate in the specimens BP300T30 and BP300T60. It is seen that with the increase of load, the neutral axis moved downward, indicating that the contribution of the CFRP plate was gradually activated, especially after the yielding of the steel beam. In addition, the strain distribution along the height of BP300T30 was linear at each load level. In comparison, the CFRP strain of BP600T60 was significantly lower than the value estimated based on the linear variation, implying that the thermally-induced softening of the bonding adhesive deteriorated the composite action between the CFRP plate and the steel beam.

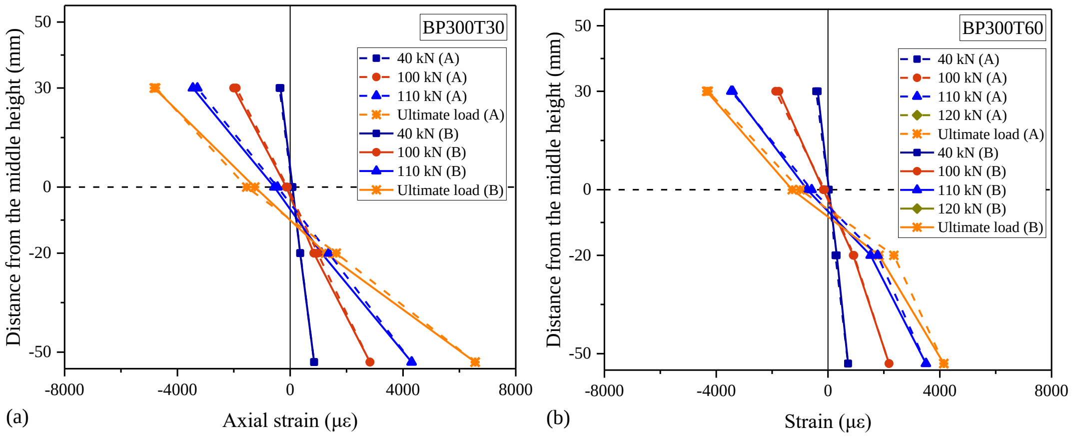

Fig. 7-16 Axial strains over the depth of CFRP-strengthened steel beams: a) BP300T30; b) BP300T60.

7.3.3.4 Relative displacements at plate ends

Fig. 7-17 compares the relative displacements measured by the LVDTs at two plate ends under different temperature conditions. The measured displacements consisted of the interfacial slip between the CFRP and steel beam and the relative displacement due to the flexural deformation of the beam. It can be clearly seen that the displacements measured in the temperatures ranging from -20 to 45 ℃ were quite close under the same mechanical loading and were much lower than that at 60 ℃, confirming that the temperature rise up to 60 ℃ significantly decreased the interfacial shear stiffness and increased deformability of the adhesive layer.

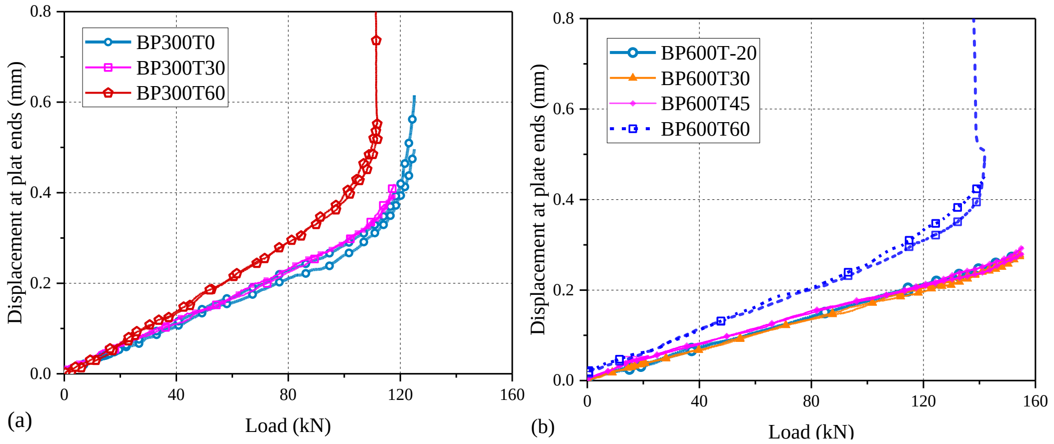

Fig. 7-17 Comparison of the relative displacements at plate ends under different temperatures: a) BP300; b) BP600.

7.4. FE MODEL AND VALDIATION

7.4.1 Description of the FE Model

The general purpose software Abaqus 6.14 was used to predict the structural behavior of CFRP-strengthened steel beams at different service temperatures, in which a two-dimensional plane-stress FE model was established. Both the CFRP plate and the steel beam were modeled with 4-node plane stress quadrilateral elements (CPS4R), while the adhesive layer was modeled with 4-node two-dimensional cohesive elements (COH2D4). The different thicknesses over the beam height (i.e., the thicknesses of flange, web, adhesive layer, CFRP plate and stiffeners) were considered by setting different out-of-plane thicknesses of the elements. In addition, the size of the elements was set to 0.2 mm in the *x*-direction, based on the trade-off of saving the computation time without losing accuracy. This element size was proved suitable to achieve accurate predictions in the previous analytical and FE study in **Chapter 3**. In the current FE model, the reference temperature (i.e., 30 ℃) was assigned for the entire specimen as an initial step. Then, the service temperature variation (i.e., thermal loading) was defined by a predefined field variable, which was uniformly distributed in the specimen as a second loading step. The mechanical load was applied to the midspan along the *y*-direction using a displacement-control manner until the test specimen failed.

The constitutive stress-strain relationship of the steel in the FE model was determined by the true (Cauchy) stresses and logarithmic strains, which were converted from the average engineering stresses and strains measured in three tensile coupon tests (as shown in **Fig. 7-3**). The reliability and accuracy of the constitutive stress-strain relationship were proved to be capable of providing accurate predictions of the un-strengthened two reference steel beams in terms of the overall load-deflection responses, as seen in **Fig. 7-18**. Some slightly lower load predictions were observed for beam B after the midspan deflections are larger than 20 mm due to the local buckling effect. Nevertheless, given that the CFRP debonding tends to occur before the steel buckling and steel stiffeners are commonly used in practice to prevent possible local bucking failure of the CFRP-strengthened steel beam, the above constitutive relationship for steel is considered reasonable enough for use in modeling the structural performance of CFRP-strengthened steel beams.

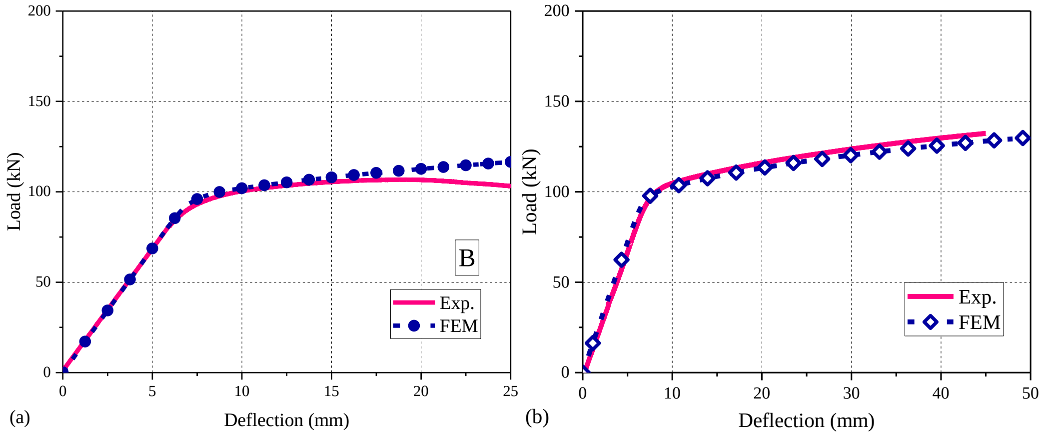

Fig. 7-18 Comparison of the load-displacement curves of un-strengthened steel beams obtained from experiments and FE modeling a) B; b) Bs.

The CFRP plate was defined as an orthotropic material. The elastic modulus in the axial direction (E_1) was obtained from the coupon tests. Other parameters, including the elastic moduli in the other two directions (E_2, E_3), Poisson's ratios (ν_{12}; ν_{13}; ν_{23}), shear modulus (G_{12}; G_{13}; G_{23}) were taken from the previous study (Zeng *et al.* 2018), in which a similar CFRP plate was used. The parameters of the CFRP plate are summarized in **Table 7-2**.

Table 7-2 Parameters of the CFRP plate.

Elastic modulus (E_1) (GPa)	Elastic modulus (E_2 & E_3) (GPa)	Poisson's ratio (ν_{12} & ν_{13})	Poisson's ratio (ν_{23})	Shear modulus (G_{12} & G_{22}) (GPa)	Shear modulus (G_{23}) (GPa)	Coefficient of thermal expansion (α_f) (/℃)
141.9	10	0.3	0.0058	25.5	3.6	4.18×10^{-6}/℃

Special consideration was paid to defining the interfacial bond behavior between the steel beam and the CFRP plate. Two-dimensional cohesive zone elements based on the coupled mixed-mode theory were adopted to simulate the interfacial behavior, in which the onsets of softening and debonding were defined by the quadratic interaction function (Eq. 7-2) and the power-law fracture criterion (Eq. 7-3), respectively.

$$\left\{\frac{\langle\sigma\rangle}{\sigma_p}\right\}^2 + \left\{\frac{\tau}{\tau_p}\right\}^2 = 1 \tag{7-2}$$

$$\left\{\frac{G_I}{G_{Ic}}\right\}^\alpha + \left\{\frac{G_{II}}{G_{IIc}}\right\}^\alpha = 1 \tag{7-3}$$

where σ and σ_p are the normal interfacial stress and the normal peak stress when the interface is subjected to a pure mode I loading. The Macaulay bracket used in the above equation indicates that the compressive stress will not cause the damage. G_I and G_{II} are the energy release rates in the shear and normal directions, respectively. G_{Ic} and G_{IIc} are the critical fracture energies in the shear and normal directions, respectively, which are determined and utilized in pure mode I and mode II analyses. In addition, the power factor (α) was taken as one as suggested by the previous studies (Zeng *et al.* 2018; Deng *et al.* 2018; Barris *et al.* 2018).

The interfacial behavior at the softening stage (i.e., between the onset of softening and the onset of debonding) was defined as a linear softening bond-slip/separation response and the scalar damage variable D was introduced to quantify the degree of damage. D was zero at the damage initiation and equaled to one at the complete interfacial debonding (Zeng *et al.* 2018; Deng *et al.* 2018).

The interfacial bond behaviors in the mode II direction (i.e., bond-slip relationship) at various temperatures were obtained from the previous CFRP-to-steel double-lap shear tests (**Chapter 6**). The configurations of the Mode II bond-slip relationships are shown in **Fig. 7-19a** and the detailed parameters are summarized in **Table 7-3**.

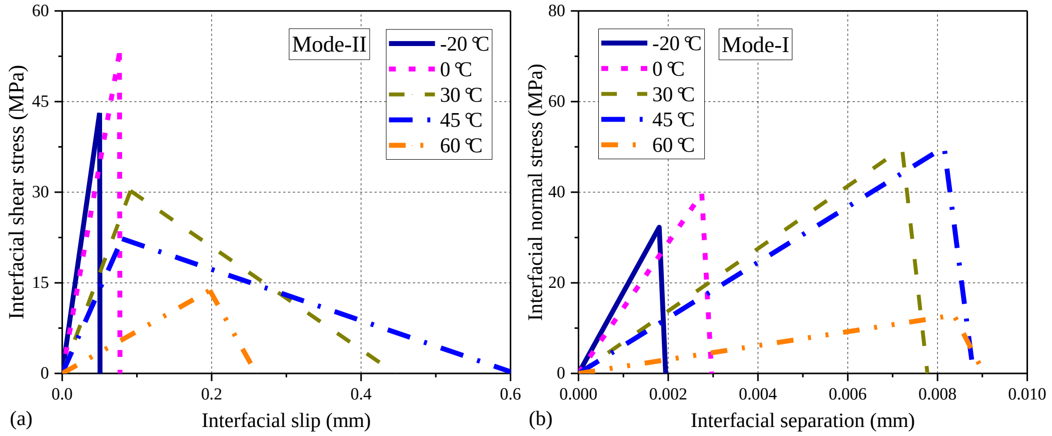

Fig. 7-19 The adopted interfacial bond behavior in FE modeling: a) mode II direction (**Chapter 6**); b) mode I direction.

Table 7-3 The interfacial bond parameters in the mode II direction.

Temperature	Interfacial shear stiffness (MPa/mm)	Peak shear stress (MPa)	Interfacial fracture energy (N/mm)
-20 ℃	861	43.1	1.09
0 ℃	693	53.0	2.05
30 ℃	331	30.2	6.74
45 ℃	278	22.3	6.76
60 ℃	69.6	13.8	1.79

The interfacial bond behavior in the mode I direction (i.e., bond-separation relationship) was also simplified to a bilinear shape with the parameters determined from the tensile tests of adhesive coupons. The tensile strength and elastic modulus of the adhesive coupons were determined as 49.7 MPa and 2.55 GPa at normal temperature. Accordingly, the peak interfacial normal stress and interfacial tensile stiffness were 49.7 MPa and 6.89 GPa/mm. In addition, the slope of the softening branch was set as 12.8 times that of the elastic branch, which was adopted in the previous FE modeling (Teng *et al.* 2015). As the temperature changes, the parameters (e.g., interfacial tensile stiffness and interfacial fracture energy) used for defining the bond behavior in the mode I direction were changed at the same rate as the corresponding parameters in the mode II direction. The obtained interfacial bond behaviors in mode I directions are shown in **Table 7-4**.

Table 7-4 The interfacial bond parameters in the mode I direction.

Temperature	Interfacial normal stiffness (MPa/mm)	Peak normal stress (MPa)	Fracture energy (N/mm)
-20 ℃	17900	32.3	0.031
0 ℃	14400	40.0	0.056
30 ℃	6890	49.7	0.194
45 ℃	6130	49.9	0.220
60 ℃	1540	12.9	0.058

Fig. 7-20 shows the debonding failure modes predicted by the FE model for the steel beams strengthened with a 300 mm CFRP plate (**Fig. 7-20a**) and a 600 mm CFRP plate (**Fig. 7-20b**), respectively. The Mises stress contours are shown in this figure. In addition, the deformation scale factor is set as 10 to make the deformation more visible.

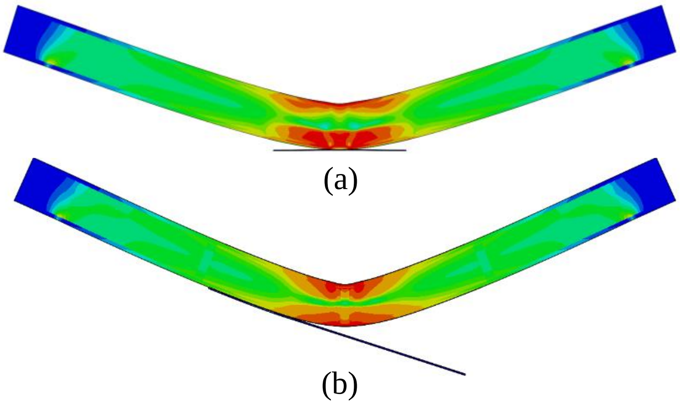

Fig. 7-20 The deformed shape of CFRP-strengthened steel beam after plate-end debonding: a) BP300; b) BP600.

7.4.2 Validation of the FE Model

7.4.2.1 Load-deflection Curves

Fig. 7-21 compares the experimental and FE predicted load-deflection curves of CFRP-strengthened steel beams at various temperatures. The dynamic failure processes at their ultimate stages (i.e., a sudden drop after the peak load due to the interfacial debonding or the CFRP rupture) could not be captured as the general-static solver (Chen *et al.* 2015) approach was adopted in the current FE model. Therefore, the FE predicted process was ended at the onset of debonding (i.e., corresponding to the interfacial stress at plate end decreasing to zero, as shown in **Fig. 7-21 a~e,i**) or the CFRP rupture (i.e., corresponding to the CFRP strain at the middle span increasing to the rupture strain, as shown in **Fig. 7-21 f~h**).

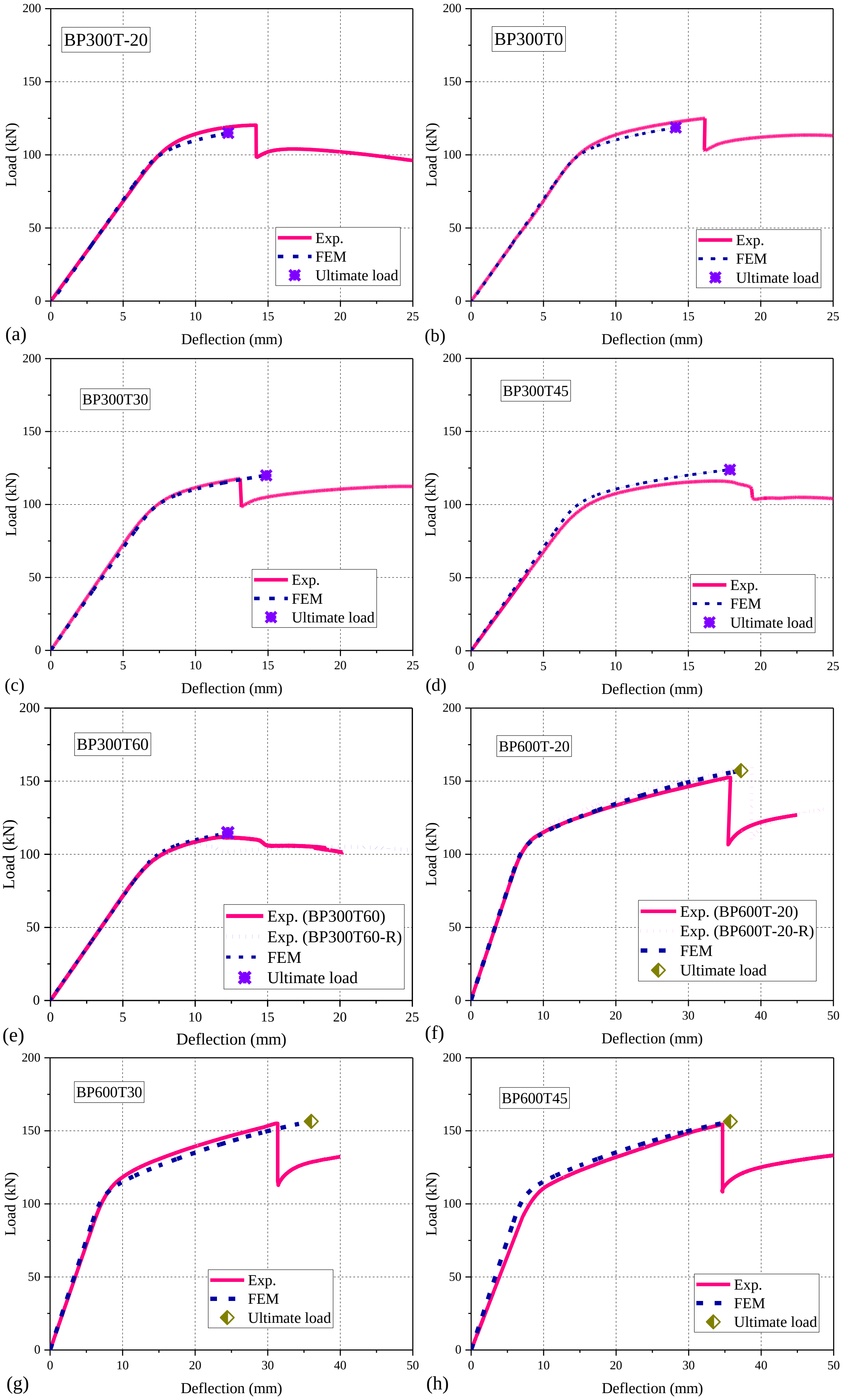
(a)
BP300T-20
(b)
BP300T0
(c)
BP300T30
(d)
BP300T45
(e)
BP300T60
Exp. (BP300T60)
Exp. (BP300T60-R)
(f)
BP600T-20
Exp. (BP600T-20)
Exp. (BP600T-20-R)
(g)
BP600T30
(h)
BP600T45
Exp.
FEM
Ultimate load
Load (kN)
Deflection (mm)
0
50
100
150
200
0
5
10
15
20
25
0
10
20
30
40
50

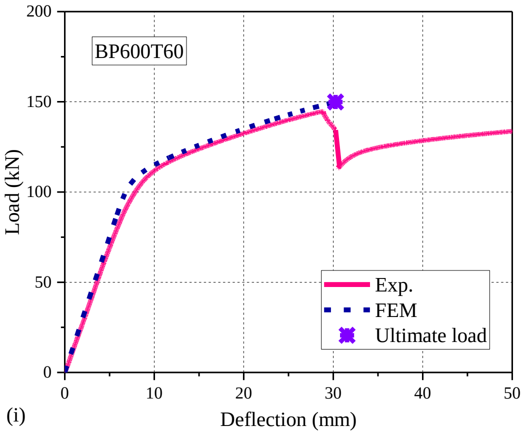

Fig. 7-21 Comparison of the load-deflection curves obtained from FE modeling and experiments: a) BP300T-20; b) BP300T0; c) BP300T30; d) BP300T45; e) BP300T60; f) BP600T-20; g) BP600T30; h) BP600T45; i) BP600T60.

All the load-deflection curves of CFRP-strengthened steel beams were very well predicted by the FE modeling, which indicated that the interfacial bond parameters adopted in both mode I (i.e., **Table 7-4**) and mode II directions (i.e., **Table 7-3**) were rational.

7.4.2.2 Distributions of the CFRP Strains

Fig. 7-22 compares the experimental and FE predicted CFRP strain distributions before applying the mechanical loading under two extreme temperatures (i.e., -20 ℃ and 80 ℃). It should be noted that the property of the strain gauge was sensitive to the temperature variation when the magnitudes of thermal strains were quite low, and thus the CFRP strains exhibited certain scatters. Nevertheless, the thermal strains in the CFRP plate obtained from FE modeling and experiments were quite close.

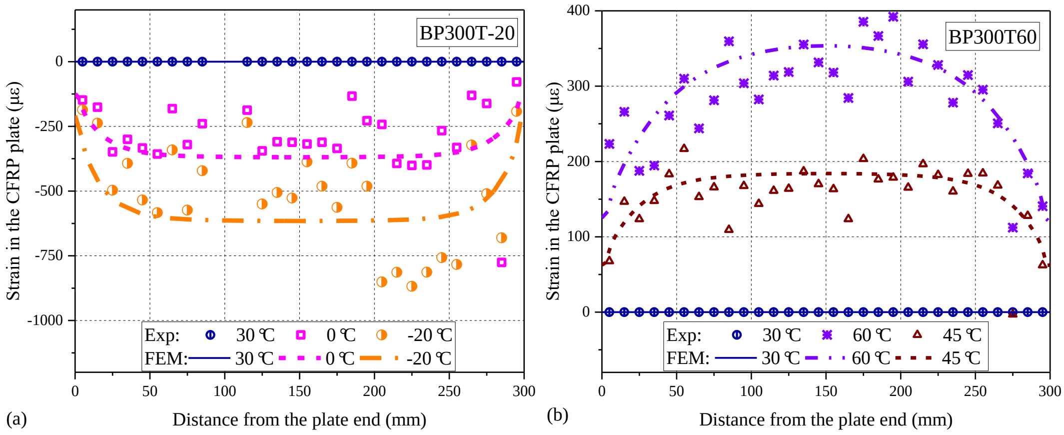

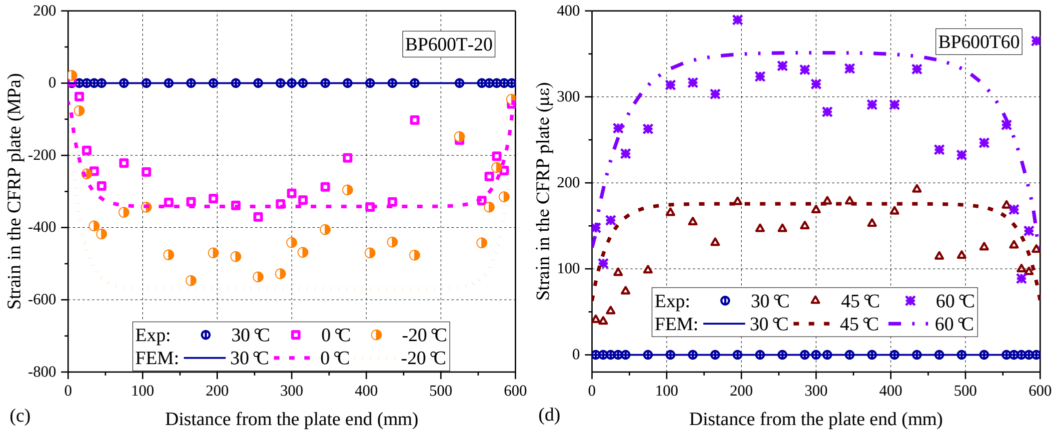

Fig. 7-22 Comparison of the distributions of CFRP strain under pure thermal loading obtained from FE modeling and experimental results: a) BP300T-20; b) BP300T60; c) BP600T-20; d) BP600T60.

Fig. 7-23 compares the distributions of CFRP strains obtained from the experiments and FE modeling under combined mechanical and thermal loading. The difference was slightly large at the ultimate state of the beam specimens with the short bond length (e.g., **Fig. 7-23 a~e**), probably due to the different bond-slip behaviors in cases of short and long bond length (Dai *et al.* 2006). However, the agreement between the experiments and FE modeling was generally acceptable for all specimens, which validated the proposed FE model. According to the **Fig. 7-21 a,b** and **Fig. 7-23 a,b**, the predicted load, deflection and CFRP strain values at the ultimate states of BP300T-20 and BP300T0 were slightly lower than the experimental data, probably due to the underestimation of bond parameters (i.e., peak shear stress and interfacial fracture energy) in the double-lap shear tests (**Chapter 6**).

In addition, the CFRP strain values at the ultimate stages of beams in BP300 series are obvious lower than that in BP600 series at all temeprature levels, indicating that the utilization efficiency of the CFRP strength was enhanced at longer CFRP plates.

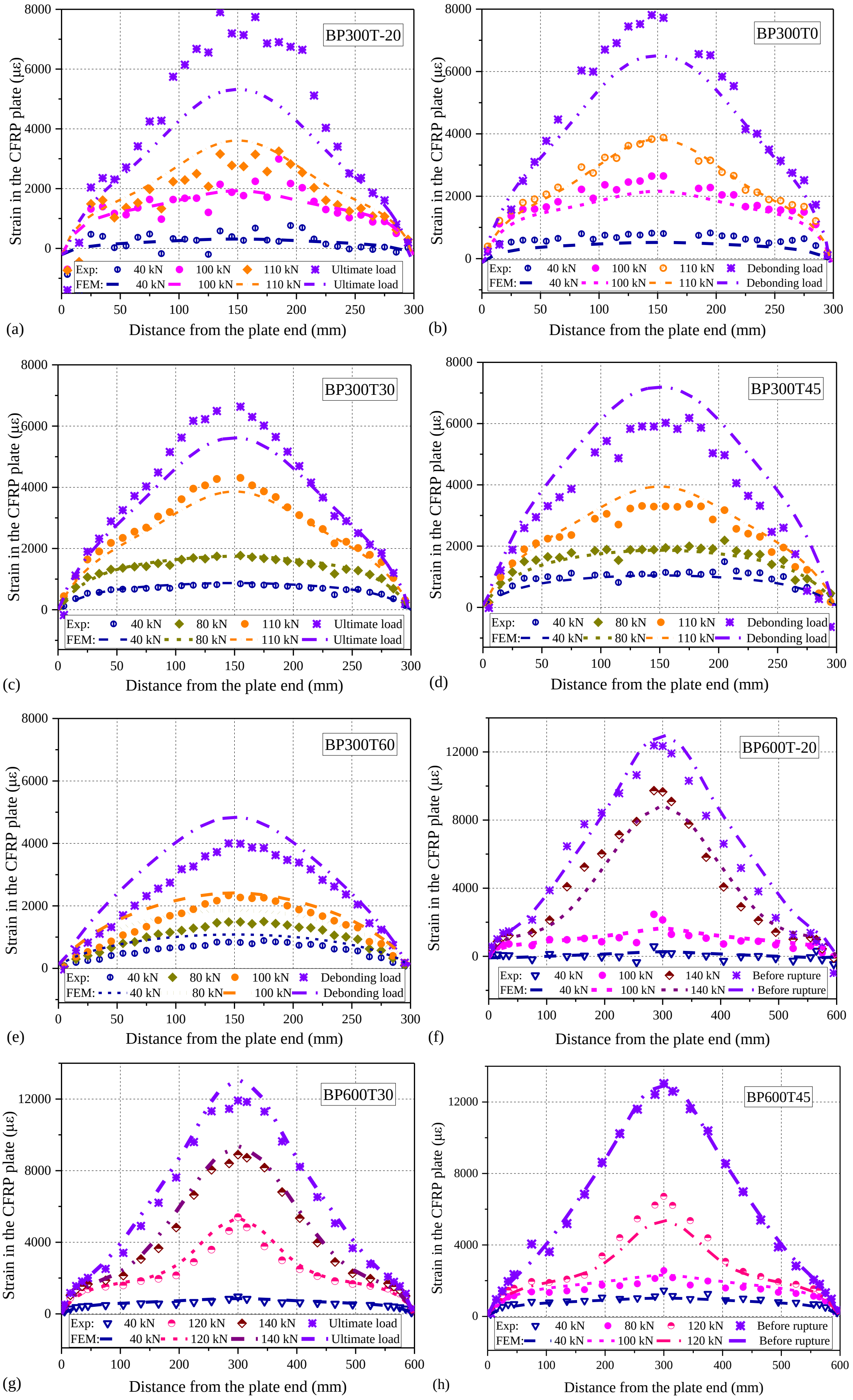
BP300T-20
Strain in the CFRP plate (με)
Distance from the plate end (mm)
Exp: 40 kN 100 kN 110 kN Ultimate load
FEM: 40 kN 100 kN 110 kN Ultimate load
BP300T0
Exp: 40 kN 100 kN 110 kN Debonding load
FEM: 40 kN 100 kN 110 kN Debonding load
BP300T30
Exp: 40 kN 80 kN 110 kN Ultimate load
FEM: 40 kN 80 kN 110 kN Ultimate load
BP300T45
Exp: 40 kN 80 kN 110 kN Debonding load
FEM: 40 kN 80 kN 110 kN Debonding load
BP300T60
Exp: 40 kN 80 kN 100 kN Debonding load
FEM: 40 kN 80 kN 100 kN Debonding load
BP600T-20
Exp: 40 kN 100 kN 140 kN Before rupture
FEM: 40 kN 100 kN 140 kN Before rupture
BP600T30
Exp: 40 kN 120 kN 140 kN Ultimate load
FEM: 40 kN 120 kN 140 kN Ultimate load
BP600T45
Exp: 40 kN 80 kN 120 kN Before rupture
FEM: 40 kN 100 kN 120 kN Before rupture
0
2000
4000
6000
8000
12000
50
100
150
200
250
300
400
500
600

(a) (b) (c) (d) (e) (f) (g) (h)

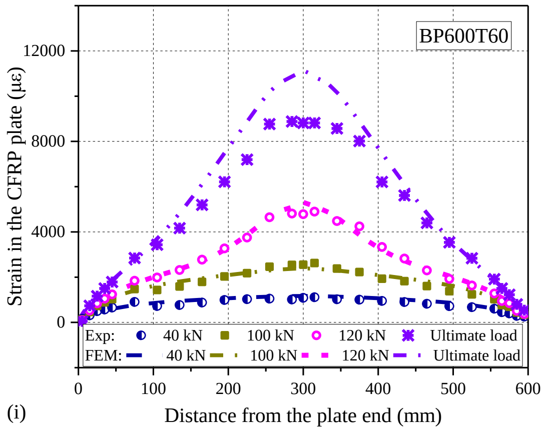

Fig. 7-23 Comparison of the distributions of CFRP strains obtained from experiments and FE modeling: a) BP300T-20; b) BP300T0; c) BP300T30; d) BP300T45; e) BP300T60; f) BP600T-20; g) BP600T30; h) BP600T45; i) BP600T60.

7.5. CONCLUSIONS

This chapter investigated the structural performance of CFRP-strengthened steel beams and examined the corresponding interface behaviors at different service temperatures ranging from -20 ℃ to 60 ℃. The following conclusions can be obtained based on the results from the experimental study and the FE modeling:

a) Steel beams strengthened with a shorter CFRP plate (i.e., 300 mm) were failed due to the plate-end debonding at all temperatures. The plate-end debonding load was increased at decreased temperatures but decreased at 60ºC. The plate-end debonding was avoided at the temperatures from -20ºC to 45ºC by adopting a longer CFRP plate (i.e., 600 mm). However, it still occurred at 60ºC, corresponding to a significantly reduced ultimate load.

b) The thermally-induced softening in the bonding adhesive at 60ºC led to the deterioration of the composite action in CFRP-strengthened steel beams, which further increased the interfacial slips at the plate ends and reduced the utilization efficiency of the CFRP's tensile strength.

c) The structural performance of CFRP-strengthened steel beams at different service temperatures could be well predicted by the proposed FE model, in which the temperature-dependent bond properties and thermal-induced deformation incompatibility were appropriately considered.

7.6. REFERENCES

Abaqus 6.14 (2014) "Documentation." Providence, RI, USA: Dassault Systemes Simulia Corporation.

Amada, S. and Satoh, A. (2000). "Fractal analysis of surfaces roughened by grit blasting. " *Journal of Adhesion Science and Technology*, 14(1): p. 27-41.

ASTM-D3039 (2017). "Standard Test Method for Tensile Properties of Polymer Matrix Composite Materials." West Conshohocken, Philadelphia (PA): ASTM International.

Barris, C., Correia, L., and Sena-Cruz, J. (2018). "Experimental study on the bond behaviour of a transversely compressed mechanical anchorage system for externally bonded reinforcement." *Composite Structures*, 200: p. 217-228.

Biscaia, H.C., and Ribeiro, P. (2019). "A temperature-dependent bond-slip model for CFRP-to-steel joints." *Composite Structures*, 217, 186-205.

Chen, G.M., Teng, J.G., Chen, J.F., and Xiao, Q.G. (2015). "Finite element modeling of debonding failures in FRP-strengthened RC beams: A dynamic approach. " *Computers & Structures*, 158: p. 167-183.

Colombi, P., and Poggi, C. (2006). "An experimental, analytical and numerical study of the static behavior of steel beams reinforced by pultruded CFRP strips." *Composite Part B-Engineering*, 37(1), 64-73

Dai, J.G., Ueda, T. and Sato, Y. (2006). Unified Analytical Approaches for Determining Shear Bond Characteristics of FRP-Concrete Interfaces through Pullout Tests, *Journal of Advanced Concrete Technology*, 4(1), 133-145.

Deng, J., and Lee, M. M. K. (2007). "Behaviour under static loading of metallic beams reinforced with a bonded CFRP plate." *Composite Structures*, 78(2), 232-242

Deng, J., Li J.H., Wang Y. and Xie W.Z. (2018). "Numerical study on notched steel beams strengthened by CFRP plates." *Construction and Building Materials* 163: 622-633.

EN ISO, 11359-2 (1999): "Plastics-Thermomechanical Analysis (TMA). Part 2: Determination of Coefficient of Linear Thermal Expansion and Glass Transition Temperature."

EN ISO, 6892-1 (2016): "Metallic Materials-Tensile Testing, Part 1: Method of Test at Room Temperature."

Fernando, D., Teng, J.G., Yu, T., and Zhao, X.L. (2013). "Preparation and Characterization of Steel Surfaces for Adhesive Bonding." *Journal of Composites for Construction*, 17(6).

Gao, W.Y., Teng, J.G., and Dai, J.G. (2012). "Effect of Temperature Variation on the Full-Range Behavior of FRP-to-Concrete Bonded Joints." *Journal of Composites for Construction*, 16(6): p. 671-683.

Gao, W.Y., Dai, J.G., and Teng, J.G. (2015). "Analysis of Mode II debonding behavior of fiber-reinforced polymer-to-substrate bonded joints subjected to combined thermal and mechanical loading. " *Engineering Fracture Mechanics*, 136: p. 241-264.

Gholami, M., Sam, A.R.M., Yatim, J.M., Tahir, M.M. (2013). "A review on steel/CFRP strengthening systems focusing environmental performance." *Construction and Building Materials*, 47: p. 301-310.

Ko, H., Matthys, S., Palmieri, A., and Sato, Y. (2014). "Development of a simplified bond stress–slip model for bonded FRP–concrete interfaces." *Construction and Building Materials*, 68: p. 142-157.

Smith, S.T. and Teng, J.G. (2001). "Interfacial stresses in plated beams." *Engineering Structures*. 23(7), 857-871.

Sahin, M.U., and Dawood, M. (2016). "Experimental Investigation of Bond between High-Modulus CFRP and Steel at Moderately Elevated Temperatures." *Journal of Composites for Construction*, 20(6), 04016049.

Stratford, T.J., and Bisby, L.A. (2012). "Effect of Warm Temperatures on Externally Bonded FRP Strengthening." *Journal of Composites for Construction*, 16(3), 235-244.

Teng, J.G., Fernando, D., and Yu, T. (2015). "Finite element modelling of debonding failures in steel beams flexurally strengthened with CFRP laminates." *Engineering Structures*, 86, 213-224.

Teng, J.G., Yu, T., and Fernando, D. (2012). "Strengthening of steel structures with fiber-reinforced polymer composites." *Journal of Constructional Steel Research*, 78, 131-143.

Teng, R., Guo, Y., Wang, H., Zhao, Z., Wang, X. (2021). "Experimental study of bending interface characteristics of CFRP-strengthened long-span steel main beams at different temperatures." *Engineering Structures*, 235.

Yang, Y., H. Biscaia, C. Chastre and M. Silva (2017). "Bond characteristics of CFRP-to-steel joints." *Journal of Constructional Steel Research* 138: 401-419.

Yoshitake, I., H. Tsuda, J. Itose and N. Hisabe (2014). "Effect of discrepancy in thermal expansion coefficients of CFRP and steel under cold temperature." *Construction and Building Materials* 59: 17-24.

Yu, T., D. Fernando, J.G. Teng and X.L. Zhao (2012). "Experimental study on CFRP-to-steel bonded interfaces." *Composites Part B-Engineering* 43(5): 2279-2289.

Zeng, J.J., Gao, W.Y., and Liu, F. (2018). "Interfacial behavior and debonding failures of full-scale CFRP-strengthened H-section steel beams." *Composite Structures*, 201, 540-552.

Zhou, H., Fernando, D., Torero, J. L., Torres, J. P., Maluk, C., and Emberley, R. (2020). "Bond Behavior of CFRP-to-Steel Bonded Joints at Mild Temperatures: Experimental Study." *Journal of Composites for Constructio*n, 24(6), 04020070.

CHAPTER 8

INTERMEDIATE CRACK-INDUCED DEBONDING IN CFRP-RETROFITTED NOTCHED STEEL BEAMS AT DIFFERENT SERVICE TEMPERATURES: EXPERIMENTAL TEST AND FINITE ELEMENT MODELING

8.1. INTRODUCTION

Existing research has been demonstrated the effectiveness of CFRP strengthening technology in enhancing the structural performance of steel beams with initial cracks under both static (Deng *et al.* 2016; Hmidan *et al.* 2011) and fatigue loadings (Chen and Huang 2019; Colombi and Fava 2015; Deng *et al.* 2022; Yu and Wu 2017). For example, Deng *et al.* (2018) reported that the load-carrying capacity of the notched steel beam under static loading was increased twice by CFRP retrofitting. In addition, the CFRP strengthening can dramatically retard the crack propagation under fatigue loading and thus extend the fatigue life of defected steel beams (Chen and Huang 2019; Colombi and Fava 2015; Yu and Wu 2017). The bonded CFRP plate bridges the two sides of a crack and effectively arrests the crack opening. However, the high tensile force sustained by the CFRP plate at the crack locations also generates stress concentrations at the bonding interface between the CFRP plate and the steel beam, which may result in the occurrence of interfacial debonding. According to the experimental observation, such interfacial debonding initiates at the cracked section, thus it is termed as intermediate crack-induced (IC) debonding. The IC debonding limits the fully utilization of the tensile strength in the CFRP plate, the increase of load-carrying capacity as well as the ductility of strengthened steel beams.

The performance of CFRP-plated steel beams can be significantly affected by the service temperature variation, especially when the load-carrying capacity is controlled by the interfacial bonding. This is because the properties of the adhesive layer, which is commonly formed by epoxy resin, may change at different service temperatures, especially when the temperature increases close to and becomes higher than the glass transition temperature (T_g) (Biscaia 2019; Dai *et al.* 2013). The reported T_g of most commercial available epoxy resin for structural bonding is around 65 ℃ (Ko *et al.* 2014) and this temperature can be achieved when the steel structure is exposed directly to the sunshine (Krzywoń 2017). In addition, according to the theoretical analysis conducted in **Chapter 5**, the thermal stress induced by elevated temperatures tends to alleviate the stress concentration near the notched section and thus improve the debonding load, and vice versa. The proposed analytical solution was validated through comparison with the finite element (FE) analysis results instead of test data. In fact, there was no test data existing on the IC debonding mechanism of CFRP-retrofitted steel beams under temperature variations. This chapter aimed to fill in this gap and conduct a comprehensive experimental study aiming to investigate how different service temperatures affect the structural performance of CFRP-retrofitted notched steel beams, which are expected to fail due to the IC debonding.

8.2. EXPERIMENTAL PROGRAM

The experimental program consisted of flexural tests on CFRP-retrofitted steel beams at various temperatures, including -20 ℃, 0 ℃, 30 ℃, 45 ℃, 60 ℃ and 80 ℃. The configuration of the test specimens is shown in **Fig. 8-1**. The design of specimens is quite similar to that in the previous experiments conducted by Deng *et al.* (2016) under normal temperature. Considering that the ‘effective bond length’ may be increased at elevated temperatures (Firmo *et al.* 2015; Gao *et al.* 2012; Zhou *et al.* 2020), the length of the CFRP plates was doubled from 400 mm to 800 mm as compared to Deng *et al.*’s experiments (2016).

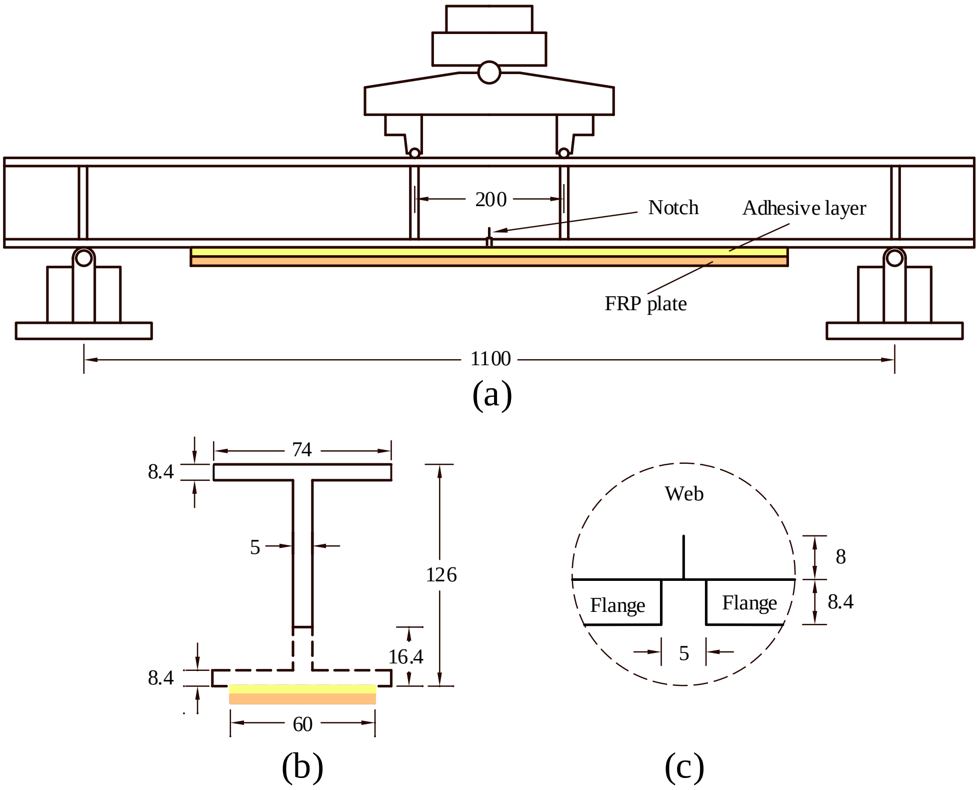

Fig. 8-1 Schematic of the CFRP-retrofitted steel beam: a) front view; b) side view; c) close view of the precast notch.

As shown in **Fig. 8-1**, CFRP-retrofitted steel beams were tested under four-point bending. The beams were supported by two roller supports at a clear span of 1.1 m and loaded by a load distributer with the constant moment zone of 0.2 m. The total length of the steel beams was 1.3 m. The steel beams were prefabricated with a notch to simulate the crack defects on the soffit of the steel beam. The notched steel beams were retrofitted by 0.8 m long CFRP plates. In addition, two different thicknesses of CFRP plates (thickness of 1.2 mm and 1.4 mm) were used. The specimens were symbolized according to the thickness of CFRP plate and the experimental temperature. For example, ‘BnP1.4T30’ represents the notched steel beam retrofitted by a 1.4 mm thick CFRP plate and tested under 30 ℃. In addition, the notched steel beam without retrofitting (Bn) was also tested for references. The details of all tested specimens are summarized in **Table 8-1**.

Table 8-1 Detail of specimens

·Specimens code		CFRP plate thickness (mm)	Test temperature (℃)
Bn		-	30
BnP1.2	BnP1.2T-20	1.2	-20
	BnP1.2T0		0
	BnP1.2T30		30
	BnP1.2T45		45
	BnP1.2T60		60
	BnP1.2T80		80
BnP1.4	BnP1.4T-20	1.4	-20
	BnP1.4T0		0
	BnP1.4T30		30
	BnP1.4T45		45
	BnP1.4T60		60
	BnP1.4T80		80

The close view of the prefabricated notch is shown in **Fig. 8-1c**. The width of the crack opening is 5 mm and height of the opening was the same as the thickness of the bottom flange. In addition, a narrow notch was cut in the web, which was perpendicular to the axis of the beam and with width of 0.18 mm and height of 8 mm. In addition, some plate stiffeners with the thickness of 6 mm were welded on both sides of the beam's web at the loading and supporting points, in order to avoid the local buckling.

8.2.1 Materials

The properties of the steel were measured according to ASTM A370, with the dimensions shown in **Fig. 8-2**. As a result, the elastic modulus, yield strength and poisson's ratio were 210.5 ± 6.5 GPa, 359.0 ± 5.8 MPa and 0.27, respectively. The properties of CFRP plates, measured according to ASTM-D3039, were given by the manufacturer. The elastic moduli of the 1.2 mm and the 1.4 mm thick CFRP plates were 171.3 ±4.2 GPa and 158.2 ±3.6 GPa, and the corresponding maximum tensile strengths were 2743.3 ±127.9 MPa and 3044.4 ±129.7 MPa, respectively. In addition, the thermal expansion ratios (CTEs) of the materials were measured by thermomechanical analysis (TMA) test, according to BS ISO 11359 (1999). The resultant CTEs for steel, 1.2 mm and 1.4 mm CFRP plates were $1.14*10^{-5}$/℃, $-9.10*10^{-7}$/℃ and $-8.48*10^{-7}$/℃, respectively.

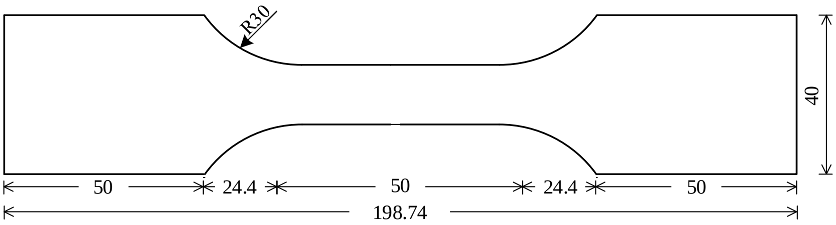

Unit: mm

Fig. 8-2 Dimensions of the steel coupons

Sikadur-330CN was adopted as the adhesive for bonding the CFRP plate onto the steel beam. The mechanical properties of the bonding adhesive at room temperature, including the tensile strength and the elastic modulus were 49.7 MPa and 2.55 GPa, respectively, as provided by the manufacturer. Moreover, the thermal deterioration of the bonding adhesive, which was prepared and cured in the same environments as the beam specimens, was measured by the dynamic mechanical analysis (DMA) following ASTM-D7028 (2007). Then the DMA test was conducted with a hearting rate of 2 ℃/min and oscillation frequency of 1 Hz on a single cantilever configuration. **Fig. 8-3** shows the measured variation of the storage (elastic) modulus, the loss (viscous) modulus and the tan delta (i.e., the ratio between the loss modulus and the storage modulus) as the temperature increases. It can be observed that, as the increase of temperature, the elastic modulus decreases slightly at a temperature lower than T_g, then decreases dramatically after the glass transition temperature (T_g). According to the different definitions of T_g (Othman *et al.* 2013), the T_g is 56.3 ℃ at onset of softening, 60.2 ℃ at peak loss modulus and 69.7 ℃ at peak tan delta.

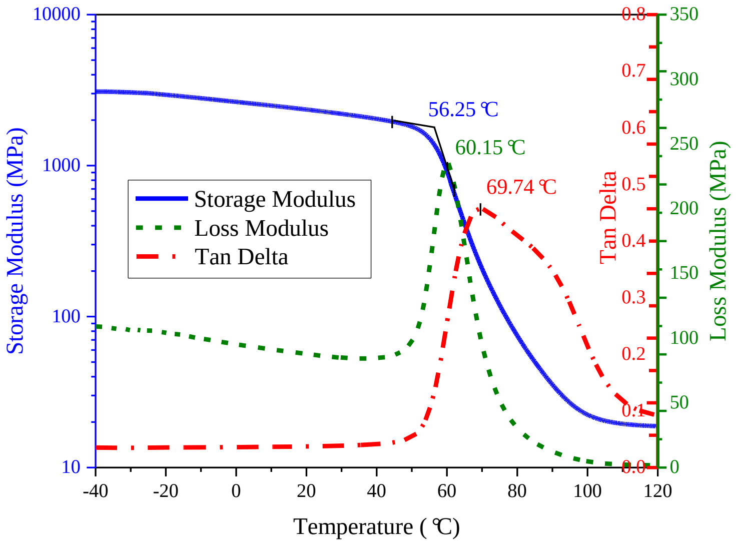

Fig. 8-3 DMA results

8.2.2 Specimens

The bottom surface of each steel beam was degreased by acetone and sandblasted to remove the oxide coating (**Fig. 8-4)**. A 0.25 mm diameter angular alumina grit was used for the sandblasting the bottom surface of each steel beam to ensure its chemical compatibility with the adhesive following the suggestion provided by Fernando *et al.* (2013). In addition, the blasting angle was controlled at about 75 ° (Amada and Satoh 2000), and the pressure was controlled within 0.4 MPa to 0.6 MPa. After sandblasting, the steel surface was cleaned away from any dust with compressed air flow. Prior to being bonded to the steel surface, the CFRP plate was carefully cleaned up with acetone using gauze. Afterwards, the CFRP plate was adhesively bonded to the steel beam within half an hour, to avoid oxidation of steel surface. As recommended by Deng and Lee (2007), more adhesives were laid along the center than the outer edges, which allowed the air trapped between the adherends to escape when they were pushed together. Then a uniform compressive stress of 4.2 kPa was applied on the top surface of the CFRP plate to ensure that the externally bonded CFRP plate and steel beam were tightly bonded together during the curing process of the CFRP strengthening system (Colombi *et al.* 2015). Afterwards, in order to avoid the occurrence of spew fillet and estimate the consumption of epoxy resin, the excess adhesive along the sides of the plate was scraped off, collected and weighted. The average thickness was about 0.37 mm. Then the CFRP-retrofitted steel beams were cured in room temperature and cured for about six months before the tests.

Fig. 8-4 Sandblasting of the steel surface

8.2.3 *Testing Procedure and Instrumentations*

The testing procedure was adopted as follows: First, the beam was put inside the environmental chamber and the internal temperature was changed; Second, after the target temperature was reached, it will be maintained at a nearly constant value. Finally, the beam was mechanically loaded until failure.

A heating and cooling system was specifically designed to tune the temperature in the chamber. The chamber was heated by electronic heating pipes while cooled down by pumping in liquid nitrogen. An electric fan was installed to assist decreasing the altitudinal temperature gradient inside the chamber. In order to monitor the temperature variations in the beam specimens, four K-type thermocouples were installed at various locations on the surface of the specimens, including the surface of CFRP plate, the beam web at mid-span location, and the upper flange of the steel beam at both ends. In order to isolate the thermal couples from the air temperature change inside the experimental chamber, they were coated with 2 mm blue tack.

Fig. 8-5 shows the change of temperatures measured at different locations of specimens under the 60 ℃ testing temperature. It can be seen that the measured temperatures were quite close to each other at various locations and changed gradually according to the set temperature. In order to avoid significant temperature gradients induced in the specimens, the temperature change was controlled at a low rate. After the measured temperature of the specimen reached the target value, the air temperature inside the chamber was regulated at a nearly constant value for at least 30 minutes, to ensure that the temperature was uniformly distributed in the specimen.

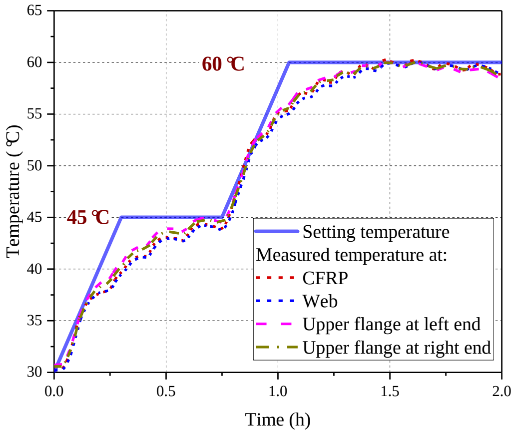

Fig. 8-5 Measured temperature history of the CFRP-retrofitted steel beam during the heating process.

The mechanical loading was applied by an electro-hydraulic loading and control system, at a constant loading speed of 3 mm/min. In addition, the two supporters and the loading points of the load distribution girder were designed using smooth rollers, which could rotate freely. This seemed to be important in previous experiments (Fu *et al.* 2018) but was often ignored. During the loading process, the load, mid-span deflection, axial strain distributions in the CFRP plate, and crack mouth open displacement (CMOD) at the notch location were acquired at a frequency of 5 Hz. The mid-span deflection was obtained from the readings of six LVDTs located at both the mid-span and two ends of the beam. The strain gauges were bonded to the surface of CFRP plates using NP-50B adhesive, which is applicable for the service temperature ranging from -30 ℃ to 300 ℃. In addition, for thermal compensation purpose, the strain gauges from same batch were attached to the TiS glass and placed near the strain measurement points (Sahin and Dawood 2016). Special considerations were given to the locations of strain gauges. The interval of strain gauges was set as 10 mm near the notch, where there is a higher magnitude of interfacial shear stress, 20 mm near the plate ends, and 30 mm between these two regions. In total, 44 strain gauges were adopted for measuring the strain distributions along the CFRP plate (refer to **Fig. 8-6** for details).

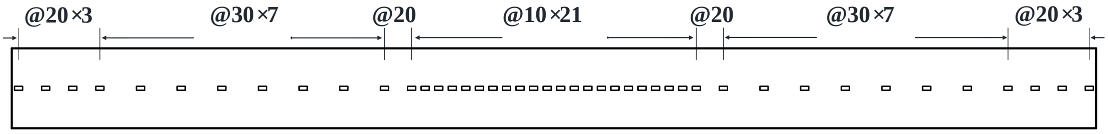

Fig. 8-6 Locations of strain gauges attached on the CFRP plate

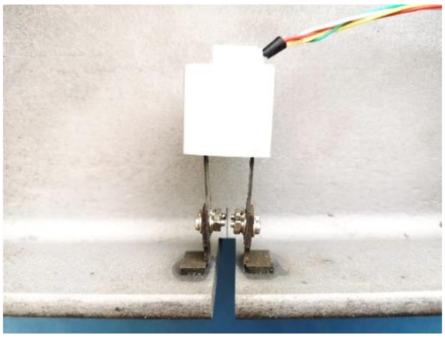

Fig. 8-7 The extensometer

The CMOD is also an important parameter to show the strengthening efficiency of CFRP plates (Chen and Huang 2019; Yu and Wu 2017). As shown in **Fig. 8-7,** at each side of the beam an extensometer was installed at the two sides of the notch of the bottom flange to measure the CMOD. To correct the eccentricity of the applied load and possible torsion of the beam during the loading process, the beam was pre-loaded to around 10 kN. Then the two measured CMODs were compared so that the loading apparatus could be adjusted where necessary.

8.3. EXPERIMENTAL RESULTS

8.3.1 Test Observations

Fig. 8-8a shows the typical failure mode of CFRP-retrofitted steel beams. Usually, the retrofitted steel beams were failed by interfacial debonding at its one side. In addition, there was some residual deformation in the steel beam after unloading. The local buckling of the steel beam was not found because of the existence of steel stiffeners. Moreover, the propagation of the prefabricated crack tip was also found in the retrofitted steel beams, mainly due to the continuous loading after the CFRP debonding. **Fig. 8-8b** shows a close view of the debonded side of the CFRP-retrofitted steel beam. After debonding, there was no residual deformation in the CFRP plate due to the material elasticity. **Fig. 8-8c&d** show the close views of the debonded interface on both the CFRP plate and substrate steel sides. It is clearly seen that the cohesive failure, for which the failure occurred inside the adhesive layer, was the dominant failure mode.

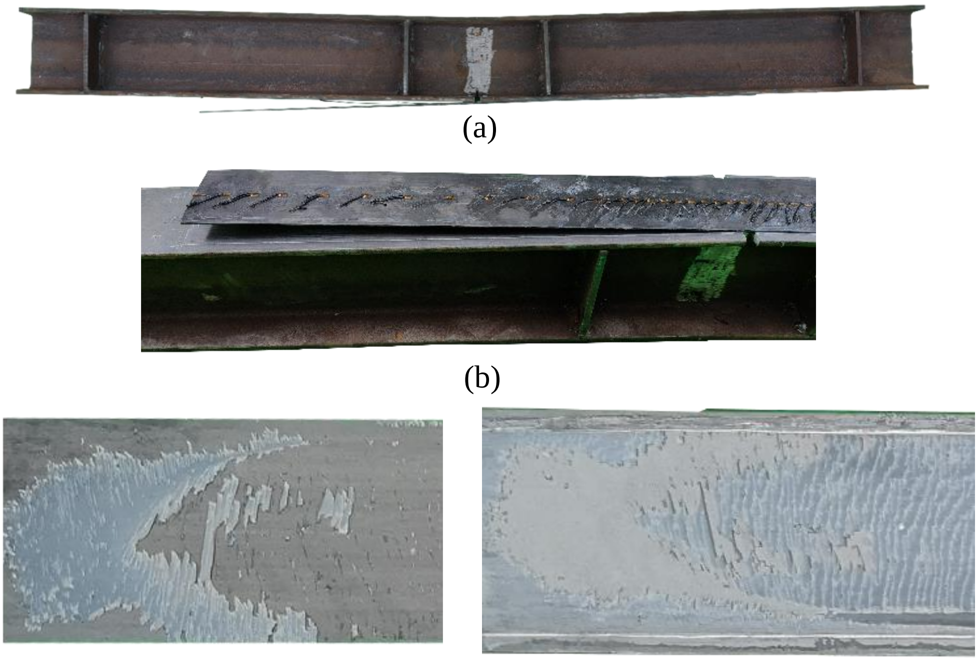
(a)

(b)

(c) (d)

Fig. 8-8 Typical failure mode of CFRP-retrofitted steel beams: a) front view; b) closed view of the debonded side; close views of the debonded surface c) on the CFRP plate; d) on the substrate steel side.

8.3.2 Structural Performance of Two CFRP-Retrofitted Steel Beams Tested at Room Temperature

Fig. 8-9 shows the load-deflection and the CMOD-load curves of two CFRP-retrofitted steel beams and the reference notched steel beam without retrofitting, which were tested at normal temperature (i.e., 30 ℃). It is seen that, under a low level of mechanical loading, the load-deflection curves exhibited typical elastic behavior and the deflection increased linearly with the applied load. For the reference notched beam without retrofitting, the flexural stiffness of the steel beam decreased after the steel yielding, and then exhibited almost plastic behavior with increasing CMOD value. In comparison, for the retrofitted steel beams, the initiation of interfacial debonding occurred at one side, which was witnessed by the reduced interfacial stress measured at this side to almost zero. The loads at the onset of debonding for both specimens were quite close (65.6 kN vs. 65.0 kN). Then the interfacial debonding propagated gradually from the notch to the plate ends with almost the constant axial force sustained by the CFRP plate at the notch location. Meanwhile, the flexural stiffness of the CFRP-retrofitted beam decreased slightly, while the steel beam remained elastic. After the steel yielded, the load increased at a much lower rate, accompanied by a rapid increase in the CMOD. Finally, the load dropped abruptly corresponding to the ultimate debonding.

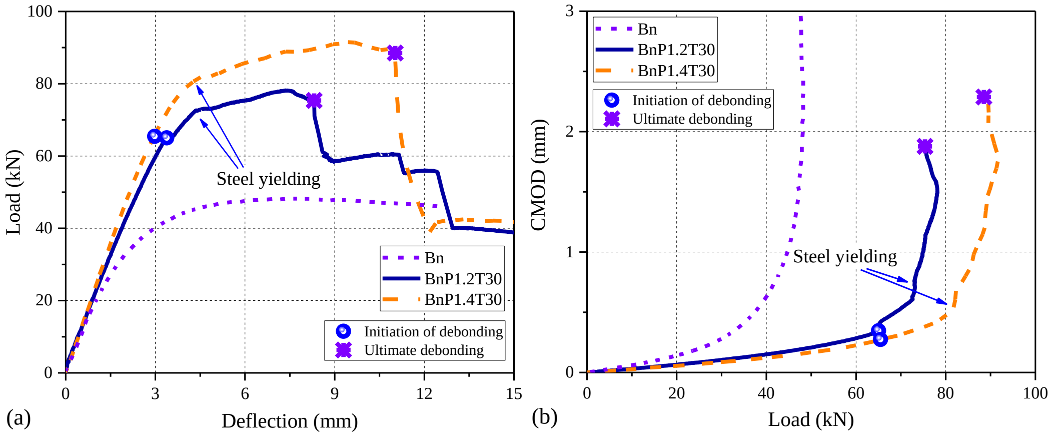

Fig. 8-9 Structural performance of two CFRP-retrofitted steel beams tested at room temperature: a) the load-deflection curves; b) the CMOD-load curves.

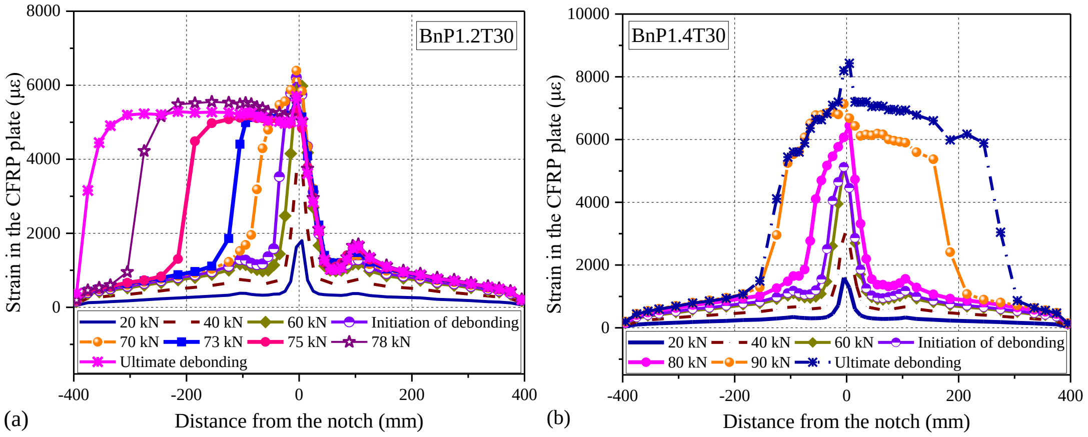

Fig. 8-10 Strain distributions in the CFRP plate: a) BnP1.2T30; b) BnP1.4T30.

The strain distributions in the CFRP plate at the different levels of loads are shown in **Fig. 8-10**. At relatively low load levels, the strains in the CFRP plate increased from zero at the end of the CFRP plate to the maximum value at the notched section. Moreover, the axial strain values at each location grew with the increased load. As seen in **Fig. 8-10**, the axial strains along the bond length of the two specimens were almost symmetrically distributed around the notch at lower load levels (e.g., 20 kN, 40 kN and 60 kN). However, when the load further increased, the initiation of interfacial debonding occurred near the notched section at one side, where the axial strains in the CFRP plate kept almost the constant, indicating a debonded interfacial zone there.

Using the measured CFRP strains along the bond length, the local interfacial shear stress ($\tau_{i+\frac{1}{2}}$) (i starts from the plate end) between two subsequent strain gauges at the locations of x_i and x_{i+1} can be derived based on the difference of the measured strains (i.e., $\varepsilon_{i+1} - \varepsilon_i$) using the following equation.

$$\tau_{i+\frac{1}{2}} = \frac{\varepsilon_{i+1} - \varepsilon_i}{x_{i+1} - x_i} E_f t_f \tag{8-1}$$

where E_f and t_f are the elastic modulus and the thickness of the CFRP plate, respectively.

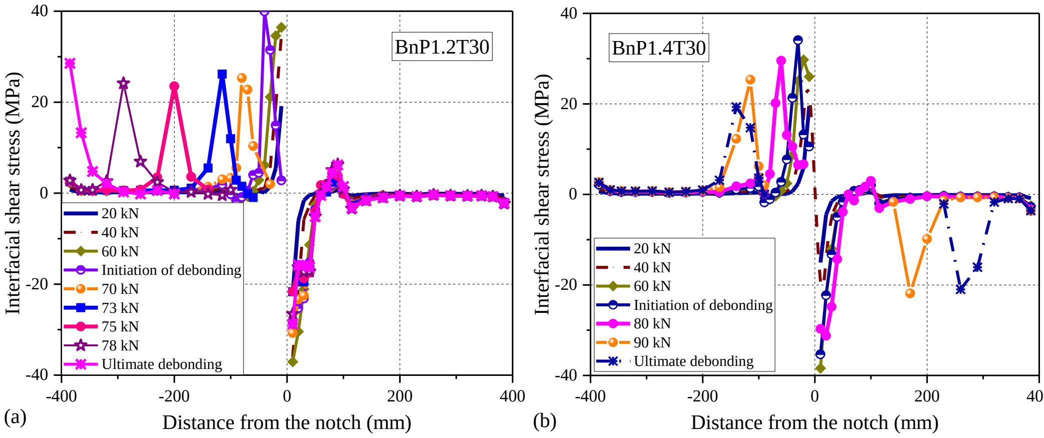

Fig. 8-11 Distributions of interfacial shear stress: a) BnP1.2T30; b) BnP1.4T30.

Fig. 8-11 shows the obtained distributions of the interfacial shear stresses in the two beams tested at 30 ℃. When the applied load was low, the entire bond interface was in the elastic (*E*) stage and the interfacial shear stresses were higher near both the notch and plate ends. After the interfacial shear stress near the notch increased to the maximum value, the interface entered into the elastic-softening (*E-S*) stage and the local interfacial shear stress started to decrease. With the further increase of the applied load, the interfacial shear stress near the notch decreased gradually to almost the zero value, implying the occurrence of local interfacial debonding. Then, during the elastic-softening-debonding (*E-S-D*) stage, the interfacial debonding propagated from the notched section to the plate end. That is, the location corresponding to the maximum shear stress shifted from the notch to the plate end. With the propagation of the debonding failure, the deflections of the CFRP-retrofitted notched steel beams grew significantly in accompany with a slight increase of the applied load. Finally, as seen in **Fig. 8-9**, an abrupt drop of the applied load occurred due to the failure of the CFRP-retrofitted steel beams (i.e., complete debonding/separation of the CFRP plate from the beam usually at one span).

8.3.3 Structural Performance of CFRP-Retrofitted Steel Beams at Other Temperatures

8.3.3.1 Load-deflection curves

Fig. 8-12 compares the load-deflection curves of the un-strengthened notched steel beam and CFRP-retrofitted steel beams at various temperatures. It is seen that the load-carrying capacity of the strengthened beams under all temperatures was significantly improved under all temperatures. However, the behaviors of the CFRP-retrofitted steel beams were quite different at different temperatures, in terms of the debonding load, member stiffnesses and ultimate deflection. The highest load-carrying capacity and ultimate deflection were achieved at 60 ℃. In comparison, both the load-carrying capacity and deformability of the CFRP-retrofitted steel beams were significantly lower at low temperatures (i.e., -20 ℃ and 0 ℃).

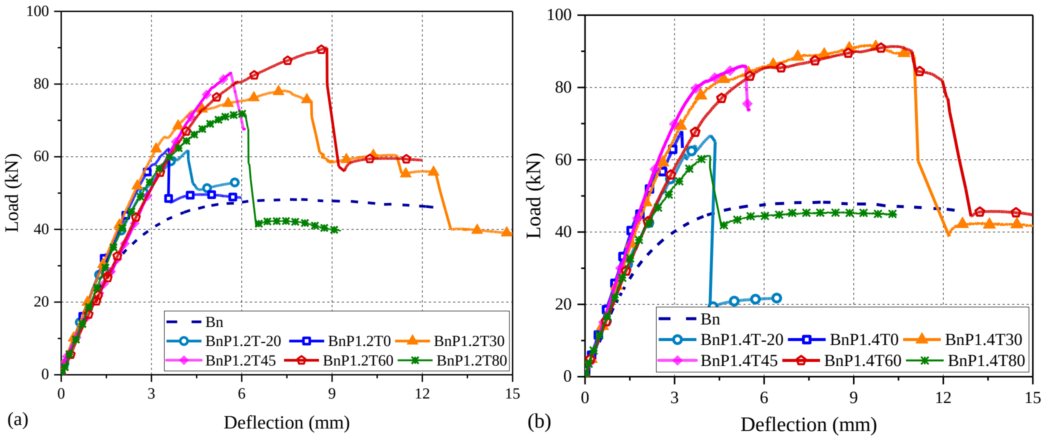

Fig. 8-12 Load-deflection curves of a) BnP1.2 and b) BnP1.4 at various temperatures.

Table 8-2 The loads of FRP-retrofitted steel beams at initiation of debonding and ultimate debonding

Specimens	Initiation of debonding (kN)	Ultimate debonding (kN)
BnP1.2T-20	23.5	61.8
BnP1.4T-20	37.5	69.2
BnP1.2T0	32.9	64.0

BnP1.4T0	43.9	68.0
BnP1.2T30	65.5	75.4
BnP1.4T30	65.0	88.5
BnP1.2T45	79.1	83.0
BnP1.4T45	81.0	85.9
BnP1.2T60	72.7	90.0
BnP1.4T60	85.4	89.9
BnP1.2T80	49.0	71.7
BnP1.4T80	47.0	61.4

Table 8-2 summarizes the initial and ultimate debonding loads of CFRP-retrofitted steel beams at different temperatures. It can be observed that the maximum load-carrying capacity was achieved at the temperatures range of 30 ℃ to 60 ℃. The variations of the initial and ultimate debonding loads as the temperature changes are shown in **Fig. 8-13**. It is seen that the ultimate and debonding load of CFRP-retrofitted steel beams increased with the increase of the temperature when the temperature was lower than 60 ℃ while dropped dramatically at 80 ℃. In addition, the load-carrying capacity of the notched steel beams retrofitted by 1.4 mm thick CFRP plates was slightly higher than that of their counterpart beams with 1.2 mm thick CFRP plates.

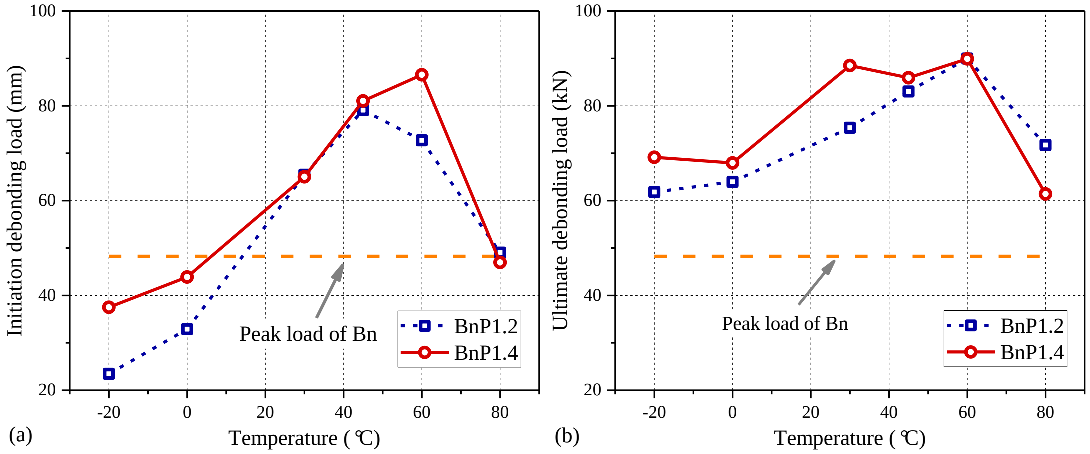

Fig. 8-13 a) Initial and b) ultimate debonding loads of CFRP-retrofitted steel beams tested at different service temperatures.

8.3.3.2 CMOD-load relationships

Fig. 8-14 compares the changes of CMOD with the load at various temperatures. It is clear that the CMOD of the notched steel beam was much lower after CFRP retrofitting, indicating that the CFRP retrofitting could effectively suppress the opening of the prefabricated notch. However, the effectiveness of CFRP retrofitting was quite different at different temperatures. Again the best crack-arresting ability was achieved at the temperatures range of 30 ℃ to 60 ℃.

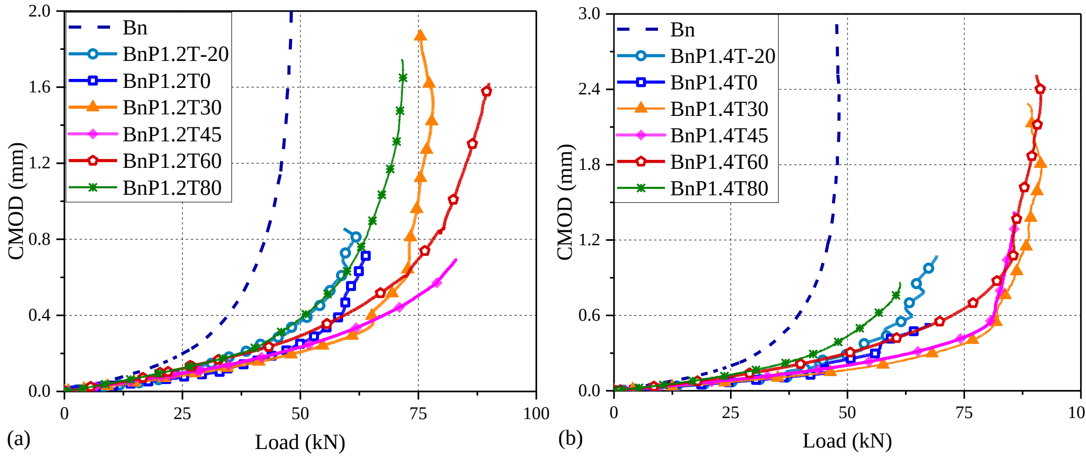

Fig. 8-14 CMOD-load curves of the beam specimens tested at different temperatures: a) strengthened with a 1.2 mm CFRP plate; b) strengthened with a 1.4 mm CFRP plate.

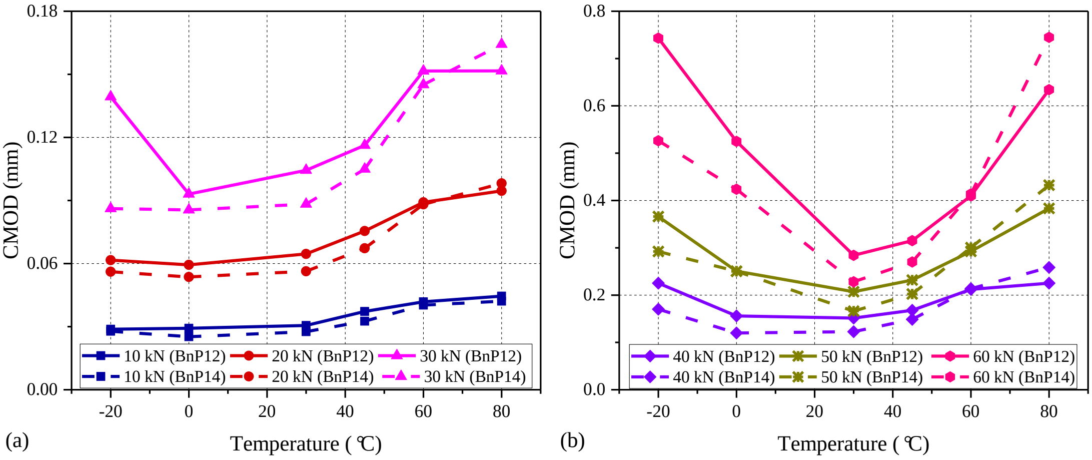

Fig. 8-15 Comparison of crack-opening displacements at various temperatures and constant mechanical loading: a) 10 kN to 30 kN; b) 40 kN to 60 kN.

Fig. 8-15 compares the values of CMOD in the beam specimens tested at different service temperatures given the same load level. It is seen that under lower load levels (i.e., at 10 kN and 20 kN), the magnitude of CMOD at -20 ℃ and 0 ℃ was smaller than that at normal and elevated service temperatures (i.e., from 30 ℃ to 80 ℃). At this load level, the adhesive layer was still in the elastic stage and the only difference of the adhesive layer is in its elastic modulus. Thus, the smaller CMOD should be attributed to the higher elastic modulus of the bonding material at lower temperatures. In comparison, after the applied load exceeded 40 kN, the CMOD at lower temperatures (i.e., -20 ℃ and 0 ℃) was much higher than that at the normal temperature (i.e., 30 ℃). This was due to the initiation of local interfacial debonding near the notch section, which deteriorated the strengthening efficiency of CFRP plate in arresting the crack opening at the notch location. In addition, the CMOD at increased temperatures (i.e., 45 ℃, 60 ℃ and 80 ℃) were higher than that at 30 ℃ at all load levels, because of the reduction of the elastic modulus of the bonding material with the increase of the service temperature. The local interfacial debonding at 80 ℃ under 60 kN further increased the CMOD.

8.3.3.3 Distributions of CFRP strains and interfacial shear stresses

Taking the load level 20 kN as an example, **Fig. 8-16** shows the strain distributions in the CFRP plate at different temperatures. It is seen that the strain values at various temperatures were similar at the notched section, but were quite different at the locations away from the notched section. Specifically, the magnitudes of CFRP strain at -20 ℃ and 0 ℃ were even negative near the plate ends because of the thermal contraction of CFRP plate and steel beam. In addition, the sharp increase of CFRP strains could be seen near the notch. The strain values in the CFRP plates at 80 ℃ were positive near the plate ends and the slope of the strains near the notch was much lower, which indicated the stress concentration near the notch section was alleviated due to the softening of the bonding adhesive at elevated temperatures.

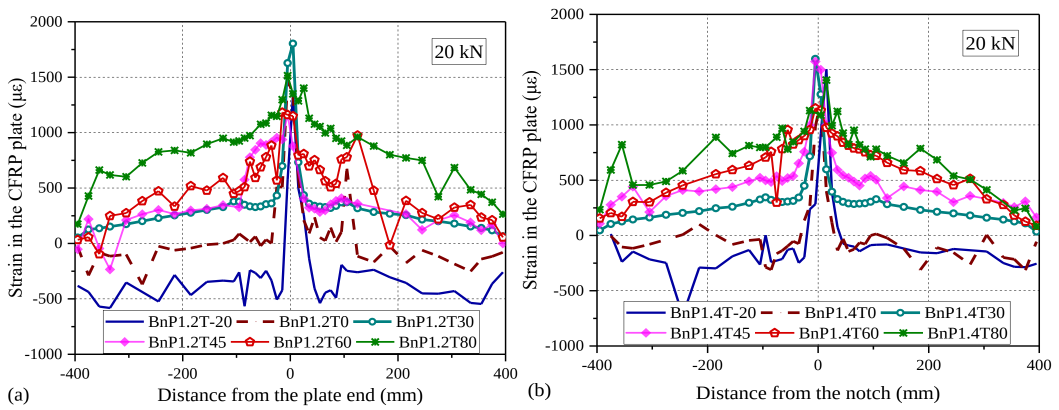

Fig. 8-16 The strain distributions in CFRP plates under 20 kN at various temperatures: a) BnP1.2; b) BnP1.4.

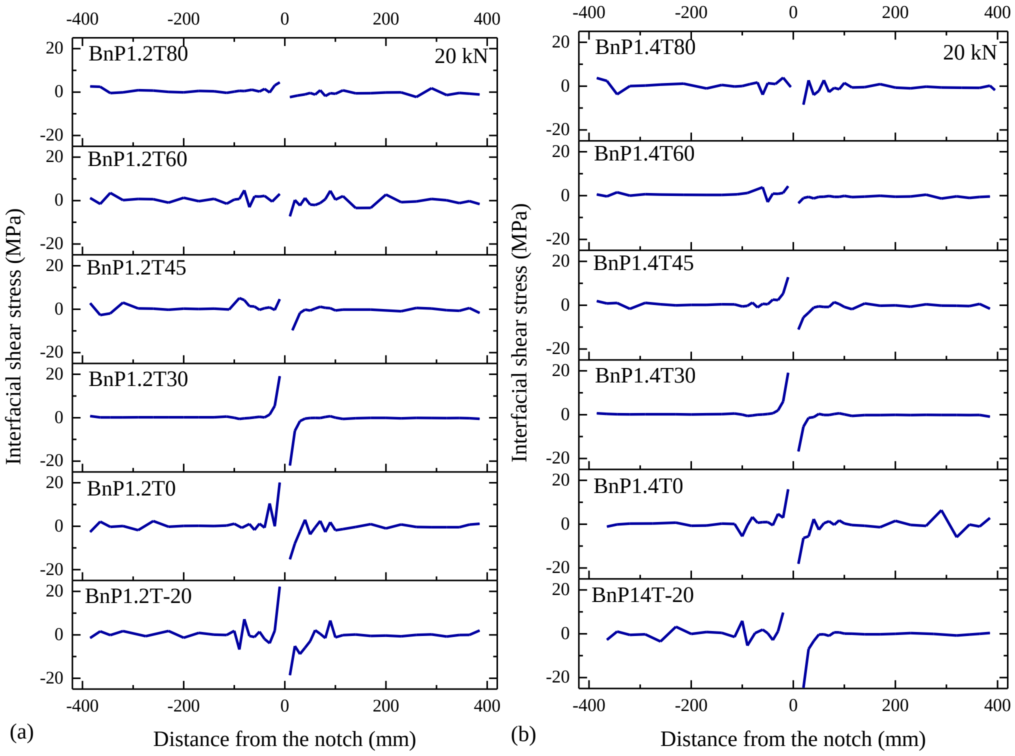

Fig. 8-17 Distributions of the interfacial shear stresses at various temperatures under 20 kN: a) BnP1.2; b) BnP1.4.

Fig. 8-17 shows the distributions of the interfacial shear stresses under 20 kN at different temperatures. It is seen that, for most cases, the interfacial shear stresses were higher near both the notch and plate ends, despite some fluctuations due to the accumulated measuring errors in the CFRP strain during the heating/cooling period. It demonstrates that the interfaces were still in *E* stage. In addition, the magnitude of interfacial shear stress near the notch at increased temperatures (i.e., 45 ℃, 60 ℃, 80 ℃) was lower than that at low (i.e., -20 ℃, 0 ℃) and normal temperatures (i.e., 30 ℃), because of the thermally-induced softening of the bonding material.

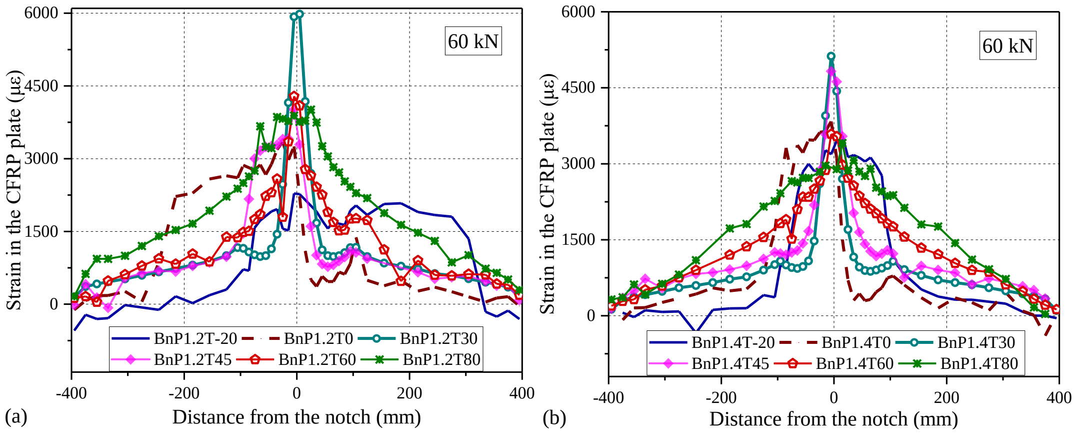

Fig. 8-18 Distributions of CFRP strains at various temperatures under 60 kN: a) BnP1.2; b) BnP1.4.

Fig. 8-18 shows the strain distributions in the CFRP plate under a higher level of mechanical loading (i.e., 60 kN) at various temperatures. It is clear that the strain value in the CFRP plate increased significantly as compared to those at 20 kN (**Fig. 8-16**). In addition, for specimens tested at the temperature range of 30 ℃ to 60 ℃, the strains in the CFRP plate almost increased linearly from the plate end to the notch location where the maximum value was reached, implying the adhesive layer in these cases was still in its elastic stage. However, the locally debonded zone could be observed for specimens tested at -20 ℃, 0 ℃ and 80 ℃ under 60 kN, which was indicated by the flat strains in the CFRP plate with large values. Especially, for BnP1.2T-20, it is seen that the length of the debonded zone on the right side was comparable to the total length of the CFRP plate, indicating that the ultimate debonding failure was approaching.

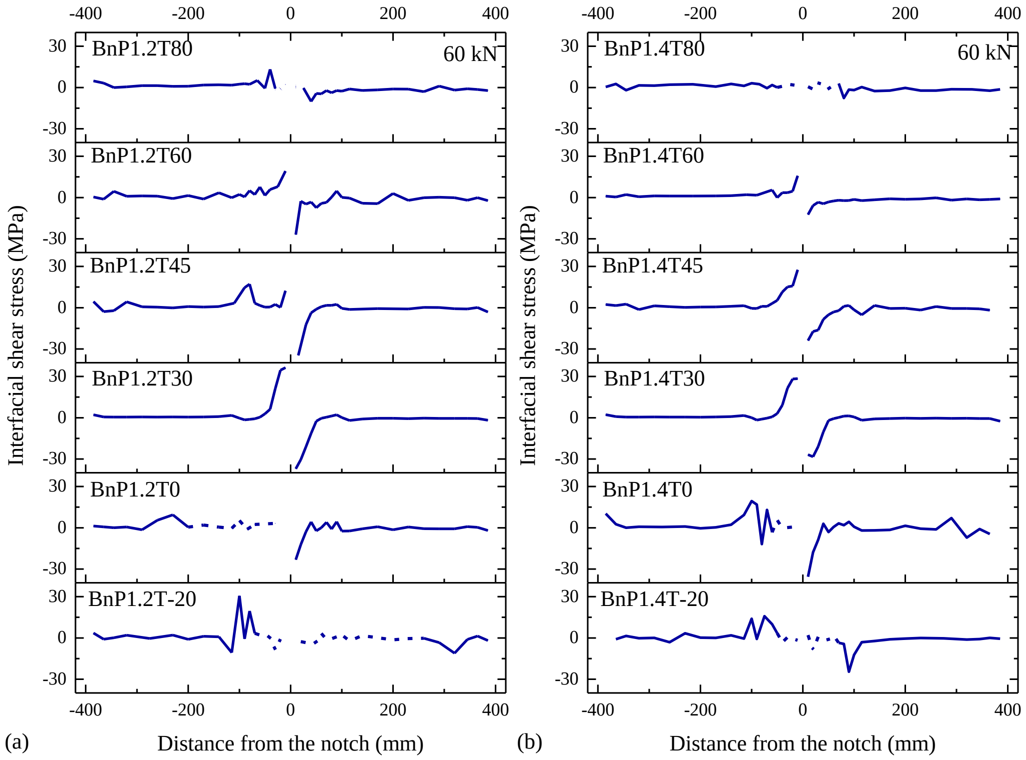

Fig. 8-19 Distributions of the interfacial shear stresses at various temperatures under 60 kN: a) BnP1.2; b) BnP1.4.

Fig. 8-19 shows the distributions of interfacial shear stresses at various temperatures under 60 kN. In this figure, the solid lines describe the distributions of interfacial shear stresses in the *E* and *E-S* zones, whereas the dash lines show the distribution of interfacial shear stress in locally debonded zone. It can be observed that the interfacial shear stress increased rapidly at the area near the notch at the temperature range of 30 ℃

to 60 ℃, which means that the interface was still in its elastic deformation stage. But for specimens tested at -20 ℃, 0 ℃ and 80 ℃, the debonded region was observed at one or both sides of the notch. In the debonded regions, the interfacial shear stresses decreased to almost the zero. The softening zone and elastic zone could be clearly differentiated near the side of the debonded region.

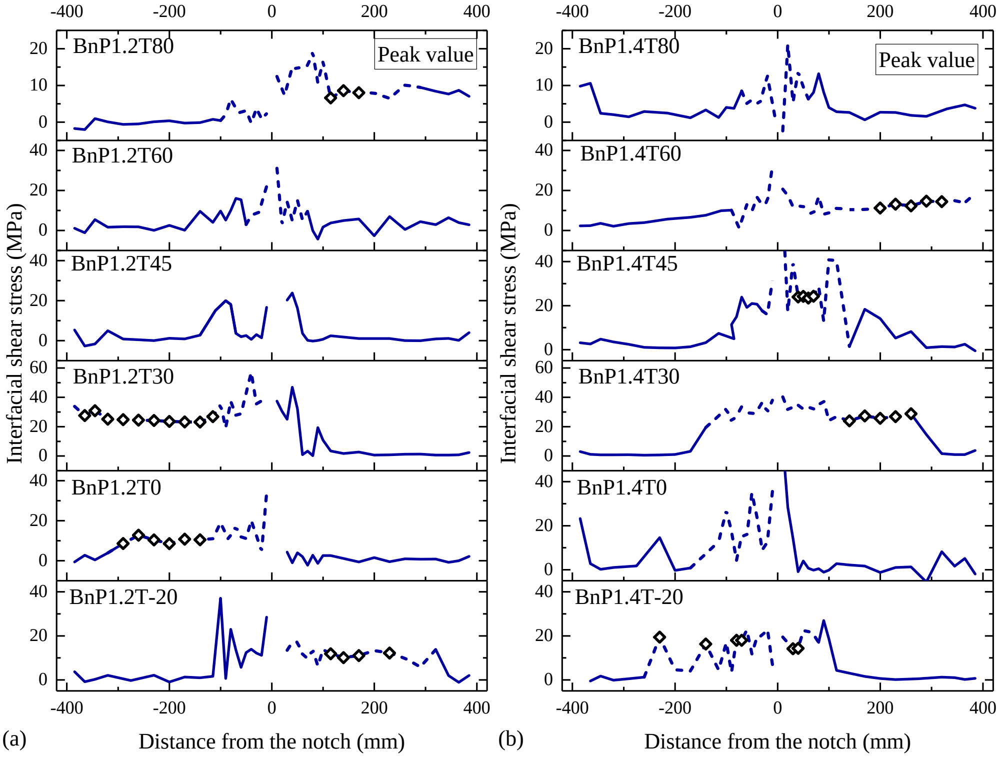

Fig. 8-20 Distributions of the peak magnitudes of interfacial shear stress at various temperatures: a) BnP1.2; b) BnP1.4.

Fig. 8-20 shows the peak value of interfacial shear stresses experienced by the bondline at different locations before the ultimate state. The dash lines in this figure illustrate that the regions exhibited clear softening and debonding stages in terms of the local bond-slip behavior. It can be observed that the peak interfacial shear stress was generally higher and waved a lot near the notch section, probably due to the local compressive stress in the direction normal to the interface near the notch (Deng *et al.* 2018). In comparison, the peak interfacial shear stresses further away from the notch section were quite close, which experienced clear *E* and *E-S* stages. The hollow symbols in this figure indicate the data points with close peak stresses and adopted for deriving the representative local bond-slip relation of this beam specimen. For some specimens (e.g., BnP1.4T80, BnP1.2T60, BnP1.2T45, BnP1.4T0), the interfacial debonding propagated suddenly from the notched section to the plate end. Under such a circumstance, the strains in the CFRP plate during the propagation of interfacial debonding could not be monitored, and as a result, the representative local bond-slip behavior of these specimens are not provided in the following paragraph.

8.3.4 Local Bond-Slip Behavior of the CFRP-to-Steel Interface at Different Temperatures

8.3.4.1 Determination of the interfacial slip

The above analyses showed that the interfacial bond behaviors of the CFRP-retrofitted steel beams are quite different at various temperatures. In determining the bond-slip relationship, the magnitude of interfacial shear stress can be derived by Eq. (1) and special attention should be paid on calculating the interfacial shear slip.

In the existing study (Zhou *et al.* 2020), the interfacial slip along the bondline was derived based on the formula proposed by Alexander JG (1996). In this method, the difference of interfacial slip ($\delta_{i+\frac{1}{2}} - \delta_{i-\frac{1}{2}}$) between the two points (i.e., $x_{i-\frac{1}{2}}$ and $x_{i+\frac{1}{2}}$) was calculated by integrating the strain in the CFRP plate along the length between these two points. Meanwhile, the measured stain by the strain gauge (ε_{fi}) at x_i between the two considered points (i.e., $x_{i-\frac{1}{2}}$, $x_{i+\frac{1}{2}}$) was approximately taken as the average strain in this region. Then the slip difference ($\delta_{i+\frac{1}{2}} - \delta_{i-\frac{1}{2}}$) can be calculated by multiplying the measured FRP strain (ε_{fi}) with the distance between the two points (i.e., $x_{i+\frac{1}{2}} - x_{i-\frac{1}{2}}$).

$$\delta_{i+\frac{1}{2}} = \delta_{i-\frac{1}{2}} + \varepsilon_{fi}(x_{i+\frac{1}{2}} - x_{i-\frac{1}{2}}) \tag{8-2}$$

where ε_{fi} is the measured strain in the CFRP plate at x_i; x_i is the location of the strain gauge. Then the interfacial slip at $x_{i+\frac{1}{2}}$ can be calculated by accumulating the interfacial slip starting from $x_{\frac{1}{2}}$.

$$\delta_{i+\frac{1}{2}} = \delta_{\frac{1}{2}} + \sum_1^i \varepsilon_{fi}(x_{i+\frac{1}{2}} - x_{i-\frac{1}{2}}) \tag{8-3}$$

Later on, Biscaia *et al.* (2015) proposed a new formula for deriving the interfacial slip between FRP and steel/concrete substrate under combined mechanical and thermal loading, in which the thermal deformations of the adherends was considered:

$$\delta_{i+1} = \delta_i + \left(\varepsilon_{fi} + \varepsilon_{fi+1}\right)\frac{(x_{i+1}-x_i)}{2} - \left(\beta\alpha_f + \alpha_s\right)\Delta T(x_{i+1} - x_i) \tag{8-4}$$

where $\beta = \frac{E_f b_f t_f}{E_s b_s t_s}$; E, b and t are the elastic modulus, width and thickness of the adherends, with subscripts f and s indicating the CFRP plate and steel substrate. ΔT is the magnitude of temperature variation.

As indicated in the previous analytical studies presented in **Chapter 5**, the interfacial shear slip was defined as the difference of axial deformation between the CFRP plate and steel/concrete substrate. However, in the above-mentioned two methods (Alexander JG 1996; Biscaia *et al.* 2015), only the strains in the CFRP plate was considered in deriving the interfacial slip, and the deformation of the concrete/steel substrate was ignored by assuming that the substrate is rigid. Such an assumption may be appropriate for FRP-to-steel/concrete bonded joints, considering that the tensile stiffness of the steel/concrete substrate is generally much higher than that of the CFRP plate and the overall strain in the substrate is negligible as compared to that of CFRP plate. However, for CFRP-strengthened steel beams, the substrate beam is subject to flexural loading and the tensile strain at the soffit of steel beam is significant. Thus, the interfacial slip should be calculated by integrating the strain difference between the CFRP plate and the soffit of steel beam. Then Eq. (8-3) is expressed as follows,

$$\delta_{i+\frac{1}{2}} = \delta_{\frac{1}{2}} + \sum_1^i(\varepsilon_{fi} - \varepsilon_{si})(x_{i+\frac{1}{2}} - x_{i-\frac{1}{2}}) \tag{8-5}$$

where ε_{si} is the axial strain of the steel beam on the bottom surface at the location of the strain gauge (x_i). ε_{si} can be calculated considering the deformation of steel beam under bending, axial loading and thermal loading by the following equation (**Chapter 3, 4, 5**).

$$\varepsilon_{si} = \frac{y_s}{E_s I_s}M_{si} - \frac{1}{E_s A_s}N_{si} + \alpha_s \Delta T \tag{8-6}$$

where M_{si} and N_{si} are the bending moment and axial force sustained by the steel beam at $x = x_i$. I_s, A_s and E_s are the second moment of inertia, sectional area and elastic modulus of the steel beam, respectively. y_s is the distance between the neutral axis and bottom surface of the steel beam. Considering the force equilibrium of the CFRP-retrofitted steel beam in its axial direction,

$$N_{fi} = N_{si} \tag{8-7}$$

where N_{fi} is the axial force resisted by the CFRP plate at $(x = x_i)$. N_{fi} can be calculated by the measured axial strain in the CFRP plate (ε_{fi}), based on the following equation:

$$N_{fi} = (\varepsilon_{fi} - \alpha_f \Delta T) E_f A_f \tag{8-8}$$

The moment equilibrium of the CFRP-retrofitted steel beam at $(x = x_i)$ can be expressed as follows,

$$M_{Ti} = M_{si} + N_{fi}(y_s + y_f + t_a) \tag{8-9}$$

where M_{Ti} is the total moment resisted by the retrofitted steel beam at x_i. y_f is the distance from the neutral axis of the CFRP plate to its bonding interface with the adhesive layer. t_a is the thickness of the adhesive layer.

By substituting Eqs. (8-7) ~ (8-9) into Eq. (8-6), the strain at soffit of the steel beam can be obtained as:

$$\varepsilon_{si} = \frac{y_s}{E_s I_s} M_{Ti} - \frac{y_s}{E_s I_s}\left(y_s + y_f + t_a\right) N_{fi} - \varepsilon_{fi}(x) + \left(\alpha_f + \alpha_s\right)\Delta T \tag{8-10}$$

For simplicity:

$$\varepsilon_{si} = \beta_2 M_{Ti} - \beta_4 \varepsilon_{fi} + \beta_5 \Delta T \tag{8-11}$$

where $\beta_2 = \frac{y_1}{E_1 I_1}$; $\beta_4 = \frac{y_s E_f A_f}{E_s I_s}\left(y_s + y_f + t_a\right) + \frac{E_f A_f}{E_s A_s}$; $\beta_5 = \beta_4 \alpha_f + \alpha_s$. The assumptions and detailed derivation process of the above formulae can be found in **Chapters 3**, **4** and **5**. Note that in the above equation, β_2, β_4 and ΔT are constants for the specimen tested at a specific service temperature, while M_{Ti} can be calculated by the applied loads.

Finally, by substituting Eq. (11) into the Eq. (5), $\delta_{i+\frac{1}{2}}$ can be computed by the following equation:

$$\delta_{i+\frac{1}{2}} = \delta_{\frac{1}{2}} + \sum_1^i \left[\varepsilon_{fi}(1 + \beta_4) - \beta_2 M_{Ti} - \beta_5 \Delta T\right]\left(x_{i+\frac{1}{2}} - x_{i-\frac{1}{2}}\right) \tag{8-12}$$

Fig. 8-21 compares the resultant distribution of the interfacial slip along the bond line determined from the proposed FE modeling and calculated from the previous

(Alexander JG 1996) and the newly proposed formula (i.e., Eq. 8-12). It seems that the previous method proposed by Alexander JG (1996) leads to an overestimation of the interfacial slip and the newly proposed formula gives a result much closer to the FE prediction.

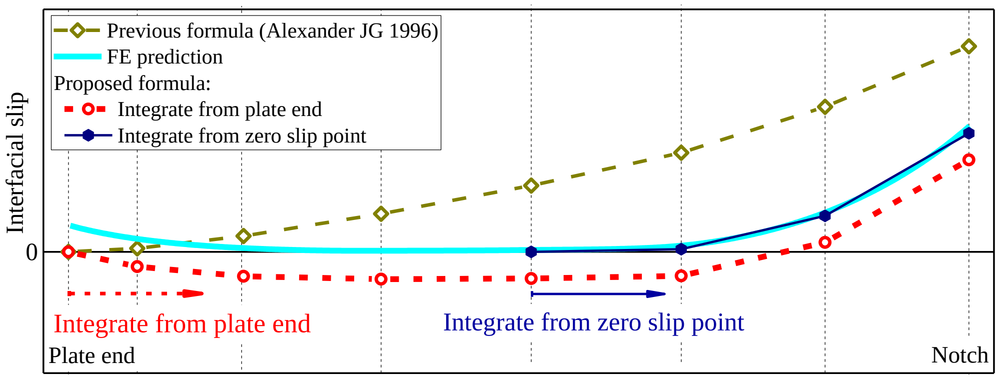

Fig. 8-21 Comparison of the interfacial slips obtained from different methods.

When using the proposed formula for deriving the interfacial slip distribution, another consideration is the selection of the first integration point. As shown in **Fig. 8-21**, if integrating the interfacial slip from the plate end and setting the interfacial slip at plate end as zero, then the calculated magnitude of interfacial slip would be negative at the areas near the plate end, where the strain on the bottom surface of the steel beam is higher than that on the CFRP plate (i.e., $\varepsilon_{fi} - \varepsilon_{si}$ is negative). In reality, the interfacial slip is not zero at the plate end (see FE prediction in **Fig. 20**), and the magnitude of interfacial slip decreases to almost zero as the distance from the plate end increases. Therefore, it is more appropriate to set the first integrating point at the place where $(\varepsilon_{fi} - \varepsilon_{si})$ is zero or a small enough positive value, so that the obtained slips through strain integration can coincide with the FE prediction (see **Fig. 8-21)**.

As clearly seen in **Fig. 8-21**, the resultant interfacial slip increases gradually from the first integration point to the notch and achieves its maximum value at the notch. The sum of interfacial slips derived from two sides of the notch (i.e., $x = -2.5\ mm$ and $x = 2.5\ mm$) form the CMOD of the notch. Thus, the CMOD at the notched section measured by the extensometer can be used to validate the proposed formula for calculating the interfacial slip.

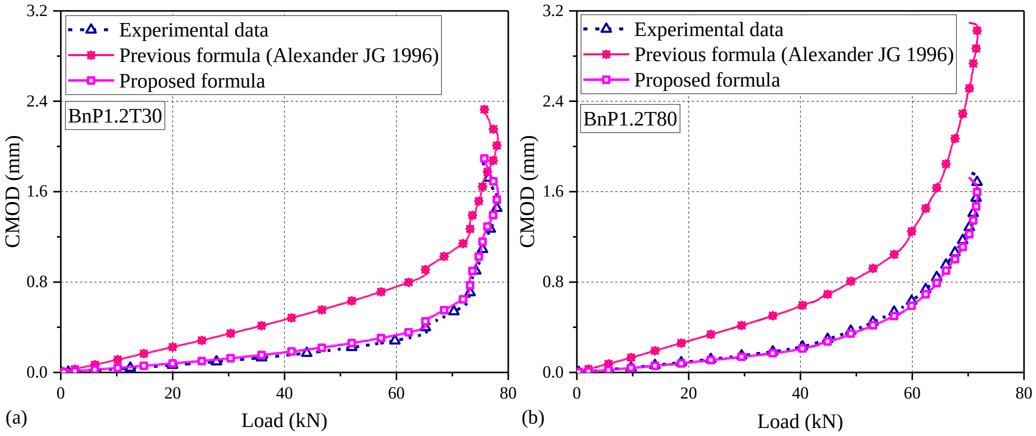

Fig. 8-22 Comparison of the CMOD measured by extensometer and derived based on measured strain: a) BnP1.2T30; b) BnP1.2T80.

Fig. 8-22 compares the sum of interfacial slips derived from the two sides of the notch based on the previous model (Alexander JG 1996) and the newly proposed formulae together with the CMOD values measured by the extensometers for BnP1.2T30 and BnP1.2T80. The CMOD measured by the extensometers was initialized as 0after the experimental temperature arrived the target temperature for eliminating the accumulated measuring errors during the temperature changing process. For easy comparison, the interfacial slip derived based on the proposed formula was also initialized as 0 at 0 kN. It is clearly seen that the proposed formula leads to a much better prediction, indicating that the assumption of rigid substrate is not suitable for CFRP-retrofitted steel beam.

8.3.4.2 Comparison of local bond-slip relationships at different temperatures

Fig. 8-23 compares the derived local bond-slip relationships obtained from BnP1.2T30 along the bondline. The interfacial stress and slip were computed using Eqs. (1) and (12), respectively. It is clearly seen that the bond-slip relationships at different locations are quite different. Specifically, the bonding interface near the notch (i.e., from -30 mm to 30 mm) generally exhibited an elastic-plastic-softening behavior, which varied dramatically within this area. This could be attributed to the effect of the interfacial compressive stress (Deng *et al.* 2016) that enhanced the local bond in mode II direction. In the existing research on analyzing the bond behavior between the CFRP plate and concrete/steel substrate under mixed-mode loading (De Lorenzis *et al.* 2013; Zeng *et al.* 2018), the effect of tensile stress in mode I direction was usually considered because it decreases the mode II bond strength. There was still lack of study on the effect of interfacial compressive stress on the mode II bond behavior.

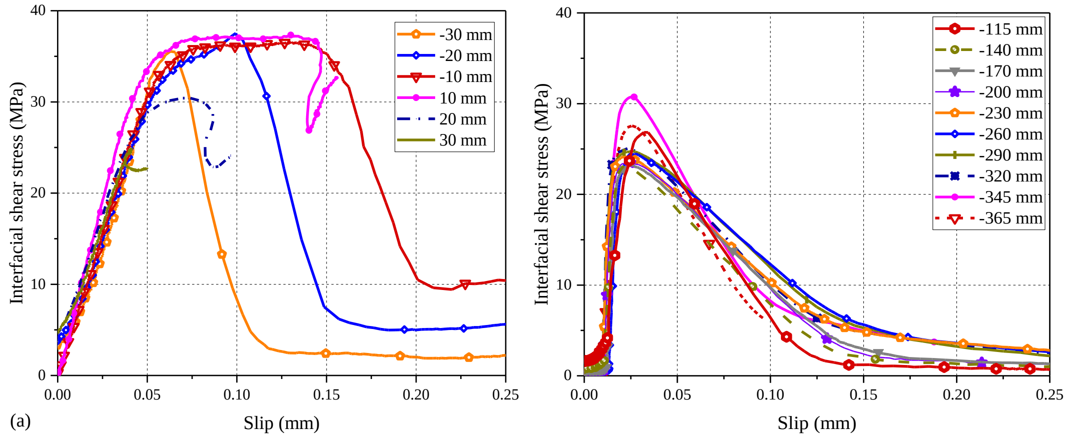

Fig. 8-23 The local bond-slip relationships obtained at different locations in BnP1.2T30: a) from -30 mm to 30 mm; b). from -365 mm to -115 mm.

Fig. 8-23b shows that the bonding interface exhibited almost the consistent bond behavior at locations further from the notch and stiffeners (i.e., from -365 mm to -115 mm), where the interfacial normal stress was marginal (Deng *et al.* 2016). This phenomenon was widely observed in the specimens conducted at normal and elevated temperatures. In this chapter, only the locations with similar local bond behaviors and far away from the notch section were considered in determining the representative local bond-slip relationships. These locations are indicated using symbols in **Fig. 8-20**.

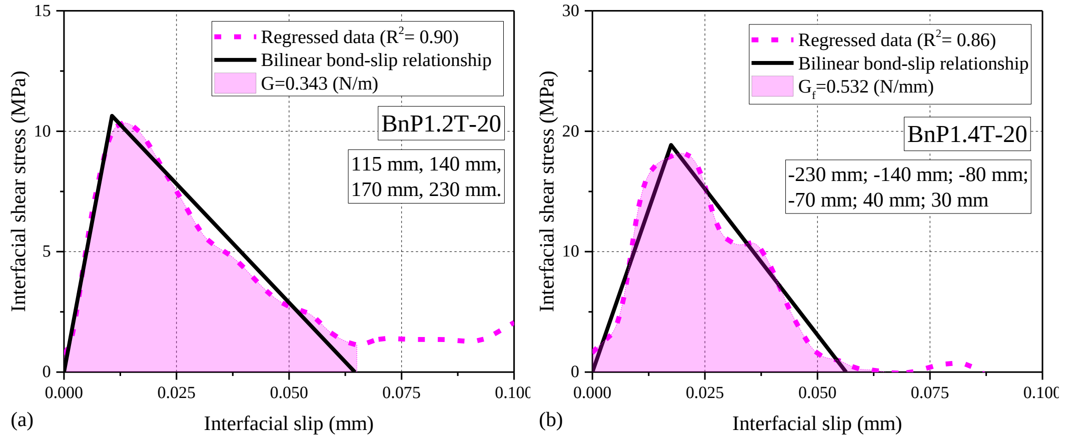

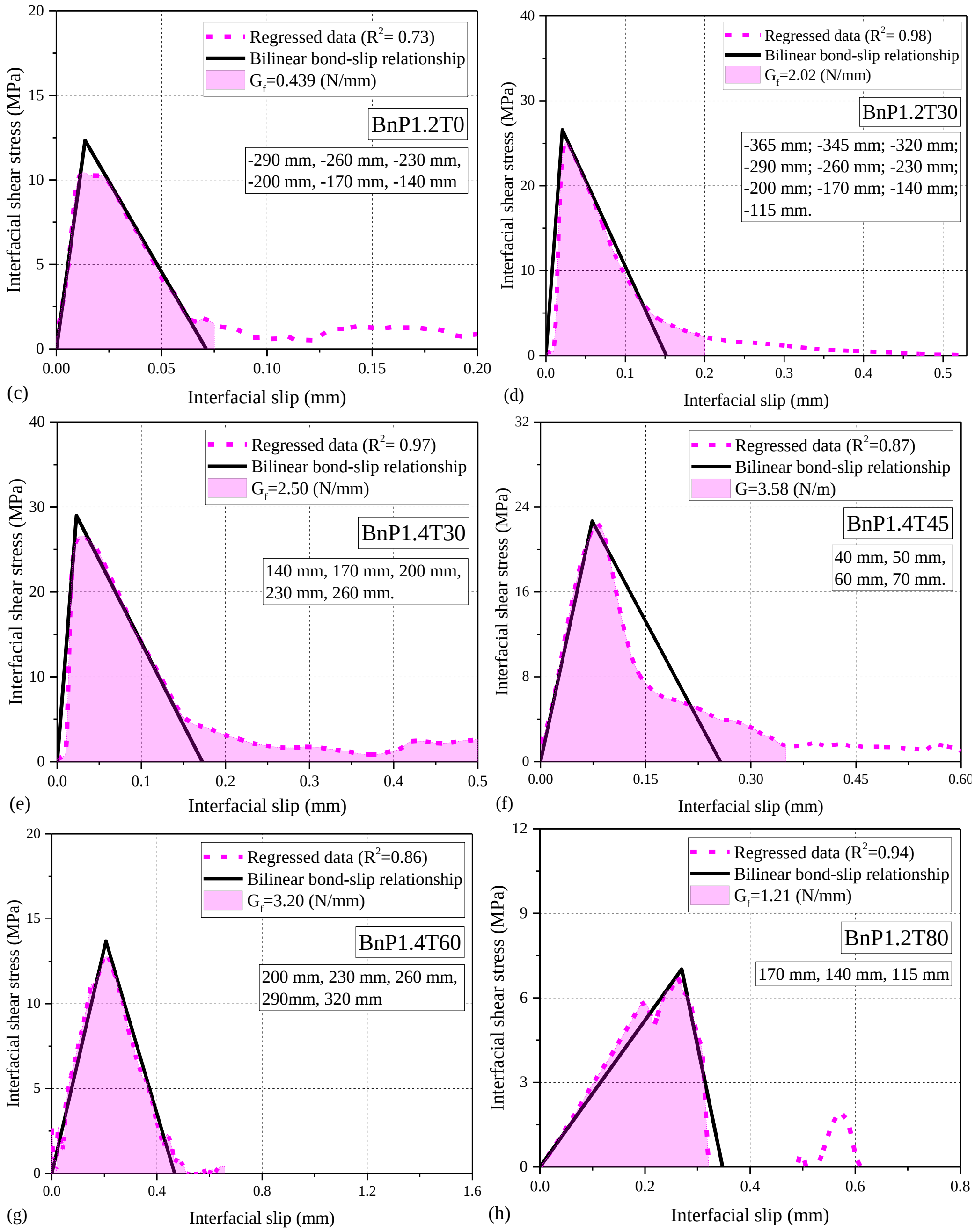

Fig. 8-24 The local bond-slip relationships in different specimens: a) BnP1.2T-20; b) BnP1.4T-20; c) BnP1.2T0; d) BnP1.2T30; e) BnP1.4T30; f) BnP1.4T45; g) BnP1.4T60; h) BnP1.2T80.

Fig. 8-24 shows the bond-slip relationships of the CFRP-to-steel interface under different service temperatures. The dash lines are the bond-slip curves derived based on the non-linear regression analysis using MATLAB (Mathworks, 2021) curve fitting box (smoothing splines with the smooth parameter set as 0.9999), which was also adopted in Zhou *et al.*'s analysis (2020). It is clear that the regressed bond-slip relationships show obvious ascending (elastic stage) and descending (softening stage) branches. Therefore, the bilinear bond-slip model with linear elastic and softening stages was used here to describe the local bond behavior in CFRP-retrofitted steel beams. The interfacial shear stiffnesses (i.e., slopes) in both elastic and softening stages were calculated based on the linear fitting method, and the interfacial fracture energy (G_f) was calculated as the area beneath the regressed bond-slip curves. Then the peak shear stress was calculated based on the determined fracture energy, and the stiffnesses in both elastic and softening branches. The finally obtained bilinear bond-slip relationships are shown by the black solid lines in **Fig. 8-24**.

Table 8-3 The parameters of the bilinear bond-slip relationships at different temperatures

Specimens	Interfacial shear stiffness (MPa/mm)	Peak shear stress (MPa)	Fracture energy (N/mm)
BnP1.2T-20	999	10.6	0.340
BnP1.4T-20	1080	18.9	0.530
BnP1.2T0	905	12.3	0.440
BnP1.2T30	1290	26.6	2.02
BnP1.4T30	1270	29.0	2.50
BnP1.4T45	308	22.7	2.91
BnP1.4T60	66.5	13.7	3.20
BnP1.2T80	26.0	7.02	1.22

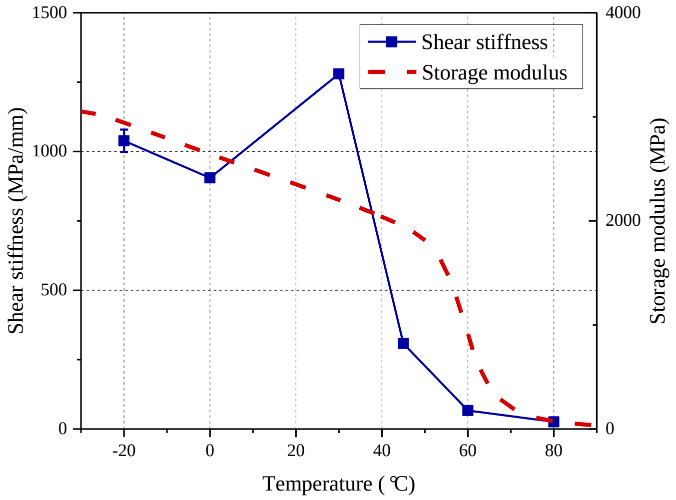

Fig. 8-25 The interfacial shear stiffness and measured storage modulus of the bonding material at various temperatures

The derived parameters of bond-slip relationships at various temperatures are summarized in **Table 8-3**. The bond properties between the CFRP and steel beams changed dramatically with the temperature variation, in terms of interfacial shear stiffness, peak shear stress and interfacial fracture energy. **Fig. 8-25** compares the interfacial shear stiffness with the storage modulus of the bonding material at different temperatures. It is seen that the interfacial shear stiffness decreases as the temperature increases, generally following the variation of the elastic modulus of the bonding material (Nguyen *et al.* 2011), indicating the thermally-induced deterioration of the material from a glassy to leathery state.

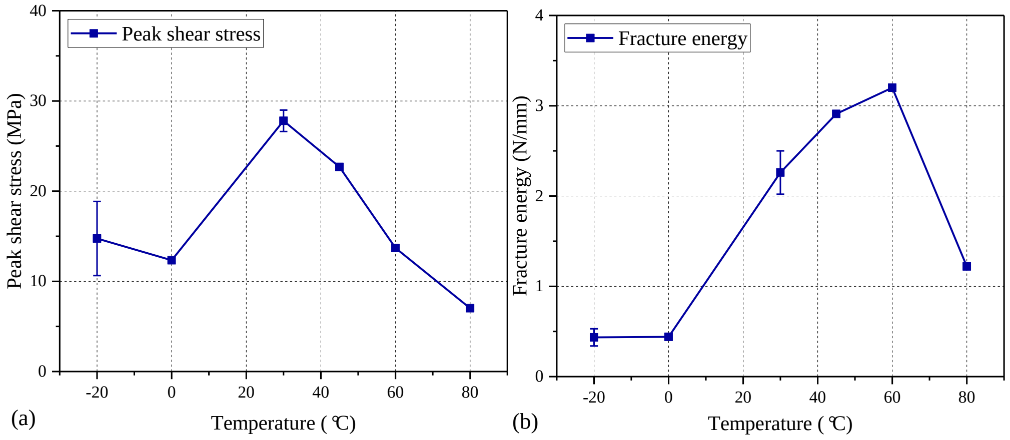

Fig. 8-26 Change of the properties of bondline at different temperatures: (a) peak shear stress; (b) fracture energy

Fig. 8-26 shows the changes of peak shear stress and interfacial fracture energy as the temperature increases. The peak shear stress and interfacial fracture energy were much lower at both very low and very high temperatures. However, the interfacial fracture energy increased from 30 ℃ to 60 ℃, while the peak shear stress decreased during this temperature range. The change of the debonding load of CFRP-retrofitted steel beams (**Fig. 8-13**) was quite close to the change of the interfacial fracture energy as the temperature varied (**Fig. 8-26b**) rather than the change of peak shear stress (**Fig. 8-26a**).

8.4. FINITE ELEMENT (FE) MODEL

8.4.1 Description of the FE Model

For better interpreting the structural performance and the IC debonding mechanism of CFRP-retrofitted steel beams at different temperatures, two-dimensional finite element modeling was conducted by commercial software Abaqus 6.14, based on the plane stress assumption. The CFRP plate and steel beam were modeled by 4-node bilinear plane stress quadrilateral (CPS4R) elements. The different widths at different heights of the specimen (i.e., the web, flange, adhesive layer and CFRP plate) were considered by adopting different out-of-plane thicknesses. The adhesive layer was modeled by 4-node two-dimensional cohesive (COH2D4) elements. The element sizes of the adherends and adhesive layer were set as 0.2 mm in the *x*-direction. The thermal loading was defined by the predefined field variable, which was uniformly distributed in the specimen. The reference temperature (i.e., 30 ℃) was set in the initial step and changed in the following steps. The beams were loaded in a displacement-controlled manner (**Fig. 8-1**).

The engineering stress-strain relationship of the steel was originally obtained from the tensile coupon tests. The engineering stress (σ_e) was computed by dividing the measured tensile force (F) by the original sectional-area (A_0); while the engineering strain (ε_e) was determined by dividing the measured deformation (δ) by the original gauge length (L_0). The engineering stress-strain relationship cannot serve as input data in the numerical analysis, because the cross-sectional area of the coupon varies throughout the test. Thus, the actual stress-strain relationship, which considered the sectional area variation, was determined by the following functions (Yao *et al.* 2018; Zhao *et al.* 2020):

$$\sigma_t = \sigma_e \times (1 + \varepsilon_e) \tag{8-13}$$

$$\varepsilon_t = ln(1 + \varepsilon_e) \tag{8-14}$$

It should be noted that the determination of actual stress-strain relationship (i.e., Eqs. 13, 14) is based on two assumptions: the sectional area is uniformly distributed over the gauge length; the volume of the coupon within the gauge length is constant (i.e., the sectional area and thickness of the coupon continuously decreases) as the tensile load increases. The former assumption makes the actual stress-strain relationship only valid prior to the occurrence of necking (Zhao *et al.* 2020). The latter assumption indicates that the actual stress-strain relationship may not facilitate a very precise prediction of the structure behavior based on the two-dimensional FE modeling, by which the variation of out-of-plane thickness cannot be modeled.

Fig. 8-27 compares the stress-strain relationships of the steel obtained based on three tensile coupons and adopted in the FE modeling. The yielding strength (i.e., 359 MPa) in the actual stress-strain relationship was inputted into the FE modeling. After yielding, the strain hardening modulus (E') was set as 2700 N/mm^2 (Byfield *et al.* 2005), which was adopted in the previous FE model of CFRP-strengthened steel beams based on shell element (i.e., also without out-of-plane thickness variations) and resulted in a very close FE prediction of the load-deflection responses to the experimental results (Fernando 2010; Teng *et al.* 2015). In addition, the J_2 flow theory was employed in this stage.

The damage of steel material and possible crack propagation of the prefabricated notch in the web of steel beam were considered by adopting the extending finite element method (XFEM), which has been widely adopted in modeling the metallic structures, such as steel pressure vessels and piping (Liu *et al.* 2012), steel pipeline (Agbo *et al.* 2020; Agbo *et al.* 2019; Ameli *et al.* 2019; Hojjati-Talemi *et al.* 2018; Lin *et al.* 2017; Lin *et al.* 2020; Liu 2017; Okodi *et al.* 2020a; 2020b; Paredes *et al.* 2016; Zhang *et al.* 2020), and aluminum plate (Schiavone *et al.* 2016). The onset damage of the steel material after the in-plane principal stress reached its material maximum in-plane principal stress (σ_{maxps}) (**Fig. 8-27**). After that, the damage variable evolved linearly with the plastic strain. Then the crack propagated after the energy dissipated per unit area exceeded the fracture energy (G_f) during the damage evolution process. In previous studies, it was found that the recommended values of σ_{maxps} and G_f is influenced by the material properties and specimen geometry (Shahzamanian *et al.* 2021), thus, they were mostly estimated and optimized by calibration with the test results (Agbo *et al.* 2019, 2020; Ameli *et al.* 2019; Lin *et al.* 2017, 2020; Liu 2017; Okodi *et al.* 2020b; Zhang *et al.* 2020).

According to the experimental observation, at larger CMOD, the necking phenomenon (i.e., decrease in the out-of-plane thickness) was observed around the notch tip, because of the intensified stress concentration. Therefore, adopting the actual stress-strain curve (i.e., coupon test results in **Fig. 8-27**) and neglecting the necking effect in the FE modeling would significantly underestimate the deflection and CMOD of the notched steel beam at same loading. In addition, there is lack of recommended values of σ_{maxps} and G_f for the adopted steel beam materials in the literature. Thus, for achieving more close modeling of the structural performance of the notched steel beam without retrofitting, the two parameters (i.e., maximum principal stress and fracture energy) at the significant plastic deformation stage were also obtained by trial-and-error analyses of the load-deflection and CMOD-load curves (Agbo *et al.* 2019, 2020; Ameli *et al.* 2019; Lin *et al.* 2017; Lin *et al.* 2020; Liu 2017; Okodi *et al.* 2020a, 2020b; Zhang *et* *al.* 2020). Finally, the two values for the best agreement were 450 MPa and 3.3×10^3 N/mm, respectively. The adopted parameters of steel are summarized in **Table 8-4**.

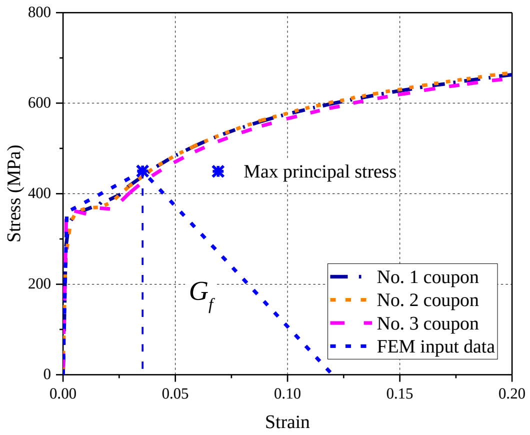

Fig. 8-27 The actual and input stress-strain relationships of the steel.

Table 8-4 Parameters of steel

Elastic modulus (E) (GPa)	Yielding stress (f_y) (MPa)	Maximum principal stress (σ_{maxps}) (MPa)	Strain hardening modulus (E') (MPa)	Fracture energy (G_f) (N/mm)	Coefficient of thermal expansion (α_s) (/℃)
210.5	359	450	2700	3300	1.14×10^{-5}

The load-deflection and CMOD-load curves predicted by the FE modeling are compared with the experimental results in **Fig. 8-28**. It is clear that the performance of the un-strengthened notched steel beam could be accurately predicted by the proposed FE modeling.

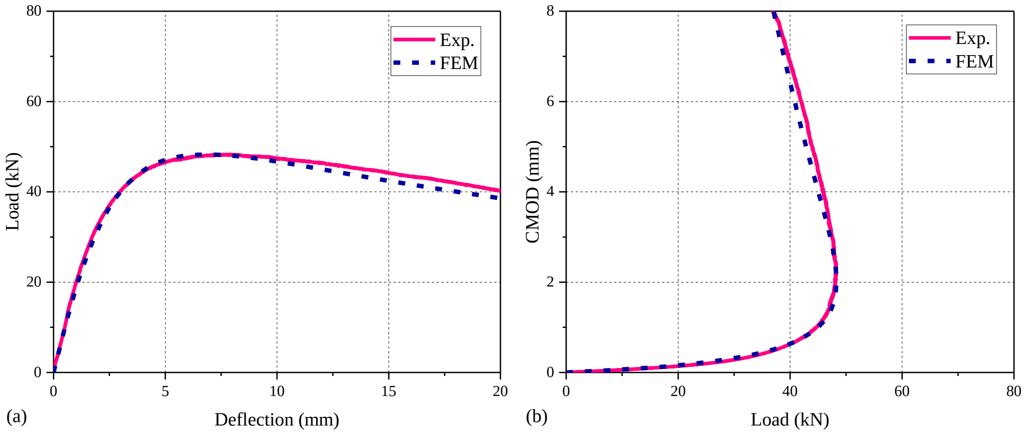

Fig. 8-28 Comparison of the structural performance of un-strengthened notched steel beam obtained from experiment and FE modeling: a) load-deflection curve; b) CMOD-load curve.

The CFRP plate was set as an orthotropic material. The elastic modulus in the axial direction (E_1) was obtained from the coupon test. Other parameters, including the elastic moduli in the other two directions (E_2, E_3), poisson's ratios (v_{12}, v_{13}, v_{23}), shear modulus (G_{12}, G_{13}, G_{23}) were taken from the previous study (Zeng *et al.* 2018), in which the similar CFRP plate was used. The parameters of the CFRP plate are shown in **Table 8-5**.

Table 8-5 Parameters of CFRP plate

CFRP plate	Elastic modulus (E_1) (GPa)	Elastic modulus (E_2&E_3) (GPa)	Poisson's ratio (v_{12}, v_{13})	Poisson's ratio (v_{23})	Shear modulus (G_{12}&G_{22}) (GPa)	Shear modulus (G_{23}) (GPa)	Coefficient of thermal expansion (α_f) (/ ℃)
1.2T	171.32	10	0.3	0.0058	25.5	3.6	-9.10×10^{-7}
1.4T	158.18	10	0.3	0.0058	25.5	3.6	-8.48×10^{-7}

Table 8-6 The interfacial bond parameters in mode I direction.

Specimens	Interfacial normal stiffness (MPa/mm)	Peak normal stress (MPa)	Interfacial fracture energy (N/mm)
BnP1.2T-20	5380	17.1	0.0295
BnP1.4T-20	5810	22.1	0.0456
BnP1.2T0	4870	18.4	0.0376
BnP1.2T30	6890	49.7	0.194
BnP1.4T30	6890	49.7	0.194
BnP1.4T45	1660	27.6	0.249
BnP1.4T60	358	13.5	0.274
BnP1.2T80	140	5.20	0.105

The determined bond-slip relationships at various temperatures (**Table 8-3**) were adopted for modeling the bond behavior in mode II direction. The bond behavior in mode I direction was also simplified as a bilinear bond-separation relationship, with the parameters determined by the tensile test on adhesive coupons. According to the test data, the tensile strength and elastic modulus of the epoxy resin at normal temperature were 49.7 MPa and 2.55 GPa, respectively. Accordingly, the peak interfacial normal stress and interfacial tensile stiffness were 49.7 MPa and 6.89 GPa/mm. In addition, the slope of the softening branch of the bond-separation relationship was set as 12.8 times of the elastic branch, which was the same as previous FE modeling (Teng *et al.* 2015). The parameters of the bond behavior in mode I direction (e.g., interfacial tensile stiffness and interfacial fracture energy) at various temperatures change at the same rate as the corresponding parameters (e.g., interfacial shear stiffness and interfacial fracture energy) in mode II direction. The resultant interfacial bond behaviors in mode I direction are shown in **Table 8-6**.

8.4.2 Comparison of the Results from Experiments and FE Modeling

8.4.2.1 Load-displacement responses

Fig. 8-29 compares the experimental and FE predicted load-displacement curves of CFRP-retrofitted steel beams at various temperatures. The data points at the onset of debonding and the ultimate stage are indicated in the figure. The initiation debonding load in the FE analysis was defined to be reached when the interfacial shear stress at the notch location decreased to zero. While the ultimate debonding load in the FE modeling was determined when the predicted length of debonded area was identical to that measured during the experiment at the ultimate debonding load. It is seen that the load-deflection behaviors predicted by the FE modeling are in close agreement with the experimental ones, which validated the FE modeling approach and the reliability of the determined bond-slip relationships.

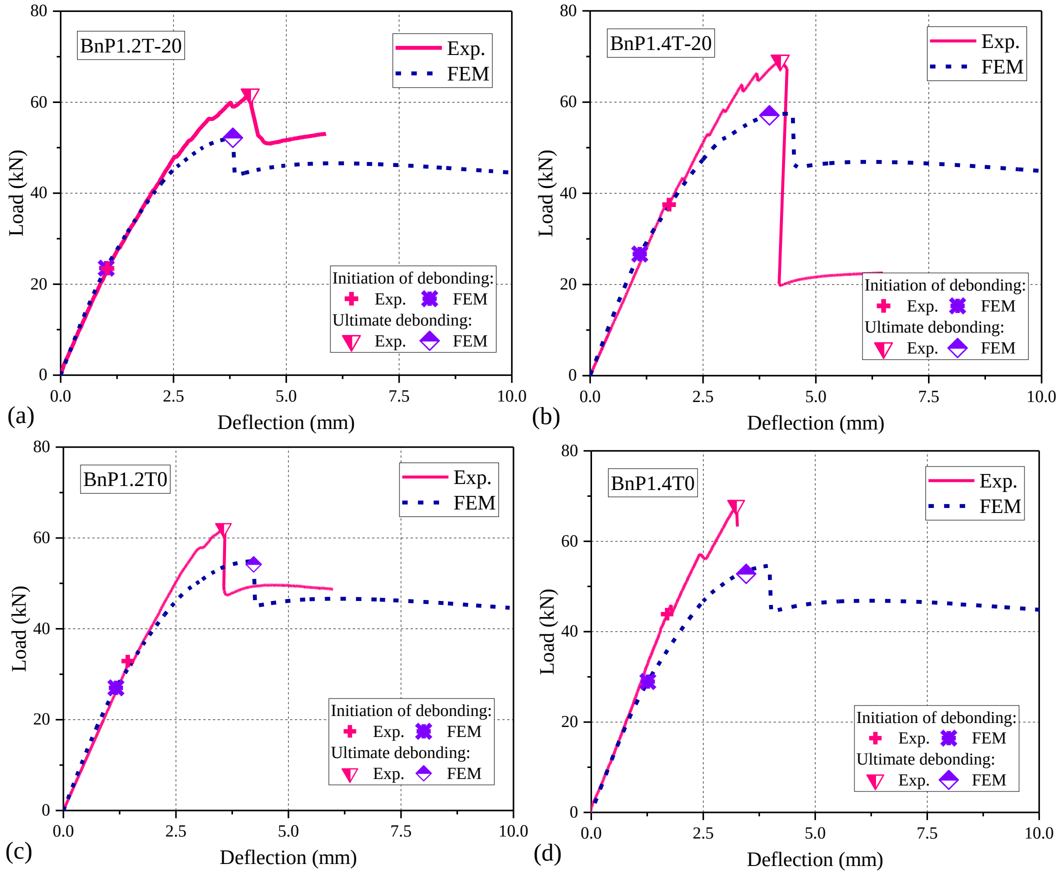

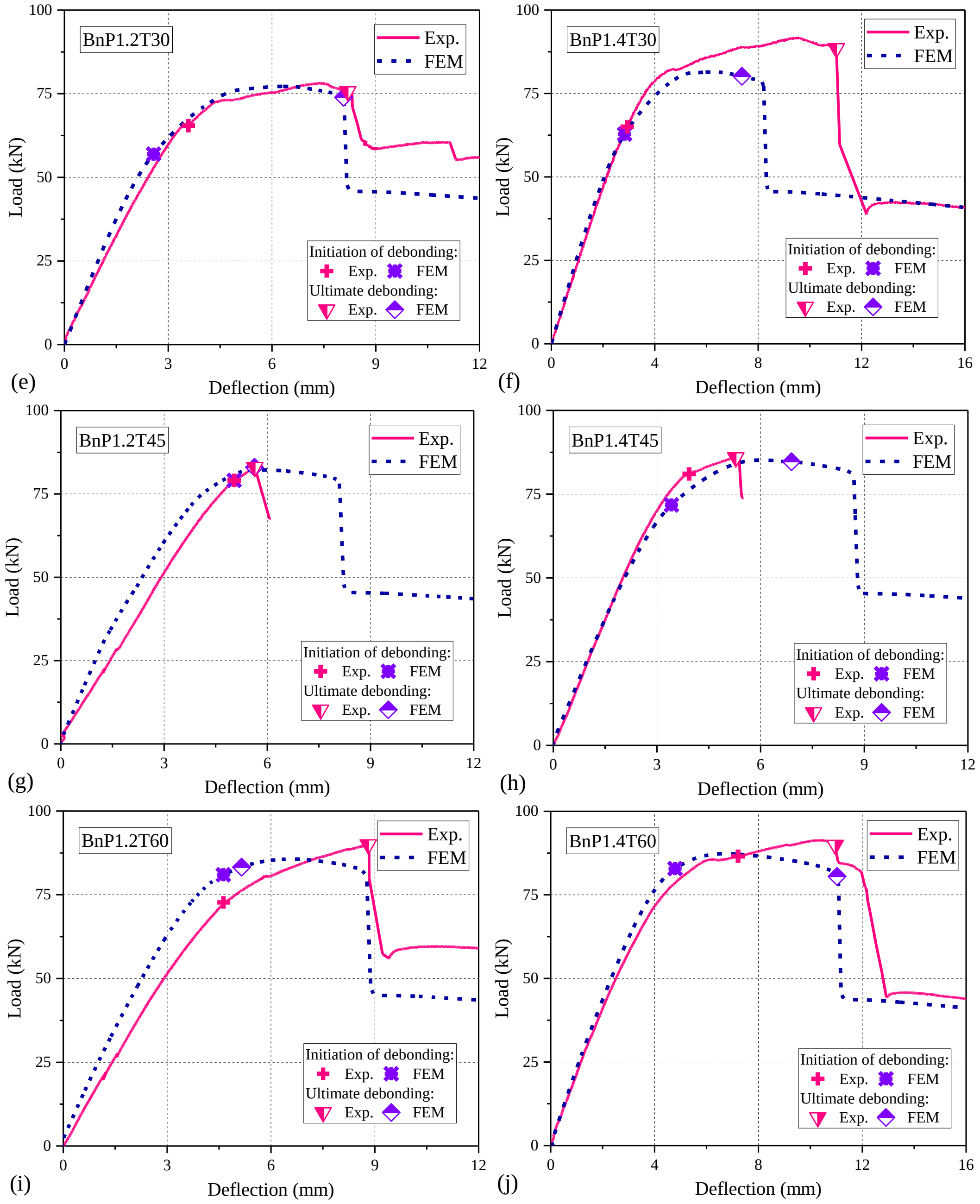
(e)
BnP1.2T30
Exp.
FEM
Initiation of debonding:
Exp. FEM
Ultimate debonding:
Exp. FEM
Load (kN)
Deflection (mm)
0
25
50
75
100
0
3
6
9
12
(f)
BnP1.4T30
Exp.
FEM
Initiation of debonding:
Exp. FEM
Ultimate debonding:
Exp. FEM
Load (kN)
Deflection (mm)
0
25
50
75
100
0
4
8
12
16
(g)
BnP1.2T45
Exp.
FEM
Initiation of debonding:
Exp. FEM
Ultimate debonding:
Exp. FEM
Load (kN)
Deflection (mm)
0
25
50
75
100
0
3
6
9
12
(h)
BnP1.4T45
Exp.
FEM
Initiation of debonding:
Exp. FEM
Ultimate debonding:
Exp. FEM
Load (kN)
Deflection (mm)
0
25
50
75
100
0
3
6
9
12
(i)
BnP1.2T60
Exp.
FEM
Initiation of debonding:
Exp. FEM
Ultimate debonding:
Exp. FEM
Load (kN)
Deflection (mm)
0
25
50
75
100
0
3
6
9
12
(j)
BnP1.4T60
Exp.
FEM
Initiation of debonding:
Exp. FEM
Ultimate debonding:
Exp. FEM
Load (kN)
Deflection (mm)
0
25
50
75
100
0
4
8
12
16

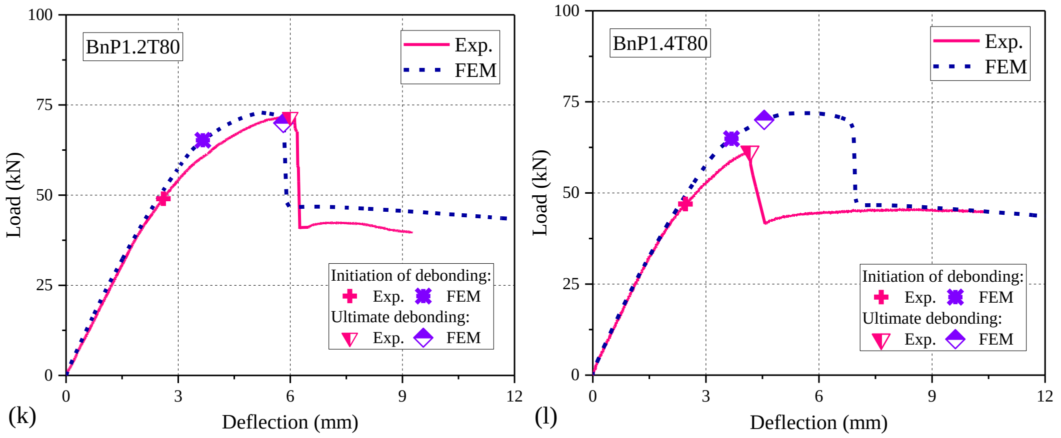

Fig. 8-29 Comparison of load-deflection curves obtained from experiments and FE modeling: a) BnP1.2T-20; b) BnP1.4T-20; c) BnP1.2T0; d) BnP1.4T0; e) BnP1.2T30; f) BnP1.4T30; g) BnP1.2T45; h) BnP1.4T45; i) BnP1.2T60; j) BnP1.4T60; k) BnP1.2T80; l) BnP1.4T80.

At -20°C and 0°C, the flexural stiffness of CFRP-strengthened steel beams predicted by FE modeling after the initiation of interfacial debonding was lower than the experimental data (**Fig. 8-29 a, b, c & d**), with a relatively large difference comparing to other temperatures. This large difference was mainly due to neglection of the temperature-dependent properties of steel and the experimental measurement. As reported in previous study (Rokilan and Mahendran 2020), the average elastic modulus and yielding strength of normal strength steel (i.e., with yielding strength as 333 MPa at 20 ℃) were increased by 1.8% and 9.4%, respectively, as the temperature decreased from 20°C to -10°C. These values were further increased by 4.9% and 18.1%, as the temperature decreased to -30°C.

8.4.2.2 Debonding load

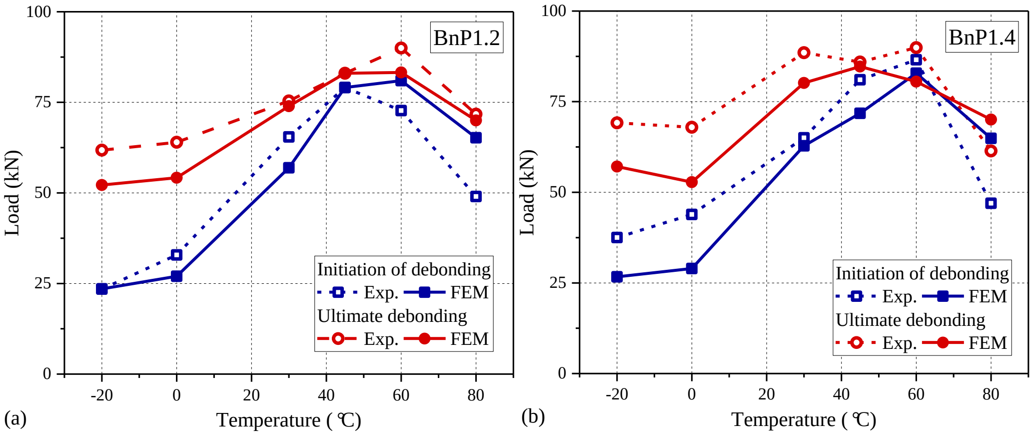

Fig. 8-30 Comparison of load at initiation and ultimate debonding obtained from experiments and FE modeling: a) BnP1.2; b) BnP1.4.

Fig. 8-30 compares the experimental and FE predicted loads at initiation and ultimate debonding states. Despite some scatters, the variation of the load-carrying capacities predicted by the FE modeling was in similar trend as the experimental data.

8.4.2.3 CMOD-load curves

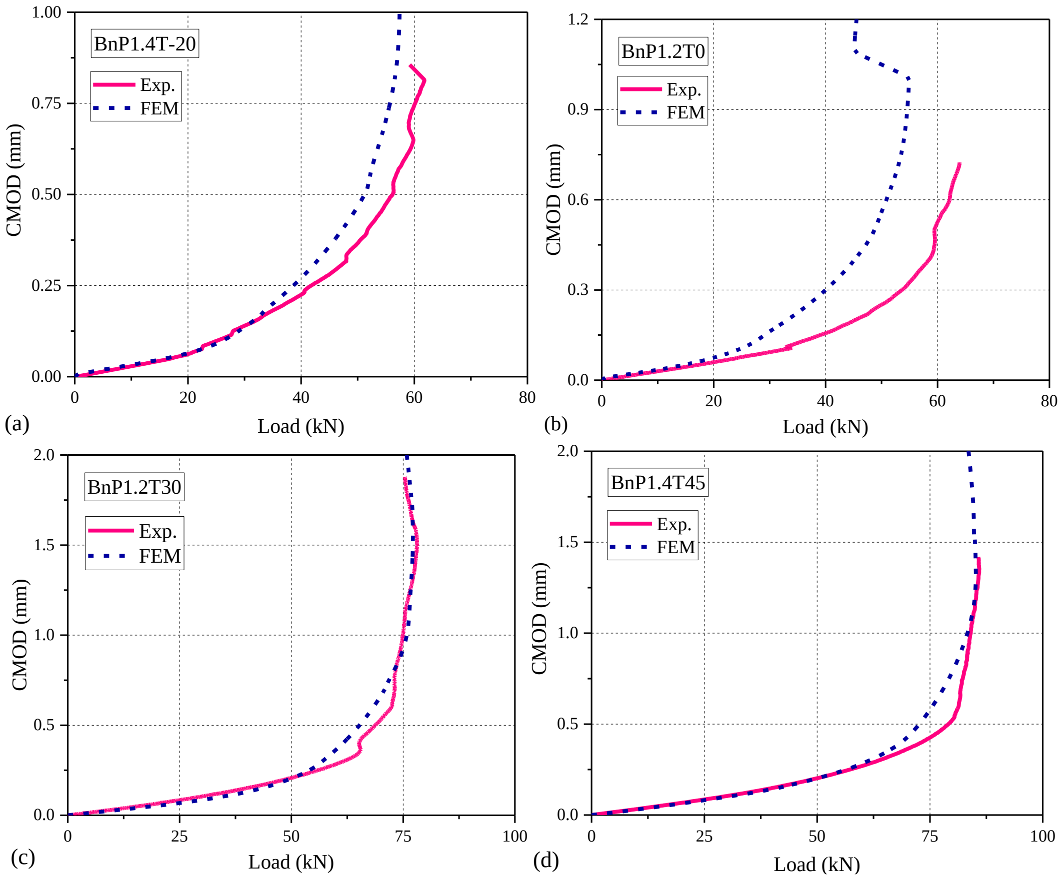

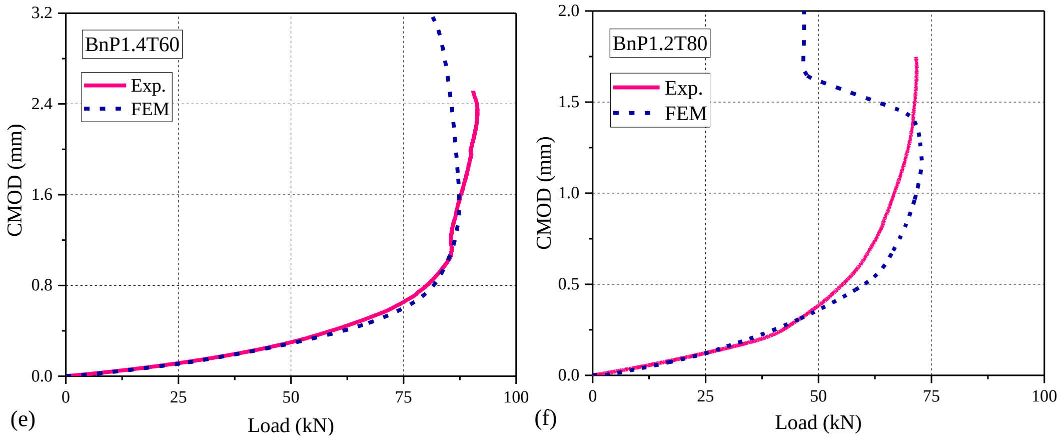

Fig. 8-31 Comparison of CMOD-load relationships obtained from experiments and FE modeling: a) BnP1.4T-20; b) BnP1.2T0; c) BnP1.2T30; d) BnP1.4T45; e) BnP1.4T60; f) BnP1.2T80.

Fig. 8-31 compares the experimental and FE predicted CMOD-load curves of CFRP-retrofitted steel beams at different temperatures. The FE results are also in close agreement with the experimental data, demonstrating that the crack-opening behavior in the strengthened beams could be well predicted.

8.4.2.4 Strain distributions in the CFRP plate

Fig. 8-32 shows the experimental and FE predicted strain distributions in the CFRP plate before applying the mechanical loading under two extreme temperatures (i.e., -20 and 80°C). It should be noted that the thermal deformation of the specimens was very small and the property of the strain gauges was sensible to the temperature variation, thus the CFRP strains exhibited significant scatter. Nevertheless, overall the predicted CFRP strains are in close agreement with the measured data.

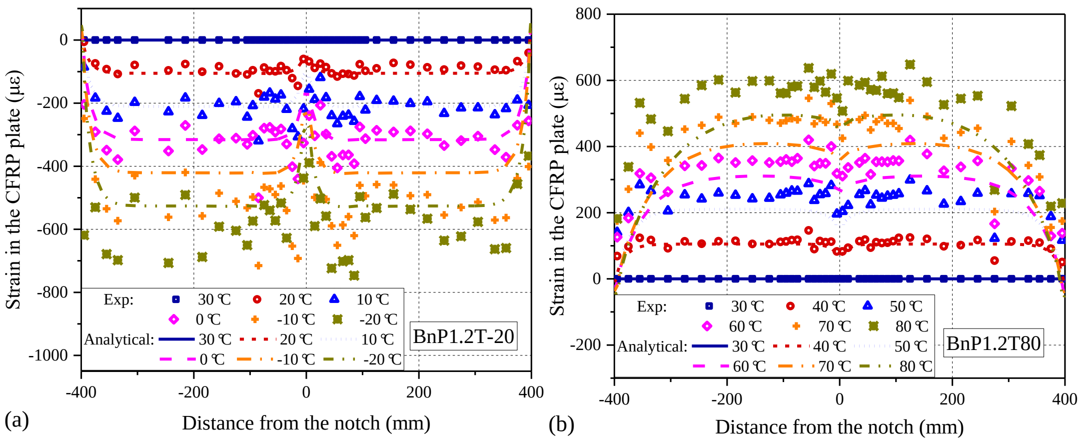

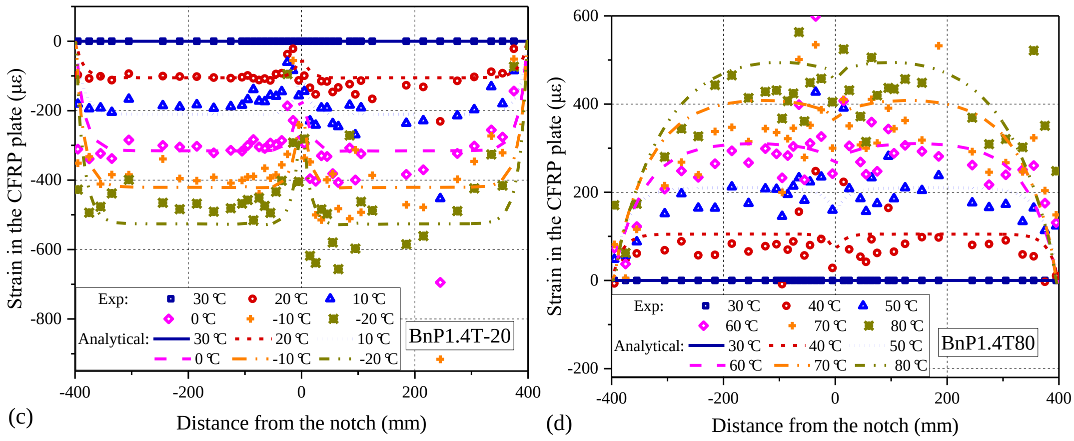

Fig. 8-32 Comparison of the experimental and FE predicted strain distributions in the CFRP plate under thermal loading only: a) BnP1.2T-20; b) BnP1.2T80; c) BnP1.4T-20; d) BnP1.4T80.

Fig. 8-33 compares the strain distributions in the CFRP plate that were obtained from the experiments and FE modeling. In general, the agreement is acceptable although relatively large scatters are observed near the notched section, where the enhanced local bond behavior exists. The deformation stage evolutions in the CFRP-retrofitted steel beams, including *E*, *E-S* and *E-S-D* stages, were well captured by the FE modeling.

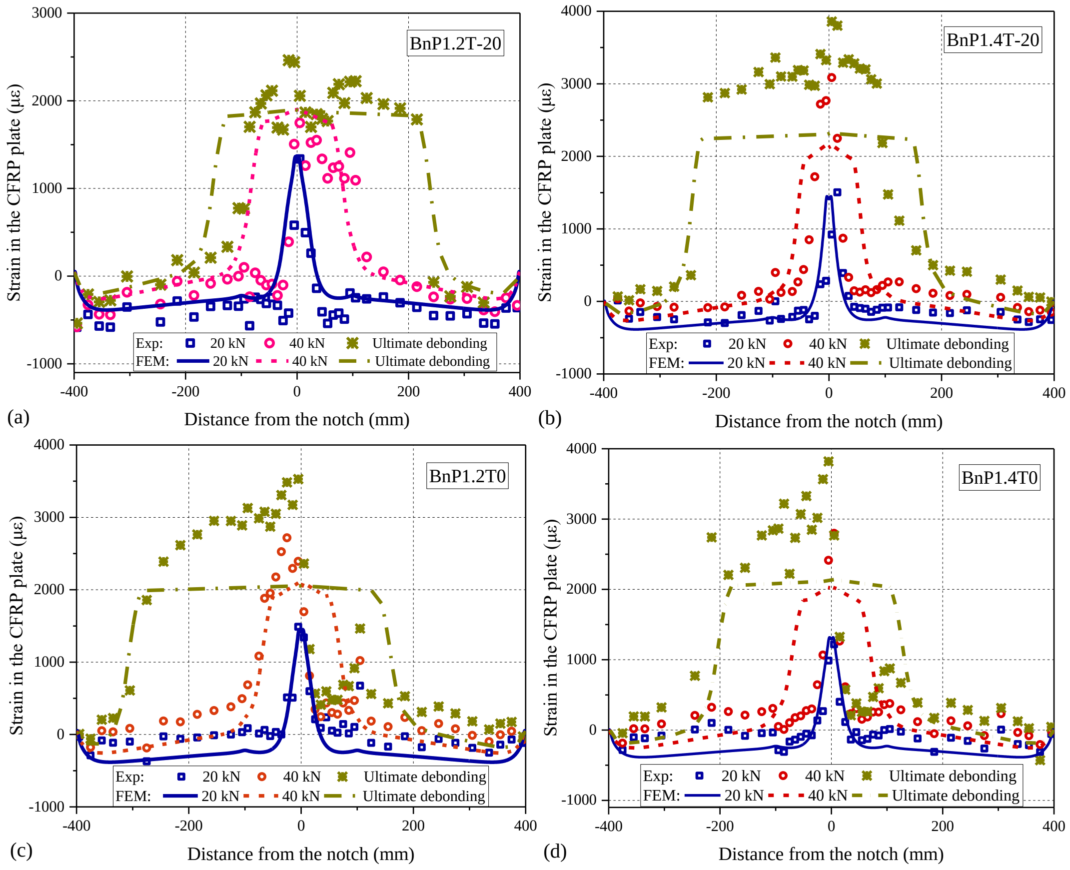

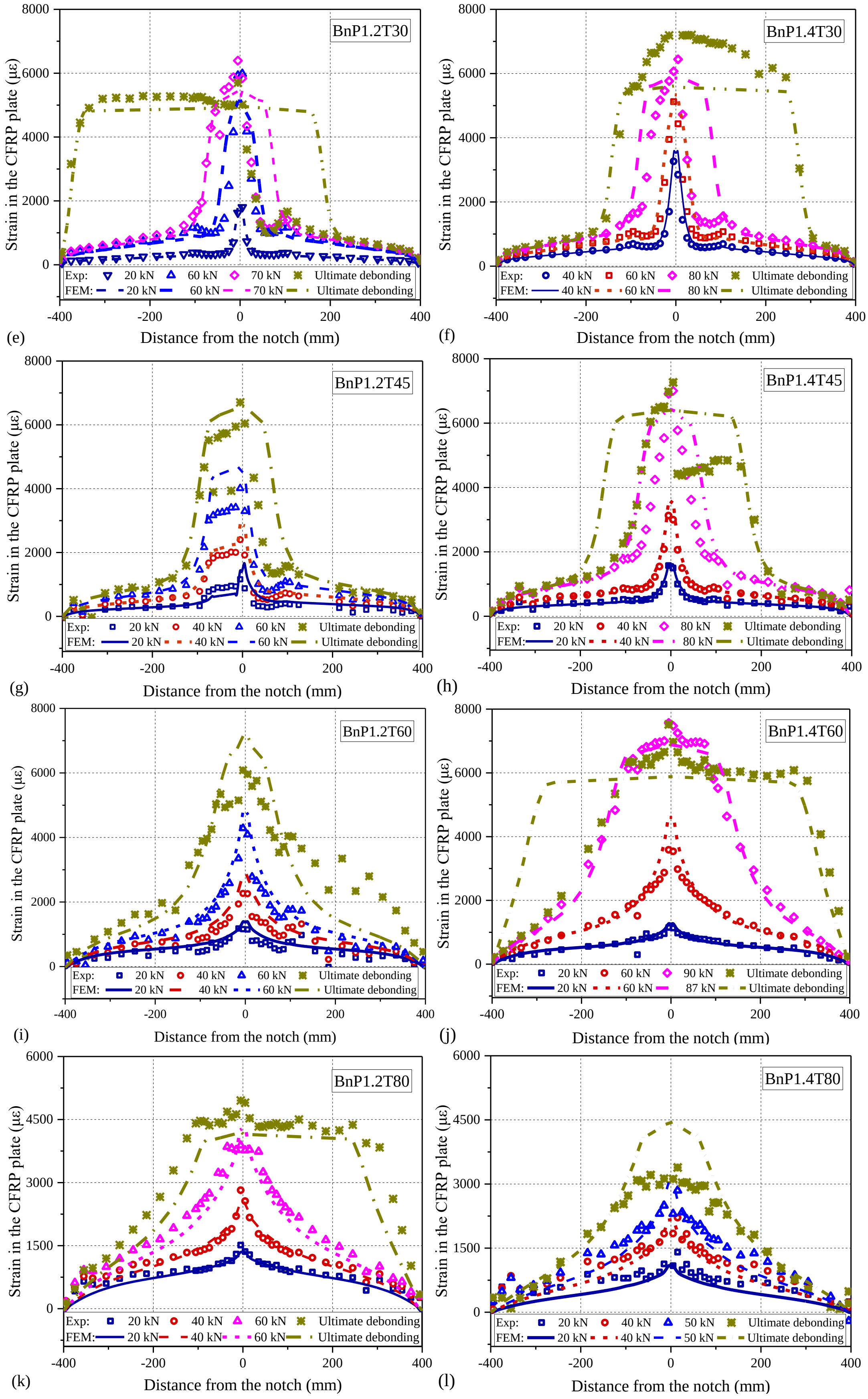

Fig. 8-33 Comparison of the experimental and FE predicted strain distributions in the CFRP plate: a) BnP1.2T-20; b) BnP1.4T-20; c) BnP1.2T0; d) BnP1.4T0; e)

BnP1.2T30; f) BnP1.4T30; g) BnP1.2T45; h) BnP1.4T45; i) BnP1.2T60; j) BnP1.4T60; k) BnP1.2T80; l) BnP1.4T80.

8.5. CONCLUSIONS

In this chapter, the structural performance of CFRP-retrofitted steel beams under flexural loading and corresponding interfacial behaviors were tested within the temperature range of -20 ℃ to 80 ℃. The following conclusions can be reached based on the experimental studies and FE modeling:

a) The load-carrying capacity of CFRP-retrofitted steel beams increased when the temperature increased from -20°C to the glass transition temperature of the bonding material (i.e., 60°C) but decreased significantly at the higher temperatures of 80°C. The debonding load was highly relevant to the interfacial fracture energy of the CFRP-to-steel interface in mode II direction.

b) The strengthening efficiency of CFRP plate in restricting the CMOD could be seriously compromised at both very low (e.g., -20°C, 0°C) and very high (e.g., 80°C) temperatures, because of the increased brittleness of bonding adhesive at decreased temperatures and decreased interfacial shear stiffness of the interface at increased temperatures.

c) The change of interfacial shear stiffness at different temperatures was associated with the change of elastic modulus of the bonding material. The interfacial fracture energy increased from -20°C to 60°C but dropped significantly at 80°C.

d) The structural performance of FRP-retrofitted steel beams at different temperatures could be accurately predicted by the proposed FE model, in which the effect of thermal stress and temperature-dependent bond properties were appropriately considered.

8.6. REFERENCES

Abaqus 6.14 (2014) "Documentation." Providence, RI, USA: Dassault Systemes Simulia Corporation.

Agbo, S., Imanpour, A., Li, Y., Kainat, M., Yoosef-Ghodsi, N., Cheng, J., and Adeeb, S. (2020). "Development of a Tensile Strain Capacity Predictive Model for API X42 Welded Vintage Pipelines." *Journal of Pressure Vessel Technology*.

Agbo, S., Lin, M., Ameli, I., Imanpour, A., Duan, D.M., Cheng, J.R., and Adeeb, S. (2019). "Evaluation of the effect of internal pressure and flaw size on the tensile strain capacity of X42 vintage pipeline using damage plasticity model in extended finite element method (XFEM)." In Proceeding of Pressure Vessels and Piping Conference, American Society of Mechanical Engineers.

Alexander JG, C.R. (1996). "Shear strengthening of small scale concrete beams with carbon fibre reinforced plastic sheets. ." In Proceeding of Annual Conference of Canadian Society for Civil Engineering 167-178.

Amada, S., and Satoh, A. (2000). "Fractal analysis of surfaces roughened by grit blasting." *Journal of Adhesion and Science and Technology*, 14(1), 27-41.

Ameli, I., Asgarian, B., Lin, M., Agbo, S., Cheng, R., Duan, D. and Adeeb, S. (2019). "Estimation of the CTOD-crack growth curves in SENT specimens using the eXtended finite element method." *International Journal of Pressure Vessels and Piping*, 169, 16-25.

ASTM-A370 (2017). "Standard Test Methods and Definitions for Mechanical Testing of Steel Products." West Conshohocken, Philadelphia (PA): ASTM International.

ASTM-D3039 (2017). "Standard Test Method for Tensile Properties of Polymer Matrix Composite Materials." West Conshohocken, Philadelphia (PA): ASTM International.

ASTM-D7028 (2007). "Standard Test Method for Glass Transition Temperature (DMA Tg) of Polymer Matrix Composites by Dynamic Mechanical Analysis (DMA)." West Conshohocken, Philadelphia (PA): ASTM International.

Biscaia, H.C. (2019). "The influence of temperature variations on adhesively bonded structures: A non-linear theoretical perspective." *International Journal of Non-Linear Mechanics*, 113, 67-85.

Biscaia, H.C., Chastre, C., Viegas, A., and Franco, N. (2015). "Numerical modelling of the effects of elevated service temperatures on the debonding process of FRP-to-concrete bonded joints." *Composites Part B: Engineering*, 70, 64-79.

BS ISO-11359 (1999). "Plastics: thermomechanical analysis (TMA). Part 2: determination of coefficient of linear thermal expansion and glass transition temperature."

Byfield, M.P., Davies, J.M., and Dhanalakshmi, M. (2005). "Calculation of the strain hardening behaviour of steel structures based on mill tests." *Journal of Constructional Steel Research*, 61(2), 133-150.

Chen, T., and Huang, C. (2019). "Fatigue tests on edge cracked four-point bend steel specimens repaired by CFRP." *Composite Structures*, 219, 31-41.

Colombi, P., and Fava, G. (2015). "Experimental study on the fatigue behaviour of cracked steel beams repaired with CFRP plates." *Engineering Fracture Mechanics*, 145, 128-142.

Dai, J.G., Gao, W.Y., and Teng, J.G. (2013). "Bond-Slip Model for FRP Laminates Externally Bonded to Concrete at Elevated Temperature." *Journal of Composites for Construction*, 17(2), 217-228.

De Lorenzis, L., Fernando, D., and Teng, J.G. (2013). Coupled mixed-mode cohesive zone modeling of interfacial debonding in simply supported strengthened beams. *International Journal of Solids and Structures*, 50(14-15), 2477-2494.

Deng, J., Jia, Y.H., and Zheng, H.Z. (2016). "Theoretical and experimental study on notched steel beams strengthened with CFRP plate." *Composite Structures*, 136, 450-459.

Deng, J., and Lee, M.M.K. (2007). "Behaviour under static loading of metallic beams reinforced with a bonded CFRP plate." *Composite Structures*, 78(2), 232-242.

Deng, J., Li, J., and Zhu, M. (2022). "Fatigue behavior of notched steel beams strengthened by a prestressed CFRP plate subjected to wetting/drying cycles." *Composites Part B: Engineering*, 230, 109491.

Deng, J., Li, J.H., Wang, Y., and Xie, W.Z. (2018). "Numerical study on notched steel beams strengthened by CFRP plates." *Construction and Building Materials*, 163, 622-633.

Fernando, D., Teng, J.G., Yu, T., and Zhao, X.L. (2013). "Preparation and Characterization of Steel Surfaces for Adhesive Bonding." *Journal of Composites for Construction*, 17(6).

Fernando, N.D. (2010). "Bond behaviour and debonding failures in CFRP-strengthened steel members." The Hong Kong Polytechnic University.

Firmo, J.P., Correia, J.R., Pitta, D., Tiago, C., and Arruda, M.R.T. (2015). "Experimental characterization of the bond between externally bonded reinforcement (EBR) CFRP strips and concrete at elevated temperatures." *Cement and Concrete Composites*, 60, 44-54.

Fu, B., Teng, J.G., Chen, G.M., Chen, J.F., and Guo, Y.C. (2018). "Effect of load distribution on IC debonding in FRP-strengthened RC beams: Full-scale experiments." *Composite Structures*, 188, 483-496.

Gao, W., Teng, J., and Dai, J.G. (2012). "Effect of temperature variation on the full-range behavior of FRP-to-concrete bonded joints." *Journal of composites for construction*, 16(6), 671-683.

Hmidan, A., Kim, Y.J., and Yazdani, S. (2011). "CFRP Repair of Steel Beams with Various Initial Crack Configurations." *Journal of Composites for Construction*, 15(6), 952-962.

Hojjati-Talemi, R., Cooreman, S., and Van Hoecke, D. (2018). "Finite element simulation of dynamic brittle fracture in pipeline steel: A XFEM-based cohesive zone approach." *In Proceeding of the Institution of Mechanical Engineering Part L-Journal of Materials*, 232(5), 357-370.

Ko, H., Matthys, S., Palmieri, A., and Sato, Y. (2014). "Development of a simplified bond stress–slip model for bonded FRP–concrete interfaces." *Construction and Building Materials*, 68, 142-157.

Krzywoń, R. (2017). "Behavior of EBR FRP Strengthened Beams Exposed to Elevated Temperature." *Procedia Engineering*, 193, 297-304.

Lin, M., Agbo, S., Cheng, J.R., Yoosef-Ghodsi, N., and Adeeb, S. (2017) "Application of the extended finite element method (XFEM) to simulate crack propagation in pressurized steel pipes." In Proceeding of Pressure Vessels and Piping Conference, American Society of Mechanical Engineers, V03BT03A024.

Lin, M., Agbo, S., Duan, D.M., Cheng, J.R., and Adeeb, S. (2020). "Simulation of crack propagation in API 5L X52 pressurized pipes using XFEM-based cohesive segment approach." *Journal of Pipeline Systems Engineering and Practice*, 11(2), 04020009.

Liu, P., Zhang, B., and Zheng, J. (2012). "Finite element analysis of plastic collapse and crack behavior of steel pressure vessels and piping using XFEM." *Journal of failure analysis and prevention*, 12(6), 707-718.

Liu, X. (2017). "Numerical and Experimental Study on Critical Crack Tip Opening Dis-Placement of X80 Pipeline Steel." *Mechanics*, 23(2), 204-208.

Mathworks. 2021. "*MATLAB version 9.10.0.1602886 (R2021a).*" Natick, MA: Mathworks

Nguyen, T.C., Bai, Y., Zhao, X.L., and Al-Mahaidi, R. (2011). "Mechanical characterization of steel/CFRP double strap joints at elevated temperatures." *Composite Structures*, 93(6), 1604-1612.

Okodi, A., Li, Y., Cheng, R., Kainat, M., Yoosef-Ghodsi, N., and Adeeb, S. (2020). "Crack Propagation and Burst Pressure of Pipeline with Restrained and Unrestrained Concentric Dent-Crack Defects Using Extended Finite Element Method." *Applied sciences*, 10(21), 7554.

Okodi, A., Lin, M., Yoosef-Ghodsi, N., Kainat, M., Hassanien, S., and Adeeb, S. (2020). "Crack propagation and burst pressure of longitudinally cracked pipelines using extended finite element method." *International Journal of Pressure Vessels and Piping*, 184, 104115.

Othman, D., Stratford, T., and Bisby, L. (2013). "A Comparison of on-site and elevated temperature cure of an FRP strengthening adhesive." *In Proceeding* of the FRPRCS11, UM, Guimar ães.

Paredes, M., Wierzbicki, T., and Zelenak, P. (2016). "Prediction of crack initiation and propagation in X70 pipeline steels." *Engineering Fracture Mechanics*, 168, 92-111.

Rokilan, M., and Mahendran, M. (2020). "Sub-zero temperature mechanical properties of cold-rolled steel sheets." *Thin-Walled Structures*, 154, 106842.

Sahin, M.U., and Dawood, M. (2016). "Experimental Investigation of Bond between High-Modulus CFRP and Steel at Moderately Elevated Temperatures." *Journal of Composites for Construction*, 20(6), 04016049.

Schiavone, A., Abeygunawardana-Arachchige, G., and Silberschmidt, V.V. (2016). "Crack initiation and propagation in ductile specimens with notches: experimental and numerical study." *Acta Mechanica*, 227(1), 203-215.

Shahzamanian, M. M., Meng, L, Muntaseer, K., Nader, Y. G., Samer, A. (2021) "Systematic literature review of the application of extended finite element method in failure prediction of pipelines." *Journal of Pipeline Science and Engineering*, 2021. 1(2): p. 241-251.

Teng, J.G., Fernando, D., and Yu, T. (2015). "Finite element modelling of debonding failures in steel beams flexurally strengthened with CFRP laminates." *Engineering Structures*, 86, 213-224.

Yao, Y., Yang, Y., He, Z., and Wang, Y. (2018). "Experimental study on generalized constitutive model of hull structural plate with multi-parameter pitting corrosion." *Ocean Engineering*, 170, 407-415.

Yu, Q.Q., and Wu, Y. F. (2017). "Fatigue Strengthening of Cracked Steel Beams with Different Configurations and Materials." *Journal of Composites for Construction*, 21(2).

Zeng, J.J., Gao, W.Y., and Liu, F. (2018). "Interfacial behavior and debonding failures of full-scale CFRP-strengthened H-section steel beams." *Composite Structures*, 201, 540-552.

Zhang, X., Okodi, A., Tan, L., Leung, J., and Adeeb, S. (2020). "Failure Pressure Prediction of Crack in Corrosion Defects in 2D by Using XFEM." In Proceeding of Pressure Vessels and Piping Conference, American Society of Mechanical Engineers.

Zhao, Z., Zhang, H., Xian, L., and Liu, H. (2020). "Tensile strength of Q345 steel with random pitting corrosion based on numerical analysis." *Thin-Walled Structures*, 148.

Zhou, H., Fernando, D., Torero, J. L., Torres, J. P., Maluk, C., and Emberley, R. (2020). "Bond Behavior of CFRP-to-Steel Bonded Joints at Mild Temperatures: Experimental Study." *Journal of Composites for Constructio*n, 24(6), 04020070.

CHAPTER 9

CONCLUSIONS AND PROSPECTS

9.1. CONCLUSIONS

9.1.1 Conclusions on the Effect of Thermal Stress on the Plate-end Debonding mechanisms of CFRP-strengthened Steel Beams

The effect of interfacial thermal stress on the plate-end debonding mechanism of CFRP-strengthened steel beams has been theoretically analyzed in **Chapters 3** and **4**. Two new analytical solutions are proposed based on pure mode II and coupled mixed-mode failure criteria, respectively. The analytical solutions are validated by comparing them with the FE results. Explicit closed-form expressions of the interfacial shear stress, interfacial slip, and axial stress in the CFRP plates have been derived. According to the results and discussion presented in **Chapters 3** and **4**, the following conclusions can be drawn:

a) The interfacial behavior between the steel beam and FRP plate can be affected by the temperature variation. The interfacial thermal stress at elevated temperatures is in the same direction as that generated by mechanical loading at the plate end and thus accelerates the deformation process of the interface.

b) The plate-end debonding load of FRP-strengthened steel beam is significantly decreased by the thermal stress at elevated temperatures. As such, special attention should be paid to the design of FRP-strengthened beams when the service temperature increase is expected.

c) The thermal stress is more significant when a thicker and stiffer FRP plate is adopted to strengthen the steel beam, for which case a longer FRP plate and additional anchorages are preferred to reduce the negative effect of temperature increase.

d) The proposed coupled mixed-mode analysis can accurately predict of the interfacial behavior and debonding load of FRP-strengthened steel beams under combined mechanical and thermal loading. In comparison, the single mode II analysis tends to overestimate the debonding load, because of the neglection of the interfacial normal stress effect.

9.1.2 Conclusions on the Effect of Thermal Stress on the Intermediate Crack-induced Debonding Loads of CFRP-retrofitted Steel Beams

The effect of thermal stress on the interfacial behavior, IC debonding load and the SIF at the notch tip of the FRP-retrofitted notched steel beam has been investigated based on a new proposed analytical solution in **Chapter 5**. The analytical solution is also validated by comparing the analytical and FE results. Explicit closed-form expressions of the interfacial shear stress, and axial force in the CFRP plates have been proposed. Based on the results and discussion presented in **Chapter 5**, the following conclusions can be drawn:

a) The interfacial thermal stress generated by the temperature increase is in the opposite direction as that generated by the mechanical loading near the intermediate crack locations and leads to an enhanced IC debonding load.

b) The stress intensity factor (SIF) at the notch tip decreases with the service temperature increase and vice versa, which should be appropriately considered in the FRP-retrofitted cracked steel beams under fatigue loading.

c) Regarding the IC debonding process occurred in the FRP-retrofitted steel beam under a specific level of mechanical loading, a temperature increase/decrease may alleviate or accelerate the interfacial stress concentrations, leading to an enhanced or declined IC debonding load, respectively.

d) The thermal stress effects are more pronounced when a thicker and stiffer FRP plate is applied for the retrofitting.

9.1.3 Conclusions on the Bond Behavior of CFRP-to-steel Bonded Joints at Different Service Temperatures

The double-lap shear tests of CFRP-to-steel bonded joints at temperatures ranging from -20 ℃ to 60 ℃ were presented in **Chapter 6**. The test results were examined and compared, including the failure modes, debonding loads, load-displacement curves, CFRP strain distributions, interfacial shear stress, and slip responses. Also, a bilinear local bond-slip model was established to describe the relationship between the shear stress and the interfacial slip (i.e., bond-slip relationship) of the bond interface at different service temperatures. An FE model was proposed to predict the bond behavior and the debonding loads of the bonded joint at different service temperatures and was validated by comparing the experimental and FE results. Based on the results and discussions presented in this chapter, the following conclusions can be drawn:

a) The service temperature variations have two different effects on the bond behavior and the related debonding loads of the bonded joint at different service temperatures, including the effect of interfacial thermal stresses and the changes in the local bond-slip behavior.

b) The debonding loads of the bonded joint are increased from a low service temperature to room temperature and then decreased at a high service temperature close to the glass transition temperature of the bonding adhesive.

c) The bilinear bond-slip model can describe the relationships between the shear stress and the interfacial slip at different service temperatures. At low service temperatures, the softening portion of the bilinear model can be neglected, and thus the bond-slip model can be simplified as the elastic-brittle model.

d) The elastic stiffness and the peak shear stress of the local bond-slip model are generally reduced with the service temperature increase, while the interfacial fracture energy decreases at both low and high service temperatures.

e) The good agreement between the test results and the corresponding FE predictions has demonstrated the reliability and accuracy of the proposed FE model.

9.1.4 Conclusions on the Structural Behavior of CFRP-strengthened Steel Beams at Different Service Temperatures: Experimental Study and FE Modeling

The structural performances of CFRP-strengthened steel beams and the correponding interfacial behaivors have been examined at temperatures ranging from -20 ℃ to 60 ℃ in **Chapter 7**. An FE model has been proposed for reproducing the interfacial behavior and the structural performance of CFRP-strengthened steel beams at various temperatures, and the bond-slip relationships determined in **Chapter 6** is adopted as the input data. The following conclusions can be reached based on the experimental studies and FE modeling:

a) Steel beams strengthened by a shorter CFRP plate (i.e., 300 mm) are failed by the plate-end debonding at all temperatures. The plate-end debonding load is increased at decreased temperatures but decreased at 60ºC. The plate-end debonding is suppressed at temperatures ranging from -20ºC to 45ºC by adopting a longer CFRP plate (i.e., 600 mm); however, it still occurred at 60ºC, corresponding to a significantly decreased ultimate load.

b) The thermally-induced softening in the bonding adhesive at 60ºC resulted in the deteriorated composite action in CFRP-strengthened steel beams, increased the interfacial slips at the plate ends, and decreased the utilization efficiency of the CFRP's tensile strength.

c) The structural performance of CFRP-strengthened steel beams at different temperatures could be well predicted by the proposed FE model, in which the temperature-dependent bond properties and thermal-induced deformation incompatibility were appropriately considered.

9.1.5 Conclusions on the Intermediate Crack-induced Debonding in CFRP-retrofitted Notched Steel Beams at Different Service Temperatures

The structural performances of CFRP-retrofitted steel beams under flexural loading and the corresponding interfacial behaviors were investigated in the temperature range of -20 ℃ to 80 ℃ in **Chapter 8**. In addition, finite element models were established to reproduce the structural behaviors. Based on the experimental studies and FE modeling, the following conclusions can be drawn:

a) The load capacities at the initial and ultimate debonding of CFRP-retrofitted steel beams are increased when the temperatures are changed from -20°C to the glass transition temperature of the bonding adhesive (i.e., 60°C), but decrease significantly at a higher temperature (i.e., 80°C).

b) The ultimate debonding load of the CFRP-retrofitted steel beam is found to be significantly affected by the interfacial fracture energy of the CFRP-to-steel interface in the mode II direction.

c) The strengthening efficiency of the CFRP plate in restricting the CMODs is seriously compromised at both very low (e.g., -20°C, 0°C) and very high (e.g., 80°C) temperatures, because of the increased brittleness of the bonding adhesive at very low temperatures and the reduced interfacial shear stiffness at very high temperatures.

d) A new formula is proposed for deriving the local bond-slip behavior of the CFRP-retrofitted steel beam, based on the measured CFRP strain. As a result, it has been found that, the changes in interfacial shear stiffness at different temperatures are related to the variations of elastic modulus of the bonding adhesive, while the interfacial fracture energy increases from -20°C to 60°C but decreases significantly at 80°C.

9.1.6 Major Conclusions

The following major conclusions were drawn from the research outputs of this thesis. According to the theoretical analyses and discussions presented in **Chapters 3**, **4** and **5**, the following conclusions can be drawn:

a) The effect of thermal stress on the plate-end debonding load of FRP-strengthened un-notched steel beam is opposite to that on the IC debonding load of FRP-retrofitted notched steel beam.

b) The effect of thermal stress is more significant when a thicker and stiffer FRP plate is adopted to strengthen the steel beam. Thus, the longer and thinner FRP plates are preferred to minimize the negative thermal stress effect on the safety of FRP-strengthened steel beams.

According to the experimental studies and discussions presented in **Chapter 6**, **7** and **8**, the following conclusions can be drawn:

a) The changes in interfacial shear stiffness at different temperatures are related to the variations in the storage modulus of the bonding adhesive.

b) The debonding loads of the CFRP-to-steel double-lap joints and CFRP-retrofitted steel beams are highly relevant to the interfacial fracture energy.

c) The structural performances of CFRP-to-steel double-lap joints and CFRP-strengthened steel beams at different temperatures can be well predicted by the FE modeling, in which the temperature-dependent bond properties and thermal-induced deformation incompatibility are appropriately considered.

9.2. RECOMMENDATIONS FOR FUTURE RESEARCH

This dissertation has been primarily concerned with the effect of temperature variation on interfacial behaviors and resultant structural performances of CFRP-strengthened steel beams. The research presented in this dissertation has advanced the understanding of the thermal effect on the interfacial debonding mechanism and structural behavior of the CFRP-strengthened steel beams. Further research is required to alleviate the thermal effect and enhance the load-carrying capacity of the CFRP-strengthened steel beams at changed temperatures:

a) The thermal deformation incompatibility between the CFRP plate and steel substrate is relevant to the difference in CTEs of the CFRP plate and steel materials. Therefore, developing a special fiber type or stacking scheme (Dong *et al.* 2018) in the pultruded FRP laminate, at which the CTE is close to that of the steel, would be helpful to decrease the interfacial thermal stress.

b) The thermally-induced softening in the bonding adhesive further deteriorated the bond strength between the CFRP plate and steel beam at moderately elevated temperatures. Previous studies demonstrated that the bond characteristics at elevated temperatures could be enhanced by increasing the curing temperature (Bai *et al.* 2014) or adding carbon nanotubes (CNTs) into the bonding adhesive (Korayem *et al.* 2016). Further experiments need to be conducted to examine the enhanced structural behavior of CFRP-strengthened steel beams at elevated temperatures with the bonding adhesive enhanced by these two methods.

c) Silane creates a stronger chemical bond between the steel and the adhesive, which enhances the ductility of the bonding behavior between the FRP composite and steel substrate. The enhancement in the bond strength was observed in previous studies, especially for the specimens failed by the adhesive failure between bonding adhesive and steel substrate (Borrie *et al.* 2021). Further experiments need to be conducted to test the structural performances of FRP-strengthened steel beams in which silanes promote adhesion.

d) The experiments in this thesis proved the increased brittles of the bonding adhesive and the decreased interfacial fracture energy at subzero temperatures. Further research needs to be conducted to enhance the ductility of the epoxy resin at subzero temperatures, which is believed to significantly enhance the debonding load and ultimate deflection of the CFRP-strengthened steel beams.

e) The anchorage system has been proven to be efficient in suppressing the occurrence of interfacial debonding and enhancing the load-carrying capacity of CFRP-strengthened steel beams at normal temperatures (Yu and Wu 2018). The anchorage system shears partial of the interfacial stress, which was originally sustained solely by the bonding adhesive. The mechanical performance of the anchorage system will not be significantly deteriorated by the temperature change, when the force is transferred by mechanical fastening rather than adhesive bonding. Thus, the developing proper anchorage systems in the CFRP-strengthened steel beams would help to alleviate the effect of temperature variation on the structural performance of the CFRP-strengthened steel beams, especially when the bonding properties are seriously compromised.

Further, the research conducted in this thesis is based on theoretical analysis and laboratory experiments. However, the FRP-strengthened steel structures, which may experience significant seasonal and daily temperature variations, are mainly served in out-door environments, such as bridges. Further research is required to extend the current research for considering the complex environments and loading conditions during the service lives of FRP-strengthened steel beams.

a) The analytical solution is derived based on the linear elastic adherends assumption in current research. It does not refer to the full stress-strain response of the substrate steel beam and limits the range of application. The nonlinear property of the steel beam needs to be considered in future research.

b) The transverse shear deformation of the steel beam is not considered in the present analytical solutions. It may lead to some inaccuracy for a beam with a lower span-to-depth ratio. The deep beam theory needs to be adopted in further research to increase the accuracy of the analytical solutions.

c) The temperature variation is assumed to be uniformly distributed along the beam. However, the temperature variation may be concentrated on one point in some cases. The analytical solutions need to be improved for interpreting the effect of non-uniformly distributed thermal loading on the structural behavior of the FRP-strengthened steel beams.

d) For FRP-strengthened steel bridges, more consideration should be paid to fatigue performance. The thermal effect on the FRP-strengthened steel beams under fatigue loading needs to be analyzed in further research.

e) In the experimental and theoretical studies, the FRP plate is applied to the steel substrate, which has essentially no existing strain. However, in practice, there will be a load-induced strain in the steel beam before bonding the FRP plates. The effect of preload is not considered in the current study and should be considered in further research.

f) The different curing periods and curing environments in the application may result in different 'degrees of cure' of the bonding adhesive. While the difference in the 'degree of cure' may result in different bond properties at normal and changed temperatures. Effect of the 'degree of cure' on the bond behaviors at different temperatures should be clarified in future research.

g) During the experiment, about two hours are spent on heating the specimen from room temperature to the experimental temperature (60°C). The effect of the post-cure on bond behavior between FRP and steel plate should be taken into consideration in future research.

9.3. REFERENCES

Bai, Y., Nguyen, T.C., Zhao, X., and Al-Mahaidi, R. (2014). "Enhancement of steel/carbon fibre-reinforced polymer adhesively-bonded joints at elevated temperatures through curing." *Australian Journal of Structural Engineering*, 15(4), 367-376.

Borrie, D., Al-Saadi, S., Zhao, X. L., Singh Raman, R. K., and Bai, Y. (2021). "Effects of CNT modified adhesives and silane chemical pre-treatment on CFRP/steel bond behaviour and durability". *Construction and Building Materials*, 273, 121803.

Dong, C., Li, K., Jiang, Y., Arola, D., and Zhang, D. (2018). "Evaluation of thermal expansion coefficient of carbon fiber reinforced composites using electronic speckle interferometry." *Optics Express*, 26(1), 531-543.

Korayem, A.H., Chen, S.J., Zhang, Q.H., Li, C.Y., Zhao, X.L., and Duan, W.H. (2016). "Failure of CFRP-to-steel double strap joint bonded using carbon nanotubes modified epoxy adhesive at moderately elevated temperatures." *Composites Part-B: Engineering*, 94, 95-101.

Yu, Q.Q., and Wu, Y.F. (2018). "Fatigue retrofitting of cracked steel beams with CFRP laminates." *Composite Structures*, 192, 232-244.